Thermal Pressurization in EM-SAGD Projects

by

Sahar Ghannadi

A thesis submitted in partial fulfillment of the requirements for the degree of

Doctor of Philosophy (PhD)

in

Petroleum Engineering

Civil and Environmental Engineering, University of Alberta

Abstract

Inductive methods such as Electromagnetic Steam-Assisted Gravity Drainage (EM-SAGD) have been identified as a technically and economically feasible recovery method for shallow oil sands reservoirs with overburdens of more than 30 meters (Koolman et al., 2008). However, in EM-SAGD projects, the caprock overlying oil sands reservoirs is also electromagnetically heated along with the bitumen reservoir. Since permeability is low in Albertan thermal project caprock formations (i.e., the Clearwater shale formation in the Athabasca deposit and the Colorado shale formation in the Cold Lake deposit), the pore pressure resulting from the thermal expansion of pore fluids may not be balanced with the fluid loss due to flow and the fluid-volume changes due to pore dilation. In extreme cases, the water boils and the pore pressure increases dramatically as a result of the phase change in the water, causing profound effective stress reduction. Once this condition is established, pore pressure increases can lead to shear failure of the caprock, the creation of micro-cracks and hydraulic fractures, and to subsequent caprock integrity failure. It is typically believed that low permeability caprocks impede the transmission of pore pressure from the reservoir, making them more resistant to shear failure. In cases of induced thermal pressurization, low permeability caprocks are not always more resistant. In this study, analytical solutions are obtained for temperature and pore pressure rises due to the constant electromagnetic heating rate of the caprock. These analytical solutions show that pore pressure increases due to electromagnetic heating depend on permeability and compressibility of the caprock formation. For stiff or low-compressibility media, thermal pressurization can cause fluid pressures to approach total confining pressure, and shear strength to approach zero for low cohesive units of the caprock (units of the caprock with high silt and sand percentage) and sections of the caprock with pre-existing fracture with no cohesion (i.e., thermal liquefaction).

Acknowledgement

Dr. Rick Chalaturnyk is one of the most wonderful persons, I have known. I always wondered where does he find all the time and energy for his administrative duties and yet be available to provide advice on technical, as well as non-technical, matters. Rick allowed me to venture different terrains on my own, but always made sure that I did not go wayward. I will always remain indebted to him for his support and guidance throughout the course of my Ph.D. and hope to continue to benefit from his experience in the future.

Table of Contents

List of Tables

List of Figures.

NOMENCLATURE

$\wp_{coil}$ = electrical current flowing in coil wires, Amp.

$\vec{B}(t)$ = flux density, Tesla (T) (=Webers per square metre, or Wb/m^2).

c_s = solids in formation specific heat capacity, J/(kg·°C).

c_{sf} = bulk formation specific heat capacity, J/(kg·°C).

c_w = condensate or water specific heat capacity, J/(kg·°C).

$\vec{D}(t)$ = electrical flux density, C/m^2, or Coulombs/m^2.

$\vec{E}(t)$ = electric field strength, V/m.

$\bar{E}$ = root mean square value of electric field, V/m.

E = elastic modulus (Young's modulus) of the porous medium, Pa.

f_s = switching frequency, Hz.

G = formation shear modulus, Pa.

g = magnitude of the gravitational acceleration, m^2/sec.

H(t) = field intensity, A-turns/m.

H_{st} = steam enthalpy, J/kg.

H_w = water enthalpy, J/kg.

$\vec{J}_c$ = conductive current, A/m^2.

$\vec{J}_d$ = displacement current, A/m^2.

K = oil sand thermal conductivity, W/m·°C.

K = caprock thermal conductivity, W/(m ºC).

k = absolute permeability of the caprock, m^2.

K_s = bulk modulus of the solid grains, Pa.

K_b = bulk modulus of the porous medium, Pa.

K_{sf} = thermal conductivity coefficients of the solid-fluid composite, W/(m·°C).

K_{sf}^{st} = thermal conductivity coefficients of the medium saturated with steam, W/(m·°C).

K_{sf}^{w} = thermal conductivity coefficients of the medium saturated with water, W/(m·°C).

K_{fr} = bulk modulus of the fractured porous medium, Pa.

J_0 = current density at the inductor surface, A/m^2.

J_z = eddy current density in the z direction, A/m^2, or Amperes/m^2.

l_{coil} = coil length, m.

$L_{Hydraulic}$ = hydraulic diffusion length, m.

$L_{Thermal}$ = thermal diffusion length, m.

L_v = latent heat or specific enthalpy, J/kg.

M = longitudinal modulus of the medium, Pa.

Δm = mass of water vaporized, kg.

$\bar{n}$ = number of coil turns per unit length, turns/m.

$\bar{n}$ = number of coil turns per unit length, turns/m.

N = number of coil turns, no unit.

N_{pe} = Péclet number, no unit.

P = fluid pressure in the caprock matrix, Pa.

P_0 = initial pore pressure in caprock, Pa.

P_{EM} = total EM power radiated across the radius r, J/ (sec m^3).

$P_{inductive}$ = total induction power radiated across radius r, J/ sec·m^3.

P_{RF} = total RF power radiated across radius r, J/ sec·m^3.

$\bar{P}_{induction}$ = total induction power radiated across radius r, J/ sec·m^2.

$\overline{P}_{RF}$ = total RF power radiated across radius r, J/ sec·m^2.

P_{int} = pressure at the steam interface, Pa.

P_{sat} = pressure on the saturation curve at the steam interface, Pa.

ΔP = pressure drop in the formation, Pa.

q_{in} = inlet flow rate per volume of the control volume, 1/sec.

q_{out} = outlet flow rate per volume of the control volume, 1/sec.

q_z = Darcy flux, m/sec.

ΔQ = heat release from temperature drop in formation, J.

ΔQ_{solid} = heat release from temperature reduction in solids, J.

ΔQ_{steam} = heat release from temperature reduction in steam, J.

ΔQ_{water} = heat release from temperature reduction in water, J.

$\dot{Q}_{EM}$ = average volumetric electromagnetic heating rate, J/ (sec m^3).

$\dot{Q}_{Induction}$ = average volumetric inductive heating rate, J/ sec·m^3.

$\dot{Q}_{RF}$ = average volumetric RF heating rate, J/ sec·m^3.

r = distance from constant temperature boundary heat source, m.

r = distance from the inductor to the core, m.

$r_{Antenna}$ = mean radius of RF antenna, m.

r_{coil} = mean radius of coil turns, m.

S_w = caprock water saturation, fraction.

t = time, sec.

T_0 = initial caprock temperature, °C.

T_{int} = caprock temperature at the steam interface, °C.

T_r = initial reservoir temperature, °C.

T_{st} = steam injection temperature, °C.

T_{steam} = steam temperature, ºC.

V_{Fluid} = volume of fluid which contains the pore space, m^3.

V_{Pore} = volume of the pore space, m^3.

V_{Solid} = volume of solid, m^3.

V_{Total} = total volume of control volume including the pore space and solid, m^3.

V_y = velocity of the advancing front of the steam chamber, m/sec.

v_z = velocity of fluid in a porous medium in the z-direction, m/sec.

$\Delta V_{phasetransition}$ = volume change of the phase transition, m^3.

z = normal distance to the caprock interface in the vertical direction, m.

$z_{Antenna}$ = vertical distance from antenna centre, m.

z_{coil} = vertical distance from coil centre, m.

z_{inj} = vertical distance from injector, m.

z_{pro} = vertical distance from producer, m.

$z_{caprock}$ = caprock vertical distance from center of the coil, m.

$z_{interface}$ = steam interface vertical distance from the bottom of the caprock, m.

α_{Biot} = Biot's coefficient (or Biot-Willis coefficient), no unit.

β_s = compressibility of solid grains, 1/Pa.

β_f = compressibility of the fluid in pore space, 1/Pa.

$\underline{\beta}_{sf}$ = compressibility of the porous medium, 1/Pa.

β_{sf} = linear elastic compressibility of the porous medium, 1/Pa.

β_{st-w} = fluid phase compressibility due to phase change, 1/Pa.

β_{st}^{vap} = equivalent compressibility of the porous medium when water flashes to steam, 1/Pa.

β_w = compressibility of the water, 1/Pa.

Δ_w = ratio of thermal diffusivity to hydraulic diffusivity of water-saturated zone, no unit.

Δ_{st} = ratio of thermal diffusivity to hydraulic diffusivity of steam-saturated zone, no unit.

δ = penetration depth, m.

$\delta_{Induction}$ = penetration depth for induction process, m.

δ_{RF} = penetration depth for RF process, m.

ε_0 = permittivity of free space or vacuum, F/m.

ε_r = relative permittivity (or dielectric constant), no unit.

ε_v = volumetric dilation, no unit.

Φ = total flux within the inductor, Wb.

ϕ = porosity of the caprock, no unit.

γ = volumetric coefficient of thermal expansion, 1/ºC.

γ_f = volumetric coefficient of thermal expansion of the pore fluid, 1/ºC.

γ_s = volumetric coefficient of thermal expansion of the solid phase, 1/ºC.

γ_{sf} = volumetric coefficient of thermal expansion of the porous medium, 1/ºC.

γ_w = volumetric coefficient of thermal expansion of the water, 1/ºC.

γ_{sf}^{dr} = drained linear volumetric thermal expansion coefficient of the porous medium, 1/°C.

γ_{sf}^{u} = undrained linear volumetric thermal expansion coefficient of the porous medium, 1/°C.

η = pitch angle of the coil, Degrees.

$\kappa_{Hydraulic}$ = hydraulic diffusivity, m^2/sec.

$\kappa_{Thermal}$ = thermal diffusivity, m^2/sec.

$\kappa_{Thermal}^{st}$ = thermal diffusivity of steam-saturated caprock, m^2/sec.

$\kappa_{Thermal}^{w}$ = thermal diffusivity of water-saturated caprock, m^2/sec.

Λ = thermal pressurization factor, Pa/°C.

Λ_{st} = thermal pressurization factor when water encroached into caprock, Pa/°C.

Λ_{st}^{vap} = thermal pressurization factor when water flashes to steam, Pa/°C.

Λ_w = thermal pressurization factor in water-saturated caprock, Pa/°C.

Λ = thermal pressurization factor, Pa/°C.

μ_0 = magnetic permeability of free space or vacuum, H/m or Wb/(A m).

μ_f = viscosity of the pore fluid, Pa.sec.

μ_r = relative magnetic permeability, no unit.

μ_r^{core} = magnetic relative permeability of the coil's core, no unit.

μ_{st} = viscosity of the steam, Pa·sec.

μ_w = viscosity of the water, Pa.sec.

ν = Poisson's ratio, no unit.

ρ = electrical resistivity of the reservoir formation, Ωm.

ρ_f = density of fluid inside the pores, kg/m^3.

ρ_r = bulk density of oil sand (including porous fluid), kg/m^3.

ρ_{st} = density of steam inside the pores, kg/m^3.

ρ_w = density of water inside the pores, kg/m^3.

$(\rho c)_{sf}$ = volumetric heat capacity of the solid-fluid composite, J/(m^3 ºC).

σ = electrical conductivity of the caprock, A/m^2.

σ_{ij} = total stress of the caprock, Pa.

σ'_{ij} = effective stress of the caprock, Pa.

σ_{zz} = total stress of the caprock in z-direction, Pa.

$\bar{\sigma}$ = average effective stress in the caprock, Pa.

τ_{zy} = shear stress in the caprock, Pa.

ξ = Boltzmann dimensionless variable for distance from the bottom of the caprock, no unit.

$\xi_{interface}$ = Boltzmann dimensionless variable of steam interface distance from the bottom of the caprock, no unit.

Ω_K = ratio of thermal conductivity coefficient of the medium saturated with steam to that saturated with water, no unit.

$\Omega_{Thermal}$ = ratio of thermal diffusivity of the media saturated with steam to that saturated with water, no unit.

Ω_μ = ratio of dynamic viscosity of the steam to that of the water, no unit.

Ω_Λ = ratio of thermal pressurization factor of the media saturated with steam in uncontained condition, to that saturated with water in uncontained condition, no unit.

Ω_Λ^{vap} = ratio of thermal pressurization factor of the media saturated with steam in contained condition, to that saturated with water in contained condition, no unit.

This page is intentionally left blank.

1. Introduction

Of Canada's 179 billion barrels of oil reserves, Alberta's oil sand contains 170.4 billion barrels of oil reserves (Government of Alberta, 2011, 2012), and with the recent increase in demand, tremendous efforts are being made to develop bitumen reservoirs in the coming decades. Steam-assisted gravity drainage (SAGD) is one successful thermal recovery technique applied to the oil sands of Alberta, Canada. Approximately 80% of the oil sands are recoverable through in-situ production (i.e., they lie at a depth of 75m to 750m with an average seam thickness of less than 20m), with only 20% recoverable by mining (i.e., they lie at a depth of 75m or less with an average seam thickness of 32m) (Government of Alberta, 2008; Vermeulen and Chute, 1983).

Viscosity is a major obstacle in the recovery of bitumen in oil sand reservoirs, and thermal recovery is considered the most effective method for lowering it. Steam-assisted gravity drainage (SAGD) is the most promising thermal recovery technique applied to Alberta oil sand reservoirs. In SAGD, two horizontal wells, a top injection well and a bottom production well (as illustrated in cross-section in Figure 1.1) are drilled in the lower part of the reservoir. In Figure 1.1, Wellpair A is in the pre-production steam circulation stage, in which thermal communication is established between the wells mainly through conductive heating. Wellpair B is in the early production stage, in which the steam chamber has not yet contacted the top of the oil formation. Wellpair C is in the lateral growth stage. Steam injected continuously through the top well flows outward and loses latent heat when it comes into contact with the cold bitumen at the edge of a steam chamber. The circulation (or start-up) phase is crucial in the SAGD process. Under in-situ conditions, bitumen has no mobility because of its high viscosity and steam injectivity is very low. Steam injection is not practical for reservoirs with low levels of water saturation. In the circulation phase the viscosity of bitumen falls several orders of magnitude and steam injectivity increases. Steam circulation extends until the oil between the injector and the producer reaches a temperature at which it is mobile. At that point, steam injection can be started.

Due to slow conductive heating during the start-up phase, operators have tried to commercialize other start-up strategies such as bull-heading of steam and electromagnetic heating. This study explores EM-heating techniques and the reduction of circulation time. Four main techniques that are under study in Alberta are the Electro-Thermal Dynamic Stripping Process (ET-DSP™) by E-T Energy, the induction heating or electromagnetic steam-assisted gravity drainage (EM-SAGD) technology by Siemens AG, Radio Frequency (RF) heating by Harris RF Energy Systems, and the Low-Pressure Electro-thermally Assisted Drainage (LEAD) process by Perpetual Energy. In this section, these heating strategies are elaborated upon and discussed.

Other major challenge for Alberta's oil industry today is to improve bitumen recovery and to reduce the steam-oil ratio in difficult geological media such as deep, heterogeneous sands and carbonates, and those with high shale content. There are also limitations on steam pressures due to low fracture gradients or low thief zone pressures, which limits steam temperatures and raises bitumen viscosities. Recovery can be improved through thermal, solvent injection, electrical and electromagnetic methods. Electromagnetic heating for in-situ production of bitumen reservoirs can be divided into three different groups: low-frequency heating (also called electrical heating[1], medium-frequency heating (i.e., inductive heating), and high-frequency heating (i.e., radio frequency and microwave heating) (Bogdanov et al., 2011 and Wacker et al., 2011). Electrical heating using low-frequency alternating current (either 50 or 60[2] Hertz, the urban and commercial power frequency) for the recovery of bitumen has been studied since the early 1970s (Chute et al., 1978; Vermeulen et al., 1979; Vermeulen and Chute, 1983, Hiebert et al., 1986; Vermeulen et al., 1988; McGee and Vermeulen, 2000; Vermeulen and McGee, 2000;

[1] There are two main types of electrical heating: ohmic and resistive heating.

[2] Lower frequencies such as 0.1 Hz have also been applied to the electrodes in some cases (Vermeulen and Chute, 1983)

McGee and Vermeulen, 2007). The technology has evolved as an additional technology to SAGD (McGee and Vermeulen, 2007). Down-hole resistive (or ohmic) heaters have also been proposed for heating near the well in heavy oil reservoirs to reduce the skin effect by near well viscosity reduction(Chute and Vermeulen, 1988; McGee et al., 1999), though this is not very efficient for bitumen reservoirs, and its depth of influence is very limited. Radio frequency (RF) electromagnetic stimulation has been proposed for heavy oil recovery heating in several studies (Abernethy, 1976; Islam et al., 1991; Sahni et al., 2000; Sayakhov et al., 2002; Carrizales et al. 2008; Davletbaev et al., 2011; Kovaleva et al., 2011). A number of field tests of bottom hole heating by radio frequency electromagnetic (RF-EM) radiation were carried out in Russia, the USA, and Canada (e.g., Kasevich et al., 1994; Spencer, 1987, 1989). These studies proved the efficiency of the radio frequency electromagnetic (RF-EM) process in heavy oil reservoirs. RF-EM has a short-range effect and this is the reason it is mostly referred as "RF-EM stimulation". Although its application in bitumen deposits is questioned, few studies such as Davletbaev et al. (2010) proved its efficiency in bitumen deposits with low water cut values (i.e., water cut <30%). Davletbaev et al. (2010) suggest using RF-EM stimulation in heavy oil production wells on early field development stage, and convert RF-EM stimulation to electric heating in production wells when the water front from the injection wells reaches the production zones.

1.1. Review of SAGD Application

Of Canada's 179 billion barrels of oil reserves, Alberta's oil sand contains 170.4 billion barrels of oil reserves (Government of Alberta, 2011, 2012), and with the recent increase in demand, tremendous efforts will be made to develop bitumen reservoirs in the coming decades. Steam-assisted gravity drainage (SAGD) is one successful thermal recovery technique applied in the Athabasca and Peace River reservoirs in Alberta, Canada. In SAGD, steam injected into a horizontal injection well is forced outward, losing its latent heat when it comes into contact with the cold bitumen at the edge of a depletion chamber. As a consequence, the viscosity of bitumen falls several orders of magnitude, and it flows under gravity toward a horizontal production well located several meters below and parallel to the injection well (i.e., 5 meters, but drilling tolerances often leave variations between 3 and 7 meters). As the oil flows away and is produced, the steam chamber expands both upwards and sideways (see Sections B and C in Figure 1.1). A cross section of the SAGD process is displayed in Figure 1.1. Section A shows the circulation stage, Section B presents the early phase in which the chamber is not well developed, and Section C presents the mature steam chamber in the injection phase.

The term "steam-assisted gravity drainage" was first developed by Roger Butler and his colleagues at Canada's Imperial Oil in the late 1970s (Al-Bahlani and Babadagli, 2009). Butler and Stephens (1981) proposed the first closed-form solution for the prediction of oil production rate in the SAGD process. In his model, known as the "Butler theory", Roger Butler described the SAGD process as when steam is injected, a steam-saturated zone, called a "steam-depletion chamber" or simply a "steam chamber" is formed, in which the temperature is that of the injected steam ($T_{chamber} = T_{steam}$). The steam flows towards the interface of the steam chamber, where it condenses and loses its latent heat by flashing to bitumen. The latent heat from steam is transferred by thermal conduction into the surrounding reservoir and mobilizes the bitumen. The steam condensate and mobile bitumen flow by gravity to the production well located below the injector from side-drained paths (see Figure 1.1).

1.2. Description of Electromagnetic (EM) Methods used in Alberta

Five main EM eletechniques that are under study in Alberta are the Electro-Thermal Dynamic Stripping Process (ET-DSP™) by E-T Energy, the Thermal Assisted Gravity Drainage (TAGD) by

Athabasca Oil Corporation (AOC), the Low-Pressure Electro-thermally Assisted Drainage (LEAD) process by Perpetual Energy, the induction heating or electromagnetic steam-assisted gravity drainage (EM-SAGD) technology by Siemens AG, and Radio Frequency (RF) heating by Harris RF Energy Systems (Melbourne, Florida, USA). Among these techniques only inductive and RF heating seems to be applicable for reducing start-up time for SAGD process. In this section, these heating strategies are elaborated upon and discussed. Although ohmic heating methods such as Perpetual LEAD, AOC TAGD and Shell In-situ Upgrading processes are not considered as electromagnetic methods, for being comprehensive these methods also discussed.

1.2.1. Resistive Heating and Electro-Thermal Dynamic Stripping Process (ET-DSP™) technology

Heating with frequencies less than 300 kHz (normally 50–60 Hz which is used for domestic power supply) includes electrical-resistive heating (ERH) (sometimes called "Joule heating") and ohmic heating. In ERH formation serves as a resistor (conductor) for the electricity. The electric current is conducted into the reservoir via the connate water. This technique utilizes downhole electrodes placed inside an injector or producer and in specific cases production casing is used as electrode. In resistive heating dissipation of electrical energy due to the resistance offered by the brine generates heat in the reservoir. This technique has been studied for the recovery of bitumen since the early 1970s (Chute et al. 1978; Vermeulen et al. 1979; Vermeulen and Chute 1983, Hiebert et al. 1986; Vermeulen et al. 1988; McGee and Vermeulen 2000; Vermeulen and McGee 2000; McGee and Vermeulen 2007). Resistive heating technology evolved as an additional technology to preheat steam drive carried out in the "PCEJ electric preheat" pilot test from 1979 to 1983 (Khosla 1985) (the operation phase of the project starts from April 20, 1981 to February 22, 1982). The test was conducted in the Athabasca lower McMurray sand located in Hangingstone project area (see Figure 1.3). This test was performed in a joint venture of Petro-Canada (now Suncor Energy), Canadian Occidental Petroleum Ltd. (now Nexen), Esso (now Imperial Oil) and Japan Canada Oil Sands (JACOS) taking the initial letters of the four companies, collectively known as the PCEJ Group (Towson and Khallad, 1991). The basic procedure was to apply 480 V AC 60 Hz 3–phase power to electrode wells until the temperature at the midpoint of the electrode well reached 65˚C, and then the steamflood was initiated to displace the heated bitumen. The pilot consists of two phases: electrical heating and steam injection. The first phase from April 20, 1981 to July 5, 1982 utilized four electrode wells arranged in a square pattern (i.e., with a side of 30.5 m). The power supplied to these electrodes was 3-phase 60 Hz with two for the wells connected to a common phase. This connection results in heating a U-pattern because there is no current flow between the two wells connected to the same phase (0˚ phase). However the major assumption for heating in U–pattern was that there is no native injectivity in oil sand reservoirs. But injectivity tests show significant injectivity to brine and steam at the base of reservoir. As a results of high injectivity the steam will short-cut across the U and U-drive will be sustained. In new design four electrode wells were run for 60 days (to tests the split phase concept) and the second phase utilized three electrode well pattern for 227 days (from July 10, 1981 to February 22, 1982). Other intent of using three electrodes pattern was to test and compare steamflood phase in heated triangle (contained between electrodes) and cold triangle sections (Khosla, 1985). For reducing the power loss the production casing is used as electrode. Inductive heating due to occurrence of eddy currents in steel casing will overheat the casing and decrease its strength which may result in its failure. Thus the packer was set at the top of the reservoir and the casing was cooled down using a diesel circulation at the upper annulus keeping the temperature below 150˚C by monitoring the return diesel temperature (not exceed 75 ˚C). Flashing and gas liberation due to heating the reservoir are major operational challenges. To accommodate with flashing the cool brine is injected to fill in the flashing zone which re-establish the conductive path and also reduce the temperature. The time required to inject brine was small and electrical heating could be resumed immediately after the injection. Another concern with flashing is current unbalance between electrodes. It happens because the other electrodes are drawing the same current as before but the current to the flashed electrode is greatly

reduced. Most power providers (such as Alberta Power Ltd.) placed constraints upon the load that limits the operation with unbalance current. This forces the PCEJ operators to control flashing by reducing the potential across high water saturated zones and regular brine injections.

ET-DSP™ is a technique initially patented by McMillan-McGee Corporation for cleaning contaminated soil and groundwater. This technique is deployed by E-T Energy for extracting bitumen from mid−range depth reservoirs (with depths of between 75 and 150 m) in which neither mining nor SAGD processes are operational. This process uses electric conductivity of connate water to propagate an alternating current between electrodes, inducing the Joule heating of the reservoir. The first field test started at Poplar Creek in 2006. ET-DSP™ is a low-frequency technique using low-frequency alternating current (either 50 or 60 Hz, the urban and commercial power frequency). On 2011, E−T Energy has entered into an agreement with Total and Alberta's Climate Change and Emissions Management Corporation (CCEMC) for Phase 1 commercial development at Poplar Creek with 10,000 bbl/d oil production with planned expansion to 40,000 to 50,000 bbl/d. In ET-DSP™, electrode wells (E-Wells) are drilled vertically in a grid pattern and spaced at roughly 16 m. Per every E-Well, extraction wells (X-Wells) or production wells must be drilled to produce heated water and bitumen. X-Wells are also drilled vertically in a grid pattern between every two injectors. In the first ET-DSP pilot test carried out from September 2006 to August 2007, McGee (2008b) presented that an average rate of increase in temperature of approximately 2°C/d and the peak temperatures of 75–80°C which both were consistent with the numerical model. An associated problem with ET-DSP™ is the appearance of hot spots around the electrodes that may be relieved by water–circulation. And due to hot spots many of the electrodes failed during the operation and they were not able to provide enough energy to the reservoir (i.e., 25% less than the target total energy). Brine is injected through E-Wells for electrical communication between injectors and producers. This is critical to maintaining electrical conductivity and enhances convective heat transfer in the reservoir and also brine penetration into the reservoir increases the electric conductivity in a large region between electrodes, which improves the heating mechanism that will be discussed in "start-up in electro-thermal heating" section. Production requires artificial lifting [ET-Energy replaced reciprocating pumps with progressive cavity pump (PCP) from 2007 (McGee, 2008a,b) due to minimal sand production] and due to low-pressure operation techniques such as "poor boy" gas-lift are not viable.

The main advantage of ET-DSP™ over PCEJ electric preheat technique is the convective heat transfer component. In PCEJ electric preheat type techniques current from electrode naturally tends to flow from the ends of the electrodes, resulting in overheating which promotes uneven heating of the reservoir. The injected brine from E-Wells flows radially toward the vacuum zones that created due to oil production from X-Wells . In contradiction to PCEJ electric preheat type electrodes this radial heating results in rapid and uniform heating of the reservoir. McGee (2008a,b) compared the temperature distribution resulting from an ET-DSP™ and an electrode with no injection of water similar to PCEJ electric preheat technique and showed that ET-DSP™ results in over ten times more oil sand being heated to above 70 °C after 60 days of operation. Although brine injection helps heat transfer by adding convection term, it creates water pathways through steam zones and results in early high water production. This process needs a minimum of 10% water saturation to function effectively, and this may result in less effective application in rich zones. Another downside of ET-DSP™ is that it is associated with extensive drilling and abandonment procedures as a result of small well spacing (8 m between E-Wells and X-Wells). To comply with new ERCB measurements, E-T Energy proposed a new completion strategy for E-Wells that uses non-metallic casing (Vinyl Ester FRP) and extends the casing and cement through the Clearwater clay-bearing formation. This is to stop clay from swelling, which may create a seal to water injection in the event of hose failure. Extra costs due to completion and abandonment and extensive drilling narrow the applicability of this process, but E-T Energy attempts to retrieve tubing, cables, hoses, and electrode wellheads from E-Wells to make it more economical. The main advantage of ET-DSP™ over SAGD is its rapid and high recovery. In a proof of concept test of ET-DSP™ from September 2006 to August 2007 75% recovery was achieved in

365 days. It must be noted that the effectiveness of ET-DSP™ similar to any resistive heating method depends strongly on reservoir salinity and water saturation.

1.2.2. Ohmic Heating and Thermal Assisted Gravity Drainage (TAGD) Technology

In previous section low frequency methods dealing with in−situ electrical resistive heating (ERH) such as ET-DSP™ and PCEJ electric preheat technologies are explained. But low-frequency methods also include down-hole resistive (or inductive heaters. In "ohmic heating" a heating element is installed inside the wellbore that turns electric current into heat that provide heat to the reservoir by thermal conduction. These have been proposed in waxy crude reservoirs to reduce the skin effect in heavy-oil reservoirs by reducing viscosity near the well (Chute and Vermeulen, 1988; McGee et al., 1999), and also in mitigating hydrate (Das, 2008). The main practice of such techniques is TAGD process deployed by Athabasca Oil Corporation (AOC) in the Leduc reservoir in its Dover West asset located within the Liege area of north–central Alberta (centered at Township 95, Range 18W4). In this technique an array of mineral-insulated (MI) heater cables installed in horizontal wells which is used to heat the reservoir via thermal conduction. Since heating by conduction is slow a large number of horizontal resistive elements are needed to mobilize the bitumen (see Figure 1.4b). Three TAGD production phases were conducted at Dover West Leduc reservoir during 2012 to 2013 were operated at low temperatures between 70 to 90 °C (Hamida and Roberts, 2014). As shown in Figure 2.8 bitumen in this range of temperature is not highly mobile (≈ 1000 cP). Since this mobility results in uneconomical oil rates AOC suggests using heaters that creates temperatures up to 300 °C which, in turn, warms the surrounding reservoir to temperatures ranging between 120°C (≈200 cP) and 160°C (≈40 cP) which is less than typical SAGD temperatures of 200°C or greater (<15 cP). In highly karstified carbonate reservoirs such as Leduc and Grosmont C and D units which are challenging for SAGD operation the high permeability of the fractured system can be used in favor of TAGD performance. This advantage is a main driver of using TAGD in the Devonian Leduc carbonate reservoir which is highly permeable and porous dolostone that is fractured with original vuggy and moldic porosity. Other advantages of TAGD process are to achieve uniform wide heating and to reduce overburden/underburden heat loss. To reduce heat loss, heaters are placed in manner to ensure that temperature at the top and bottom of the reservoir is at minimum temperature that provides enough mobility for bitumen (≈120°C). After reaching the peak production, to ensure that the average pattern temperature remains within the optimal temperature (120–160°C) and heat loss stays minimal Hamida and Roberts (2014) suggest lowering the heater power in the upper rows and gradually move down to lower rows. For decline-production stage, Hamida and Roberts (2014) suggest to turned down or shutoff most heaters and let the reservoir drain slowly. In TAGD process high temperatures are not required, and electric heaters provide enough heat to mobilize bitumen and drain by gravity. Although the main drive mechanism is gravity, connate-water flashing and solution-gas evolution provides extra drive energy. No need for steam generation facility makes the initial capital investment of a TAGD project is significantly lower than a comparable SAGD project. AOC is currently operating the fourth phase of TAGD field test, and also planning to move towards utilizing this technique commercially.

Electric heaters can also be used for in–situ upgrading such as *Shell's In-situ Conversion Process (Shell ICP)*. In this technique electrical heating elements are used to heat the reservoir to between 340 and 370 °C over a period of four years and as a result kerogen in oil shale is converted into shale oil and gases, which are then flow to the surface through recovery wells (Shell Canada Resources 2007 and Ryan et al. 2010). Similar technique has been developed by shell to convert the bitumen into lighter crude oil and gas while still underground called In-situ Upgrading Process (IUP) (Karanikas 2012; Wellington et al. 2005). In past experiments Shell successfully used ICP to extract light oil from kerogen-bearing shale in Colorado, USA and began IUP in 2004 and completed in 2008 that upgraded bitumen from Bluesky formation in Peace

River Viking Pilot located in Alberta, Canada. The latter pilot is still running and still has confidential status. Over 100,000 bbl of 30 to 49 °API oil is produced from 8-10 °API bitumen using ICP. In Peace River project combination of 7 heaters, 11 heater/producers, 3 producers and 8 observation wells were drilled in four parallel rows. Although heat transfer from electric heaters is slow it is predictable and significant upgrading is achieved. The main disadvantage was that high energy is required to increase temperature to raise temperature to 380−430°C which is required to trigger upgrading (Wellington et al. 2005).

Shell Canada began construction of the "North Field Pilot Test" in early 2012 that applied for regulatory approval in November 2007 (SURE Northern Energy 2007). The upgrading is expected to raise the oil in Grosmont reservoir from 7 °API to 40 °API. Shell has asked that its Grosmont pilot be granted experimental and confidential status for the five-year project term and for three more years after completion. And the company said it may apply for an extension of the confidentiality period as it evaluates the pilot's performance and decides whether to build a commercial project. As a results no public data is available on North Field Pilot Test (Roche 2008). It must be noted that the common low voltage (fewer than 600 V) electric heaters cannot be used for IUP because of large parasitic energy loss in the overburden, operating temperature (>400°C) and short lengths of heaters (<250 ft ≈76 m). For this purpose a medium-voltage (4160 V) mineral-insulated (MI) heater cables are used. These electric heaters are providing 1 kW/m power and are manufactured in lengths up to 2000 m without splices by MCAAA Ltd. (splice can increase the diameter at the splice by about a factor of three times which is problematic concern for completion operation). Sandberg (2015) shows that overburden energy loss can be reduced from 51.9% to 11.8% by using medium- voltage (4160 V) electric heaters.

1.2.3. Low Pressure Electro-thermally Assisted Drainage (LEAD) technology

The LEAD process developed by Perpetual Energy uses ohmic heating (resistance electric heaters) concurrent with injection of water and/or solvent. In late–2015, Perpetual Energy is planning to conduct this process in the Bluesky Formation in the Panny area of Northeast Alberta (see Figure 1.3) (Regulatory approval of the pilot project to assess the proprietary LEAD technology was received on July 24, 2014 but due to low oil price environment they decide to postpone the project). This formation, while too viscous for conventional cold production (50,000 cP at reservoir temperature≈11˚C), does not require as much heat as Athabasca SAGD projects due to its much lower level of viscosity (ranging between 9,000 and 68,000 cP). Bluesky is a good quality reservoir in homogeneous shoreface sand but it is thin with average pay thickness of 11m and also existing depleted gas pool which limited high pressure operations. Since these concerns will limit SAGD operation, Perpetual Energy suggested LEAD process in order to manage depleted gas zone operating at low pressures (Perpetual Energy, 2015). In the LEAD process, two parallel horizontal wells use electrical cables to create heat in the target zone. Water and/or diluent (solvent) are injected in these two horizontal wells to further reduce viscosity. The producer is drilled horizontally at the bottom of the reservoir half way between two heaters/injectors (see Figure 1.4c). For phase 1 of LEAD process the cyclic heat stimulation/production is suggested in order to reduce solvent loss.

Authors believes that LEAD process is not viable for low mobility oil sand reservoirs due to the lack of communication between injector/heater and producer, which is in turn due to the low mobility of injected water and the large distance between injector/heater and producer. In SAGD processes, initial mobility is achieved at the circulation stage after a few months for wells only 5 m apart. With the current well configuration in the LEAD process, the start-up phase would last many years in Athabasca oil sand reservoirs. It must be noted that the LEAD process can be viable for those Athabasca oil sand reservoirs with low in–situ viscosity (< 150,000 cP) and high water mobility.

1.2.4. Electromagnetic steam-assisted gravity drainage (EM-SAGD) technology

In electromagnetic inductive heating, a medium-frequency electric field is applied in the range of 1 kHz to 200 kHz (Wacker et al., 2011). There are a few cases in which the electromagnetic coil resonates and is excited at frequencies as low as 60 Hz (Vermeulen and Chute, 1983). The frequency applied in inductive heating is three orders of magnitude smaller than that applied in radio frequency heating and six orders of magnitude smaller than that applied in microwave heating. Siemens AG is has worked with industrial partners to test the technique, running an EM loop along the SAGD well pairs to electromagnetically heat and soften bitumen (Ghannadi et al., 2014). Technical principles of inductive heating in the EM-SAGD process were reported by Koolman et al. (2008). Inductive heating was initiated in the laboratory using a frequency of 142 kHz. Koolman et al. (2008) compared EM-SAGD versus conventional SAGD processes for shallow reservoirs with low maximum operating pressure (MOP) (≤ 2.2 MPa). They reported the 38% improvement by using the EM-SAGD process compared to conventional SAGD.

Electromagnetic steam-assisted gravity drainage (EM-SAGD) is an alternative method of steam injection that uses inductive heating and steam injection simultaneously (Sahni et al., 2000; Gunal and Islam, 2000). In EM-SAGD, a medium-frequency electric field is produced by a subsurface coil fed from a converter located on the surface. A large solenoidal coil, called the inductor, is placed horizontally within the pay zone. This inductor produces an alternative magnetic field in the reservoir. Eddy currents are generated in the reservoir by the electric field surrounding the inductive cable loop, and are directed opposite to compensate for the source magnetic field from the inductor (Koolman, et al., 2008). In initial design Siemens AG suggested running an EM loop along the SAGD well pairs located with small offset at the midpoint between the injector and the producer. However, in their final design, the EM loop is located on top of the injector at a distance of 5 m (see Figure 1.4e).

As no contact is needed to generate the currents, neither brine injection (such as electrical resistive heating due to the low electrical conductivity of the steam bubble at 60 Hz), nor well stimulation is necessary (Wacker et al., 2011). Also, due to deep electromagnetic penetration, no tight drilling pattern (such as that required for electrical resistive heating) is necessary. The disadvantage of the process is that it requires one extra well; and a need for expensive fiberglass casings.

As mentioned, a medium-range frequency is generally used for electromagnetic induction heating (Wacker et al., 2011), with low frequencies used in some specific cases (Vermeulen and Chute, 1983). The trade-off between medium-frequency electromagnetic induction heating and low-frequency electrical resistive heating is embedded in different dominant physics and oil sand properties. Since the electrical conductivity of oil sand formations increases as the square of the water content (i.e., $\sigma \approx 5 \times 10^{-4} w^2$ at room temperature, where w is the water content in weight percent), Athabascan oil sand, typically with a moisture content of 1 to 6 % (Vermeulen and Chute, 1983) permits currents to flow at 60 Hz from one electrode to another in electrical resistive heating, even if they are several hundred metres apart. Figure 1.2d presents the penetration depth variation for resistive heating. High-frequency electromagnetic waves are completely absorbed by such a formation within a very short distance (i.e., 1 to 5 metres for 10 MHz, or 10 to 50 centimetres for 1 GHz, as illustrated in Figure 1.2d for oil sand reservoirs), and will not effectively heat the reservoir. In reservoirs with low water saturations (S_w), while electrical conductivity falls rapidly and resistive heating is nearly impossible to conduct, an electromagnetic wave can propagate over much larger distances and can be effectively conducted (Vermeulen and Chute, 1983).

The heat generation mechanism in inductive and RF heating is different. Inductive heating is based on the Joule effect of the induced alternating electromagnetic induction of the eddy currents. The conducting path for the eddy currents is through the continuous connate water surrounding the nonconductive sand particles. Electrical energy in the eddy currents is converted into heat along these pathways because of the electrical resistivity of the connate water, which contains a large number of ions resulting from dissolved salts. The heat is transferred to oil and

sand particles by conduction, raising the temperature in the reservoir volume over time. In contradiction to inductive heating, at high frequencies such as those of RF and microwave heating, displacement current and the electrical polarization effect are the main heating components, and conduction current or eddy current loss should be neglected. Figure 1.2c presents the ratio of conduction current (or eddy current loss) to displacement current for oil sand reservoirs with different water content, calculated as:

$$\frac{|J_c|_{max}}{|J_d|_{max}} = \frac{\sigma}{\omega \varepsilon_0 \varepsilon_r} \quad 1$$

As shown, for frequencies lower than 100 kHz (i.e., in the range of inductive heating such as EM-SAGD), this ratio is in the range of 100 to 1000. This shows the dominance of conductive current (or eddy current loss) over displacement current in inductive heating (Figure 1.2c). For further discussion, refer to 156876-PA (Ghannadi et al. 2014).

EM-SAGD can be useful for very deep thermal operations (where wellbore heat loss is significant and the quality of steam reaching the formation is very low), in thin pay-zones (where heat losses to adjacent, non-oil-bearing formations may be significant), and where injecting steam may be environmentally unacceptable (such as through permafrost) or uneconomical (as on space-limited offshore platforms). It can also be useful in low-permeability reservoirs (where injected fluid may have difficulty penetrating deep into the reservoir) and in heterogeneous reservoirs (where high-permeability streaks or fractures may cause early injected fluid breakthrough and reduce sweep) (Sahni et al., 2000). Though EM-SAGD looks promising in theory, there are two problems. The first is a lack of technology to drill horizontal wells that can be drilled upward and end at the surface (as inductors must be drilled horizontally and end at the surface to create closed loops to feed subsurface coils from a converter located on the surface). The second is a need for expensive fiberglass casings (as induction drastically warms steel casings). While Siemens AG tried to test the technique in Alberta Oilsands Clearwater West project (Alberta Oilsands Inc., 2010), the cancellation of Phases 1 and 2 left the application of this process unclear.

1.2.5. High Frequency Techniques and Effective Solvent Extraction Incorporating Electromagnetic Heating (ESEIEH™) technology

In radio frequency (RF) heating the energy applies to the reservoir by EM-waves in the RF ranges. Then the radial heating is achieved by converting the wave into heat through dielectric dissipation. Several studies have proposed the use of RF electromagnetic stimulation for heavy oil recovery heating (Abernethy, 1976; Islam et al., 1991; Sahni et al., 2000; Sayakhov et al., 2002; Carrizales et al. 2008; Davletbaev et al., 2011; Kovaleva et al., 2011). A number of field tests of bottom-hole heating by radio frequency electromagnetic (RF-EM) radiation were carried out in Russia, the United States, and Canada (e.g., Kasevich et al., 1994; Spencer, 1987, 1989). These proved the efficiency of the radio frequency electromagnetic (RF-EM) process in heavy oil reservoirs. Due to its short-range effect, RF-EM is mostly referred to as “RF-EM stimulation”. A few studies such as Davletbaev et al. (2010) did prove its efficiency in bitumen deposits with low water cut values (i.e., <30%). Davletbaev et al. (2010) suggested using RF-EM stimulation in heavy oil production wells in the early field development stage, and converting RF-EM stimulation to electric heating in production wells when the water front from the injection wells reaches the production zones. RF heating applies frequencies over the ranges 0.3 MHz to 300 MHz, and MW heating applies frequencies greater than 300 MHz (Koolman et al., 2008), well above the inductive heating frequencies. In radio frequency (RF) and microwave heating, since water molecules have both positive and negative poles (i.e., hydrogen has a positive pole, and oxygen a negative pole), they tend to behave like microscopic magnets. As the positive half cycle of the microwave penetrates the medium, it attracts the negative pole of the molecules. The microwave field attempts to align water molecules with this positive field of energy. Then, when the microwave alternates to the negative half cycle, the negative poles are repelled and the

positive poles are attracted, causing a "flipping" motion. This agitation and flipping causes heat inside the medium, called "dipole friction of molecules" (Davletbaev et al., 2011), and the heating process is called "dielectric loss". In RF there is an added efficiency loss due to energy-conversion step (i.e., need to convert electricity to an electromagnetic wave and then convert the wave to heat).

Although SAGD is a proven technology for Athabasca oil sand deposits and RF-EM application in bitumen deposits to replace SAGD is questionable, utilizing RF-EM technique for start-up phase of SAGD can be attractive. Since 2009, Harris, Laricina Energy, Nexen Inc. (a subsidiary of CNOOC Limited), Suncor Energy, and Alberta's Climate Change and Emissions Management Corporation (CCEMC) (i.e., a not-for-profit organization with a mandate to establish or participate in funding initiatives that reduce greenhouse gas emissions and support adaptation) made up the Effective Solvent Extraction Incorporating Electromagnetic Heating (ESEIEH™, pronounced "easy") Consortium. The goal is to replace steam for in-situ bitumen extraction with EM-heating in combination with solvent dilution. In 2012, RF heating technology was evaluated and tested in Florida. Then, Phase I of the ESEIEH™ process [U.S. patent 8776877 (Trautman et al., 2013)] project started with the installation of RF antennas designed by Harris at a face of Suncor's North Steepbank mine north of Fort McMurray. In January 2012, the mine face test was declared a success and confirmed the ability to generate, propagate, and distribute electromagnetic heat in an oil sand formation. The consortium (with Laricina Energy opting out and being replaced by Devon Energy) is currently in Phase II, exploring scaled pilot tests started on early July 2015 in Suncor's Dover facility (see Figure 1.3). Phase II followed the configuration presented in Figure 1.4f combining solvent injection with RF-heating. To ensure better mobility and dissolution solvent is injected in vapour condition. To keep solvent vaporized, the solvent line serpentines three times between the choke and the centre isolator to increase the available surface area for heat transfer to the solvent (Despande et al., 2015).

1.3. Review of Caprock integrity in SAGD and EM-SAGD projects

Although SAGD is a very promising alternative to classical in-situ bitumen recovery methods such as fracture-assisted cyclic steam stimulation (FCSS) and cyclic steam stimulation (CSS), there are some problems associated with it. These include maintaining caprock integrity in SAGD operations, resulting in a steam release and considerable caprock and ground surface deformation; shear slip failure, resulting in injection or production casing failure and well abandonment; and reservoir deformations causing surface deformations such as heaving (Collins, 2005, 2007; Dusseault and Collins, 2008).

Caprock integrity assessments have become key in the design and operation of SAGD projects, and a critical element in the selection of a maximum steam injection operating pressure. Caprock integrity is concerned with hydraulic integrity and mechanical integrity. The first refers to the existence of a hydraulic barrier for reservoir fluids preventing hydrocarbons from migrating upwards through the caprock to shallow groundwater aquifers or the ground surface. The second refers to caprock formation failure, which can endanger future infill drilling or cause surface heave (i.e., that is a reflect of considerable deformations in the caprock) (Yuan et al., 2011a).

Caprock integrity is the subject of many studies following the catastrophic failure of the caprock seal at the Joslyn Creek SAGD project on May 18, 2006 (Uwiera-Gartner et al., 2011a, 2011b; Yuan et al., 2011a, 2011b). Joslyn failure caused consequences such as: steam release; a crater created at failure location; many trees were knocked down; and bitumen spread over the location. But no one was injured or killed. For this incident, two reports were released by the Alberta Government: "Total E&P Canada Ltd., Surface Steam Release of May 18, 2006, Joslyn Creek SAGD Thermal Operation, ERCB Staff Review and Analysis, February 11th, 2010", and "Summary of Investigations into the Joslyn May 18th, 2006 Steam Release, Total E&P Canada Ltd.". These reports have been summarized by Mike Carlson in a technical paper in "Detailed

Consideration of the Proposed Joslyn Failure Mechanism". Carlson (2012) summarized causes of Joslyn failure by Total as:

1. A chimney at the top of the pay zone, involving sand dilation;
2. A lateral extension of the pressurized zone below the shale barrier in the Upper McMurray formation;
3. Shear failures at the edge of the pressurized zone, causing the steam breaching within a gas zone in the Upper McMurray and/or Wabiskaw C sand or in the water sand in Wabiskaw A;
4. Significant water and steam storage in the localized steam chamber; and,
5. A catastrophic shear failure of the Clearwater caprock.

The ERCB agreed with some, and gave their suggestion for Total's most likely steam release scenario as follows:

ERCB agrees that the mini-frac test result indicates that only horizontal fracturing would occur at Joslyn failure;

Development of a dilation chimney is unlikely in 4 month circulation period;

ERCB concerns the accuracy of seismic results since they are in short distances (i.e., the vertical wells were within 20 m of the injector);

ERCB agrees with explosive nature of chamber required storage of the steam and hot water; and,

ERCB agrees that Total's geomechanical modelling which shows shear failure in the caprock due to pooling of high pressure steam and water beneath the Clearwater caprock formation.

Although a Joslyn failure report by the Total is logical in many scopes; understanding this failure as well as future caprock failures require extensive researches. One of the main missing in this analysis can be "Thermal Induced Pressurization".

The Joslyn failure had a major impact on the licensing of new SAGD projects with the Alberta's Energy Resources Conservation Board (ERCB). As a result of this failure, ERCB modified the existing application guidelines and directives (e.g., Directive 051) to include an assessment of caprock integrity. Caprock assessments conducted to date have incorporated varying levels of detail and complexity in each of the major elements of the study, but no studies have focussed on induced thermal-pressurization and more specifically that caused by electromagnetic heating in EM-SAGD projects.

While there are many aspects of caprock integrity, shear slip failure between caprock and reservoir is not discussed in ERCB directives, though it has been the topic of a few studies (e.g., Talebi et al., 1998; Dusseault et al., 2001; Smith et al., 2002; Wong and Chau, 2004) mostly focused on CSS projects. Talebi et al. (1998) reported a well-casing failure due to caprock slip at the level of the Colorado Shale formation in a CSS project at the Cold Lake deposit. Some 250 wells have failed at the Cold Lake heavy-oil field near the base of the Colorado Shale, and at the top of the producing reservoir (Dusseault et al., 2001). Dusseault et al. (2001) attribute these shear failures to localized shear displacements on weak bedding planes because of cyclic reservoir heave and compaction, in turn due to pressure and thermally-induced expansion and contraction of the oil sands. Wong and Chau (2004) also mentioned a possibility of local slips of up to 12 cm along a large discontinuity of low shear resistance (such as a clay seam or fracture) in steam projects. Smith et al. (2002) evaluated the slips causing casing failures for a high percentage of failed wells (> 88%) in the Clearwater bitumen zone top in the Cold Lake field.

Although many researchers are attributing the slip failure to lateral shear in the production zone, which results in horizontal displacements (AEUB Decision 99-22), the induced pore pressure effect should not be neglected. The weakening effect of increases in pore pressure may weaken the caprock formation locally and cause localized plastic deformation or rapid fracture initiation. The effect of pore pressure is more pronounced in the case of EM-SAGD, since heat

generated from eddy currents in electromagnetic heating is independent of shale thermal conductivity and may warm up the highly resistive formation locally. Also, in low water saturated formations, water can be driven off by heating above the steam point (Vermeulen and Chute, 1983), and the resulting phase change can raise the pore pressure enormously and initiate microfractures.

Assessing both hydraulic and mechanical risks to caprock integrity and the risk of shear slip failure present a significant challenge to oil and gas industry engineers dealing with both standard SAGD and EM-SAGD projects. This study addresses these issues as ones of "thermal pressurization"; or commonly known as "thermo-hydro-mechanical pressurization"; in caprock. Put simply, thermal pressurization is overpressure due to thermal expansion of fluid, which either quickly dissipates (in high-permeability shales) or accumulates (in low-permeability shales). It happens when the thermal expansion of pore fluids exceeds that of the pore space. In this case, the pore space stiffness tries to act against the expansion of the pore fluid volume, and compresses the fluid by increasing pore pressure to minimize its increase in volume. Thermal pressurization increases pore pressure and results in effective stress reduction. At low confining pressures, the shear strength of rock drops significantly due to effective stress reduction (Handing and Hager, 1957), leading to inadvertent hydraulic fracturing within the reservoir (Khan et al., 2010). In general, thermal pressurization partially reduces caprock shear strength and makes it more prone to fail against shear stresses developed by the SAGD operation, in order to sustain asset integrity throughout the SAGD operation. The thermal pressurization may also induce tensile failure, but in this study we focus on failures (i.e., shear failure) that results in from effective stress reduction.

1.4. Statement of the problem

Oil sand operation is growing more difficult with increase in oil price as well as dealing with challenging reservoirs. Viscosity is a major obstacle in the recovery of bitumen in oil sand reservoirs, and thermal recovery is considered the most effective method for lowering it. Steam-assisted gravity drainage (SAGD) is the most promising thermal recovery technique applied to Alberta oil sand reservoirs. Due to slow conductive heating during the start-up phase, operators have tried to commercialize other start-up strategies such as bull-heading of steam and electromagnetic heating. This study explores EM-heating techniques and the reduction of circulation time. Four main techniques that are under study in Alberta are the Electro-Thermal Dynamic Stripping Process (ET-DSP™) by E-T Energy, the induction heating or electromagnetic steam-assisted gravity drainage (EM-SAGD) technology by Siemens AG, Radio Frequency (RF) heating by Harris RF Energy Systems, and the Low-Pressure Electro-thermally Assisted Drainage (LEAD) process by Perpetual Energy.

The objective of this research is to develop a theoretical framework for evaluation of pressurization in caprocks and shale ambiguities within reservoirs due to EM-heating and SAGD process. For facing this challenge start-up heating for different EM processes is explored and compared against field data.

1.5. Research Objectives

The objective of this research program is to develop the analytical and numerical solutions to simulate the thermal induced pressurization subject to constant electromagnetic heating rate of the caprock. For this purpose both analytical solutions is used for coupling different physics associated with EM-SAGD technique such as: thermal fluid flow, electro-magnetic heating and geomechanical plastic failure analysis. In this study different standard cases of shallow reservoir conditions are studied and compare conventional SAGD and EM-SAGD processes.

1.6. Scope of Thesis

The research objectives will be achieved through integrated theoretical development. The steps taken to achieve wanted scope are outlined as:

Induction and Radio−Frequency Heating Start-Up

Steam-assisted gravity drainage (SAGD) is the method of choice to extract bitumen from Athabasca oil sand reservoirs in Western Canada. Under reservoir conditions, bitumen is immobile due to high viscosity and its typically high level of saturation limits the injectivity of steam. In current industry practice, steam is circulated within injection and production wells. Operators keep the steam circulating until mobile bitumen breaks through the producer and communication is established between the injector and the producer. The “start-up” (or “circulation”) phase is a time-consuming process taking three or more months. A variety of processes are used to minimize the length of the start-up phase, such as *electromagnetic (EM) heating in* either the induction (medium frequency) or *radio frequency* (*RF*) ranges. Knowledge of the size of the hot zone formed by steam circulation and of the benefits of simultaneous EM-heating techniques increases understanding of the start-up process and helps to minimize start-up duration. The aim of the present work is to introduce an analytical model to predict start-up duration for steam circulation with and without EM heating. Results reveal that induction slightly decreases start-up time at frequencies smaller than 10 kHz, and that at 100kHz it can reduce start-up time to 30% of that under original steam circulation conditions.

Thermo-Hydro-Mechanical Pressurization in Two-Phase Flow

Steam-assisted gravity drainage (SAGD) is one successful thermal recovery technique applied in Alberta oil sand reservoirs. When considering in situ production from bitumen reservoirs, viscosity must be reduced for the bitumen to flow toward the production well. Steam injection is currently the most promising thermal recovery method. While steam flooding has proved to be a commercially viable way to extract bitumen from bitumen reservoirs, caprock integrity and the risk of losing steam containment can be challenging operational problems. Since permeability is low in Albertan thermal project caprock formations, heating greatly increases the pressure on any water trapped in pores as a result of water thermal expansion. This water also sees a great increase in volume as it flashes to steam, causing a large effective stress reduction. Once this condition is established, pore pressure increases can lead to caprock shear failure, and to subsequent caprock integrity failure or potential casing failure. It is typically believed that low-permeability caprocks impede the transmission of pore pressure from reservoirs, making them more resistant to shear failure (Collins, 2005, 2007). Considering the “thermo-hydro-mechanical pressurization” physics, low-permeability caprocks are not always more resistant. As the steam chamber rises into the caprock, the heated pore fluids may flash to steam. Consequently, there is a vapour region between the steam chamber interface penetrated into the caprock and the water region within the caprock which is still at subcritical state.

Thermal Pressurization in Electromagnetic Steam-Assisted Gravity Drainage (EM-SAGD) Projects

Inductive methods such as Electromagnetic Steam-Assisted Gravity Drainage (EM-SAGD) have been identified as a technically and economically feasible recovery method for shallow oil sands reservoirs with overburdens of more than 30 meters (Koolman et al., 2008). However, in EM-SAGD projects, the caprock overlying oil sands reservoirs is also electromagnetically heated along with the bitumen reservoir. Since permeability is low in Albertan thermal project caprock formations (i.e., the Clearwater shale formation in the Athabasca deposit and the Colorado shale formation in the Cold Lake deposit), the pore pressure resulting from the thermal expansion of pore fluids may not be balanced with the fluid loss due to flow and the fluid-volume changes due to pore dilation. In extreme cases, the water boils and the pore pressure increases dramatically as a result of the phase change in the water,

causing profound effective stress reduction. Once this condition is established, pore pressure increases can lead to shear failure of the caprock, the creation of micro-cracks and hydraulic fractures, and to subsequent caprock integrity failure. It is typically believed that low permeability caprocks impede the transmission of pore pressure from the reservoir, making them more resistant to shear failure (Collins, 2005, 2007). In cases of induced thermal pressurization, low permeability caprocks are not always more resistant. In this study, analytical solutions are obtained for temperature and pore pressure rises due to the constant electromagnetic heating rate of the caprock. These analytical solutions show that pore pressure increases due to electromagnetic heating depend on permeability and compressibility of the caprock formation. For stiff or low-compressibility media, thermal pressurization can cause fluid pressures to approach hydrostatic pressure, and shear strength to approach zero for low cohesive units of the caprock (units of the caprock with high silt and sand percentage) and sections of the caprock with pre-existing fracture with no cohesion (i.e., thermal liquefaction).

1.7. Organization of thesis

Chapter 2 describes the Induction and Radio−Frequency Heating Start-Up. This matter is satisfied by analytical formulation and it comparison with field results.

Chapter 3 describes the Thermo-Hydro-Mechanical Pressurization in Two-Phase (Steam/Water) Flow and its Application in Low-Permeability Caprock Formations in Steam-Assisted Gravity Drainage Projects are also explored.

In chapter 4 Induced Thermal Pressurization in Clearwater Shale Caprock in Electromagnetic Steam-Assisted Gravity Drainage (EM-SAGD) Projects.

The last chapter integrates the different aspects of this study which were discussed in the previous chapters and summarizes the main conclusions. The recommendations for future research are also given in this chapter.

1.8. References

Abernethy, E.R., 1976. Production Increase of Heavy Oils by Electromagnetic Heating, *Journal of Canadian Petroleum Technology*, Vol. **15**, No. **3**, pp. 91-97.

Albahlani, A.M., Babadagli, T., 2008. A Critical Review of the Status of SAGD: Where Are we and What Is Next?, *SPE Western Regional and Pacific Section AAPG Joint Meeting*, Bakersfield, California, 29 March-2 April, SPE 113283.

Butler, R.M., Stephens, D.J., 1981. The Gravity Drainage of Steam-Heated Heavy Oil to Parallel Horizontal Wells, *Journal of Canadian Petroleum Technology*, Vol. **20**, No. **2**, pp. 90-96.

Carlson, M.R., 2012. Detailed Consideration of the Proposed Joslyn Failure Mechanism, *Canadian Energy Technology & Innovation*, Vol. **1**, No. **1**, pp. 12-19, CETI-12-036.

Carrizales, M.A., Lake, L.W., Johns, R.T., 2008. Production Improvement of Heavy Oil Recovery by Using Electromagnetic Heating, *SPE Annual Technical Conference and Exhibition*, Denver, Colorado, USA, 21-24 September, SPE 115723-MS.

Chute, F.S., Vermeulen, F.E., 1988. Present and Potential Applications of Electromagnetic Heating in the In-Situ Recovery of Oil, *OSTRA Journal of Research*, Vol. **4**, pp. 19-33.

Chute, F.S., Vermeulen, F.E., Cervenan, M.R., 1978. Physical Modelling of the Electrical Heating of the Oil Sand Deposits, Technical Report, AOSTRA Agreement #31, Applied Electromagnetics Group, University of Alberta.

Collins, P.M., 2005. Geomechanical Effects on the SAGD Process, SPE Reservoir Evaluation & Engineering, *2005 SPE International Thermal Operations and Heavy Oil Symposium*, Calgary, Alberta, Canada, 1-3 November, 2005.

Collins, P.M., 2007. Geomechanical Effects on the SAGD Process, SPE Reservoir Evaluation & Engineering, Vol. **10**, No. **4**, pp. 367-375, SPE 97905-PA.

Davletbaev, A.Y., Kovaleva, L.A., Babadagli, T., 2010. Heavy Oil and Bitumen Recovery Using Radiofrequency Electromagnetic Irradiation and Electrical Heating: Theoretical Analysis and Field Scale Observations, *Canadian Unconventional Resources and International Petroleum Conference*, Calgary, Alberta, Canada, 19-21 October, SPE 136611-MS.

Davletbaev, A.Y., Kovaleva, L.A., Babadagli, T., 2011. Mathematical Modeling and Field Application of Heavy Oil Recovery by Radio-Frequency Electromagnetic Stimulation, *Journal of Petroleum Science and Engineering*, Vol. 78, No. 3-4, pp. 646-653.

Dusseault, M.B., Bruno, M.S., Barrera, J., 2001. Casing Shear: Causes, Cases, Cures, *SPE Drilling & Completion*, Vol. **16**, No. **2**, pp. 98-107, SPE 72060-PA.

Dusseault, M.B., Collins, P.M., 2008. Geomechanics Effects in Thermal Processes for Heavy Oil Exploitation, CSEG RECORDER June 2008

Dusseault, M.B., Collins, P.M., 2008. Geomechanics Effects in Thermal Processes for Heavy Oil Exploitation, *Canadian Society of Exploration Geophysicists (CSEG) Recorder*, Vol. **33**, pp. 20-23.

Ghannadi, S., Irani, M., Chalaturnyk, R., 2013. Evaluation of Induced Thermal Pressurization in Clearwater Shale Caprock in Electromagnetic Steam-Assisted Gravity Drainage (EM-SAGD) Projects, *SPEJ*, SPE-152217-PA.

Government of Alberta, 2011. Alberta Oil Sands Industry (AOSID) - Quarterly Update Summer 2011, Reporting on the period: March 5, 2011 to June 3, 2011, www.albertacanada.com

Government of Alberta, 2012. www.energy.gov.ab.ca/OilSands/1715.asp

Gunal, G.O., Islam, M.R., 2000, Alteration of Asphaltic Crude Rheology with Electromagnetic and Ultrasonic Irradiation, *Petroleum Science and Engineering*, Vol. **26**, No. **1-4**, pp. 263-272.

Handin, J., Hager, R.V. Jr., 1957. Experimental Deformation of Sedimentary Rocks under Confining Pressure: Tests at Room Temperature on Dry Samples, *Bulletin of the American Association of Petroleum Geologists*, Vol. **41**, No. **1**, pp. 1-50.

Hiebert A.D., Vermeulen, F.E., Chute, F.S., Capjack, C.E., 1986. Numerical Simulation Results for the Electrical Heating of Athabasca Oil-Sand Formations, SPE Reservoir Engineering, Vol. **1**, No. **1**, pp. 76-84.

Islam, M.R., Wadadar, S.S., Banzal, A., 1991. Enhanced Oil Recovery of Ugnu Tar Sands of Alaska Using Electromagnetic Heating with Horizontal Wells, Paper SPE 22177, *International Arctic Technology Conference,* Anchorage, Alaska, US, 29-31 May.

Kasevich, R.S., Price, S.L., Faust, D.L., Fontaine, M.F., 1994. Pilot testing of a radio frequency heating system for enhanced oil recovery from diatomaceous earth, *69th Annual Technical Conference and Exhibition*, New Orleans, USA, 25-28 September.

Khan, S., Han, H., Ansari, S., Khosravi, N., 2010. An Integrated Geomechanics Workflow for Caprock-Integrity Analysis of a Potential Carbon Storage Site, *International Conference on CO_2 Capture, Storage, and Utilization*, New Orleans, Louisiana, USA, 10-12 November, SPE 139477.

Koolman, M., Huber, N., Diehl, D., Wacker, B., 2008. Electromagnetic Heating Method to Improve Steam Assisted Gravity Drainage, *International Thermal Operations and Heavy Oil Symposium*, 20-23 October 2008, Calgary, Alberta, Canada, SPE117481-MS, doi:10.2118/117481-MS.

Kovaleva, L., Davletbaev, A., Babadagli, T., Stepanova, Z., 2011. Effects of Electrical and Radio-Frequency Electromagnetic Heating on the Mass Transfer Process During Miscible Injection for Heavy-Oil Recovery, *Energy and Fuels*, Vol. **25**, No. **2**, pp. 482-486.

McGee, B.C.W., Vermeulen, F. E., Yu, L., 1999. Field test of electrical heating with horizontal and vertical wells, CHOA Handbook, 2nd Edition, ISBN 0969521316, pp. 565-572.

McGee, B.C.W., Vermeulen, F.E., 2000. In-Situ Electromagnetic Heating for Hydrocarbon Recovery and Environmental Remediation; *Journal of Canadian Petroleum Technology*, Distinguished Authors Series, Vol. **39**, No. **8**, pp. 24-28.

McGee, B.C.W., Vermeulen, F.E., 2007. The Mechanisms of Electrical Heating for the Recovery of Bitumen From Oil Sands, *Journal of Canadian Petroleum Technology*, Vol. **46**, No. **1**, pp. 28-34.

McGee, B.C.W., Vermeulen, F.E., and Yu, L., 1999. Field Test of Electrical Heating with Horizontal and Vertical Wells, *Journal of Canadian Petroleum Technology*, Vol . **38**, No. **3**, pp. 46-53.

Sahni, A., Kumar, M., Knapp, R.B., 2000. Electromagnetic Heating Methods for Heavy Oil Reservoirs, *SPE/AAPG Western Regional Meeting*, Long Beach, California, 19-23 June, SPE 62550.

Sayakhov, F.L., Kovaleva, L.A., Nasyrov, N.M., 2002. Heat and Mass Transfer in the Well-Stratum System under the Electromagnetic Action on Massive Oil Deposits, *Journal of Engineering Physics and Thermophysics*, Vol. **75**, No. **1**,.pp. 126-133.

Smith, R.J., Alinsangan, N.S., Talebi, S., 2002. Microseismic Response of Well Casing Failures at a Thermal Heavy Oil Operation, *SPE/ISRM Rock Mechanics Conference*, Irving, Texas, 20-23 October, SPE78203.

Spencer, H.L. 1987. Electromagnetic Oil Recovery Ltd. Calgary.

Spencer, H.L., 1989. Electric Heat Breaks Paraffins, Boosts Production, *Enhanced Recovery Week*, 30.10, pp. 1-2.

Talebi, S., Nechtschein, S., Boone, T.J., 1998. Seismicity and Casing Failures Due to Steam Stimulation in Oil Sands, *Pure Applied Geophysics*, Vol. **153**, pp. 219-233.

Uwiera-Gartner, M.M.E., Carlson, M.R., Palmgren, C.T.S., 2011a. Evaluation of the Clearwater Formation Caprock for a Proposed, Low-Pressure, Steam-Assisted Gravity Drainage Pilot Project, *SPE Annual Technical Conference and Exhibition*, Denver, Colorado, USA, 30 October-2 November, 2011, SPE 147302, doi:10.2118/147302-MS.

Uwiera-Gartner, M.M.E., Carlson, M.R., Walters, D., Palmgren, C.T.S., 2011b. Geomechanical Simulation of Caprock Performance for a Proposed, Low Pressure, Steam-Assisted Gravity Drainage Pilot Project, *Canadian Unconventional Resources Conference*, Calgary, Alberta, Canada, 15-17 November, 2011, SPE 148886, doi:10.2118/148886-MS.

Vermeulen F.E., Chute, F. S., 1983. Electromagnetic Techniques in the In-Situ Recovery of Heavy Oils, *Journal of Microwave Power*, Vol. **18**, No. **1**, pp. 15-29.

Vermeulen, F., McGee, B., 2000. In-Situ Electromagnetic Heating for Hydrocarbon Recovery and Environmental Remediation, Vol. **39**, No. **8**, pp. 25-29.

Vermeulen, F.E., Chute, F.S., Cervenan, M.R., 1979. Physical Modelling of the Electromagnetic Heating of Oil Sand and Other Earth-Type and Biological Materials, *Canadian Electrical Engineering Journal*, Vol. **4**, pp. 19-28.

Vermeulen, F.E., Chute, F.S., Mcpherson, R.G., 1988. Physical Modelling of Electrothermal Processes in Oil Sand, *Alberta Oil Sands Technology and Research Journal of Research*, Vol. **4**, pp. 299-305.

Wacker, B., Karmeileopardus, D., Trautmann, B., Helget, A., Torlak, M., 2011. Electromagnetic Heating for In-Situ Production of Heavy Oil and Bitumen Reservoirs, *Canadian Unconventional Resources Conference*, Calgary, Alberta, Canada, 15-17 November, CSUG/SPE 148932.

Wong, R.C.K., Chau, K.T., 2004. Casing Impairment Induced by Shear Slip along a Weak Layer in Shale due to Fluid (Steam) Injection, *Canadian International Petroleum Conference*, Calgary, Alberta, Canada, 8-10 June.

Yuan, Y., Xu, B., Palmgren C., 2011a. Design of Caprock Integrity in Thermal Stimulation of Shallow Oil-Sands Reservoirs, *Canadian Unconventional Resources Conference*, Calgary, Alberta, Canada, 15-17 November, 2011, SPE 149371.

Yuan, Y., Xu, B., Yang, B., 2011b. Geomechanics for the Thermal Stimulation of Heavy Oil Reservoirs-Canadian Experience, *SPE Heavy Oil Conference and Exhibition*, Kuwait City, Kuwait, 12-14 December, SPE 150293, doi:10.2118/150293-MS.

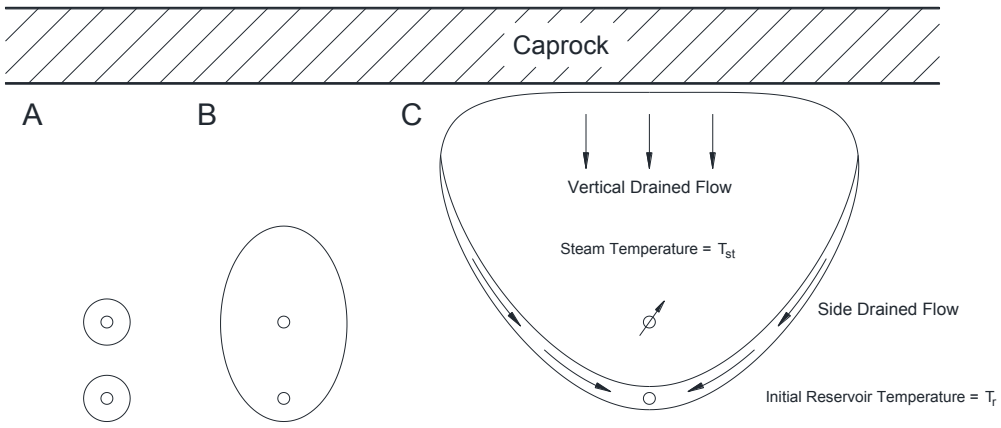

Figure 1.1. Cross-section of SAGD process; Section A presents circulation phase, Section B presents early phase, and Section C presents steam injection phase.

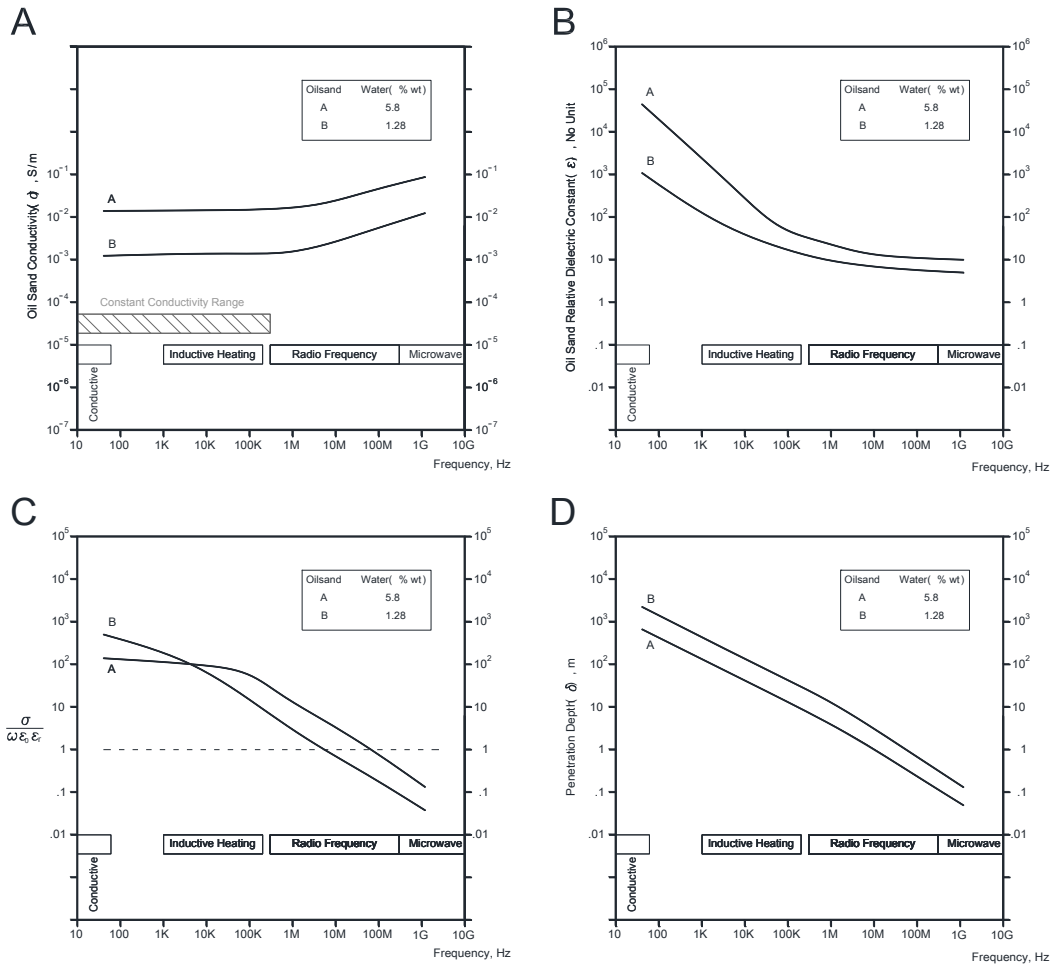

Figure 1.2. Average oil sand conductivity (Section A), relative dielectric constant (Section B), loss tangent (Section C) and penetration depth (Section D) a function of frequency

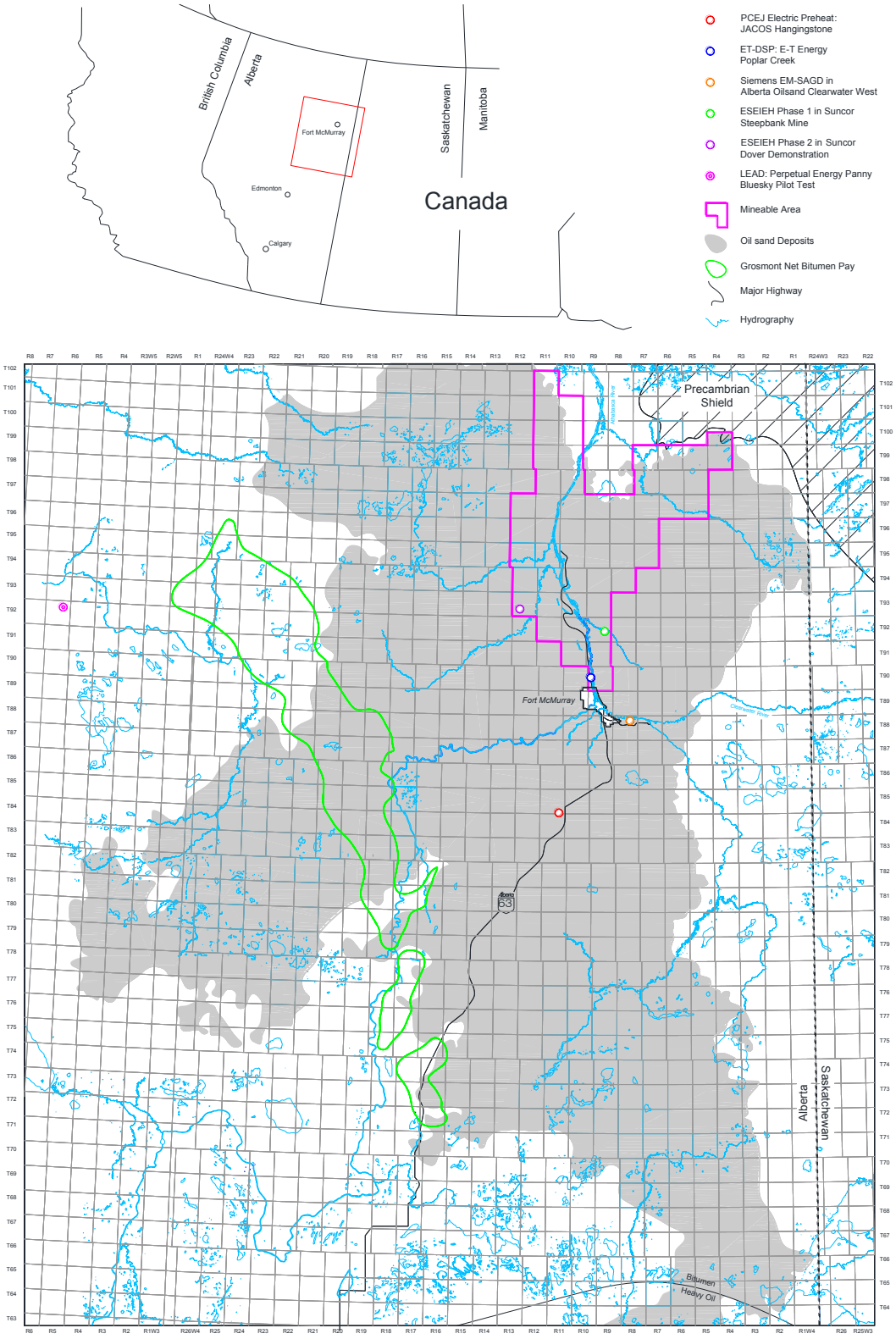

Figure 1.3. Location of major EM operations in the Athabasca area.

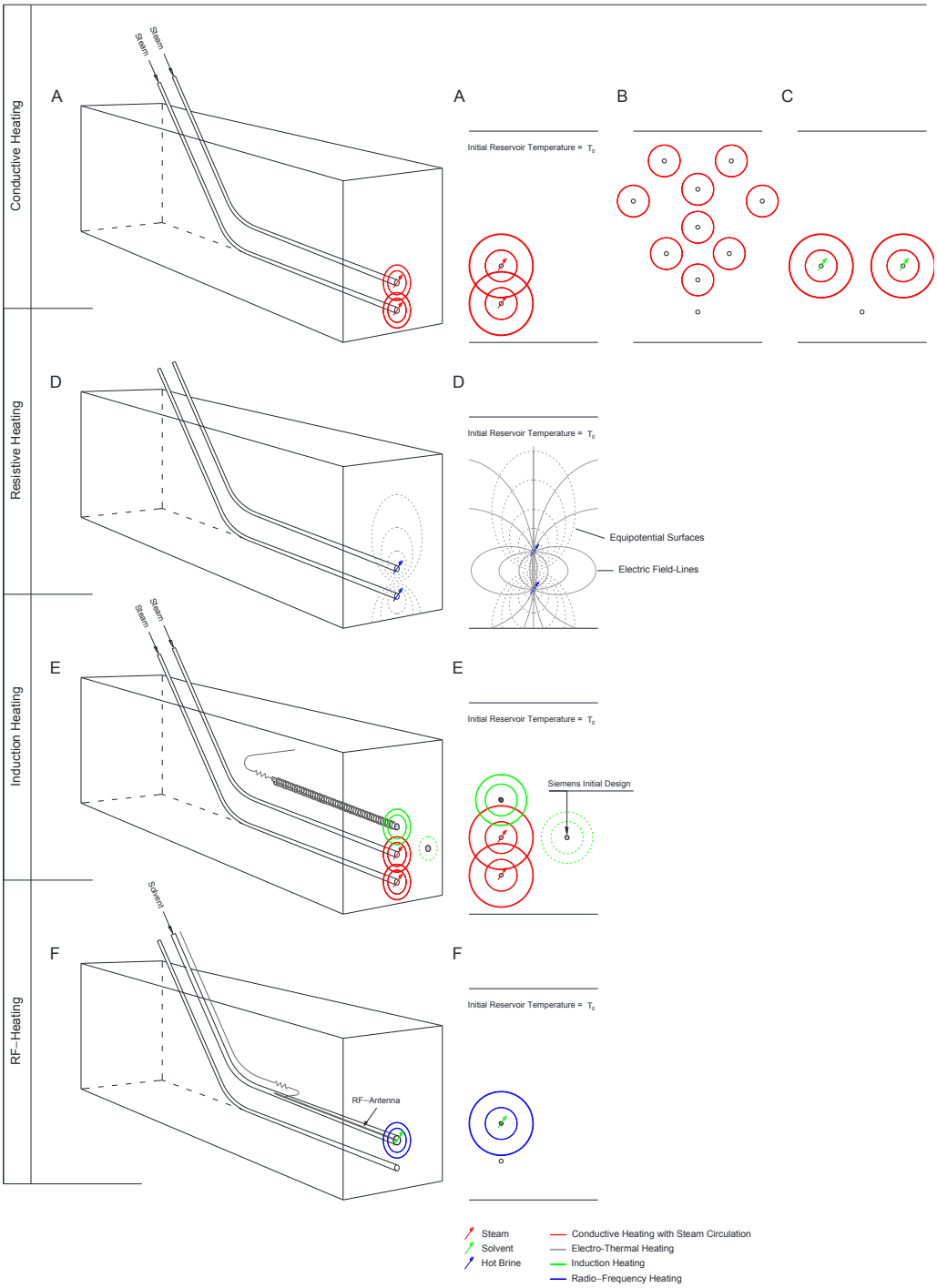

Figure 1.4. Illustration of different start-up techniques in Athabasca reservoirs: SAGD process (Section A), TAGD process (Section B), LEAD process (Section C), GEAGD process (Section D), Siemens suggested EM-SAGD process (Section E), and Harris ESEIEH process (Section F).

This page is intentionally left blank.

2. Induction and Radio–Frequency Heating Start-Up[3]

2.1. Introduction

Steam-assisted gravity drainage (SAGD) is the method of choice to extract bitumen from Athabasca oil sand reservoirs in Western Canada. Under reservoir conditions, bitumen is immobile due to high viscosity and its typically high level of saturation limits the injectivity of steam. In current industry practice, steam is circulated within injection and production wells. Operators keep the steam circulating until mobile bitumen breaks through the producer and communication is established between the injector and the producer. The "start-up" (or "circulation") phase is a time-consuming process taking three or more months. A variety of processes are used to minimize the length of the start-up phase, such as *electromagnetic (EM) heating in* either the induction (medium frequency) or *radio frequency* (*RF*) ranges. Knowledge of the size of the hot zone formed by steam circulation and of the benefits of simultaneous EM-heating techniques increases understanding of the start-up process and helps to minimize start-up duration.

The purpose of start-up is communication between injector and producer, after which it is terminated. This section presents the mathematical background for SAGD (purely conduction), EM-SAGD (inductive and conduction) and ESEIEH™ (RF heating). The physics of different start-up strategies are used to calculate start-up termination time for a homogenous system.

2.1. Start-up in SAGD process

In order to initiate a SAGD process, thermal communication must be established between injector and producer. Start-up of a SAGD process in oil sand reservoirs requires the establishment of oil mobility between the well pair. This requires heating the fluid between injector and producer to a temperature at which the oil will flow from injector to producer. In reservoirs with low water mobility, conductive heating is the only heating mechanism, and convection does not play a role until at least some thermal communication is established between injector and producer. This is due to bitumen immobility, which is in turn due to the high viscosity and very low effective permeability of steam condensate under in situ conditions. Accordingly, a start-up phase is required for a SAGD operation, during which both injector and producer are put under steam circulation. This is designed to establish inter-well communication, which is theoretically achieved when the mid-interval (or mid-point) temperature reaches the mobilization temperature. It is accepted in the industry that there are two different threshold temperatures for bitumen mobilization.

First, mobilization temperature is defined as the lowest temperature at which bitumen mobility can accelerate diffusion and dispersion of a solvent. In this study, since shear wave velocity induced at seismic is absorbed by bitumen at a viscosity of around 10,000 cP, this value is considered a threshold for such mobilization. Although diffusion increases with temperature, very high temperatures are not needed for it to occur. This is proved by processes such as vapour extraction (VAPEX), which runs at reservoir temperature (i.e., 10 to 20°C), and N-SOLV, which operates at temperatures between 40 and 50°C. Figure 2.8 shows that viscosity of 10,000 cP is relevant for temperatures of 46 to 56°C for Athabasca and Peace River oil sand reservoirs. This study considers the average of this range (51°C) as the mobilization temperature. For diffusion-

[3] A version of this *chapter* has been published. Ghannadi, S., Irani, M. and Chalaturnyk, R., in SPEJ Journal, Preprint. SPE-178427-PA. (2015); and selected JCPT Tech Briefs, SPE-0315-081-JCPT in JCPT **54**(2): 81-84; and SPE-170037-MS presented in SPE Heavy Oil Conference-Canada, Calgary, Alberta, Canada, 10-12 June, 2014.

controlled systems such as Expanding Solvent-SAGD (ES-SAGD) and the ESEIEH™ process, which control system is solvent diffusion into bitumen.

In this study, the first mobilization is called diffusion-controlled mobilization, which is the proper value to use for solvent diffusion/dispersion and mass transfer phenomena. The second, heating mobilization, is the proper value to use for thermal processes such as SAGD. Edmunds and Gittins (1991) indicate that for SAGD processes, once thermal conduction via steam circulation has heated bitumen to between 50 and 100°C, the bitumen is sufficiently mobile that it can be displaced by hot water and rapid convectional heating can occur. Yuan and McFarlane (2011) suggested a temperature at the midpoint between injector and producer of 70 to 90°C to determine the steam circulation period, and an average of 80°C was settled on for practical usage. This study defines the end of the start-up period for SAGD and induction heating processes as the point at which maximum bitumen viscosity along the midpoint between the well pair reaches 1000 cP. Figure 2.8 shows that this viscosity relates to a temperature range of 75 to 85°C for Athabasca and Peace River oil sand reservoirs. Thus, the average temperature of 80°C is suggested, which is identical to Yuan and McFarlane (2011).

For the cylinder with radial and axial symmetry, the heat-conduction equation is:

$$\underbrace{\frac{1}{r}\frac{\partial}{\partial r}\left(Kr\frac{\partial T}{\partial r}\right)}_{\text{Conduction heat transport}} = \underbrace{\rho_r c_{pr}\left(\frac{\partial T}{\partial t}\right)}_{\text{Internal Heat Storage}} \quad (2)$$

Assuming that thermal conductivity is independent of temperature, Equation 2 yields:

$$\frac{\partial^2 T}{\partial r^2}+\frac{1}{r}\frac{\partial T}{\partial r}=\frac{\rho_r c_{pr}}{K}\left(\frac{\partial T}{\partial t}\right)=\frac{1}{\kappa_{Thermal}}\left(\frac{\partial T}{\partial t}\right) \quad (3)$$

in which T is reservoir temperature; ρ_r is reservoir density; c_{pr} is reservoir specific heat capacity; K is thermal conductivity of the reservoir, and $\kappa_{Thermal}$ is thermal diffusivity of the reservoir, which is given by:

$$\kappa_{Themal}=\frac{K}{\rho_r c_{pr}} \quad (4)$$

Before steam injection phase (see Figure 1.1), conduction is the only mechanism in most oil sand reservoirs (due to low levels of water mobility). Since the thermal diffusivity of McMurray shale is very close to that of lean, rich McMurray oil sand, system-wide constant thermal diffusivity can be assumed for circulation time due to the short-range effect of circulation in the interval of 5m.

Duong et al. (2008) give a basic line-source solution for transient heat conduction in a cylindrical medium (similar to pressure diffusion in an infinite acting reservoir):

$$T=T_{res}-\left(\frac{q}{4\pi K}\right)E_i\left(-\frac{r^2}{4\lambda\kappa_{Thermal}t}\right) \quad (5)$$

in which λ is the time conversion factor from days to seconds (8.64×10^4), and E_i is the exponential integral function. Equation 5 assumes uniform constant temperature as an initial condition for solution:

$$T(r,0)=T_{res} \quad (6)$$

and the boundary conditions are:

$$T(r=0,t)=T_{st} \quad 7$$

$$T(r\to\infty,t)=T_{res} \quad 8$$

in which T_{st} is steam temperature at circulation, and T_r is reservoir temperature. The temperature rise ($T_z - T_{res}$) at point during circulation is given by:

$$T_z - T_{res} = -\left(\frac{q_{inj}}{4\pi K}\right)E_i\left(-\frac{(z_{inj})^2}{4\lambda\kappa_{Thermal}t}\right)-\left(\frac{q_{pro}}{4\pi K}\right)E_i\left(-\frac{(z_{pro})^2}{4\lambda\kappa_{Thermal}t}\right) \quad 9$$

Using Equation 9, the temperature rise at the injector can be calculated as:

$$T_{st}^{inj} - T_{res} = -\left(\frac{q_{inj}}{4\pi K}\right)E_i\left(-\frac{(OD_{inj}/2)^2}{4\lambda\kappa_{Thermal}t}\right)-\left(\frac{q_{pro}}{4\pi K}\right)E_i\left(-\frac{(z_{int})^2}{4\lambda\kappa_{Thermal}t}\right) \quad 10a$$

$$T_{st}^{pro} - T_{res} = -\left(\frac{q_{inj}}{4\pi K}\right)E_i\left(-\frac{(z_{int})^2}{4\lambda\kappa_{Thermal}t}\right)-\left(\frac{q_{pro}}{4\pi K}\right)E_i\left(-\frac{(OD_{pro}/2)^2}{4\lambda\kappa_{Thermal}t}\right) \quad 10b$$

The heat rate at injector and producer can be calculated by solving linear equations with two equations (Equations 10a, 10b) and two variables (unknowns), as:

$$q_{inj} = 4\pi K\frac{(T_{st}^{inj}-T_{res})E_i\left(-\frac{(z_{int})^2}{4\lambda\kappa_{Thermal}t}\right)-(T_{st}^{pro}-T_{res})E_i\left(-\frac{(OD_{inj}/2)^2}{4\lambda\kappa_{Thermal}t}\right)}{E_i\left(-\frac{(OD_{inj}/2)^2}{4\lambda\kappa_{Thermal}t}\right)E_i\left(-\frac{(OD_{pro}/2)^2}{4\lambda\kappa_{Thermal}t}\right)-\left[E_i\left(-\frac{(z_{int})^2}{4\lambda\kappa_{Thermal}t}\right)\right]^2} \quad 11a$$

$$q_{pro} = 4\pi K\frac{(T_{st}^{pro}-T_{res})E_i\left(-\frac{(z_{int})^2}{4\lambda\kappa_{Thermal}t}\right)-(T_{st}^{inj}-T_{res})E_i\left(-\frac{(OD_{pro}/2)^2}{4\lambda\kappa_{Thermal}t}\right)}{E_i\left(-\frac{(OD_{inj}/2)^2}{4\lambda\kappa_{Thermal}t}\right)E_i\left(-\frac{(OD_{pro}/2)^2}{4\lambda\kappa_{Thermal}t}\right)-\left[E_i\left(-\frac{(z_{int})^2}{4\lambda\kappa_{Thermal}t}\right)\right]^2} \quad 11b$$

Substituting heat rates from Equations 11a and 11b into Equation 9, the temperature at any location during circulation is given by:

$$T_z - T_{res} = \left\{\begin{array}{l}\left[(T_{st}^{pro}-T_{res})E_i\left(-\frac{(z_{int})^2}{4\lambda\kappa_{Thermal}t}\right)-(T_{st}^{inj}-T_{res})E_i\left(-\frac{(OD_{pro}/2)^2}{4\lambda\kappa_{Thermal}t}\right)\right]E_i\left(-\frac{(z_{inj})^2}{4\lambda\kappa_{Thermal}t}\right)\\ +\left[(T_{st}^{inj}-T_{res})E_i\left(-\frac{(z_{int})^2}{4\lambda\kappa_{Thermal}t}\right)-(T_{st}^{pro}-T_{res})E_i\left(-\frac{(OD_{inj}/2)^2}{4\lambda\kappa_{Thermal}t}\right)\right]E_i\left(-\frac{(z_{pro})^2}{4\lambda\kappa_{Thermal}t}\right)\end{array}\right\} \quad 12$$

$$\div\left\{\left[E_i\left(-\frac{(z_{int})^2}{4\lambda\kappa_{Thermal}t}\right)\right]^2-E_i\left(-\frac{(OD_{inj}/2)^2}{4\lambda\kappa_{Thermal}t}\right)E_i\left(-\frac{(OD_{pro}/2)^2}{4\lambda\kappa_{Thermal}t}\right)\right\}$$

Figure 2.9 shows that in major SAGD projects, liner size is identical in both injector and producer. Because steam circulates in at similar saturated steam temperatures, steam temperature in both wells are also similar to one another (T_{st}). Also, knowing: $z_{inj}+z_{pro}=z_{int}$, Equation 12 yields:

$$T_z - T_{res} = (T_{st} - T_{res}) \frac{E_i\left[-\frac{(z_{inj})^2}{4\lambda\kappa_{Thermal}t}\right] + E_i\left[-\frac{(z_{pro})^2}{4\lambda\kappa_{Thermal}t}\right]}{E_i\left[-\frac{(z_{int})^2}{4\lambda\kappa_{Thermal}t}\right] + E_i\left[-\frac{(OD/2)^2}{4\lambda\kappa_{Thermal}t}\right]}$$
$$= (T_{st} - T_{res}) \frac{E_i\left[-\frac{(z_{inj})^2}{4\lambda\kappa_{Thermal}t}\right] + E_i\left[-\frac{(z_{int} - z_{inj})^2}{4\lambda\kappa_{Thermal}t}\right]}{E_i\left[-\frac{(z_{int})^2}{4\lambda\kappa_{Thermal}t}\right] + E_i\left[-\frac{(OD/2)^2}{4\lambda\kappa_{Thermal}t}\right]} \quad 13$$

It must be noted that in some operations such as Leismer (Statoil Canada) and MacKay River (Suncor Energy) pressure at the injector is slightly higher (20–50 kPa) to induce downward flow to the producer. Under these conditions, steam temperatures are slightly different at injector and producer. Substituting mid-interval distance for both z_{inj} and z_{pro} into Equations 12 and 13 yields Equations 14a and 14b, respectively:

$$T_{int/2} - T_{res} = \left\{ \begin{array}{l} (T_{st}^{inj} - T_{res})\left[E_i(-\frac{(z_{int})^2}{4\lambda\kappa_{Thermal}t}) - E_i(-\frac{(OD_{pro}/2)^2}{4\lambda\kappa_{Thermal}t})\right] \\ + (T_{st}^{pro} - T_{res})\left[E_i(-\frac{(z_{int})^2}{4\lambda\kappa_{Thermal}t}) - E_i(-\frac{(OD_{inj}/2)^2}{4\lambda\kappa_{Thermal}t})\right] \end{array} \right\} \times E_i(-\frac{(z_{int}/2)^2}{4\lambda\kappa_{Thermal}t})$$
$$\div \left\{ \left[E_i(-\frac{(z_{int})^2}{4\lambda\kappa_{Thermal}t})\right]^2 - E_i(-\frac{(OD_{inj}/2)^2}{4\lambda\kappa_{Thermal}t}) E_i(-\frac{(OD_{pro}/2)^2}{4\lambda\kappa_{Thermal}t}) \right\} \quad 14a$$

$$T_{int/2} - T_{res} = \frac{2(T_{st} - T_{res})\, E_i(-\frac{(z_{int}/2)^2}{4\lambda\kappa_{Thermal}t})}{\left[E_i(-\frac{(z_{int})^2}{4\lambda\kappa_{Thermal}t}) + E_i(-\frac{(OD/2)^2}{4\lambda\kappa_{Thermal}t})\right]} \quad 14b$$

Figure 2.13 shows the procedure suggested in this study to calculate circulation time. As shown in Figure 2.13, temperature variation is calculated as a function of time, and then temperature is calculated related to mobilization for the proposed condition. For example, Figure 2.17a illustrates the variation of mid-interval temperature rise versus circulation time for different thermal diffusivities and liner sizes. If a similar graph is created for a liner size of 5" to 10" and calculated circulation time at 51°C (suggested mobilization-temperature) is evaluated for every liner size, graphs similar to Figure 2.17b can be created to address liner size variation. Figure 2.17b shows that similar results can be presented for diffusion-controlled temperatures (for ES-SAGD start-up).

The solution for circulation in SPE178427 is based on Duong et al. (2008). They used a basic line source solution for transient heat conduction in cylindrical medium. The limitation in this solution is an assumption of constant heat flux at wellbore boundary. This cause an error in the solution for temperature variation in the reservoir.

Fine grid size *CMG-STARS* model is created to test the Equation 14a vs. the numerical simulation to verify the solution. For fully conduction (no convection) system the porosity should be assigned zero:

```
POR CON             0.0
```

To apply the temperature the initial temperature is given as 12°C (the common reservoir temperature in MacKay River and most shallow SAGD projects):

```
TEMP CON           12
```

Then the steam circulation temperature (214°C) should be assigned to the grid cell presenting the circular wellbore as an initial condition (as well as heaters function):

```
*MOD
1494     1:1     238   =  214
1495     1:1     238   =  214
…
1506     1:1     238   =  214
```

Heaters should also be assigned to the grid cell presenting the circular wellbore. For considering the constant temperature the U factor is suggested infinity or large numbers such as 1×10^{10}:

```
UHTR IJK
1494 1:1     238     1E10
1495 1:1     238     1E10
…
1506 1:1     238     1E10

TMPSET IJK
1494 1:1     238     214
1495 1:1     238     214
…
1506 1:1     238     214
```

Since grids are 1 cm×1 cm for a wellbore of 10 5/8”; 577 grids are needed to represent the wellbore, and code has to be developed for defining the representing grids. The results of the *CMG-STARS* model are compared to solution presented in Eq. 14a for mid-point and for every point in the reservoir.

In Figure 2.10a the temperature contour (Isotherm contour lines) for CMG model vs. Eq. 14a are compared. The error for colder points is increasing. As shown in Figure 2.10b the error at mid-point is at its maximum. The temperature variation at mid-point vs. time is compared for CMG simulation and analytical model in Figure 2.10c. Numerical simulation which can be defined as exact solution is greater than temperatures calculated from Eq. 14a. The error is less than 10% after the first third month and it is slightly greater for smaller thermal diffusivities (see Figure 2d).

Heat rate at injector and producer can be calculated from solving linear equations with two equations for constant temperature at inner points in injector and producer as:

$$\vec{q}_{inj}=\vec{q}_{pro}=\vec{q}_{BC}=-\frac{4\pi K(T_{st}-T_{res})}{E_i\left[-\frac{(z_{int})^2}{4\lambda\kappa_{Thermal}t}\right]+E_i\left[-\frac{(OD/2)^2}{4\lambda\kappa_{Thermal}t}\right]} \qquad 15$$

Required power to keep temperature constant at sand face can be calculated from Eq. 15:

$$\dot{H}_{required}=|\vec{q}_{BC}|L_{well} \qquad 16$$

The absolute sign in Eq. 15 is due to negative sign convention for added heat. Knowing the injected rate the provided power is given by:

$$\dot{H}_{injection} = q_{st}\,\rho_w L_v X \qquad 17$$

In steam circulation if the provided power (Eq. 17) is less than required power (Eq. 1617) only part of the well would be heated and the rest would stay cold. As shown in Fig 3 the required power for lean zones is higher due to greater thermal conductivity. For rich zones common circulation rates (i.e., steam injection of 3 m^3/hr) and providing quality greater than 0.6 can be considered as a constant tempertature boundary condition for most circulation duration. On other side using common electrical heaters can be suggested as constant heat flux boundary for the first 2-3 months.

Assuming the steam latent heat is the only source of heating the reservoir in steam circulation, the length of heated section in circulation can be calculated from equalizing Eqs. 1617 and 17:

$$if\ \dot{H}_{injection} < \dot{H}_{required}:$$
$$L_{hot} = \frac{q_{st}\,\rho_w L_v X}{|\vec{q}_{BC}|} \qquad 18$$

Based on Eq. 18the hot part of the well in toe injection is calculated for different steam rates in Figure 2.12.

2.2. Start-up in Ohmic Heating (Using Electric Heaters)

In ohmic heating heat transferred from the surface of the electric heater elements into the reservoir by thermal conduction. Notable examples of this approach are induction heating (Kahn et al., 2001) and resistive heating elements (such heaters have been used in Shell IUP, N-solv™, TAGD and LEAD processes). Similar to SAGD process conduction heating is the dominant heat transfer (McGee and Donaldson 2009) and governing equation is given by:

$$\underbrace{\frac{\partial^2 T}{\partial r^2} + \frac{1}{r}\frac{\partial T}{\partial r}}_{Conduction} = \frac{\rho_r c_{pr}}{K}\left(\frac{\partial T}{\partial t}\right) \qquad 19$$

Solution for Equation 19 can be given for two different boundary conditions: constant heat flux and constant sand face temperature. Moini and Edmunds (2013) mentioned that "electrical power of the (electric heater) rod is the known parameter … and the unknown is the temperature on the wellbore wall (sand face)". But in common practice target temperature on the sand face is given to electric heater provider as a requirement ($T_{well} = T_{electrode}$). Thus, in this study Equation 19 is solved for constant sand face temperature (Carslaw and Jaeger, 1959):

$$T = (T_{electrode} - T_{res}) + \frac{2(T_{electrode} - T_{res})}{\pi} \times \int_0^{\infty} \exp(-\kappa_{Thermal}\,u^2 t)\,\frac{J_0(ur)Y_0(u\times OD/2) - J_0(u\times OD/2)Y_0(ur)}{[J_0(u\times OD/2)]^2 + [Y_0(u\times OD/2)]^2}\,\frac{du}{u} \qquad 20$$

where, $T_{electrode}$ is operating temperature of the electric heater. In case of using a pair of electric heaters temperature can be predicted using Equation 13 replacing the T_{st} with target temperature of the electric heater.

Electric heaters heat transfer mechanism is similar to SAGD operation and not providing shorter start-up time so in this study we did not discuss these heaters in detail. Although ohmic techniques is heating the reservoir via conduction they can be useful for shallow operations that low MOP limits the steam injection pressure and associated steam temperature. And electrical heaters can provide high temperatures independent of MOP.

2.3. Start-up in Electro-Thermal Heating with Conduction Only

The governing energy conservation equation describing the transient temperature distribution for electro-thermal heating is described as:

$$\underbrace{\frac{1}{r}\frac{\partial}{\partial r}\left(Kr\frac{\partial T}{\partial r}\right)}_{\text{Conduction Heat Transport}} + \dot{Q}_{\text{Electro}-\text{Thermal}} = \underbrace{\rho_r c_{pr}\left(\frac{\partial T}{\partial t}\right)}_{\text{Internal Heat Storage}} \quad 21$$

Equation 21 consists of heat transfer by conduction and the distribution of electric power radially from the electrode (McGee and Donaldson 2009). Combining the electric charge-conservation equation with Ohm's law, the electric-potential equation can be written as (Bogdanov et al., 2011):

$$-\nabla_r \cdot (\sigma \nabla_r V) = 0 \quad 22$$

where σ is the electrical conductivity of the oil sand, and V is electric potential. For radial geometry the solution for Equation 22 is given by:

$$-r\sigma \cdot \nabla_r V = J/2\pi = \frac{\wp_{electrode}}{2\pi L_{electrode}} \quad 23$$

where J is electric current per unit thickness that is equal to $\wp_{electrode}/L_{electrode}$. Integrating Equation 23 between the electrode ($r_{electrode}$) and external (R_{ext}) radii, one obtains the electric current at given potential between electrode and external radii (Bogdanov et al., 2011):

$$J = \frac{2\pi(V_{electrode} - V_{ground})}{\int_{r_{electrode}}^{R_{ext}} \frac{dr}{\sigma r}} = \frac{2\pi V_{electrode}}{\int_{r_{electrode}}^{R_{ext}} \frac{dr}{\sigma r}} \quad 24$$

External radius (R_{ext}) must be chosen large enough that the outer boundary does not affect the temperature profile but never larger than drainage radius. In theory R_{ext} should be large enough that $T(R_{ext}) = T_{res}$. In this study three times the injector and producer distance (i.e., 15 m) is assumed. Knowing that the heating power density is defined as:

$$\dot{Q}_{\text{Electro}-\text{Thermal}} = \sigma \left|\nabla_r V\right|^2 \quad 25$$

By substituting electro-thermal heating term from Equation 25 into Equation 21 we have (McGee and Donaldson 2009):

$$\underbrace{\frac{\partial^2 T}{\partial r^2}+\frac{1}{r}\frac{\partial T}{\partial r}}_{\text{Conduction}}+\underbrace{\frac{1}{\sigma K}\left(\frac{\wp_{electrode}}{2\pi L_{electrode} r}\right)^2}_{\text{Electro}-\text{Thermal Heating}}=\frac{\rho_r c_{pr}}{K}\left(\frac{\partial T}{\partial t}\right) \quad 26$$

where $\wp_{electrode}$ is electrical current flowing in electrode, $L_{electrode}$ is length of the electrode, and σ is electrical conductivity of the oil sand reservoir (the reservoir bulk electric conductivity). Suggesting that conduction is minimal and also the ground potential is equal to zero, the increase in temperature is given by:

$$\frac{dT}{dt}=\frac{\sigma\left|\nabla_r V\right|^2}{\rho_r c_{pr}}=\frac{\sigma V_{electrode}^2}{\rho_r c_{pr}}\frac{1}{r^2\left[Ln(R_{ext}/r_{electrode})\right]^2} \quad 27$$

Or,

$$T-T_{res}=\frac{\sigma V_{electrode}^2}{\rho_r c_{pr}}\frac{1}{r^2\left[Ln(R_{ext}/r_{electrode})\right]^2}t \quad 28$$

In electro-thermal heating process heat is created in the reservoir as electrical current passes through the connate water. At low frequencies (300 kHz) the reservoir behaves as a resistor, and electrical energy converts to heat by ohmic loss. Suggesting that conduction is minimal and also the ground potential is equal to zero, the increase in temperature is given by:

$$T-T_{res}=\frac{\sigma V_{electrode}^2}{\rho_r c_{pr}}\frac{1}{r^2\left[Ln(R_{ext}/r_{electrode})\right]^2}t \quad 29$$

where, σ is electrical conductivity of the oil sand reservoir (the reservoir bulk electric conductivity), $r_{electrode}$ and R_{ext} are the electrode and external radii, and $V_{electrode}$ is electric-potential input given at the electrode. It must be noted that electrical conductivity (σ) varies by time since it changes with the water saturation, the temperature and the salt concentration, but in this study for simplicity we assumed that is constant. Electro-thermal power density for two electrodes into the reservoir is given by:

$$\dot{Q}_{Electro-Thermal}=\frac{\sigma V_{electrode}^2}{\left[Ln(R_{ext}/r_{electrode})\right]^2}\left[\frac{1}{r}+\frac{1}{z_{int-elect}-r}\right]^2 \quad 30$$

As shown in Figure 2.14a the power density is improved using two electrodes. The purpose of showing this data is to emphasize the benefits of introducing two electrodes versus one electrode. It must be noted that localized heating near the surface of the electrode remains an issue for two electrodes, but the power density distribution becomes much more uniform and as shown in Figure 2.14a the time to reach target temperatures is reduced four times for two electrodes case. The temperature profile along a line connected by two electrode wells is given by:

$$T-T_{res}=\frac{\sigma V_{electrode}^2}{\rho_r c_{pr}}\frac{1}{\left[Ln(R_{ext}/r_{electrode})\right]^2}\left[\frac{1}{r}+\frac{1}{z_{int-elect}-r}\right]^2 t \quad 31$$

Reduction of start-up time by four times is economic trade-off for using two electrodes. Figure 1.4d presents a configuration of gas and electrical heating-assisted gravity-drainage (GEAGD) process which includes a pair of horizontal wells that acts as electric dipole moments [China patent 101892826A (Di et al., 2013) and 101892826B (Liguo et al., 2013)]. Configuration given in GEAGD can be used for SAGD start-up. In case of two electrodes the temperature at mid-point can be evaluated from electrode temperature using the following equation (Liguo et al., 2011):

$$T_{mid} - T_{res} = \left[\frac{z_{int}}{8 r_{electrode}} \sqrt{\left(\frac{z_{int}}{2 r_{electrode}} \right)^2 - 1} \right] (T_{electrode} - T_{res}) \qquad 32$$

Since the fluid communication between the injector and the producer is controlled by the mid-point temperature and the electrode temperature is limited to reduce the start-up time the simplest action is to increase electrode radius. Although electrode radius is constraint to well radius, we can increase the effective electrode radius by injecting brine without having to increase the actual electrode radius. For using Equation 32 after brine injection electrode radius ($r_{electrode}$) should be replaced by brine affected zone radius (r_{brine}). The effect of brine injection on start-up time is presented in Figure 2.14b. As shown in Figure 2.14b the brine injection for enhancing the start-up in SAGD operation would not be sufficient enough due to limitations in distance between the SAGD well pairs. Other downside of electro-thermal heating is that the liberation of gas from bitumen which happens in low temperature will be decreasing the conductivity of the surrounding the wellbore and then stops the electrical current and heating phenomenon.

2.4. Start-up in Electro-Thermal Heating with Convective Heating by Brine Injection

The governing equation is given by (McGee and Donaldson 2009):

$$\underbrace{\frac{\partial^2 T}{\partial r^2} + \frac{1}{r}\frac{\partial T}{\partial r}}_{\text{Conduction}} + \underbrace{\frac{1}{\sigma K}\left(\frac{\wp_{electrode}}{2\pi L_{electrode} r} \right)^2}_{\text{Electro-Thermal Heating}} - \underbrace{\left(\frac{\rho_w c_{pw}}{K} \frac{Q_w}{2\pi L} \right) \frac{1}{r}\frac{\partial T}{\partial r}}_{\text{Convection due to Brine Injection}} = \frac{\rho_r c_{pr}}{K} \left(\frac{\partial T}{\partial t} \right) \qquad 33$$

where the boundary condition is $T_{well} = T_{electrode}$. In this process the water heats up mainly due to resistive heating and convection. Neglecting heat conduction Equation 33 for a single horizontal well can be written as:

$$\rho_r c_{pr} \left(\frac{\partial T}{\partial t} \right) + \rho_w c_{pw} \frac{Q_w}{2\pi L_{electrode}} \left(\frac{1}{r}\frac{\partial T}{\partial r} \right) = \frac{\sigma}{r^2} \left(\frac{V_{electrode} - V_{ground}}{Ln\left(\frac{R_{ext}}{r_w} \right)} \right)^2 \qquad 34$$

Another variation of electro-thermal heating introduces convective heating by brine injection at the electrode. Due to the appearance of hot spots around the electrodes water–circulation is a common procedure in resistive heating applications. But in this process brine is not injected mainly for relieving the appearance of hot spots in the vicinity of electrodes and not mainly for increasing the salinity and increasing the of bulk electrical conductivity of the reservoir. But is injected mainly for introducing the convection heat transfer mechanism to improved and enhanced the heating in the reservoir. Notable examples of this approach is ET-DSP™ demonstrated by E-T Energy which they reduced the electrode spacing from 7 to 10 m for electro-thermal with conduction to 19 to 20 m for electro-thermal with convection (McGee and

Donaldson 2009). The temperature distribution due to resistive heating and convection (by brine injection) and neglecting the heat transfer by thermal conduction is given by:

$$\text{if } r \le \sqrt{R_{ext}^{\,2} - 2\Gamma_1 t}: \quad T = T_{res} - \frac{\Gamma_2}{\Gamma_1}\text{Ln}\left(\frac{R_{ext}}{\sqrt{r^2 + 2\Gamma_1 t}}\right) + \frac{\Gamma_2}{\Gamma_1}\text{Ln}\left(\frac{R_{ext}}{r}\right) \tag{35a}$$

$$\text{if } r > \sqrt{R_{ext}^{\,2} - 2\Gamma_1 t}: \quad T = T_{res} + \frac{\Gamma_2}{\Gamma_1}\text{Ln}\left(\frac{R_{ext}}{r}\right) \tag{35b}$$

where,

$$\Gamma_1 = -\frac{\rho_w c_{pw}}{\rho_r c_{pr}} \frac{Q_w}{2\pi r L_{electrode}} \tag{36a}$$

$$\Gamma_2 = \frac{\sigma}{\rho_r c_{pr}} \left(\frac{V_{electrode} - V_{ground}}{\text{Ln}\left(\frac{R_{ext}}{r_w}\right)}\right)^2 = \frac{\sigma}{\rho_r c_{pr}} \left(\frac{V_{electrode}}{\text{Ln}\left(\frac{R_{ext}}{r_w}\right)}\right)^2 \tag{36b}$$

It must be noted for good mobility reservoirs such as Suncor Firebag and Nexen Long Lake the external radius (R_{ext}) can be assumed equal to pay thickness or larger since the evidence from bull-heading shows that drainage radius is extensive in these operations. For positive values of Q_w (i.e., the case of water injection) Equation 35a and b at near wellbore does not provides a stable solution. Since Equation 35a and b are stable for negative Q_w (i.e., the case of water production) following solution is given for injected water as:

$$\text{if } r \le \sqrt{R_{ext}^{\,2} + 2\Gamma_1 t}: \quad T = T_{res} - \frac{\Gamma_2}{\Gamma_1}\text{Ln}\left(\frac{R_{ext}}{\sqrt{r^2 - 2\Gamma_1 t}}\right) + \frac{\Gamma_2}{\Gamma_1}\text{Ln}\left(\frac{R_{ext}}{r}\right) + 2\frac{\Gamma_2 t}{r^2} \tag{37a}$$

$$\text{if } r > \sqrt{R_{ext}^{\,2} + 2\Gamma_1 t}: \quad T = T_{res} + \frac{\Gamma_2}{\Gamma_1}\text{Ln}\left(\frac{R_{ext}}{r}\right) + 2\frac{\Gamma_2 t}{r^2} \tag{37b}$$

The final term is equivalent to twice a value of Equation 28 which implies the resistive heating with no convective heating (brine injection or production). In presented equations the radius of the well is suggested to be equal to the electrode radius which implies that the casing pipe is used as an electrode with (fiberglass) electric isolation joints attached to the ends. Since the temperature is increased over the reservoir volume by time and then the variations of water saturation and temperature affect the bulk electrical conductivity of the reservoir is changing by time. But for simplicity in Equation 37a and b the electrical conductivity of the reservoir is constant and independent of temperature, saturation profile, also the maximum temperature is limited to the boiling temperature of water, and the convection problem is modeled with an incompressible fluid

Temperature variation along the line connecting the injector and producer for electro-thermal in convective and non-convective heating is presented in Figure 2.15a and b. as shown the temperature will rise significantly surrounding the electrode but temperature will stay low at further points even in lean zones with 10 times higher electric conductivity. The presented model shows that the maximum temperature in case of water production may be half a meter away from the wellbore.

Figure 2.15c and d are presenting the mid-point temperature variation for electro-thermal in convective and non-convective heating. As shown in Figure 2.15d in case of bitumen rich zones even with 1000 m^3/day water injection the increase in temperature is small. It must be noted for bitumen rich zone reaching injectivity of 100 m^3/day is mostly problematic (for Firebag thermal project the maximum has been seen was 120 m^3/day). Since in most SAGD operations the sweetest spot of the reservoir (with low mobility and low electric conductivity) is located at the bottom of the pay and well pairs are attempted to drill close to the bottom of the pay zone to capture most bitumen the electro-thermal heating with/without brine injection cannot be a preferable method for mobilizing the bitumen in start-up phase.

The presented equations are for homogeneous reservoirs and in case of heterogeneous reservoirs commercial software such as: *TCTM* (developed by Alberta Innovates Technology Futures previously known as Alberta Research Council), *TETRAD* (Vinsome and Shook 1993), and *CMG–STARS* which provides fully-coupled thermal multiphase flow and resistive heating can be used.

The final term in Equation 37a and b is equivalent to twice a value of the resistive heating with no convective heating (brine injection or production) presented as:

$$\frac{\Gamma_2 t}{r^2} = \frac{\sigma V_{electrode}^2}{\rho_r c_{pr}} \frac{1}{r^2 \left[Ln(R_{ext}/r_{electrode}) \right]^2} t = T_{conductive} - T_{res} \qquad 38$$

which shows that temperature profile is depending on the electric-conductivity distribution, the electrode electric potential, and the distance from the electrode centre (r).in SPE178427 the derivation for Equation 37a and b is not presented. As illustrated in Figure 2.16 in the solution for considering convection due to brine production the extra temperature resulted from injection is assumed equal to decrease in temperature due to brine production:

$$\Delta T_{pro} = \Delta T_{inj} \qquad 39$$

Then:

$$T_{pro} = T_{conductive} - \Delta T_{inj} = 2\left(T_{conductive} - T_{res}\right) - T_{inj} = 2\frac{\Gamma_2 t}{r^2} + 2T_{res} - T_{inj} \qquad 40$$

Substituting T_{inj} into Eq. 16 will result in Eqs. 12a and b.

2.5. Start-up in Induction Heating

The following is the energy conservation equation describing the transient temperature distribution in a conduction-dominated heat transfer system for the cylinder with radial and axial symmetry:

$$\underbrace{\frac{1}{r}\frac{\partial}{\partial r}\left(Kr\frac{\partial T}{\partial r}\right)}_{\text{Conduction heat transport}} + \overbrace{\dot{Q}_{EM}}^{EM-heating} = \underbrace{\rho_r c_{pr}\left(\frac{\partial T}{\partial t}\right)}_{\text{Internal Heat Storage}} \qquad 41$$

which yields:

$$\frac{\partial^2 T}{\partial r^2}+\frac{1}{r}\frac{\partial T}{\partial r}+\frac{\dot{Q}_{EM}}{K}=\frac{1}{\kappa_{Thermal}}\left(\frac{\partial T}{\partial t}\right) \quad 42$$

The rate of inductive heat generation is presented with respect to r in Appendix B (see Figure 1.4):

$$\dot{Q}_{EM}=\dot{Q}_{Inductive}=\left(\frac{dQ}{dt}\right)_{Inductive}=-\frac{\partial P_{inductive}(r)}{\partial r}=\frac{2}{\delta_{Inductive}}\bar{P}_{inductive}\exp\left[-\frac{2}{\delta_{Inductive}}(z_{inj}+z_{coil})\right] \quad 43$$

, in which $\bar{P}_{inductive}$ is calculated in Appendix B as:

$$\bar{P}_{inductive}=\frac{\sigma}{8}\left[\omega\mu_0\mu_r^{core}\wp_{coil}r_{coil}\times\frac{N}{\ell_{coil}}\times\cot(\eta)\right]^2 \quad 44$$

, in which $\wp_{coil}$ is the current flowing in the wires of the coil, or simply the coil current, N is the number of coil turns, l_{coil} is the mean length of the coil,. μ_r^{core} is the magnetic relative permeability of the coil's core, η is a pitch angle of the coil, σ is electrical conductivity of oil sand, and ω is the angular frequency of the current. $\delta_{Inductive}$ is penetration depth, and is described in metres as (Ghannadi et al. 2013):

$$\delta_{Inductive}=503\sqrt{\frac{\rho}{\mu_r f_s}}=503\sqrt{\frac{1}{\mu_r f_s\sigma}} \quad 45$$

, in which ρ is the electrical resistivity of the reservoir formation; σ is the conductivity; and f_s is the switching frequency (Hz) or cycles per second. As in the case of non-ferrous materials such as oil sand, magnetic relative permeability is very close to one, Equation 45 can be presented in simpler form:

$$\delta_{Inductive}=503\sqrt{\frac{\rho}{f_s}}=503\sqrt{\frac{1}{f_s\sigma}} \quad 46$$

It must be noted that in this analysis, eddy current heat loss dominates, the inductor coil stands alone, there is no other electrically-conductive structure in proximity, and the inductor is an infinitely long single-layer solenoid producing a homogeneous magnetic field.

The partial differential equation governing the heat transport for inductive-heating converts to:

$$\underbrace{2\pi L\times\frac{\partial}{\partial r}\left(Kr\frac{\partial T}{\partial r}\right)}_{\text{Conductionheat transport}}+\underbrace{\frac{2}{\delta_{Inductive}}\bar{P}_{inductive}\exp\left[-\frac{2}{\delta_{Inductive}}(z_{inj}+z_{coil})\right]}_{\text{Induction-Heating}}+\underbrace{\rho_r c_{pr}q_c\frac{\partial T}{\partial r}}_{\text{Condensate Convection}}=\underbrace{2\pi Lr\times\left[\rho_r c_{pr}\left(\frac{\partial T}{\partial t}\right)\right]}_{\text{Internal Heat Storage}} \quad 47$$

Neglecting condensate convection and temperature-independent thermal conductivity, the heat transport for RF heating is simplified as:

$$\frac{\partial^2 T}{\partial r^2}+\frac{1}{r}\frac{\partial T}{\partial r}+\frac{1}{K\times 2\pi r L}\frac{2}{\delta_{Inductive}}\overline{P}_{inductive}\exp\left[-\frac{2}{\delta_{Inductive}}(z_{inj}+z_{coil})\right]=\frac{1}{\kappa_{Thermal}}\left(\frac{\partial T}{\partial t}\right) \quad 48$$

As shown in Ghannadi et al. (2013), for 1 to 10 kHz, conductive heating dominates the heat transfer. This study suggests that temperature at interval is mainly dominated by heat from injector and producer steam circulation (constant temperature boundary), and that heat generated from inductive heating does not dissipate, but accumulates independent from conductive heating. In this regard, Equation 42 is simplified to:

$$\frac{\partial^2 T}{\partial r^2}+\frac{1}{r}\frac{\partial T}{\partial r}=\frac{1}{\kappa_{Thermal}}\left(\frac{\partial T}{\partial t}\right) \quad 49a$$

$$\frac{1}{K\times 2\pi r L}\dot{Q}_{inductive}=\frac{1}{\kappa_{Thermal}}\left(\frac{\partial T}{\partial t}\right) \quad 49b$$

Equation 13 yields the solution for Equation 49a at any location between injector and producer, as Equation 49b is solved simply as:

$$\Delta T=\frac{1}{2\pi(z_{inj}+z_{coil})L}\times\frac{1}{\rho_r c_{pr}}\dot{Q}_{inductive}t=\frac{1}{2\pi(z_{inj}+z_{coil})L}\times\frac{2}{\rho_r c_{pr}\delta_{Inductive}}\overline{P}_{inductive}\exp\left[-\frac{2}{\delta_{Inductive}}(z_{inj}+z_{coil})\right]t \quad 50$$

Substituting Equation 50 into Equation 48 yields:

$$T_z-T_{res}=(T_{st}-T_{res})\frac{E_i\left[-\frac{(z_{inj})^2}{4\lambda\kappa_{Thermal}t}\right]+E_i\left[-\frac{(z_{int}-z_{inj})^2}{4\lambda\kappa_{Thermal}t}\right]}{E_i\left[-\frac{(z_{int})^2}{4\lambda\kappa_{Thermal}t}\right]+E_i\left[-\frac{(OD/2)^2}{4\lambda\kappa_{Thermal}t}\right]}+\frac{1}{2\pi(z_{inj}+z_{coil})L}\times\frac{2}{\rho_r c_{pr}\delta_{Inductive}}\overline{P}_{inductive}\exp\left[-\frac{2}{\delta_{Inductive}}(z_{inj}+z_{coil})\right]t \quad 51$$

The physical meaning of Equation 51 is that the formation does not lose heat to or gain heat from its surroundings. In this case, the lowest temperature is not located at mid-point, but can be found using a derivative of Equation 51 equal to zero. Knowing that:

$$\frac{\partial E_i(x)}{\partial x}=-\frac{\exp(x)}{x} \quad 52$$

, the derivation of temperature versus z is given by:

$$\frac{\partial(T_z-T_{res})}{\partial z_{inj}}=\frac{(T_{st}-T_{res})}{E_i\left[-\frac{(z_{int})^2}{4\lambda\kappa_{Thermal}t}\right]+E_i\left[-\frac{(OD/2)^2}{4\lambda\kappa_{Thermal}t}\right]}\left\{\frac{1}{z_{inj}}\exp\left[-\frac{(z_{inj})^2}{4\lambda\kappa_{Thermal}t}\right]-\frac{1}{(z_{int}-z_{inj})}\exp\left[-\frac{(z_{int}-z_{inj})^2}{4\lambda\kappa_{Thermal}t}\right]\right\}$$
$$-\frac{1}{2\pi(z_{inj}+z_{coil})L}\times\frac{4}{\rho_r c_{pr}(\delta_{Inductive})^2}\overline{P}_{Inductive}\exp\left[-\frac{2}{\delta_{Inductive}}(z_{inj}+z_{coil})\right]t \quad 53$$
$$-\frac{1}{2\pi(z_{inj}+z_{coil})^2 L}\times\frac{2}{\rho_r c_{pr}\delta_{Inductive}}\overline{P}_{inductive}\exp\left[-\frac{2}{\delta_{Inductive}}(z_{inj}+z_{coil})\right]t=0$$

The location of minimum temperature is a function of time, and can be calculated at every time using *Microsoft Office Excel's Solver* add-on. It must be noted, as shown in Figure 2.18a, that for constant EM-frequency, the location of minimum temperature tends towards the producer. For low frequencies early in start-up, and for applied frequencies of less than 10 kHz, the

minimum temperature is located at mid-interval. For higher frequencies, it tends towards the producer (see Figure 2.18b). For simplicity, in this study the location of minimum temperature is suggested to be at mid-point for the range of practical EM-applied frequencies.

Figure 2.19 illustrates variation of temperature in mid-interval between injector and producer for SAGD start-up and EM-SAGD start-up. As shown, temperature increases rapidly for frequencies greater than 10 kHz.

2.6. Start-up in RF heating or the ESEIEH™ process

Since the early 1970s, research into the use of RF energy as a means to effectively heat heavy oil reservoirs has led to incremental technology advancements. In the Effective Solvent Extraction Incorporating Electromagnetic Heating (ESEIEH™) process suggested by Harris, the dielectric heating of oil sand is combined with the injection of a solvent such as propane or butane to reduce bitumen viscosity. Because solvent diffusion increases based on initial oil viscosity (Das and Butler 1996), heating is used to accelerate diffusion. Heating decreases the viscosity of the native bitumen and subsequently increases the diffusion rate of the solvent into the bitumen. Thus, the end of the start-up period for ESEIEH™ processes should be calculated based on a diffusion-controlled mobilization threshold. This threshold is suggested as a minimum viscosity of 1000 cP, equivalent to a temperature range of 46 and 56°C for Athabasca and Peace River oil sand reservoirs (see Figure 2.8), or 51°C as the average value.

Heat transfer in RF heating follows Equation 41. The difference is in the rate of heat generation, presented with respect to r (see Figure 1.4):

$$\dot{Q}_{EM} = \dot{Q}_{RF} = \left(\frac{dQ}{dt}\right)_{RF} = -\frac{\partial P_{RF}(r)}{\partial r} = \frac{2}{\delta_{RF}} \bar{P}_{RF} \exp\left[-\frac{2}{\delta_{RF}}(z_{Antenna} - r_{Antenna})\right] \quad 54$$

, in which $\bar{P}_{RF}$ is given for a general form by:

$$\bar{P}_{RF} = \frac{\sigma + \omega\varepsilon \tan\delta}{2}\left|\vec{E}\right|^2 = \frac{\sigma + \omega\varepsilon_0\varepsilon_r \tan\delta}{2}\left|\vec{E}\right|^2 \quad 55$$

For high frequencies such as RF, as shown in Figure 1.2c, because dielectric heating is the main thermal process (i.e., $\sigma \ll \omega\varepsilon_0\varepsilon_r \tan\delta$), Equation 55 yields:

$$\bar{P}_{RF} = \omega\varepsilon_0\varepsilon_r \tan\delta \bar{E}^2 = \omega\varepsilon \tan\delta \bar{E}^2 \quad 56$$

, in which ω is the angular frequency of the current, ε_0 is permittivity of free space or vacuum, ε_r is relative permittivity or dielectric constant (ε' notation used in some literature), $\bar{E}$ is the root mean square value of the electric field, which is equal to $1/\sqrt{2}$ times the E-field amplitude (V/m), and $\bar{P}_{RF}$ is the EM wave power per unit solid angle irradiated by the antenna, which is a given value for every antenna. The tangent of dielectric loss angle ($\tan\delta$) is often called the loss tangent or the dissipation (power) factor of the formation. For a given formation, it is given by (Nottenburg et al., 1980):

$$\tan\delta = \frac{\varepsilon''}{\varepsilon_r} = \frac{\sigma_{ac}}{\omega\varepsilon_r} = \frac{\sigma_{dielectric} + \sigma_{ohmic}}{\omega\varepsilon_r} \quad 57$$

in which ε'' is the dielectric loss. σ_{ac} is the alternating current (AC) electric conductivity, which consists of dipolar relaxation losses ($\sigma_{dielectric}$) and ohmic losses (σ_{ohmic}) (i.e., direct current conductivity) arising from migration of free charge carries. Knowing the dielectric loss tangent ($\tan\delta$) as mentioned in Equation 57, RF power is given by:

$$\overline{P}_{RF} = \omega\varepsilon_0\varepsilon''\overline{E}^2 \qquad 58$$

δ_{RF} is penetration depth for RF application. Penetration depth (δ) is described in a more general expression (Ghannadi et al. 2013):

$$\delta = \frac{1}{\omega}\left\{\left(\frac{\mu_0\mu_r\varepsilon_0\varepsilon_r}{2}\right)\left[\sqrt{1+\left(\frac{\sigma}{\omega\varepsilon_0\varepsilon_r}\right)^2}-1\right]\right\}^{-1/2} \qquad 59$$

For RF heating applications, in the case of poor conductors (non-metals) such as oil sand at high frequencies, the factor on the right increases and the following formula can be used:

$$\delta_{RF} \approx 2\rho\sqrt{\frac{\varepsilon_0\varepsilon_r}{\mu_0\mu_r}} \qquad 1 >> \sigma/\omega\varepsilon_0\varepsilon_r \text{ (see Figure 1.2c)} \qquad 60$$

Because non-ferrous materials such as oil sand have a magnetic relative permeability very close to one, Equation 60 can be presented in simpler form:

$$\delta_{RF} \approx 0.0053\rho\sqrt{\varepsilon_r} \qquad 1 >> \sigma/\omega\varepsilon_0\varepsilon_r \text{ (see Figure 1.2c)} \qquad 61$$

As seen in Equation 60, in RF heating applications, penetration depth is independent of applied frequency. Figure 1.2d presents the calculated penetration depth based on Equation 59 for a medium-frequency electric field range and common oil reservoirs range. The Athabasca oil sand reservoir shown in Figure 1.2d allows penetration in the range of 10 to 100 metres for EM-SAGD and 0.1 to 10 metres for the ESEIEH^{TM} process.

The partial differential equation governing heat transport for RF heating suggesting the cylindrical coordinates is given by:

$$\underbrace{2\pi L\times\frac{\partial}{\partial r}\left(Kr\frac{\partial T}{\partial r}\right)}_{\text{Conductionheat transport}} + \underbrace{\frac{2}{\delta_{RF}}\overline{P}_{RF}\exp\left[-\frac{2}{\delta_{RF}}(z_{Antenna}-r_{Antenna})\right]}_{\text{RF–Heating}} + \underbrace{\rho_r c_{pr} q_c\frac{\partial T}{\partial r}}_{\text{Condensate Convection}} = \underbrace{2\pi Lr\times\left[\rho_r c_{pr}\left(\frac{\partial T}{\partial t}\right)\right]}_{\text{Internal Heat Storage}} \qquad 62$$

Neglecting condensate convection and temperature-independent thermal conductivity, heat transport for RF heating is simplified as:

$$\frac{\partial^2 T}{\partial r^2}+\frac{1}{r}\frac{\partial T}{\partial r}+\frac{1}{K\times 2\pi r L}\times\frac{2}{\delta_{RF}}\overline{P}_{RF}\exp\left[-\frac{2}{\delta_{RF}}(z_{Antenna}-r_{Antenna})\right]=\frac{1}{\kappa_{Thermal}}\left(\frac{\partial T}{\partial t}\right) \qquad 63$$

As there is no steam circulation in the ESEIEH process, the only heat source is RF heating. Suggesting that heat generated from inductive heating does not dissipate, the conductive term can be neglected and Equation 63 converted to:

$$\frac{1}{2\pi r L}\times\frac{2}{\rho_r c_{pr}\delta_{RF}}\bar{P}_{RF}\exp\left[-\frac{2}{\delta_{RF}}(z_{Antenna}-r_{Antenna})\right]=\left(\frac{\partial T}{\partial t}\right) \quad 64$$

The solution for Equation 64 is given by:

$$\Delta T=\frac{\dot{Q}_{RF}}{\rho_r c_{pr}}t=\frac{1}{2\pi z_{Antenna}L}\times\frac{2}{\rho_r c_{pr}\delta_{RF}}\bar{P}_{RF}\exp\left[-\frac{2}{\delta_{RF}}(z_{Antenna}-r_{Antenna})\right]t \quad 65$$

Substituting Equation 50 into Equation 48 yields:

$$T_z-T_{res}=\frac{1}{2\pi z_{Antenna}L}\times\frac{2}{\rho_r c_{pr}\delta_{RF}}\bar{P}_{RF}\exp\left[-\frac{2}{\delta_{RF}}(z_{Antenna}-r_{Antenna})\right]t \quad 66$$

Phase II of the ESEIEH^{TM} process involves installation. ESEIEH^{TM} is planned to operate in pilot form at Suncor's Dover facility in 2015. Phase I of ESEIEH^{TM} involved installing RF antennas designed by Harris at a face of Suncor's North Steepbank mine. In Phase I, three vertical observation wells were installed at an offset of 0.5 m from the edge of the RF antenna. These were built from Centron fiberglass tubing to minimize interference with the EM fields that were broadcast from the antenna (Trautman and Macearlane, 2014). Harris developed and used the *Coupled Electromagnetic Reservoir Simulator (CEMRS)* tool to couple *CMG–STARS* with *ANSYS HFSS*. The thermal and multiphase flow in a porous medium is simulated in CMG-STARS, and RF is simulated within ANSYS HFSS. This study uses Equation 66 as a simple tool to predict temperature in the start-up stage. Figure 2.20 compares temperature profiles from vertical instrumentation bore OB2 (located at the centre line of the RF antenna) and calculates the temperature from Equation 66. Power varied in Phase I of ESEIEH^{TM}, increasing linearly to 49 kW or 4 kW/m for the 12.25-metre-long antenna for the first 14 days and run at this power until Day 17. Then power was dropped to 1 kW/m. In Figure 2.20, the average power used was 1 kW/m for 1.82 days' duration and 3 kW/m for 20 days' duration. Figure 2.20 shows temperature yielding large values for distances smaller than the penetration depth (δ_{RF}) (i.e., 1.5 m based on Equation 61 for σ of 0.01 S/m, and ε_r of 8 for rich oil sand at 6.78 MHz). Thus, the temperature profile is bounded for distances smaller than δ_{RF} and suggested as constant for this interval.

Equation 66 can be used to calculate the start-up duration for different temperature criteria. Using the diffusion-controlled mobilization criterion (or 51 °C), the start-up time is given by:

$$t=\pi r L\rho_r c_{pr}\delta_{RF}\frac{51-T_{res}}{\bar{P}_{RF}\exp\left[-\frac{2}{\delta_{RF}}(z_{Antenna}-r_{Antenna})\right]} \quad 67$$

The time for reaching mobilization temperature (or 80 °C) is given by:

$$t=\pi r L\rho_r c_{pr}\delta_{RF}\frac{80-T_{res}}{\bar{P}_{RF}\exp\left[-\frac{2}{\delta_{RF}}(z_{Antenna}-r_{Antenna})\right]} \quad 68$$

The variation of RF heating start-up time versus delivered power density from RF–antenna is calculated using Equation 67 and presented in Figure 2.21. Penetration depth is calucated at 6.78 MHz, suggested by Harris for Phase I and II of ESEIEH^{TM}. The use of the 6.78 MHz ±15 kHz frequency band is subject to the industrial, scientific, and medical (ISM) radio band. Figure 2.21 shows that for Phase II of the ESEIEH^{TM} process, 1.5 months is needed to heat up the formation at the location of the producer (at 5m distance from antenna/injector) to 51°C. Equation 68 can

be used if an antenna is used for the thermal mobilization process with no solvent injection, or in case butane is used instead of propane.

The validity of Lambert's law is questionable for RF-heating processes such as ESEIEH™. Although, the complexity of the formulations limits the analytical solution and there is no solution to date to capture the formulation associates with the near-field region. One may consider the comparison of numerical simulation with the solution presented in SPE178427 as a future work to measure the error in such formula. Saeedfar et al. (2016) claimed that the maximum energy dissipation of RF waves takes place, is in the near-field region and not in the far-field region, and using Lambert's law will providing less heating within the reservoir.

Other concern is that the EM properties are continually changing during the RF-heating process because of water saturation and temperature change and also frequency dependency (especially the oil sand electrical conductivity). Although, capturing this feature is very difficult in analytical models.

Other question came in the effect of "neglecting the antenna shortout" in SPE178427. For a linearly polarized antenna such as dipole antenna which has been used in ESEIEH™ process, performance is often described in terms of its principal E- and H-plane patterns. The E-plane is defined as "the plane containing the electric field vector and the direction of maximum radiation," and the H-plane as "the plane containing the magnetic-field vector and the direction of maximum radiation." The total power radiated from dipole antenna and its intensity is normally presented by 3-dimensional pattern and its principal E- and H-plane patterns. The polar diagram of a dipole antenna in free space is presented in Figure 2.22. The radiation of a dipole antenna is symmetrical in azimuthal directions, it has 2 lobes 90 and 270^{o} angles. As shown in Figure 2.22 the spatial variation of the fields as a function of direction from the antenna are given by $\sin\theta$. For a vertical antenna oriented along the z-axis, the radiation will be maximum in the x-y plane. Theoretically, there is no radiation along the z-axis far from the antenna, and the maximum radiation happens at the center of antenna in the x-y plane (see Figure 2.23d, e and f).

The start-up of ESEIEH™ process is ramp-up by developing the desiccated zone. Electric conductivity is close to zero within desiccated zone due to steam development. The energy of RF waves will not be dissipated within desiccated zone and helps the wave to move to reservoir at the edge of vapour (or desiccated) zone. Penetration depth of infinity shown in Fig. 12a means no energy loss in that medium. The penetration depth is in order of meters and it will yield deeper for rich oil zones (Figure 2.23a,b and c). modelling of desiccation zone in RF-heating regarding the ESEIEH™ process is critical which is neglected in SPE178427.

2.7. Conclusions

Temperature enhancement of electromagnetic heating takes place with high frequencies (or high coil current). High-frequency EM-SAGD applications (i.e., with frequencies greater than 10 kHz) can rapidly increase temperature. Such applications may result in thermal pressurization of caprock, and must be explored with great care. This study assumes uniform heat influx along the injector and producer and ideal well conformance. Uniform steam is impossible to achieve in dual tubing configuration due to pressure drops along long tubing and annuluses. Further investigations should focus on the effects of well conformance on SAGD and EM-SAGD start-up.

For RF heating processes such as ESEIEH^{TM}, start-up time is totally related to power, but in the range of practically delivered power used by Harris, start-up times can be reduced to less than two months. It must be noted that RF heating frequencies are limited to 6.78 MHz based on the ISM radio band, and that the only practical variant is delivered power density from RF antennae.

2.8. References

Abernethy, E.R., 1976. Production Increase of Heavy Oils by Electromagnetic Heating, *JCPT*, **15**(3): 91-97.

Barranger, J., 1965. Hysteresis and Eddy-Current Losses of a Transformer Lamination Viewed as an Application of the Poynting Theorem, NASA Technical Note.

Bogdanov, I.I., Torres, J.A., Akhlaghi, H.A., Kamp, A.M., 2011. The Influence of Salt Concentration in Injected Water on Low-Frequency Electrical-Heating-Assisted Bitumen Recovery, *SPEJ*, **16**(3): 548-558.

Brace, W.F., Orange, A.S., 1966. Electrical Resistivity Changes in Saturated Rock under Stress, *Science*, **153**(3743):1525-1526.

Brace, W.F., Orange, A.S., 1968. Electrical Resistivity Changes in Saturated Rocks during Fracture and Frictional Sliding, *Journal of Geophysical Research*, **73**(4): 1433-1445.

Butler, R., 1998, SAGD comes of age!, *JCPT*, **37**(7): 9-12.

Carrizales, M.A., Lake, L.W., Johns, R.T., 2008. Production Improvement of Heavy Oil Recovery by Using Electromagnetic Heating, *SPE Annual Technical Conference and Exhibition*, Denver, Colorado, USA, 21-24 September, SPE 115723-MS.

Chalaturnyk, R., 1996. Geomechanics of the Steam Assisted Gravity Drainage Process in Heavy Oil Reservoirs. Ph.D. Thesis, University of Alberta. 576 pages.

Chute, F.S., Vermeulen, F.E., 1988. Present and Potential Applications of Electromagnetic Heating in the In-Situ Recovery of Oil, *OSTRA Journal of Research*, **4**: 19-33.

Chute, F.S., Vermeulen, F.E., Cervenan, M.R., 1978. Physical Modelling of the Electrical Heating of the Oil Sand Deposits, Technical Report, AOSTRA Agreement #31, Applied Electromagnetics Group, University of Alberta.

Davletbaev, A.Y., Kovaleva, L.A., Babadagli, T., 2010. Heavy Oil and Bitumen Recovery Using Radiofrequency Electromagnetic Irradiation and Electrical Heating: Theoretical Analysis and Field Scale Observations, *Canadian Unconventional Resources and International Petroleum Conference*, Calgary, Alberta, Canada, 19-21 October, SPE 136611-MS.

Davletbaev, A.Y., Kovaleva, L.A., Babadagli, T., 2011. Mathematical Modeling and Field Application of Heavy Oil Recovery by Radio-Frequency Electromagnetic Stimulation, *Journal of Petroleum Science and Engineering*, Vol. **78**, No. **3-4**, pp. 646-653.

Davletbaev, A.Y., Kovaleva, L.A., Nasyrov, N.M., 2008. Numerical Simulation of Injection of a Solvent into a Production Well under Electromagnetic Action, *Fluid Dynamics*, **43**(4): 583-589.

Davletbaev, A.Y., Kovaleva, L.A., Nasyrov, N.M., 2009. An Investigation of the Processes of Heat And Mass Transfer in a Multilayer Medium under Conditions of Injection of a Miscible Agent with Simultaneous Electromagnetic Stimulation, *High Temperature*, Vol. **47**, No. **4**, pp. 574-579.

Duong, A.N., Tomberlin, T.A. and Cyrot, M., 2008. A New Analytical Model for Conduction Heating during the SAGD Circulation Phase, International Thermal Operations and Heavy Oil Symposium, 20-23 October, Calgary, Alberta, Canada, http://dx.doi.org/10.2118/117434-MS

Edmunds, N.R. and Gittins, S.D., 1991. Effective Steam Assisted Gravity Drainage to Long Horizontal Well Pairs , Presented at the CIM/AOSTRA 1991 Technical Conference, Banff, Alberta, Canada, April 21 24.

Ghannadi, S., Irani, M., Chalaturnyk, R., 2014. Evaluation of Induced Thermal Pressurization in Clearwater Shale Caprock in Electromagnetic Steam-Assisted Gravity-Drainage Projects, *SPEJ*, **19**(03): 443-462. http://dx.doi.org/10.2118/156876-PA.

Harris web site, http://harris.com.

Hiebert A.D., Vermeulen, F.E., Chute, F.S., Capjack, C.E., 1986. Numerical Simulation Results for the Electrical Heating of Athabasca Oil-Sand Formations, *SPE RE*, **1(**1**):** 76-84.

Irani, M. and Ghannadi, S. 2013. Understanding the Heat-Transfer Mechanism in the Steam-Assisted Gravity-Drainage (SAGD) Process and Comparing the Conduction and Convection Flux in Bitumen Reservoirs. *SPE J*. **18**(1): 134-145. SPE-163079-PA. http://dx.doi.org/10.2118/163079-PA.

Islam, M.R., Wadadar, S.S., Banzal, A., 1991. Enhanced Oil Recovery of Ugnu Tar Sands of Alaska Using Electromagnetic Heating with Horizontal Wells, Paper SPE 22177, *International Arctic Technology Conference,* Anchorage, Alaska, US, 29-31 May.

Kasevich, R.S., Price, S.L., Faust, D.L., Fontaine, M.F., 1994. Pilot testing of a radio frequency heating system for enhanced oil recovery from diatomaceous earth, *69th Annual Technical Conference and Exhibition*, New Orleans, USA, 25-28 September.

Khan, S., Han, H., Ansari, S., Khosravi, N., 2011. Geomechanical Modeling to Assess Caprock Integrity in Oil Sands, *CSPG CSEG CWLS Convention*.

Khosla, A., 1985. Application Of Computer Modelling To The PCEJ Electric Preheat/Steamdrive Athabasca Pilot, *Annual Technical Meeting*, June 2-5, Edmonton, Alberta, Canada ,PETSOC-85-36-51, http://dx.doi.org/10.2118/85-36-51.

Koolman, M., Huber, N., Diehl, D., Wacker, B., 2008. Electromagnetic Heating Method to Improve Steam Assisted Gravity Drainage, paper 1177481 presented in Proceedings of the *International Thermal Operations and Heavy Oil Symposium*, 20−23 October 2008, Calgary, Alberta, Canada, SPE117481-MS, doi:10.2118/117481−MS.

Kovaleva, L., Davletbaev, A., Babadagli, T. and Stepanova, Z., 2011. Effects of Electrical and Radio-Frequency Electromagnetic Heating on the Mass Transfer Process During Miscible Injection for Heavy-Oil Recovery, *Energy and Fuels*, Vol. **25**, No. **2**, pp. 482-486.

Lindberg, W.R., Thomas, R.R. and Christensen, R.J., 1985. Measurements of Specific Heat, Thermal Conductivity and Thermal Diffusivity of Utah Tar Sands, *Fuel*, **64**: 80-85.

McGee, B.C.W., Vermeulen, F. E., Yu, L., 1999. Field test of electrical heating with horizontal and vertical wells, CHOA Handbook, 2nd Edition, ISBN 0969521316, pp. 565-572.

McGee, B.C.W., Vermeulen, F.E., 2000. In-Situ Electromagnetic Heating for Hydrocarbon Recovery and Environmental Remediation; *Journal of Canadian Petroleum Technology*, Distinguished Authors Series, Vol. **39**, No. **8**, pp. 24-28.

McGee, B.C.W., Vermeulen, F.E., 2007. The Mechanisms of Electrical Heating for the Recovery of Bitumen From Oil Sands, *JCPT*, **46**(1): 28-34.

McGee, B.C.W., Vermeulen, F.E., and Yu, L., 1999. Field Test of Electrical Heating with Horizontal and Vertical Wells, *Journal of Canadian Petroleum Technology*, **38**(3): 46-53.

Mukhametshina, A. and Martynova, E. 2013. Review Article: Electromagnetic Heating of Heavy Oil and Bitumen: A Review of Experimental Studies and Field Applications, Journal of Petroleum Engineering, Vol. **2013**, Article ID 476519, 7 pages, doi:http://dx.doi.org/10.1155/2013/476519

Nottenburg, R., Rajeshwar, K., Pai Verneker, V., and Dubow, J., 1980. A. C. Electrical Conductivity of Potassium Perchlorate, *Journal of Physics and Chemistry of Solids*, **41**: 271-277.

Ovalles, C., Fonseca, A., Lara, A., Alvarado, V., Urrecheaga, K., Ranson, A., Mendoza, H., 2002. Opportunities of Downhole Dielectric Heating in Venezuela: Three Case Studies Involving Medium, Heavy and Extra-Heavy Crude Oil Reservoirs, *International Thermal Operations and Heavy Oil Symposium and International Horizontal Well Technology Conference*, Calgary, Alberta, Canada, 4-7 November, SPE 78980.

Parsche, F. E., 2013. Electromagnetic Heat Treatment Providing Enhanced Oil Recovery, Patent Application No. WO2012173921 A3, CA2838439A1, US20120318498 and WO2012173921A2, Filing date: Jun 11, 2012, Applicant: Harris.

Popović , Z., Popović, B., 2000. Introductory Electromagnetics, 1st Edition, Prentice Hall, Inc.

Rajeshwar, K., Jones, D. B. and DuBow, J. B., 1982. Thermophysical Characterization of Oil Sands. 1. Specific Heats, *Fuel*, Vol. **61**, March, pp. 237-239.

Rudnev, V., Loveless, D., Cook, R., Black, M., 2003. Handbook of Induction Heating, Marcel Dekker, 796 pages, ISBN: 0824708482.

Sahni, A., Kumar, M., Knapp, R.B., 2000. Electromagnetic Heating Methods for Heavy Oil Reservoirs, *SPE/AAPG Western Regional Meeting*, Long Beach, California, 19-23 June, SPE 62550.

Sayakhov, F.L., Kovaleva, L.A., Nasyrov, N.M., 2002. Heat and Mass Transfer in the Well-Stratum System under the Electromagnetic Action on Massive Oil Deposits, *Journal of Engineering Physics and Thermophysics*, Vol. **75**, No. **1**,.pp. 126-133.

Spencer, H.L. 1987. Electromagnetic Oil Recovery Ltd. Calgary.

Trautman, M., Ehresman, D., Edmunds, N., Taylor, G., Cimolai, M., 2013. Effective Solvent Extraction System Incorporating Electromagnetic Heating, Patent No. US8616273 B2 and US20120118565, Filing date: Nov 17, 2010, Original Assignee: Harris and Laricina Energy.

Trautman, M. and Macearlane, B., 2014. Experimental and Numerical Smulation Results from a Radio Frequency Heating Test in Native Oil Sands at the North Steepbank Mine, presented at World Heavy Oil Congress 2014, New Orleans, Louisiana, USA, WHOC14-301.

Vermeulen F.E., Chute, F. S., 1983. Electromagnetic Techniques in the In-Situ Recovery of Heavy Oils, *Journal of Microwave Power*, **18**(1): 15-29.

Vermeulen, F., McGee, B., 2000. In-Situ Electromagnetic Heating for Hydrocarbon Recovery and Environmental Remediation, **39**(8):25-29.

Vermeulen, F.E., Chute, F.S., Cervenan, M.R., 1979. Physical Modelling of the Electromagnetic Heating of Oil Sand and Other Earth-Type and Biological Materials, *Canadian Electrical Engineering Journal*, **4**: 19-28.

Vermeulen, F.E., Chute, F.S., Mcpherson, R.G., 1988. Physical Modelling of Electrothermal Processes in Oil Sand, *Alberta Oil Sands Technology and Research Journal of Research*, **4**:299-305.

Vittoratos, E. 1986. Interpretation of Temperature Profiles From the Steam-Stimulated Cold Lake Reservoir. Presented at the 56th California Regional Meeting of SPE, Oakland, California, USA, 2–4 April. SPE-15050-MS. http://dx.doi.org/10.2118/15050-MS.

Voltmer, D.R., 2007. Fundamentals of Electromagnetics 2: Quasistatics and Waves, Morgan and Claypool, 196 pages, ebook, ISBN: 1598291734.

Wacker, B., Karmeileopardus, D., Trautmann, B., Helget, A., Torlak, M., 2011. Electromagnetic Heating for In-Situ Production of Heavy Oil and Bitumen Reservoirs, *Canadian Unconventional Resources Conference*, Calgary, Alberta, Canada, 15-17 November, CSUG/SPE 148932.

Wright, B. N., Dickey, D. L., Hewit, R. C., 2013. Subterranean Antenna Including Antenna Element and Coaxial Line therein and Related Methods, Patent Application No. WO2013192124 A2 and US20130334205, Filing date: Jun 18, 2013, Applicant: Harris.

Xie, J. and Zahacy, T.A., 2011. Understanding cement mechanical behavior in SAGD wells, World Heavy Oil Congress, Edmonton, Alberta, March 14-17, Paper WHOC11-557.

Yuan, J,Y, McFarlane, R., 2011. Evaluation of Steam Circulation Strategies for SAGD Start-Up, *JCPT*, Vol. **50(1)**: 20–32. doi:http://dx.doi.org/10.2118/143655-PA

Zahn, M., 1979. Electromagnetic Field Theory: A Problem Solving Approach, Wiley, 298 pages, ISBN: 0471021989.

Zinn, S., Semiatin, S.L., 1988. Elements of Induction Heating: Design, Control, and Applications, Electric Power Research Institute, Carnes Publication Services Inc.

Tables

Table 2.1. Parameters used for McMurray oil sand formation in Figure 2.14 and Figure 2.15.

Parameter	Used in Figure 2.14a	Used in Figure 2.14b	Used in Figure 2.15a and b	Used in Figure 2.15c and d
McMurray oil sand thermal properties:				
c_{pr}, J/kg·°C	N/A	2000 [a]	2000 [a]	2000 [a]
ρ_r, kg/m^3	N/A	2100 [a]	2100 [a]	2100 [a]
Reservoir initial temperature, °C	N/A	12 [b]	12 [b]	12 [b]
Injected brine properties:				
c_{pw}, J/kg·°C	N/A	N/A	4213 [c]	4213 [c]
ρ_w, kg/m^3	N/A	N/A	959.3 [c]	959.3 [c]
McMurray oil sand reservoir electrical properties:				
σ, no unit	Var.	0.001	Var.	Var.
Electrode properties:				
Electrode radius ($r_{electrode}$), m	0.0889 (OD = 7")	0.0889 (OD = 7")	0.0889 (OD = 7")	0.0889 (OD = 7")
Well (or electrode) length, m	N/A	N/A	1000	1000
Electric-potential input given at the electrode, V	240 [d]	240 [d]	100	240 [d]
Water injection/production, m^3/day	N/A	N/A	10	Var.

[a] Suggested for rich oil sand at low temperatures (≤ 50˚C).

[b] Suncor's MacKay River initial reservoir temperature.

[c] Water properties at 100 ˚C using the following equations from Butler (1990):

$$\rho_w = 1001.7 - 0.1616 \times T - 0.00262 \times T^2 \qquad 10 \le T \le 290^{\circ}C$$

$$c_{pw} = 1000\left(4.182 - 1.5 \times 10^{-4} T + 3.44 \times 10^{-7} T^2 + 4.26 \times 10^{-8} T^3\right) \qquad 10 \le T \le 240^{\circ}C$$

[d] High range of the possible electrode voltage to show the poor mobilization capability of the electro-thermal heating for SAGD start-up process.

Table 2.2. Parameters used for McMurray oil sand formation in Figure 2.18 and Figure 2.19.

Parameter	Value Range	Used in Figure 2.18	Used in Figure 2.19
McMurray oil sand thermal properties:			
K, W/m·°C	1.7 [a]-2.7 [b]	N/A	N/A
c_{pr} , J/kg·°C	644.05 [c]	644.05	644.05
ρ_r , kg/m^3	1710 [d]-2150 [d]	2100	2100
$\kappa_{Thermal}$, W/m·°C	7.0×10^{-7} [e]	7.0×10^{-7}	7.0×10^{-7}
Reservoir initial temperature, °C	12 [f]-15 [g]	15	15
UTF steam injection temperature, °C	205 [g]-225 [h]	225	225
McMurray oil sand reservoir magnetic properties:			
μ_r , no unit	1	1	1
Coil properties:			
Coil radius, m		0.10	0.10
Coil length, m		500	500
Number of turns, no unit		200	200
Pitch angle, degrees		15	15
Vertical distance of injector from coil centre, m		5	5
Coil current, A	48 to 84 [i]	10	10
Core magnetic relative permeability, no unit	1000 to 6000	1000	1000

[a] Suggested for very rich oil sand at low temperatures. Although values as high as 4.03 are also measured by Scott and Seto (1986), authors still believe 1.70 is the high range of thermal conductivity for oil-saturated oil sand.

[b] Suggested for lean oil sand at low temperatures.

[c] Calculated at steam temperature (i.e., 225°C) based on the following equation suggested by by Rajeshwar et al. (1982) (with correlation coefficient of 0.99):

$$c_{pr}(\mathrm{J/kg\cdot^{o}C}) = 379 + 1.178T(^{o}\mathrm{C})$$

[d] Suggested by Lindberg et al. (1985).

[e] Initially suggested by Vittoratos for Cold Lake reservoir (for rich oil sand), and then endorsed by Seto and Bharatha (1991) for Cold Lake oil sand reservoir (i.e., Clearwater Formation).

[f] Suggested by Edmunds (2000) for UTF Phase B project.

[g] Irani and Ghannadi (2013).

[h] Suggested by Neil Edmunds for UTF project based on personal communication.

[i] Evaluated based on Vermeulen and Chute (1983).

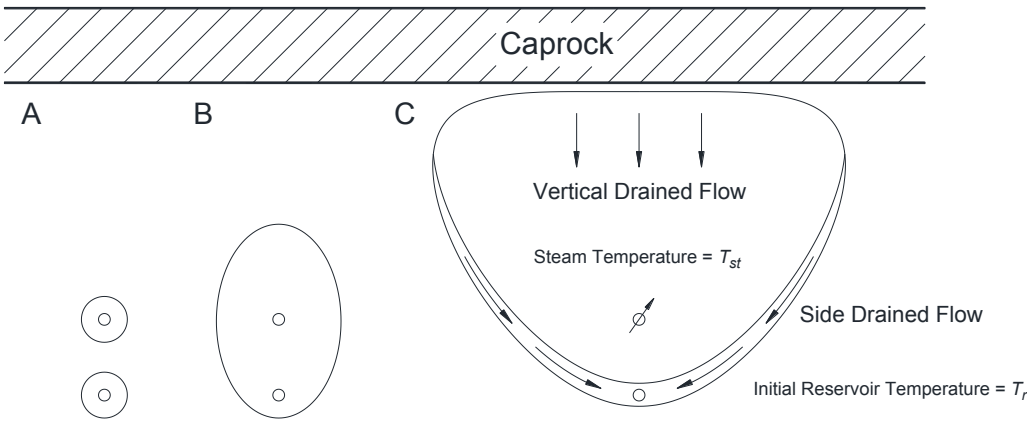

Figure 2.5. Cross-section of SAGD process; Section A presents circulation phase, Section B presents early phase, and Section C presents steam injection phase (Modified from Irani and Ghannadi, 2013).

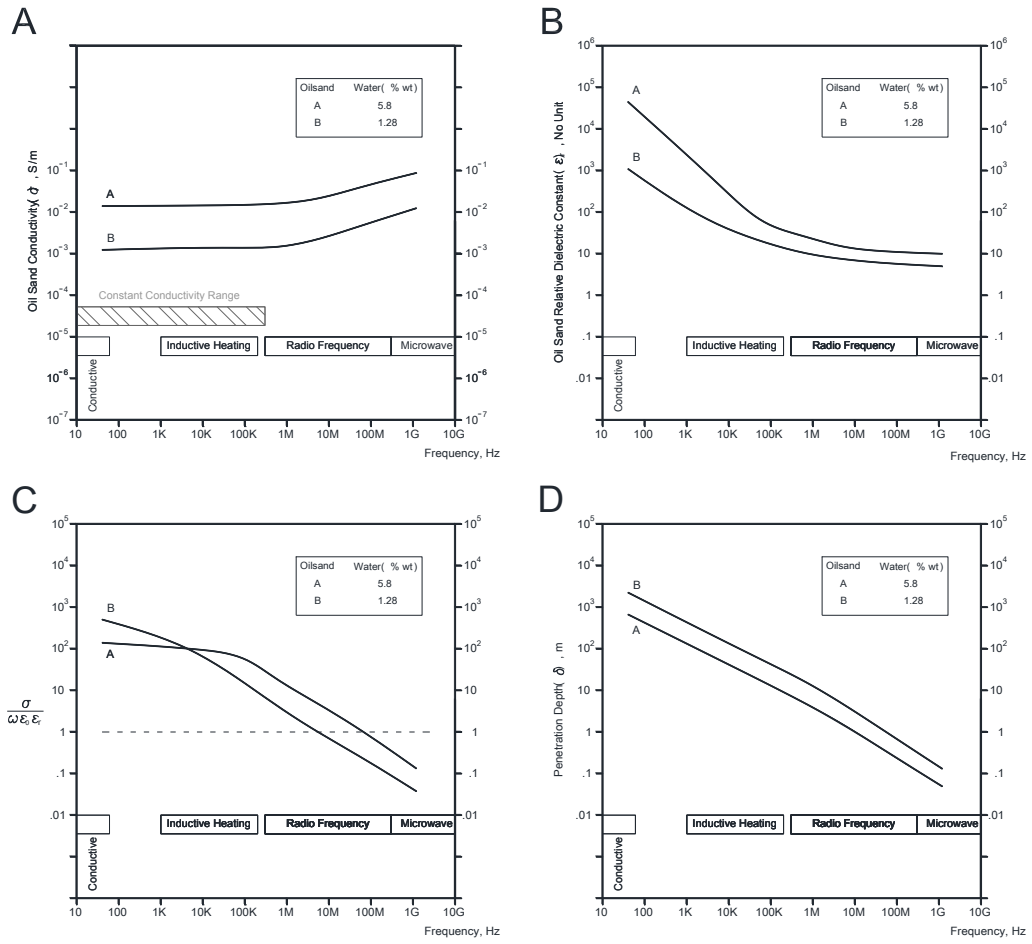

Figure 6. Average oil sand conductivity (Section A), relative dielectric constant (Section B), loss tangent (Section C), and penetration depth (Section D) as function of frequency (Modified from Ghannadi et al., 2013).

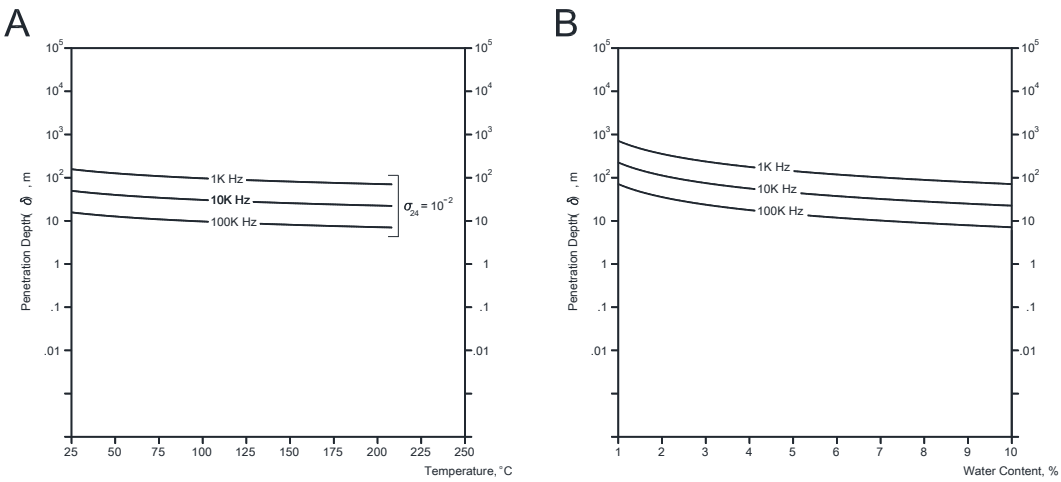

Figure 2.7. Variation of oil sand penetration depth as function of temperature (Section A), and as function of water content (Section B) (Modified from Ghannadi et al., 2013).

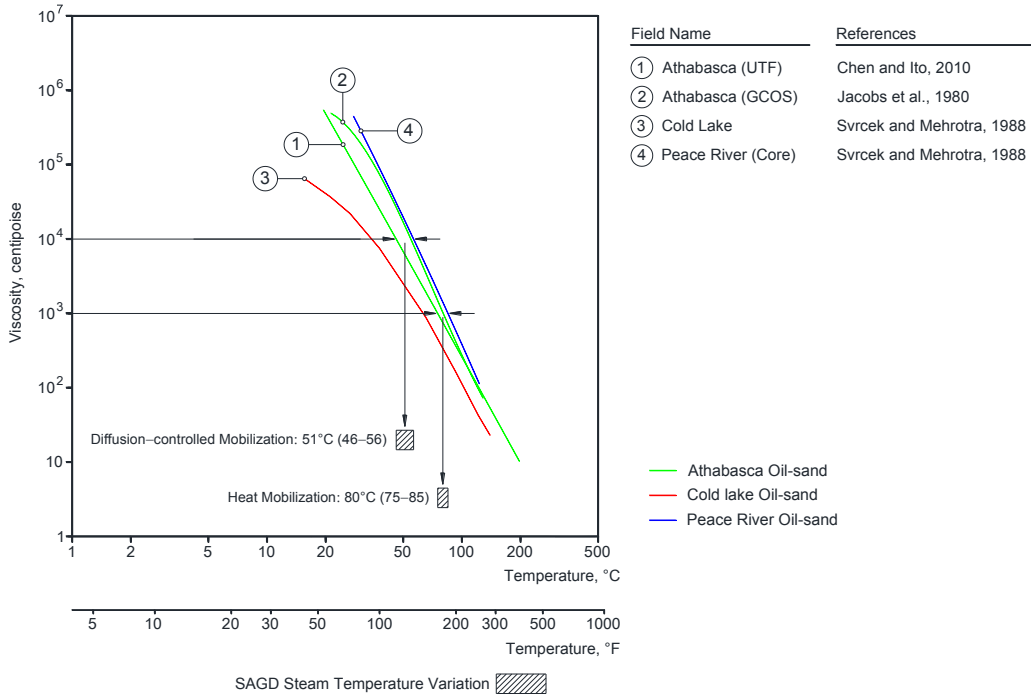

Figure 2.8. Variation of viscosity versus temperature. Temperature range for heat mobilization (end of SAGD and EM-SAGD start-up) and diffusion-controlled mobilization (end of ESEIEH™ start-up) illustrated based on relevant viscosity.

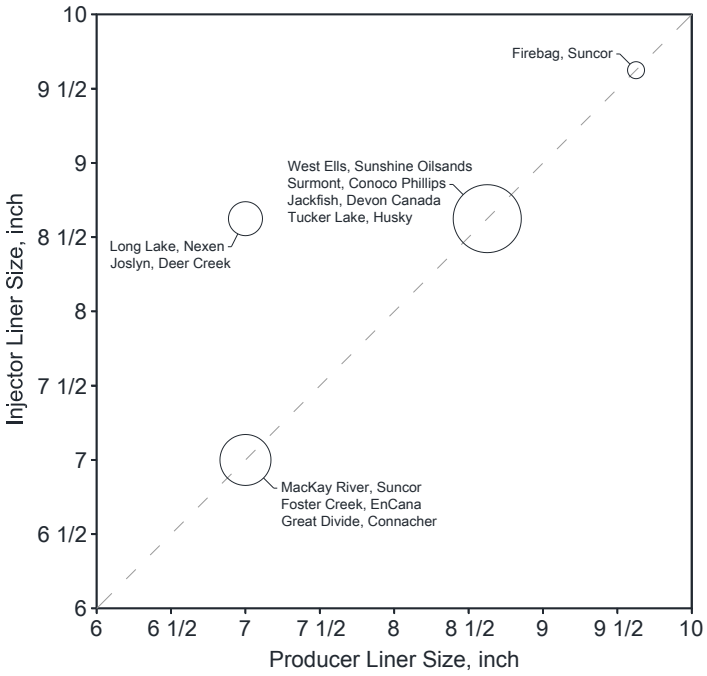

Figure 2.9. Variation injector and producer liner size for Alberta SAGD projects. Circle size shows number of projects for which specified liner sizes for injector and producer are used.

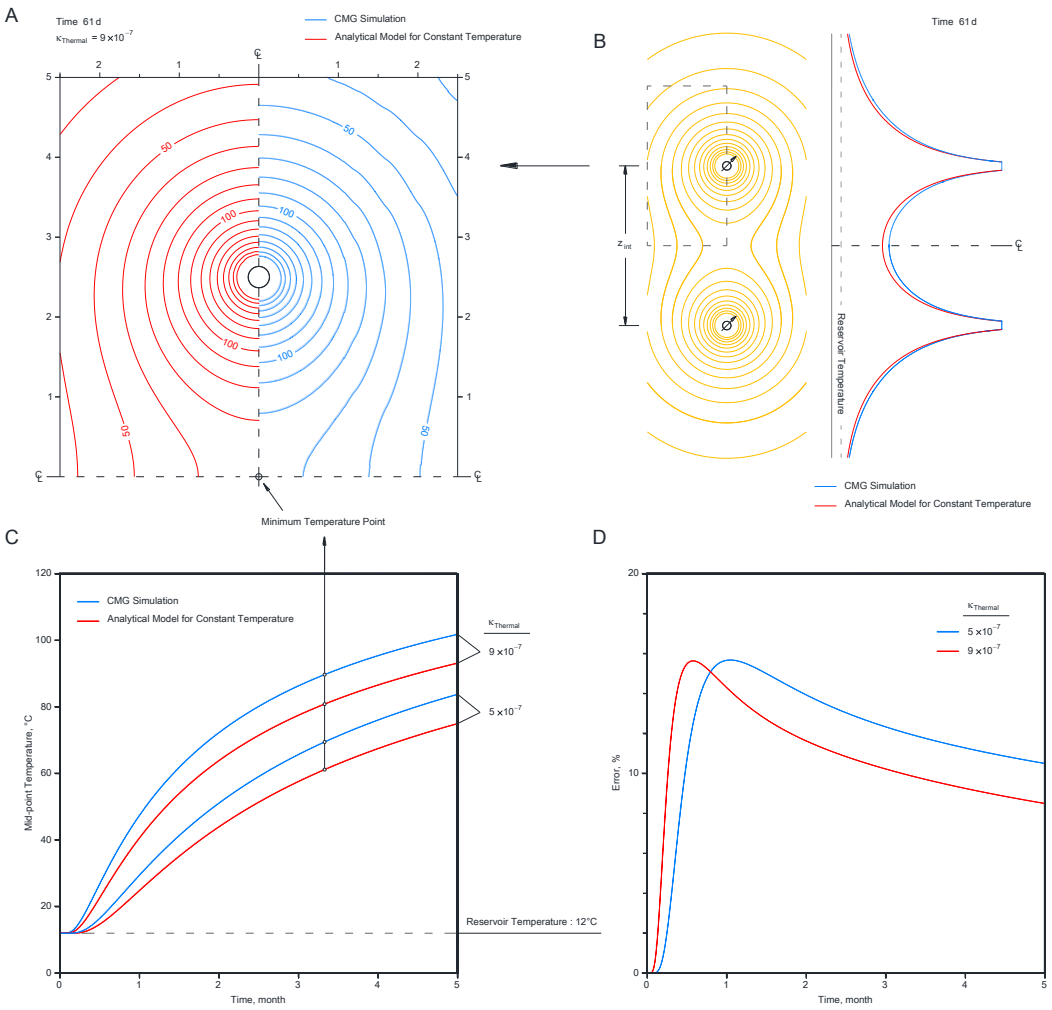

Figure 2.10. Visualisation of temperature contours after 2 months for CMG simulation and analytical model (Section A); temperature variation along a line connected injector and producer (Section B); the temperature variation at mid-point and its comparison for CMG simulation and analytical model (Section C), and the error between CMG simulation and analytical model for mid-point (Section D).

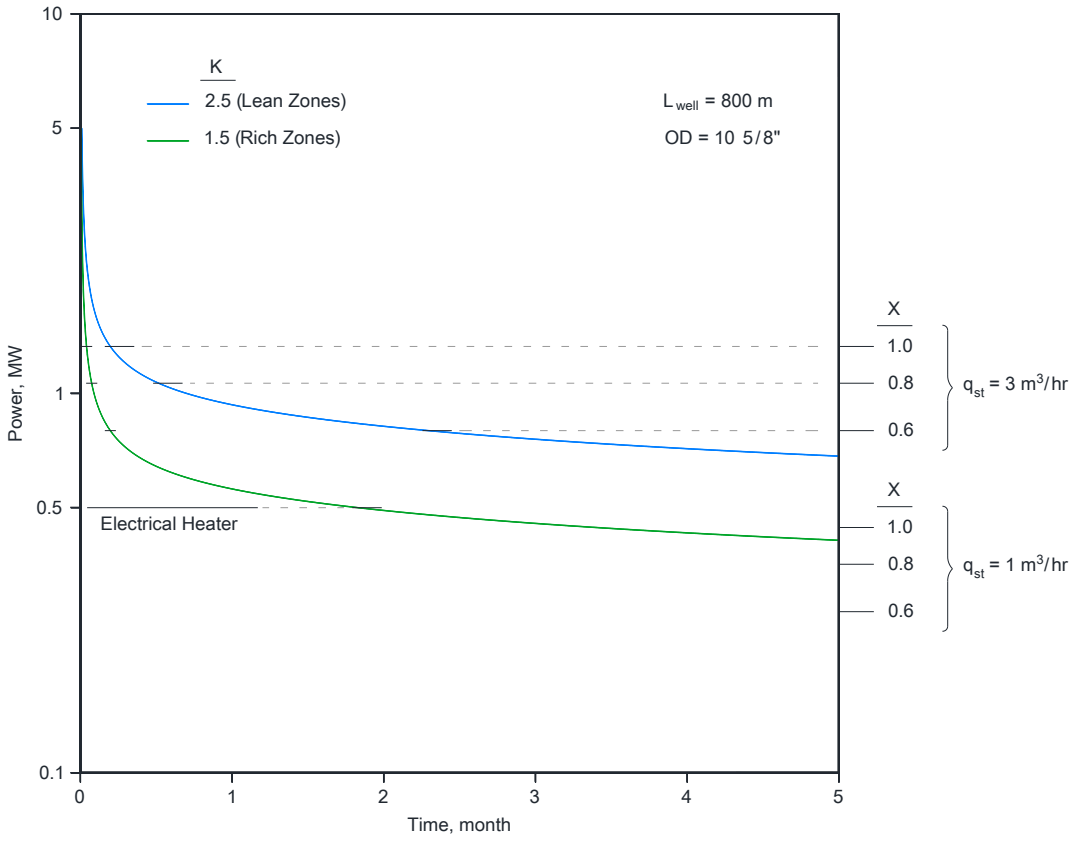

Figure 2.11. Variation of required power in circulation to keep constant temperature at the sandface based on Eq. 5 for rich and lean zones.

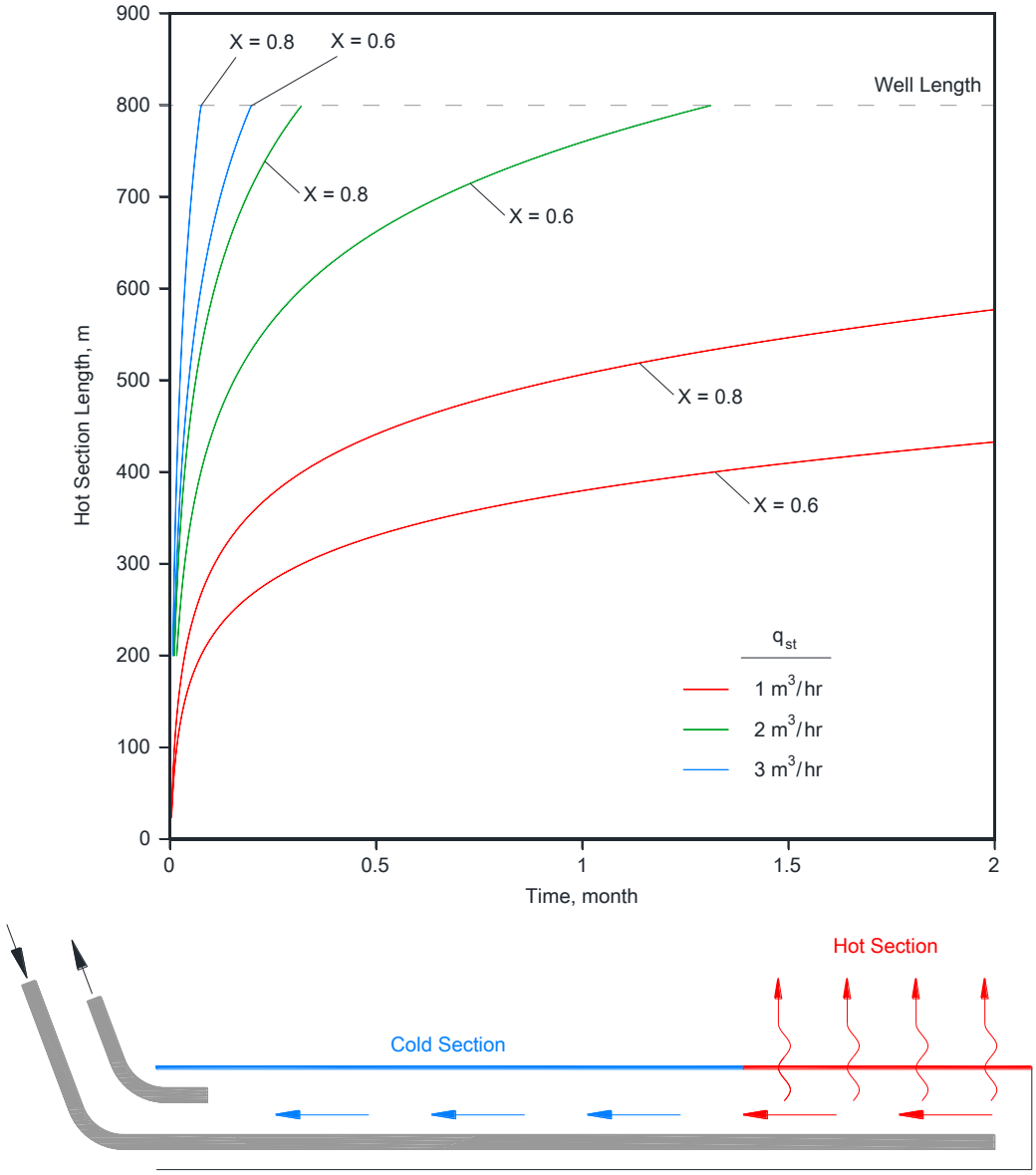

Figure 2.12. Hot section growth vs. time for different steam injection rates .

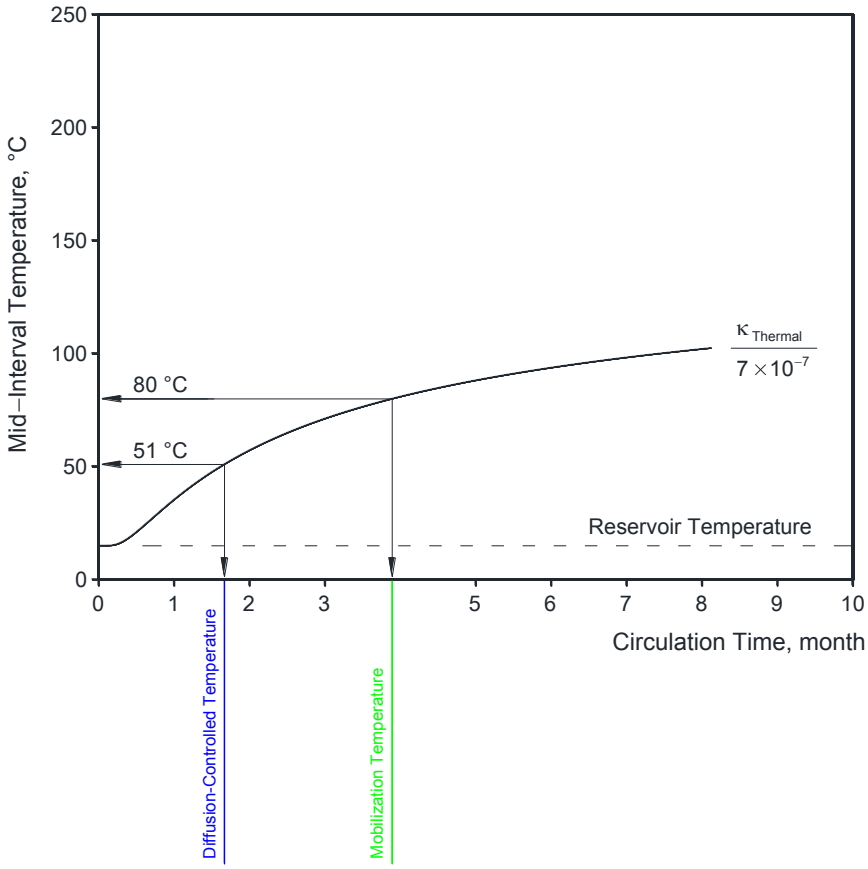

Figure 2.13. Evaluation of circulation time as a function of mobilization and diffusion-controlled temperatures.

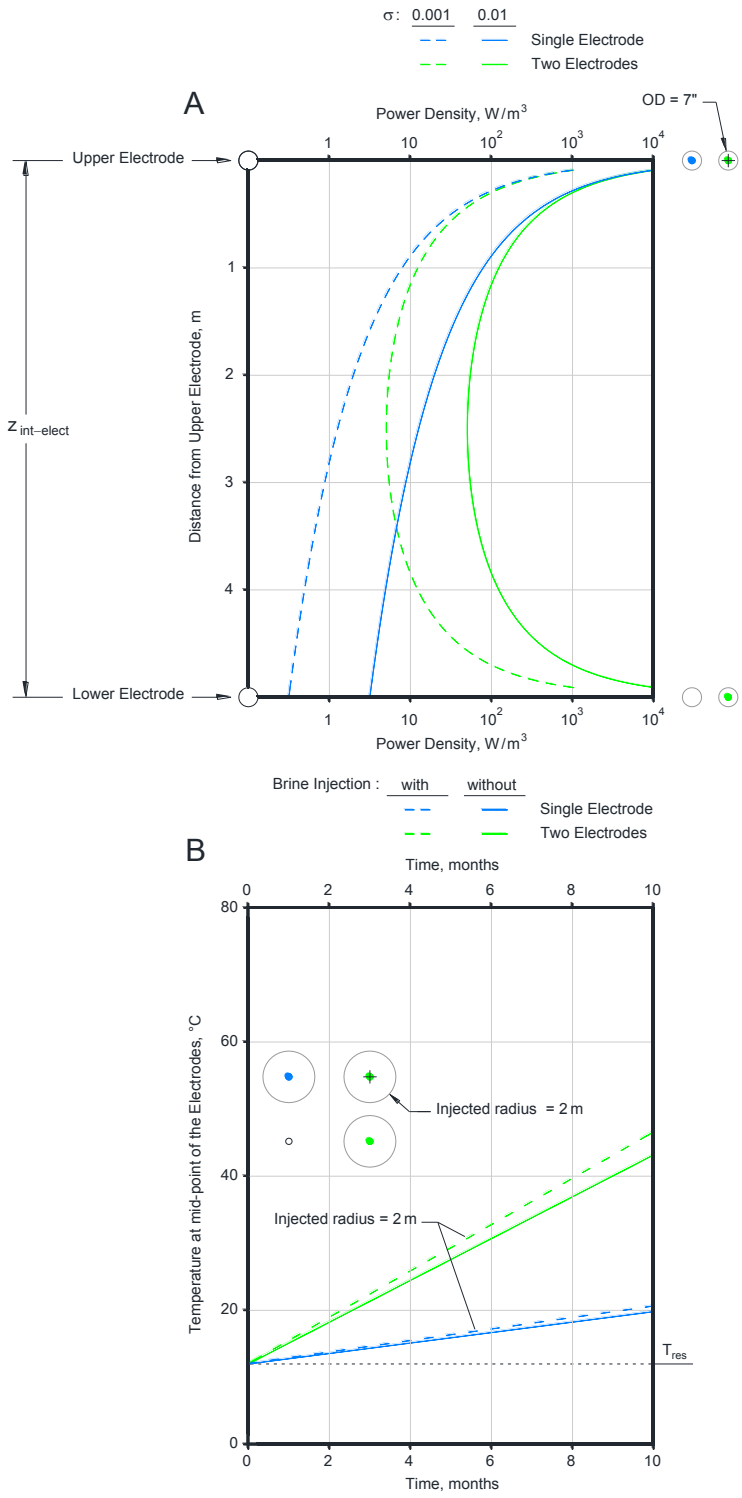

Figure 2.14. In Section A the variation of the power density along the line connecting two electrode wells spaced 5 m apart. The purpose of showing this data is to emphasize the benefits of introducing two electrodes versus one electrode. The mid-point temperature variation versus time is presented in Section B. The purpose of showing this data is to emphasize the impracticality of brine injection in electro-thermal heating for increasing the electrical conductivity of electrode surroundings. See Table 2.1 for electrode and reservoir properties.

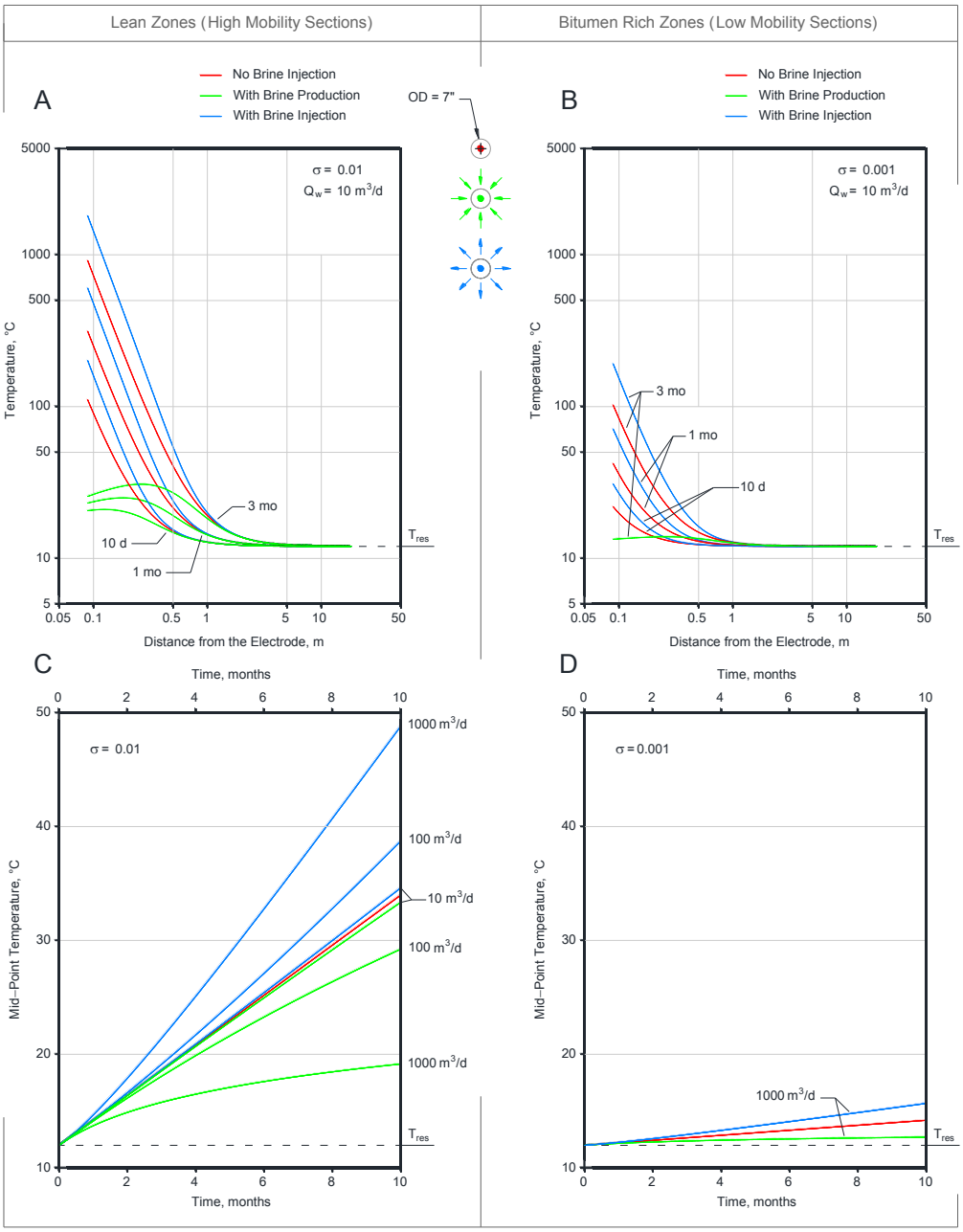

Figure 2.15. Temperature profile versus distance from the electrode for electro-thermal in convective and non-convective heating in lean zones (Section A) and in bitumen rich zones (Section B); and mid-point temperature variation (wells spaced 5 m apart) in lean zones (Section C) and in bitumen rich zones (Section D). See Table 2.1 for electrode and reservoir properties.

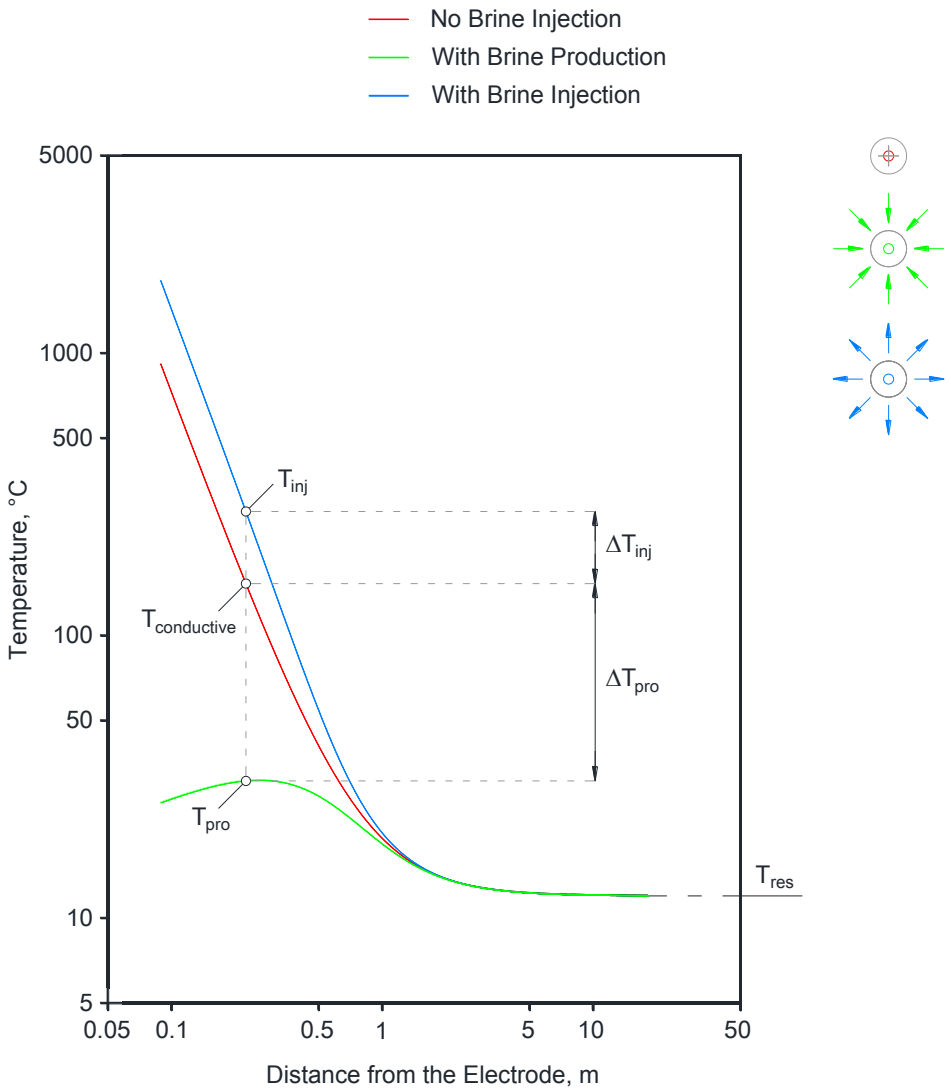

Figure 2.16. Illustration of temperature profile for Electro-Thermal Heating with convective heating by brine production.

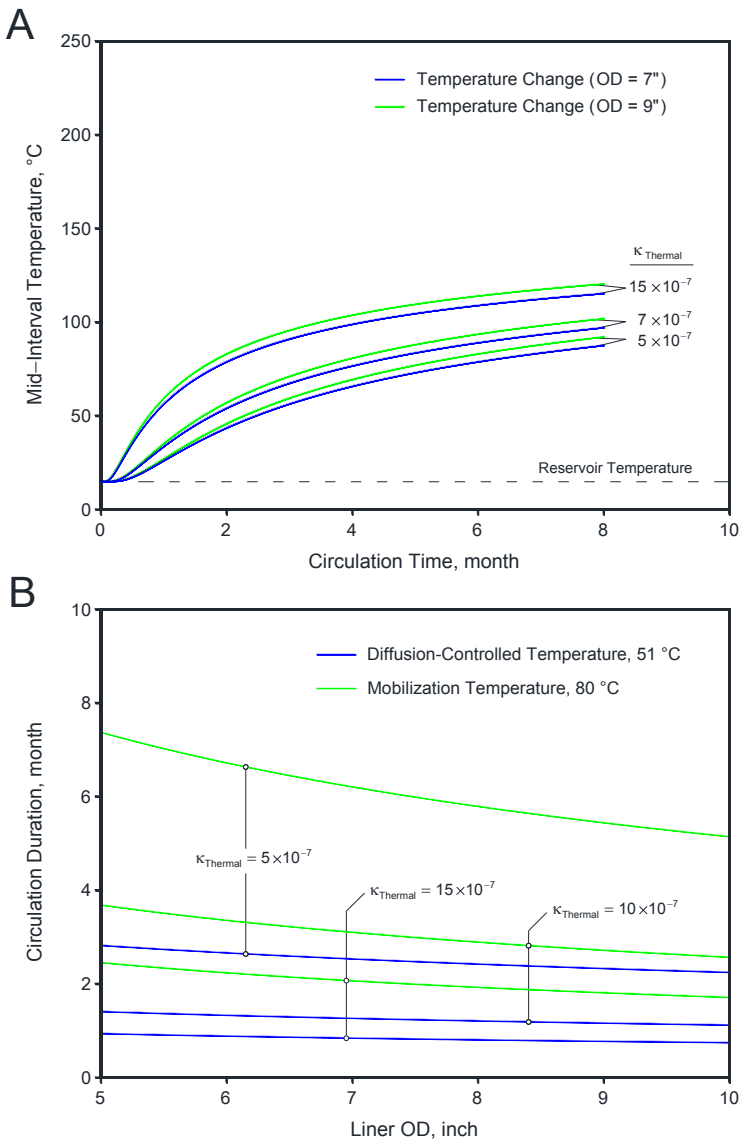

Figure 2.17. Variation of mid-interval temperature rise versus circulation time (Section A), and evaluation of circulation time for mobilization (for SAGD start-up) and diffusion-controlled (for solvent injection start-up) temperature versus liner OD size (Section B).

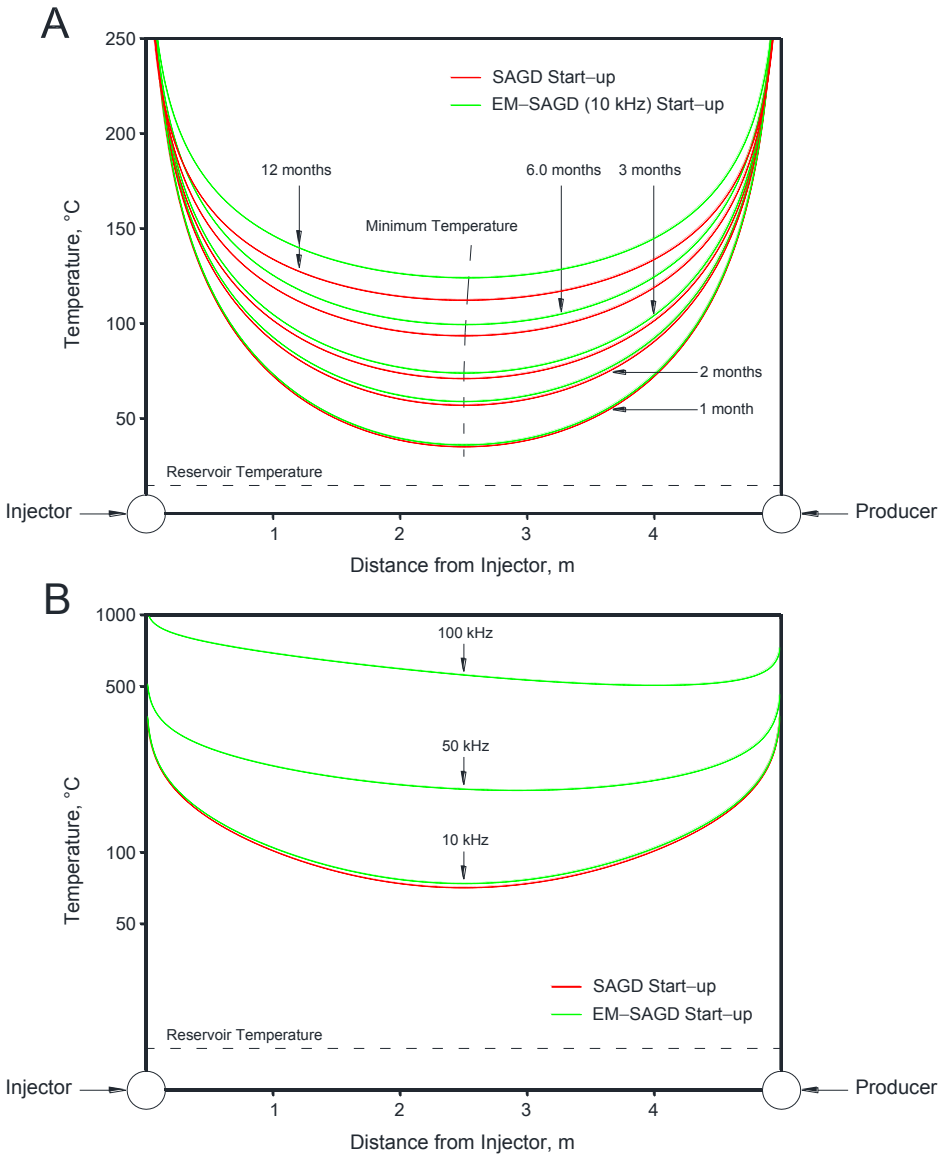

Figure 2.18. Variation of temperature along distance between injector and producer in SAGD start-up and in EM-SAGD start-up for different start-up durations (Section A), and for different applied frequencies (Section B). See Table 2.2 for reservoir properties.

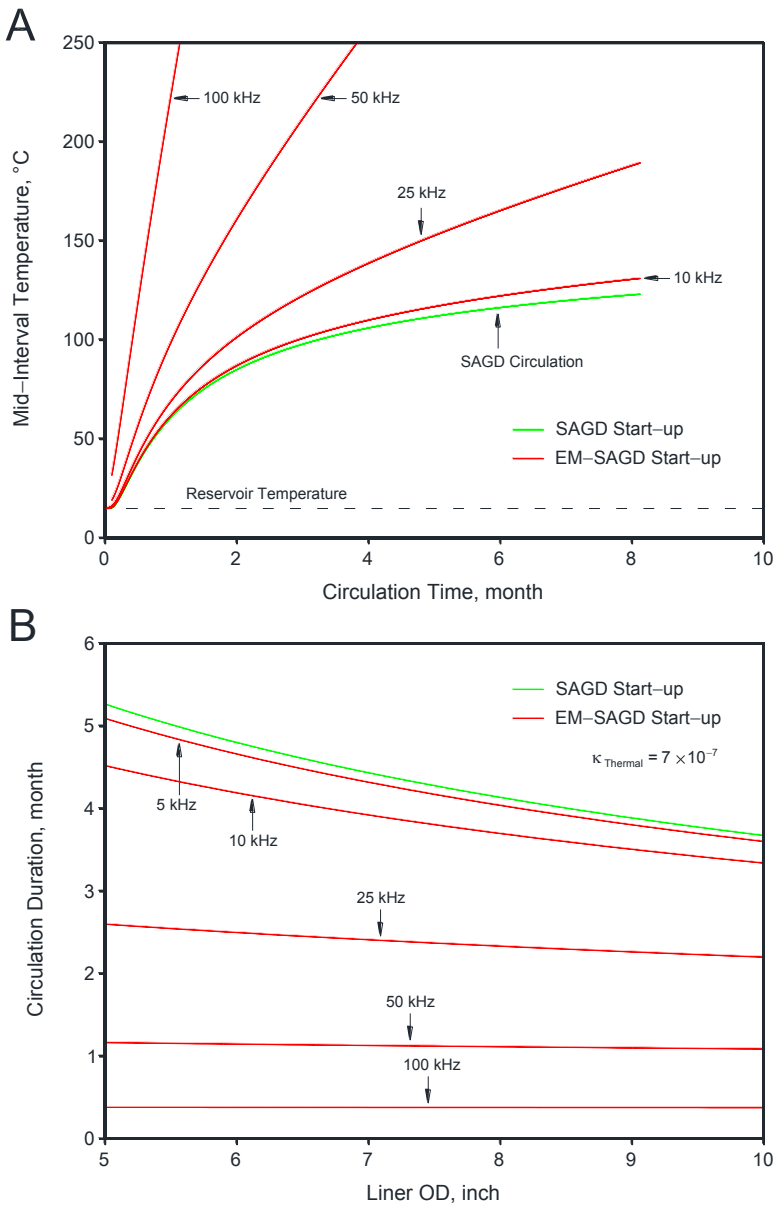

Figure 2.19. Variation of temperature in mid-interval between injector and producer for SAGD start-up and EM-SAGD start-up for different applied frequencies. See Table 2.2 for reservoir properties.

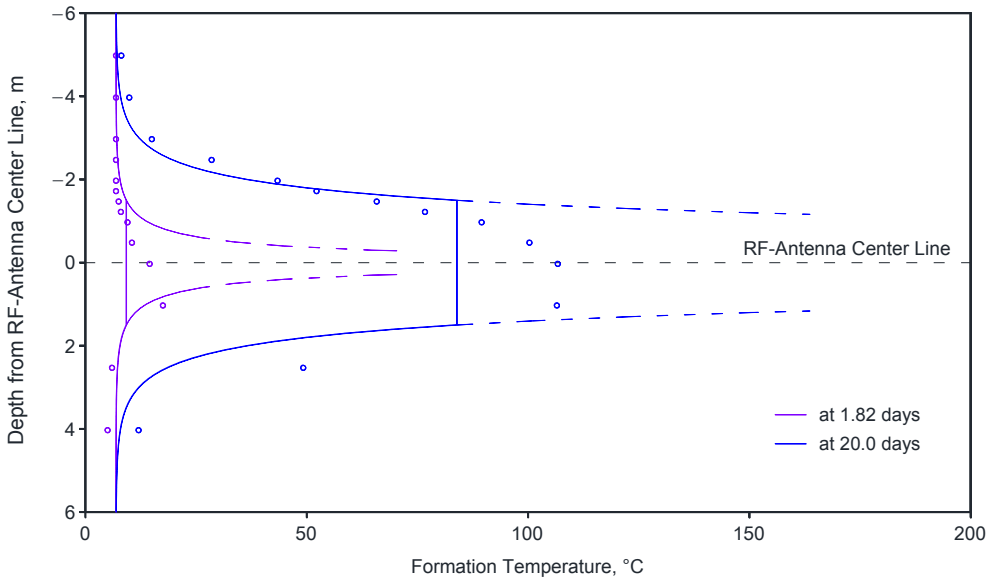

Figure 2.20. Comparison of temperature profiles from vertical instrumentation bore OB2 (located at centre line of RF antenna) and temperature as calculated using Equation 66 for ESEIEH™ Phase I implemented at face of Suncor's North Steepbank mine.

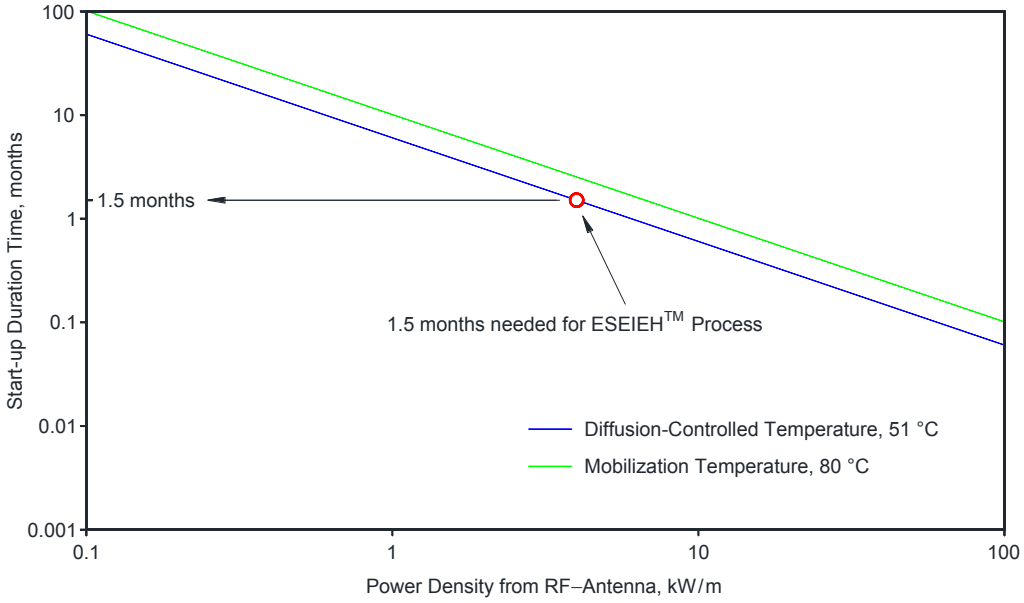

Figure 2.21. Variation of RF heating start-up time versus delivered power density from RF antenna.

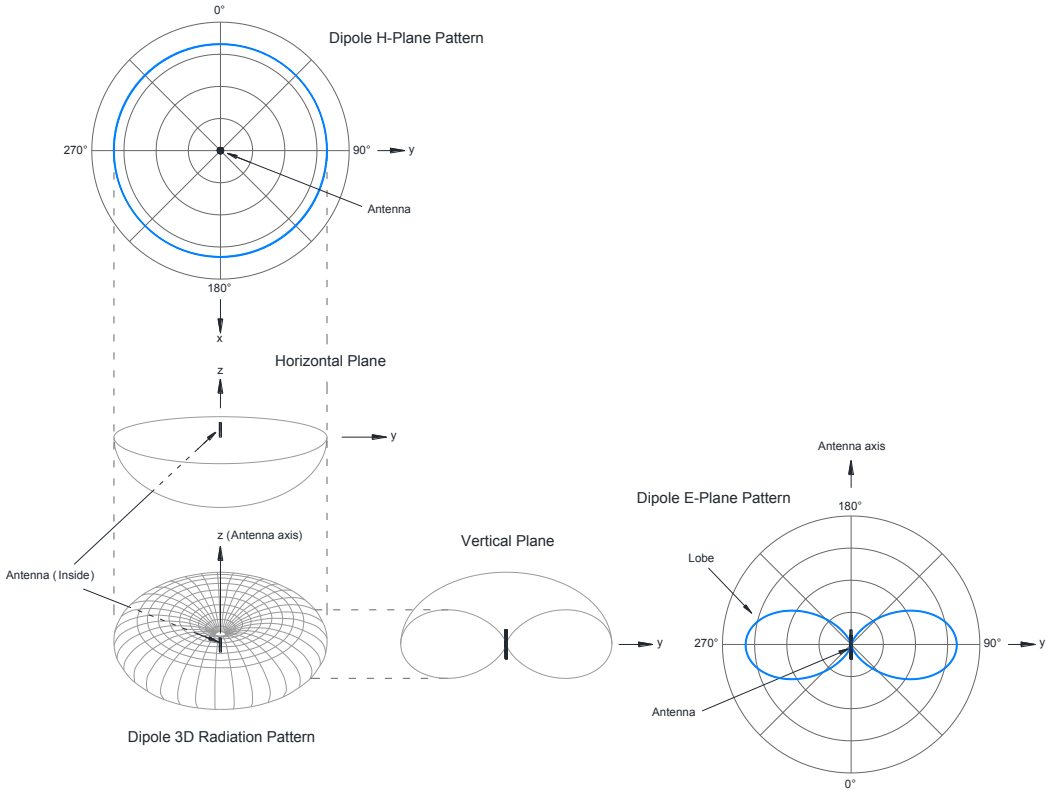

Figure 2.22. Illustration of omnidirectional antenna pattern for dipole antenna.

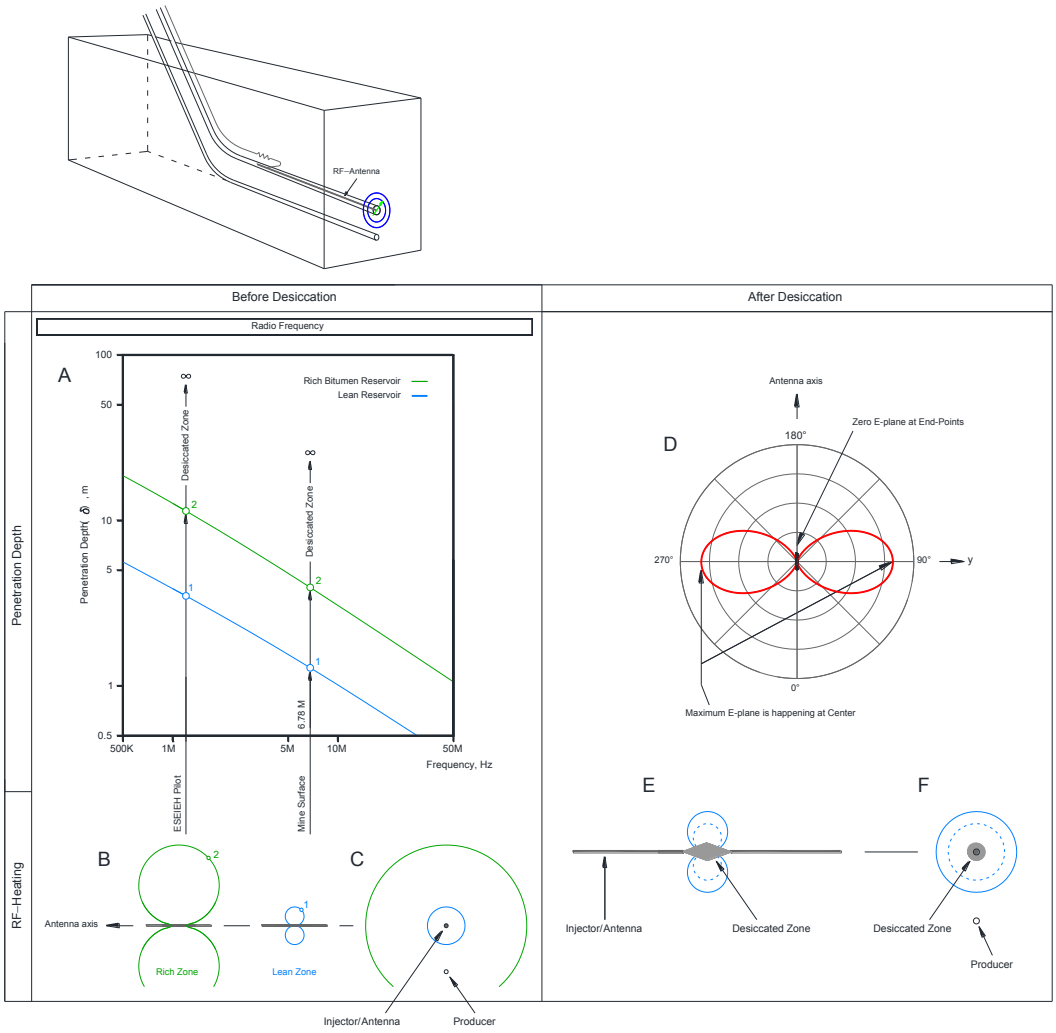

Figure 2.23. Illustration of development of Harris ESEIEH process.

This page is intentionally left blank.

3. Thermo-Hydro-Mechanical Pressurization in Two-Phase Flow[4]

3.1. Introduction

Alberta's oil sands contain 170.4 billion of Canada's 179 billion barrels of oil reserves (Government of Alberta, 2011, 2012). With recent increases in demand, tremendous efforts are being made to develop bitumen reservoirs in the coming decades. Steam-assisted gravity drainage (SAGD) is one successful thermal recovery technique applied to the oil sands of Alberta. Approximately 80% of these oil sands are recoverable through in situ production, with only 20% recoverable by mining (Government of Alberta, 2008).

In SAGD, two horizontal wells, a top injection well and a bottom production well, are placed in the lower part of the oil sand formation (as illustrated in cross section in Figure 1.1), typically between five and seven metres apart. In Figure 1.1, wellpair A is in the pre-production steam circulation stage, where thermal communication is established between the wells, wellpair B is in the early production stage, where the steam chamber has not yet contacted the top of the oil formation, and wellpair C is in the lateral growth stage. Steam injected continuously through the top well flows outward and loses its latent heat when it comes into contact with the cold bitumen at the edge of a steam chamber. The viscosity of bitumen falls several orders of magnitude when heated (typically from 2-5 million cP to 5-10 cP). Under gravity, it drains together with condensate to the lower production well. As the oil is removed from the reservoir, the steam chamber expands both upwards and sideways. Butler's SAGD method (Butler, 1998) has been a standard technique in Athabasca deposits bitumen recovery for the past thirty years. It has been commercialized and is considered both technically and economically successful. However, there are limitations with any technique, and those of SAGD include the requirement of high vertical permeability and issues around caprock integrity for shallow formations and thin caprocks. The latter item is the main object of this study.

3.2. Caprock integrity in SAGD projects

Although SAGD has become a popular alternative to classical in situ bitumen recovery methods, implementation challenges remain. In SAGD operations, steam injection raises reservoir pressure and temperature, altering reservoir stresses sufficiently to cause shear failure within and beyond the growing steam chamber (Collins, 2005, 2007). Potential caprock shear failure as a result of shear stress and pore pressure increase may result in steam releases to the surface or to upper aquifers. It may also cause casing failure and surface heaving (Collins, 2005, 2007; Dusseault and Collins, 2008a, 2008b).

Caprock integrity assessments have become key in the design and operation of SAGD projects, and in the selection of a maximum steam injection operating pressure. Caprock integrity is concerned with both hydraulic and mechanical integrity. Hydraulic integrity refers to the existence of a hydraulic barrier for reservoir fluids that prevents hydrocarbons from migrating upwards through the caprock to shallow groundwater aquifers or the ground surface. Mechanical integrity refers to caprock formation failure that can endanger future infill drilling or cause surface heave (i.e., that is a reflect of considerable deformations in the caprock) (Yuan et al., 2011a). Caprock integrity is the subject of many studies following the catastrophic failure of the caprock seal at the Joslyn Creek SAGD project on May 18, 2006 (Total E&P Canada Ltd., 2007; ERCB, 2010; Uwiera-Gartner et al., 2011a, 2011b; Yuan et al., 2011a, 2011b). As a result of this failure, Alberta Energy Regulator (AER) [it was *known as* the "Alberta's Energy Resources Conservation Board (ERCB)" *prior to* Jun 17, 2013] modified the existing application guidelines and directives (e.g., Directive 051) to include an assessment of caprock integrity. Caprock

[4] A version of this *chapter* has been published. Ghannadi, S., Irani, M. and Chalaturnyk, R., in SPEJ Journal, **19**(6): 1126-1150. SPE-165544-PA. (2014), and 165544-MS presented in SPE Heavy Oil Conference-Canada, Calgary, Alberta, Canada, 11-13 June 2013.

assessments conducted to date have incorporated varying levels of detail and complexity in each of the major elements of the study, but no studies have focused on thermo-hydro-mechanical pressurization.

While there are many aspects of caprock integrity, shear slip failure between caprock and reservoir is not discussed in AER directives, though it has been the topic of a few studies mostly focused on CSS projects (e.g., Talebi et al., 1998; Dusseault et al., 2001; Smith et al., 2002; Wong and Chau, 2004). Talebi et al. (1998) reported a well-casing failure due to caprock slip at the level of the Colorado shale formation in a CSS project at the Cold Lake deposit. Some 250 wells have failed at the Cold Lake heavy-oil field near the base of the Colorado shale, and at the top of the producing reservoir (Dusseault et al., 2001). Dusseault et al. (2001) attributed these shear failures to localized shear displacements on weak bedding planes. These are due to cyclic reservoir heave and compaction, which in turn is due to pressure and thermally induced expansion and contraction of the oil sands. Wong and Chau (2004) also mentioned a possibility of local slips of up to 12 cm along a large discontinuity of low shear resistance (such as a clay seam or fracture) in steam projects. Smith et al. (2002) evaluated the slips causing casing failures for a high percentage (>88%) of failed wells in the Clearwater bitumen zone top in the Cold Lake field. In complex formations such as Athabasca, different formations can act as a hydraulic seal. Figure 3.25 compares the particle size distribution (PSD) of Clearwater in the Fort McMurray area with that of other main formations in Athabasca. Figure 3.25 shows a wide range in the particle size distribution curves for all test soil samples. All formations also have high silt content, which may cause low cohesive streaks within the caprock. These low cohesive streaks can be mobilize easily due to thermal pressurization effect. Although many researchers are attributing the slip failure to lateral shear in the production zone, which results in horizontal displacements (AEUB Decision 99-22), the induced pore pressure effect should not be neglected, especially in formations with high silt content such as Wabiskaw and IHS formations. This is more pronounced once realized that Wabiskaw and IHS formations are considered a seal for some of the SAGD projects (see Appendix C for more details on Wabiskaw and IHS formations sealability effectiveness). Elevated thermal induced pore pressures may weaken the caprock formation locally and cause localized plastic deformation or rapid fracture initiation.

Ghannadi et al. (2013) are among the few who have studied thermal pressurization (commonly known as 'thermo-hydro-mechanical pressurization') in caprock formations for SAGD processes. They studied thermal pressurization in EM-SAGD applications, examining the relative roles of frequencies in electromagnetic heating. It was concluded that the induced thermal pressure in low-compressibility mediums is comparable even for low frequencies, and can be problematic for shallow reservoirs. The present study develops equations for fluid mass and thermal energy conservation, and presents analytical solution to evaluate the thermo-hydro-mechanical pressurization in low-permeability caprocks and the induced pressure in steam and water progression within the caprock. This study can be used to evaluate rises in temperature and pore pressure within saturated low-permeability caprocks heated by steam chamber intrusion for both one-phase and two-phase flow in porous media.

3.3. Model and Mathematical Description

Thermal pressurization can be evaluated by solving the equations for fluid mass and thermal energy conservation. In this study, these two sets of equations are developed and then solved for both one-phase and two-phase flow in porous media. In the following sections, the different physics of thermal pressurization in SAGD processes are presented via the simplified geometry of a caprock presented in Figure 1.4.

This study neglects fluid flow that is due to buoyancy. It is obvious that due to density differences between steam and water, buoyancy is a major component in vertical flow into porous media. However, there are conditions under which buoyancy can be neglected: Under the first, undrained conditions, the water is heated in a constant volume, greatly increasing the pressure of water trapped in pores, and buoyancy is minor even after it flashes into steam;

Under the second, the time for heat transfer and thermo-hydro-mechanical pressurization is short in comparison with initiation and domination of the buoyancy-driven flows (for example, in low-perm caprocks thermal-pressurization can easily result in a pressure rise of 0.5 MPa at the interval of 10 meters. This is equivalent to 50 kPa/m pressure gradient which is five times greater than hydrostatic pressure gradient at this interval). This applies for low-permeability formations or large differential pressure gradients within the medium. Both conditions are identical to caprock formations in SAGD process. Under the third, fluid moves horizontally and flows normal to the gravitational force.

The long-term response in SAGD caprock formation is characterized by "hydrothermal convection", which is driven by the buoyancy effect. In contrast, the early response is characterized by "thermal pressurization". Transitions from thermal pressurization to buoyancy-dominated flow depend on caprock formations, and happen anywhere from hours to weeks after that steam chamber reaches the bottom of the caprock. Authors believed that the major effect of "thermal pressurization" in SAGD processes occurs in the short term. Thus, this study looks at the short-term response of heat transfer and neglects buoyancy-induced flows.

3.4. Fluid Mass Conservation Equation (or Fluid Flow Governing Equation)

This section presents the "fluid mass conservation" equation for a porous medium consisting of a solid matrix and the fluid which contains the pore space. The pore structure is a homogeneous and isotropic elastic matrix containing interconnected pores saturated with single-phase fluid (either steam or water). In this section, equation terms are assigned numbers and letters: Numbers are associated to an equation where a term is presented for the first time, and letters when there are more than one term in a single equation. While uncommon, this method of presentation allows readers to follow the steps in a presented derivation.

For a control volume (C.V.) the rate of change of volume inside the volume is given by the difference between the volume flow rate in and the volume flow rate out. For a single flow coming in (q_{in}) and a single flow coming out (q_{out}) a change in fluid storage inside pores is equal to the difference between the inlet and outlet flow rates:

$$\underbrace{\left[q_{in}-q_{out}\right]_{Fluid}}_{1-A}=\underbrace{\left[\frac{1}{V_{Fluid}}\left(\frac{\partial V_{Fluid}}{\partial t}\right)\right]_{Storage}}_{1-B} \qquad 69$$

where q_{in} and q_{out} are the inlet (volume entering C.V.) and outlet (volume leaving C.V.) flow rates per volume of the control volume, respectively; and V_{Fluid} is the volume of fluid which contains the pore space. The left side of Equation 69, the difference between the inlet and outlet mass flow rates, consists of the rate of fluid transport along the flow path (i.e., the z-direction), the change in fluid mass along the flow path, and the change in fluid mass due to the difference in thermal expansion of the fluid and solid phases:

$$q_{in}-q_{out}=\underbrace{-\left\{\frac{\partial q_z}{\partial z}\right\}}_{2-A}\underbrace{-\left[\frac{1}{V_{Fluid}}\left(\frac{\partial V_{Fluid}}{\partial z}\right)q_z\right]_{z-z}}_{2-B}+\underbrace{\frac{1}{V_{Total}}\left(\frac{\partial V_{Total}}{\partial t}\right)_P}_{2-C} \qquad 70$$

where q_z is the rate of fluid transport along the flow path (i.e., the z-direction), which is expressed as the Darcy flux and can be calculated as:

$$q_z=-\frac{k}{\mu_f}\left(\frac{\partial P}{\partial z}-\rho_f g\right) \qquad 71$$

where k is the absolute permeability, μ_f is the dynamic viscosity of the fluid (in this study, water), ρ_f is the density of the fluid (in this study, water), and g is the magnitude of the gravitational acceleration. By assuming that the fluid flow due to gravitational forces is negligible, Equation 71 can be shortened to:

$$\underbrace{q_z = -\frac{k}{\mu_f}\left(\frac{\partial P}{\partial z}\right)}_{4-A} \quad 72$$

The second term on the right hand side of Equation 70 represents the change in fluid mass along the flow path, which is given as the volume contraction or expansion of the single-phase fluid in the pore structure as a result of changes in temperature and pressure:

$$\underbrace{\left[\frac{1}{V_{Fluid}}\left(\frac{\partial V_{Fluid}}{\partial z}\right)q_z\right]_{z-z}}_{2-B} = \underbrace{\frac{1}{V_{Fluid}}\left(\frac{\partial V_{Fluid}}{\partial z}\right)}_{5-A}q_z \quad 73$$

The volume change as a result of changes in temperature and pressure is given by:

$$\underbrace{\frac{1}{V_{Fluid}}\left(\frac{\partial V_{Fluid}}{\partial z}\right)}_{5-A} = \underbrace{\beta_f\left(\frac{\partial P}{\partial z}\right) - \gamma_f\left(\frac{\partial T}{\partial z}\right)}_{6-A} \quad 74$$

where β_f is the compressibility of the fluid in the pore space; γ_f is the volumetric thermal expansion coefficient (i.e., the 3-dimensional thermal expansion coefficient) of the fluid (in this study, water or steam). The compressibility of the fluid in the pore space (β_f) is given by:

$$\beta_f = -\frac{1}{V_{Fluid}}\left(\frac{\partial V_{Fluid}}{\partial P}\right)_T \quad 75$$

where V_{Fluid} is the volume of fluid which contains the pore space, and the subscript T indicates that the temperature is held constant during the pressure contraction. Also, the volumetric coefficient of thermal expansion of the fluid in the pore space (γ_f) is given by:

$$\gamma_f = \frac{1}{V_{Fluid}}\left(\frac{\partial V_{Fluid}}{\partial T}\right)_P \quad 76$$

where V_{Fluid} is the volume of fluid which contains the pore space, and the subscript P indicates that the pressure is held constant during thermal expansion. Substituting Equation 74 (Term 6-A) into Equation 73 yields:

$$\underbrace{\left[\frac{1}{V_{Fluid}}\left(\frac{\partial V_{Fluid}}{\partial z}\right)q_z\right]_{z-z}}_{2-B} = \overbrace{\left\{\underbrace{\beta_f\left(\frac{\partial P}{\partial z}\right) - \gamma_f\left(\frac{\partial T}{\partial z}\right)}_{6-A}\right\}}^{9-A}q_z \quad 77$$

The third term on the right side of Equation 70 (Term 2-C) represents the change in fluid volume due to the difference in thermal expansion of the fluid and solid phases. Since solid and fluid moving in different directions the difference in thermal expansion is presented by "plus" sign. Solid expansion forces the pore fluid towards the pore volume boundaries, and increases the fluid pressure. It must be noted in this study the volumetric thermal expansion of the pore volume is presented using volumetric thermal expansion coefficient of the porous medium (γ_{sf}) (see Equation 84). In other word pore volume expansion creates space for pore fluid, and as a result, reduces pore pressure. On the other side, the solids and the pore fluid thermal expansion will result in larger pore pressure. This term can be expanded as:

$$\underbrace{\frac{1}{V_{Total}}\left(\frac{\partial V_{Total}}{\partial t}\right)_P}_{2-C} = \underbrace{\frac{1}{V_{Total}}\left(\frac{\partial V_{Solid}}{\partial t}\right)_P}_{10-A} + \underbrace{\frac{1}{V_{Total}}\left(\frac{\partial V_{Fluid}}{\partial t}\right)_P}_{10-B} \quad 78$$

The terms on the right side of Equation 78 (Terms 10-A and 10-B) can be presented separately as:

$$\underbrace{\frac{1}{V_{Total}}\left(\frac{\partial V_{Solid}}{\partial t}\right)_P}_{10-A} = \underbrace{(1-\phi)\gamma_s \frac{\partial T}{\partial t}}_{11a-A} \quad 79a$$

$$\underbrace{\frac{1}{V_{Total}}\left(\frac{\partial V_{Fluid}}{\partial t}\right)_P}_{10-B} = \underbrace{\phi\gamma_f \frac{\partial T}{\partial t}}_{11b-A} \quad 79b$$

where ϕ is the porosity of the porous medium and γ_s is the volumetric thermal expansion coefficient (i.e., the 3-dimensional thermal expansion coefficient) of the solid phase. Substituting Equations 79a and 79b (terms 11a-A and 11b-A) into Equation 78 yields:

$$\underbrace{\frac{1}{V_{Total}}\left(\frac{\partial V_{Total}}{\partial t}\right)_P}_{2-C} = \underbrace{(1-\phi)\gamma_s \frac{\partial T}{\partial t}}_{11a-A} + \underbrace{\phi\gamma_f \frac{\partial T}{\partial t}}_{11b-A} = \underbrace{\left[(1-\phi)\gamma_s + \phi\gamma_f\right]\frac{\partial T}{\partial t}}_{12-A} \quad 80$$

By substituting Equations 77 (Term 9-A) and 80 (Term 12-A) into Equation 70, the terms on the left side of Equation 69 (Term 1-A) yield:

$$\underbrace{\left[q_{in} - q_{out}\right]_{Fluid}}_{1-A} = -\left\{\frac{\partial q_z}{\partial z}\right\} - \underbrace{\left\{\beta_f\left(\frac{\partial P}{\partial z}\right) - \gamma_f\left(\frac{\partial T}{\partial z}\right)\right\}q_z}_{9-A} + \underbrace{\left[(1-\phi)\gamma_s + \phi\gamma_f\right]\frac{\partial T}{\partial t}}_{12-A} \quad 81$$

The term on the right side of Equation 69 (Term 1-B), which represents change in fluid storage inside pores, can be expanded as:

$$\underbrace{\left[\frac{1}{V_{Fluid}}\left(\frac{\partial V_{Fluid}}{\partial t}\right)\right]_{Storage}}_{1-B} = \underbrace{\frac{1}{V_{Total}}\left(\frac{\partial V_{Pore}}{\partial t}\right)}_{14-A} + \underbrace{\left[\frac{1}{V_{Total}}\left(\frac{\partial V_{Fluid}}{\partial t}\right) - \frac{1}{V_{Total}}\left(\frac{\partial V_{Solid}}{\partial t}\right)\right]_T}_{14-B} \quad 82$$

The first term on the right side (Term 14-A) represents the change in fluid mass due to volumetric dilation of the porous medium:

$$\underbrace{\frac{1}{V_{Total}}\left(\frac{\partial V_{Pore}}{\partial t}\right)}_{14-A} = \underbrace{\frac{\partial \varepsilon_v}{\partial t}}_{15-A} \quad 83$$

As discussed in Appendix E, for a linear-elastic porous medium, the volumetric strain is given by the following, which is identical to Equation C23 (see Figure 3.27):

$$\underbrace{\frac{\partial \varepsilon_v}{\partial t}}_{15-A} = \underbrace{\beta_{sf}\frac{\partial P}{\partial t} + (\gamma_{sf} - \gamma_s)\frac{\partial T}{\partial t}}_{16-A} \quad 84$$

where β_{sf} and γ_{sf} are the linear elastic compressibility and volumetric thermal expansion coefficient of the porous medium. Laboratory work defines two different linear volumetric thermal expansion coefficients: *undrained* (γ_{sf}^{dr}) and *drained* (γ_{sf}^{u}). Since the former includes the increase in volume owing to an increase in pore pressure, it is the larger of the two (Settari, 1992). Since this study presents separately the porous volumetric deformation from pore-pressure change, the latter of the coefficients should be considered ($\gamma_{sf} = \gamma_{sf}^{dr}$).

$$\frac{\partial \varepsilon_v}{\partial t} = \beta_{sf}\frac{\partial P}{\partial t} + (\gamma_{sf}^{dr} - \gamma_s)\frac{\partial T}{\partial t} \quad 85$$

where β_{sf} is the compressibility of the porous medium due to a pore pressure change *while holding applied stress constant.* Under conditions in which the Biot's coefficient (α_{Biot}) is equal to 1 (Biot's coefficient value for different formations is discussed in Appendix D, and the value of one is a reasonable suggestion for shallow shale formations such as Colorado shale and Clearwater shale formations), β_{sf} is equal to the compressibility of the porous medium under drained conditions. This is obtained by measuring the volumetric strain due to changes in applied stress *while holding pore pressure constant*. The compressibility of the porous medium is much lower under drained conditions.

As discussed in Appendix E, knowing that the vertical movement is a major component of caprock deformation, the compressibility of the solid-fluid or the porous medium (β_{sf}) is given by the following, which is identical to Equation C24):

$$\beta_{sf} = \frac{(1-2\nu)\alpha_{Biot}}{2G(1-\nu)} = \frac{(1+\nu)(1-2\nu)\alpha_{Biot}}{E(1-\nu)} \quad 86$$

where E and G are the elastic and shear moduli of the formation, respectively; and ν is Poisson's ratio. While heave and vertical movement is a major component of caprock deformation above the SAGD steam chmaber (Yuan et al. 2011a, 2013), there is an associated lateral movement in heaving distortion. For the *sake of simplicity, and* for *practical* purposes, horizontal movements can be ignored and we *can* assume that caprock only moves vertically. Modifications to this assumption have to be studied for very deep reservoirs such as Venezuelan oil sand reservoirs.

Term 14-B from Equation 82 presents the change in fluid mass due to the difference in compressibility between the fluid and solid phases. This term can be expanded as:

$$\underbrace{\left[\frac{1}{V_{Total}}\left(\frac{\partial V_{Fluid}}{\partial t}\right) - \frac{1}{V_{Total}}\left(\frac{\partial V_{Solid}}{\partial t}\right)\right]_T}_{14-B} = \underbrace{\frac{1}{V_{Total}}\left(\frac{\partial V_{Fluid}}{\partial t}\right)_T}_{19-A} - \underbrace{\frac{1}{V_{Total}}\left(\frac{\partial V_{Solid}}{\partial t}\right)_T}_{19-B} \quad 87$$

Volume changes resulting from pressure increases for fluids and solids are given, respectively, as:

$$\underbrace{\frac{1}{V_{Total}}\left(\frac{\partial V_{Fluid}}{\partial t}\right)_T}_{19-A} = \underbrace{\phi\beta_f \frac{\partial P}{\partial t}}_{20a-A} \quad 88a$$

$$\underbrace{\frac{1}{V_{Total}}\left(\frac{\partial V_{Solid}}{\partial t}\right)_T}_{19-B} = \underbrace{-(1-\phi)\beta_s \frac{\partial \bar{\sigma}}{\partial t}}_{20b-A} \quad 20b$$

where $\bar{\sigma}$ is the average change in value of effective normal stress acting on the solid grains. $\bar{\sigma}$ can be given as a function of pore pressure assuming constant total stress (using Equation B-4, constant total stress is discussed in Appendix D):

$$\frac{\partial}{\partial t}\bar{\sigma} = -\alpha_{Biot}\frac{\partial}{\partial t}P \quad 89$$

Substituting Equation 89 into Equation 88b yields:

$$\underbrace{\frac{1}{V_{Total}}\left(\frac{\partial V_{Solid}}{\partial t}\right)_T}_{19-B} = \underbrace{-(1-\phi)\beta_s \frac{\partial \bar{\sigma}}{\partial t}}_{20b-A} = \underbrace{(1-\phi)\,\beta_s \alpha_{Biot}\frac{\partial P}{\partial t}}_{22-A} \quad 90$$

Substituting Equations 88a (Term 20a-A) and 88b (Term 22-A) into Equation 87 yields:

$$\underbrace{\left[\frac{1}{V_{Total}}\left(\frac{\partial V_{Fluid}}{\partial t}\right) - \frac{1}{V_{Total}}\left(\frac{\partial V_{Solid}}{\partial t}\right)\right]_T}_{14-B} = \left[\underbrace{\phi\beta_f \frac{\partial P}{\partial t}}_{20a-A} - \underbrace{(1-\phi)\,\beta_s \alpha_{Biot}\frac{\partial P}{\partial t}}_{22-A}\right] = \underbrace{\left[\phi\beta_f - (1-\phi)\,\beta_s \alpha_{Biot}\right]\frac{\partial P}{\partial t}}_{23-A} \quad 91$$

where β_f and β_s are the compressibilities of the fluid and solid phases, respectively.

Substituting Equations 83 (Term 15-A) and 91 (Term 23-A) into Equation 82, the term on the right hand side of Equation 69 (Term 1-B) is calculated as:

$$\underbrace{\left[\frac{1}{V_{Fluid}}\left(\frac{\partial V_{Fluid}}{\partial t}\right)\right]_{Storage}}_{1-B} == \underbrace{\frac{\partial \varepsilon_v}{\partial t}}_{15-A} + \underbrace{\left[\phi\beta_f - (1-\phi)\,\beta_s \alpha_{Biot}\right]\frac{\partial P}{\partial t}}_{23-A} \quad 92$$

Substituting Equations 70 (Term 2-A), 77 (Term 9-A), 80 (Term 12-A), 83 (term 15-A) and 91 (Term 23-A) into Equation 69 yields the "fluid mass conservation" equation:

$$\underbrace{-\left\{\frac{\partial q_z}{\partial z}\right\}}_{2-A}\underbrace{-\left\{\beta_f\left(\frac{\partial P}{\partial z}\right)-\gamma_f\left(\frac{\partial T}{\partial z}\right)\right\}q_z}_{9-A}+\underbrace{\left[(1-\phi)\,\gamma_s+\phi\gamma_f\right]\frac{\partial T}{\partial t}}_{12-A}=$$
$$\underbrace{\frac{\partial\varepsilon_v}{\partial t}}_{15-A}+\underbrace{\left[\phi\beta_f-(1-\phi)\,\beta_s\alpha_{Biot}\right]\frac{\partial P}{\partial t}}_{23-A} \quad (93)$$

Substituting the Darcy flux from Equation 72 (Term 4-A) and the volumetric strain rate from Equation 84 (Term 16-A) into Equation 93 yields:

$$-\frac{\partial}{\partial z}\underbrace{\left\{-\frac{k}{\mu_f}\left(\frac{\partial P}{\partial z}\right)\right\}}_{4-A}-\left\{\beta_f\left(\frac{\partial P}{\partial z}\right)-\gamma_f\left(\frac{\partial T}{\partial z}\right)\right\}\underbrace{\left\{-\frac{k}{\mu_f}\left(\frac{\partial P}{\partial z}\right)\right\}}_{4-A}+$$
$$\left[(1-\phi)\,\gamma_s+\phi\gamma_f\right]\frac{\partial T}{\partial t}=\underbrace{\beta_{sf}\frac{\partial P}{\partial t}+(\gamma_{sf}-\gamma_s)\frac{\partial T}{\partial t}}_{16-A} \quad (94)$$
$$+\left[\phi\beta_f-(1-\phi)\,\beta_s\alpha_{Biot}\right]\frac{\partial P}{\partial t}$$

Finally, with small modifications, the "fluid mass conservation" equation is given by:

$$\frac{\partial}{\partial z}\left(\frac{k}{\mu_f}\frac{\partial P}{\partial z}\right)+\frac{k}{\mu_f}\left[\beta_f\left(\frac{\partial P}{\partial z}\right)^2-\gamma_f\left(\frac{\partial T}{\partial z}\right)\left(\frac{\partial P}{\partial z}\right)\right]+$$
$$\left[\phi\gamma_f+(2-\phi)\gamma_s-\gamma_{sf}\right]\frac{\partial T}{\partial t}=\left[\phi\beta_f-(1-\phi)\beta_s\alpha_{Biot}+\beta_{sf}\right]\frac{\partial P}{\partial t} \quad (95)$$

Undrained conditions can be suggested, assuming the formation hydraulic permeability is zero (*Zero hydraulic permeability* implies that fluid is unable to flow in any direction which can be similar to the condition that the *boundaries* of a *system* are defined as a *close boundary*. Either zero hydraulic permeability or close boundary system can be used to define the *undrained system*. In this study we use zero hydraulic permeability that can be incorporated in the closed form equations easier than using boundary equations). Equation 95 is simplified to:

$$\frac{\partial P}{\partial T}=\frac{\phi\gamma_f+(2-\phi)\gamma_s-\gamma_{sf}}{\phi\beta_f-(1-\phi)\beta_s\alpha_{Biot}+\beta_{sf}} \quad (96)$$

Equation 96 reflects the increase in fluid pressure per unit change in temperature of a constant volume of a bulk porous medium under undrained conditions. The coefficient of "thermo-hydro-mechanical pressurization" (or simply the coefficient of thermal pressurization) (Λ), defining the increase in fluid pressure per unit change in temperature of a constant volume of a bulk porous medium is given by:

$$\Lambda=\frac{\phi\gamma_f+(2-\phi)\gamma_s-\gamma_{sf}}{\phi\beta_f-(1-\phi)\beta_s\alpha_{Biot}+\beta_{sf}} \quad (97)$$

Equation 97 can be simplified by considering two factors. Firstly, Figure 2.18 compares the thermal expansion of the fluid portion (i.e., $\phi\gamma_f$) and the thermal expansion of the solid-matrix portion (i.e., $(2-\phi)\gamma_s-\gamma_{sf}$). The latter is negligible in comparison with the former for formations with porosities greater than 8% for temperatures above 25ºC:

$$\phi\gamma_f \gg (2-\phi)\gamma_s-\gamma_{sf} \qquad \phi>0.082 \quad (98)$$

Table 2.2 lists the properties used to analyze the comparison of the thermal expansion of the fluid portion and the thermal expansion of the solid-matrix portion in Equation 98. Secondly, for media with appreciable porosity such as the Clearwater shale formation, the Biot's coefficient (α_{Biot}) is approximately equal to 1 (discussed in detail in Appendix D). Suggesting a Biot's coefficient (α_{Biot}) equal to 1 and neglecting both the thermal expansion of the solid-matrix portion (i.e., $(2-\phi)\gamma_s-\gamma_{sf}$) and the solid grains compressibility, Equation 97 can be simplified as:

$$\Lambda = \frac{\phi\gamma_f}{\phi\beta_f + \beta_{sf}} \quad 99$$

For cases in which porous medium compressibility (β_{sf}) is much larger than fluid compressibility:

$$\beta_{sf} \gg \phi\beta_f \quad 100$$

As shown in Figure 3.29, this assumption is only valid for water-saturated shale formations, and the cases which steam is introduced to the medium either from vaporization (red line) or from steam diffused from steam chamber into the caprock (green line), the fluids compressibility must be included into Equation 99. The thermal pressurization (Λ) in Equation 99 can be approximated as:

$$\Lambda \approx \frac{\phi\gamma_f}{\beta_{sf}} \qquad \beta_{sf} \gg \beta_f;\ \phi\gamma_f \gg (2-\phi)\gamma_s - \gamma_{sf} \quad 101$$

For cases in which porous medium compressibility (β_{sf}) is much less than fluid compressibility:

$$\phi\beta_f \gg \beta_{sf} \quad 102$$

The thermal pressurization (Λ) in Equation 99 can be approximated as:

$$\Lambda \approx \frac{\gamma_f}{\beta_f} \qquad \beta_{sf} \ll \beta_f;\ \phi\gamma_f \gg (2-\phi)\gamma_s - \gamma_{sf} \quad 103$$

As shown in Figure 3.29, this assumption is not valid for water-saturated shale formations, but it can be a valid assumption for steam-saturated caprocks at low temperatures, which is only plausible at shallow caprocks. Using Equation 103, the thermal pressurization factor for stiff caprocks saturated with water is given by:

$$\Lambda = \left(\frac{\partial P}{\partial T}\right)_\rho = \frac{\gamma_w}{\beta_w} \quad 104$$

where γ_w is the thermal expansion of water and β_w is the compressibility of the water. Variation of the incremental thermal pressurization (or thermal pressurization coefficient) of steam for drained conditions is calculated based on Equation 105 and presented in Figure 1.2a. Using Equation 103, the thermal pressurization factor for stiff caprocks saturated with steam is given by:

$$\Lambda = \left(\frac{\partial P}{\partial T}\right)_\rho = \frac{\gamma_{st}}{\beta_{st}} \quad 105$$

where γ_{st} is the thermal expansion of steam and β_{st} is the compressibility of the steam. Variation of the incremental thermal pressurization (or thermal pressurization coefficient) of steam for drained conditions is calculated based on Equation 105 and presented in Figure 1.2b.

Variation of the incremental thermal pressurization of steam under undrained conditions can be studied, assuming that water vaporizes and transforms into steam without pressure communication, causing pressure reduction during and after vaporization. In this section, the work by Grant and Sorey (1979) is used and modified to fit our problem.

Assuming a fully saturated medium, the volume of fluid in the pore space is equal to the pore space which contains the fluid (i.e., $V_{Fluid} = V_{Pore}$). Then, the total combined volume of the solid and the fluid is given by:

$$V_{Total} = V_{Solid} + V_{Pore} = V_{Solid} + V_{Fluid} \quad 106$$

where V_{Total} is the total volume of the medium; V_{Solid} is the volume of the solid portion in the medium; V_{Pore} is the pore volume of the medium; and V_{Fluid} is the volume of the fluid portion in the medium. Using porosity (ϕ) defined as:

$$\phi = \frac{V_{Pore}}{V_{Total}} \quad 107$$

the following identities are calculated:

$$V_{Fluid} = \phi V_{Total} \quad 108\text{-a}$$

$$V_{Solid} = (1-\phi) V_{Total} \quad 108\text{-b}$$

There are three portions of heat release from temperature drops in formations. The first decreases the temperature of solids, the second decreases the temperature of water, and the third decreases the temperature of steam:

$$\Delta Q = \Delta Q_{solid} + \Delta Q_{water} + \Delta Q_{steam} \quad 109$$

On the saturation line, the enthalpy of steam is nearly constant (Grant and Sorey, 1979):

$$\Delta Q_{steam} \approx 0 \quad 110$$

Considering constant enthalpy of steam (Equation 110), the heat required for a change in formation temperature is calculated as:

$$\Delta Q = \Delta Q_{solid} + \Delta Q_{water} = \Delta T\left(V_{Solid}\rho_s c_s + V_{Fluid} S_w \rho_w c_w\right) = V_{Total}\Delta T\left[(1-\phi)\rho_s c_s + \phi S_w \rho_w c_w\right] \quad 111$$

The released heat is absorbed by the latent heat needed for boiling [The term "boiling" is used for a phase transition from liquid to gas occurring at or above the boiling temperature. The term "evaporation" should only be used for the phase transition from liquid to gas occurring below the boiling temperature at a given pressure]. The mass of water vaporized can be calculated as:

$$\Delta m = \frac{\Delta Q}{H_{st} - H_w} = \frac{\Delta Q}{L_v} \quad 112$$

where, H_{st} is the enthalpy of steam; H_w is the enthalpy of water; and L_v is the enthalpy of water boiling (or *latent heat* of *vaporization*) equal to $H_{st} - H_w$. The latent heat of vaporization is the amount of heat required to vaporize a unit mass of a liquid without a change in temperature (i.e., for water to change to steam).

Substituting Equation 111 into Equation 112 yields:

$$\Delta m = \frac{V_{Total}\Delta T\left[(1-\phi)\rho_s c_s + \phi S_w \rho_w c_w\right]}{L_v} \quad 113$$

The volume occupied by water before boiling is given by:

$$\Delta V_w = \frac{\Delta m}{\rho_w} \quad 114$$

The volume presented in Equation 114 expands after boiling and occupies the volume given by:

$$\Delta V_{st} = \frac{\Delta m}{\rho_{st}} \quad 115$$

Then, an increase in volume is:

$$\Delta V = \Delta m\left(\frac{1}{\rho_{st}} - \frac{1}{\rho_w}\right) = \Delta m\,\frac{\rho_w - \rho_{st}}{\rho_w \rho_{st}} \quad 116$$

Substituting Equation 113 into Equation 116 yields:

$$\Delta V = \frac{\rho_w - \rho_{st}}{\rho_w \rho_{st}}\,\frac{V_{Total}\Delta T\left[(1-\phi)\rho_s c_s + \phi S_w \rho_w c_w\right]}{L_v} \quad 117$$

If the pressure drop (ΔP) is small, the pressure and temperature will remain on the saturation curve, and the temperature drop can be calculated as:

$$\Delta T = \frac{\Delta P}{(dP_{sat}/dT)} \quad 118$$

Using the Clausius-Clapeyron equation, the slope of the vapour pressure curve (dP_{sat}/dT) along the saturation curve is given by:

$$\frac{dP_{sat}}{dT} = \frac{L_v}{T(^\circ K)\Delta V_{phasetransition}} = \frac{L_v}{T(^\circ K)}\left(\frac{1}{\rho_{st}} - \frac{1}{\rho_w}\right) = \frac{\rho_w \rho_{st}}{\rho_w - \rho_{st}}\,\frac{L_v}{T(^\circ C) + 273.15} \quad 119$$

where $\Delta V_{phasetransition}$ is the volume change of the phase transition and L_v is the latent heat.

Substituting Equation 119 into Equation 118 yields:

$$\Delta T = \Delta P\left(\frac{\rho_w - \rho_{st}}{L_v\,\rho_w\rho_{st}}\right)(T+273.15) \quad 120$$

Then, substituting Equation 120 into Equation 117 yields:

$$\Delta V = V_{Total}\,\Delta P\left(\frac{\rho_w - \rho_{st}}{L_v\,\rho_w\rho_{st}}\right)^2 (T+273.15)\left[(1-\phi)\rho_s c_s + \phi S_w \rho_w c_w\right] \quad 121$$

Then, the fluid phase compressibility due to phase change is given by:

$$\beta_{st-w} = \frac{1}{V_{Fluid}}\frac{\Delta V}{\Delta P} = \frac{1}{\phi V_{Total}}\frac{\Delta V}{\Delta P} \quad 122$$

Then, substituting Equation 121 into Equation 122 yields:

$$\beta_{st}^{vap} = \frac{(1-\phi)\rho_s c_s + \phi S_w \rho_w c_w}{\phi}\left(\frac{\rho_w - \rho_{st}}{L_v\,\rho_w\rho_{st}}\right)^2 (T+273.15) \quad 123$$

As shown in Figure 1.2c, for the range of SAGD injection temperatures, the water density is much larger than the steam density (i.e., $\rho_w \gg \rho_{st}$). Then it can be suggested that:

$$\rho_w - \rho_{st} \approx \rho_w \quad 124$$

Substitution of Equation 124 into Equation 123 yields:

$$\beta_{st}^{vap} = \frac{(1-\phi)\rho_s c_s + \phi S_w \rho_w c_w}{\phi}\left(\frac{1}{L_v\,\rho_{st}}\right)^2 (T+273.15) \quad 125$$

Using Equation 103, the thermal pressurization factor for stiff caprocks saturated with water before vaporization (i.e., $S_w = 1$), in conditions under which the vaporized steam cannot leak off from the porous medium under undrained conditions, is given by:

$$\Lambda = \left(\frac{\partial P}{\partial T}\right)_{\rho} = \frac{\gamma_{st}}{\beta_{st}^{vap}} = \frac{\phi}{(1-\phi)\rho_s c_s + \phi\rho_w c_w}(L_v\,\rho_{st})^2\,\frac{\gamma_{st}}{(T+273.15)} \quad 126$$

The thermal-pressurization factor of vaporized steam under undrained conditions is calculated based on Equation 126 and presented Figure 1.2d. Overall, the thermal pressurization factor for water-saturated caprocks, including the formation compressibility, is given as:

$$\Lambda = \frac{\phi\gamma_w}{\phi\beta_w + \beta_{sf}} \quad 127$$

For steam-saturated caprocks (and for vaporization in high-permeability caprocks, off which steam can leak after vaporization), it is given as:

$$\Lambda = \frac{\phi\gamma_{st}}{\phi\beta_{st} + \beta_{sf}} \quad 128$$

For vaporized steam in low-permeability caprocks, off which steam cannot leak after vaporization, it is given as:

$$\Lambda = \frac{\phi\gamma_f}{\phi\beta_{st}^{vap} + \beta_{sf}} = \frac{\phi\gamma_{st}}{\left[(1-\phi)\rho_s c_s + \phi\rho_w c_w\right]\left(\frac{1}{L_v\,\rho_{st}}\right)^2 (T+273.15) + \beta_{sf}} \quad 129$$

Equations 127, 128, and 129 are presented in Figure 1.2a, Figure 1.2b, and Figure 1.2d, respectively. Phase boundaries for ice, water, and steam are in modified form from Sato et al. (1991) and presented in Figure 3.31a. Figure 3.31a defines, in magnified format, the relevant phase regarding each curve defining different thermal pressurization factors in Figure 3.31b.

The parameter called hydraulic diffusivity ($\kappa_{Hydraulic}$) is defined as the rate at which the disturbance in fluid pressure propagates from the thermal source:

$$\kappa_{Hydraulic} = \frac{k}{\mu_f\left(\phi\beta_f - (1-\phi)\beta_s + \beta_{sf}\right)} \quad 130$$

For a compressible medium such as the Clearwater formation, hydraulic diffusivity ($\kappa_{Hydraulic}$) can be approximated using:

$$\kappa_{Hydraulic} \approx \frac{k}{\mu_w \beta_{sf}} \qquad \beta_{sf} \gg \beta_f \qquad 131$$

As shown in Figure 3.29, this assumption is only valid for water-saturated shale formations. In the same manner, for a stiff porous medium such as consolidated sandstone reservoirs, hydraulic diffusivity ($\kappa_{Hydraulic}$) can be approximated using:

$$\kappa_{Hydraulic} \approx \frac{k}{\phi \mu_w \beta_w} \qquad \beta_{sf} \ll \beta_f \qquad 132$$

As shown in Figure 3.29, this assumption is not valid for water-saturated shale formations, but it can be a valid assumption for steam-saturated caprocks at low temperatures, which is only plausible at shallow caprocks. The final modified form of Equation 95 is simplified as follows, by substituting Equations 97 and 130:

$$\kappa_{Hydraulic}\left(\frac{\partial^2 P}{\partial z^2}\right) + \kappa_{Hydraulic}\left[\beta_f\left(\frac{\partial P}{\partial z}\right)^2 - \gamma_f\left(\frac{\partial T}{\partial z}\right)\left(\frac{\partial P}{\partial z}\right)\right] + \Lambda\frac{\partial T}{\partial t} = \frac{\partial P}{\partial t} \qquad 133$$

and,

$$\kappa_{Hydraulic}\left(\frac{\partial^2 P}{\partial z^2}\right)(1+\beta_f) - \kappa_{Hydraulic}\left[\gamma_f\left(\frac{\partial T}{\partial z}\right)\left(\frac{\partial P}{\partial z}\right)\right] + \Lambda\frac{\partial T}{\partial t} = \frac{\partial P}{\partial t} \qquad 134$$

As shown in Figure 3.29, for both steam and water, the compressibility of the fluid is significantly smaller than unity (i.e., $\beta_f \ll 1$). Consequently, Equation 133 is simplified as:

$$\kappa_{Hydraulic}\left(\frac{\partial^2 P}{\partial z^2}\right) - \kappa_{Hydraulic}\left[\gamma_f\left(\frac{\partial T}{\partial z}\right)\left(\frac{\partial P}{\partial z}\right)\right] + \Lambda\frac{\partial T}{\partial t} = \frac{\partial P}{\partial t} \qquad 135$$

3.5. Thermal Energy Conservation Equation (or Heat Flow Governing Equation)

This section presents the "thermal energy conservation" equation for a porous medium consisting of a solid matrix and the fluid which contains the pore space. The pore structure is homogeneous and contains interconnected pores saturated with single-phase fluid. A change in thermal energy inside a porous medium is given by Ghannadi et al. (2013):

Conduction Heat Flux – Convective Heat Flux to the Outer Medium + Reversible Work Due to the Pressure Change = Change in the Internal Heat Storage 136

"*Conduction heat flux*" is given by:

$$\text{Conduction Heat Flux} = \frac{\partial}{\partial z}\left(K_{sf}\frac{\partial T}{\partial z}\right) \qquad 137$$

where T is the temperature, and K_{sf} is the thermal conductivity of the solid-fluid composite. "*Convective heat flux*" is given by:

$$\text{Convective Heat Flux} = \rho_f c_f q_z\left(\frac{\partial T}{\partial z}\right) \qquad 138$$

where T is the temperature; K_{sf} is the thermal conductivity of the solid-fluid composite; $\rho_f c_f$ is the heat capacity of the fluid inside the pores; and q_z is the Darcy flux of fluid transport along the flow path in the z-direction within the caprock expressed in Equations 71 and 72. Though it is presented differently in different literature (e.g., Mase and Smith, 1985, 1987), this study represents "*Reversible work due to the pressure change*" using the equation proposed by Delaney (1982):

$$\text{Reversible Work Due to the Pressure Change} = \phi T\left(\frac{\partial P}{\partial T}\right)_{\rho_f}\left(\frac{\partial v_z}{\partial z}\right) \qquad 139$$

where v_z is the velocity of fluid in a porous medium in the z-direction expressed as a function of the Darcy flux:

$$v_z = \frac{q_z}{\phi} \quad 140$$

Substituting Equation 140 into Equation 139 yields:

$$\text{Reversible Work Due to the Pressure Change} = T\left(\frac{\partial P}{\partial T}\right)_\rho \left(\frac{\partial q_z}{\partial z}\right) \quad 141$$

The "*reversible work*" term is insignificant and can be neglected for most of the problems (Ghannadi et al., 2013). "*Change in the internal heat storage*" is given by:

$$\text{Change in the Internal Heat Storage} = (\rho c)_{sf} \frac{\partial T}{\partial t} \quad 142$$

where $(\rho c)_{sf}$ is the heat capacity of the solid-fluid composite. Substituting Equations 137, 138, 141, and 142 into Equation 136 yields:

$$\frac{\partial}{\partial z}\left(K_{sf}\frac{\partial T}{\partial z}\right) - \rho_f c_f q_z \left(\frac{\partial T}{\partial z}\right) + T\left(\frac{\partial P}{\partial T}\right)_\rho \left(\frac{\partial q_z}{\partial z}\right) = (\rho c)_{sf}\frac{\partial T}{\partial t} \quad 143$$

Neglecting the "r*eversible work due to the pressure*" term yields:

$$\frac{\partial}{\partial z}\left(K_{sf}\frac{\partial T}{\partial z}\right) - \rho_f c_f q_z \left(\frac{\partial T}{\partial z}\right) = (\rho c)_{sf}\frac{\partial T}{\partial t} \quad 144$$

Substituting the Darcy flux from Equation 72 into Equation 144 yields the final form of the heat flow governing equation:

$$\frac{\partial}{\partial z}\left(K_{sf}\frac{\partial T}{\partial z}\right) + \left(\rho_f c_f \frac{k}{\mu_f}\right)\left(\frac{\partial T}{\partial z}\right)\left(\frac{\partial P}{\partial z}\right) = (\rho c)_{sf}\frac{\partial T}{\partial t} \quad 145$$

which yields:

$$\frac{K_{sf}}{(\rho c)_{sf}}\left(\frac{\partial^2 T}{\partial z^2}\right) + \left(\frac{(\rho c)_f}{(\rho c)_{sf}}\frac{k}{\mu_f}\right)\left(\frac{\partial T}{\partial z}\right)\left(\frac{\partial P}{\partial z}\right) = \frac{\partial T}{\partial t} \quad 146$$

The thermal diffusivity of the formation ($\kappa_{Thermal}$) is given by:

$$\kappa_{Themal} = \frac{K_{sf}}{(\rho c)_{sf}} \quad 147$$

The convection controller number (N_{conv}) is the ratio of the rate of heat convection due to flow (or convection gradient) to the rate of heat conduction (or conduction gradient):

$$N_{conv} = \frac{(\rho c)_f}{(\rho c)_{sf}}\frac{k}{\mu_f\ \kappa_{Thermal}} \quad 148$$

Following these definitions, the final format of Equation 143 is presented as:

$$\kappa_{Thermal}\left(\frac{\partial^2 T}{\partial z^2}\right) + N_{conv}\ \kappa_{Thermal}\left(\frac{\partial T}{\partial z}\right)\left(\frac{\partial P}{\partial z}\right) = \frac{\partial T}{\partial t} \quad 149$$

Equation 149 can be used to quantifies the effect of convection by comparing N_{conv} to one. In shale formations, letting $(\rho c)_f/(\rho c)_{sf} \approx 1$; $\mu_f = \mu_w = 10^{-3}$ Pa.sec; and $\kappa_{Thermal}$ vary from 10^{-7} to 10^{-5}, Figure 3.32 illustrates how the convection controller number varies with permeability (Ref: Ghannadi et al., 2013). It also shows that for shale formations, when permeability varies from 10^{-19} to 10^{-16} m^2 (Neuzil, 1994), the convection controller number (N_{conv}) varies from 10^{-9} to 10^{-7}. These values show negligible convection controller numbers ($N_{conv} \ll 1$) for shale formations. Therefore, in shale caprock formations such as the Clearwater formation, heat transfer is accomplished with little convection in comparison with conduction, and convection can be neglected in caprock. Then, the simplified format of the thermal transport governing Equation 149 is presented as:

$$\kappa_{Thermal}\left(\frac{\partial^2 T}{\partial z^2}\right)=\frac{\partial T}{\partial t} \quad 150$$

Mase and Smith (1987) suggested the following Péclet number (N_{pe}) for thermal-pressurization problems: Controller

$$N_{Pe}=\frac{(\rho c)_f}{(\rho c)_{sf}}\phi\gamma_w\left(T_{st}-T_0\right) \quad 151$$

Based on Equations 148 and 151 the convection controller number can be given as a function of Péclet number:

$$N_{conv}=\frac{\kappa_{Hydraulic}}{\kappa_{Thermal}}\frac{1}{\Lambda\left(T_{st}-T_0\right)}N_{Pe} \quad 152$$

3.6. Analytical Solution for One-Phase Flow (Water)

An analytical solution is available for the energy equation neglecting the convection (Equation 150). In this study, a dimensionless analytical solution is presented to be consistent with the next solution for a two-phase solution. Dimensionless temperature ($\overline{T}$) and pressure ($\overline{P}$) are given as:

$$\overline{T}=\frac{T-T_0}{T_{st}-T_0} \quad 153$$

$$\overline{P}=\frac{1}{\Lambda}\sqrt{\frac{\kappa_{Hydraulic}}{\kappa_{Thermal}}}\frac{P-P_0}{T_{st}-T_0} \quad 154$$

and the dimensionless distance from the bottom of the caprock is also given by the following (sometimes called a Boltzmann transformation):

$$\xi=\frac{z}{L_{Thermal}}=\frac{z}{\sqrt{4\kappa_{Thermal}t}} \quad 155$$

where $L_{Thermal}$ is the thermal conduction length defined as:

$$L_{Thermal}=\sqrt{4\kappa_{Thermal}t} \quad 156$$

and reflects the distance a temperature perturbation propagates by thermal conduction from its heat source in time "t" (Lachenbruch, 1980; Delaney, 1982; Mase and Smith, 1987).

Boundary conditions for a caprock with dimensionless temperature ($\overline{T}$) and pressure ($\overline{P}$) are given as:

$$\overline{T}(0)=1 \quad 157a$$

$$\overline{T}(\infty)=0 \quad 157b$$

$$\frac{\partial\overline{P}(0)}{\partial\xi}=0 \quad 157c$$

$$\overline{P}(\infty)=0 \quad 157d$$

Equations 153 and 154 are substituted into Equations 135 and 150, yielding:

$$\frac{\partial^2\overline{T}}{\partial\xi^2}+2\xi\frac{\partial\overline{T}}{\partial\xi}=0 \quad 158$$

$$\frac{\partial^2\overline{P}}{\partial\xi^2}+2\frac{\kappa_{Thermal}}{\kappa_{Hydraulic}}\xi\frac{\partial\overline{P}}{\partial\xi}=2\sqrt{\frac{\kappa_{Thermal}}{\kappa_{Hydraulic}}}\xi\frac{\partial\overline{T}}{\partial\xi}+\frac{\partial\overline{P}}{\partial\xi}\frac{\partial\overline{T}}{\partial\xi}\gamma_w(T_{st}-T_0) \quad 159$$

The "dimensionless thermal energy conservation" equation (Equation 158) is solved in many pieces of literature such as Bird (1960):

$$\bar{T} = \mathrm{erfc}(\xi) \qquad 160$$

Knowing that the derivative of the complementary error function for ξ is given by:

$$\frac{\partial}{\partial \xi}\mathrm{erfc}(\xi) = -\frac{2}{\sqrt{\pi}}\exp(-\xi^2) \qquad 161$$

Differentiating Equation 160 and substituting it into the "dimensionless fluid-mass conservation" equation (Equation 159) yields:

$$\frac{\partial^2 \bar{P}}{\partial \xi^2} + 2\frac{\kappa_{Thermal}}{\kappa_{Hydraulic}}\xi\frac{\partial \bar{P}}{\partial \xi} = -\frac{4}{\sqrt{\pi}}\sqrt{\frac{\kappa_{Thermal}}{\kappa_{Hydraulic}}}\xi\exp(-\xi^2) - \frac{2}{\sqrt{\pi}}\gamma_w(T_{st}-T_0)\exp(-\xi^2)\frac{\partial \bar{P}}{\partial \xi} \qquad 162$$

Normally, the term regarding the thermal expansion of pore fluids along the flow path is negligible (i.e., the second term on the right hand side is small), and the solution for the simplified case is given by:

$$\bar{P} = \frac{\mathrm{erfc}(\sqrt{\kappa_{Thermal}/\kappa_{Hydraulic}}\,\xi) - \sqrt{\kappa_{Thermal}/\kappa_{Hydraulic}}\,\mathrm{erfc}(\xi)}{1-\kappa_{Thermal}/\kappa_{Hydraulic}} \qquad 163$$

For high-permeability formations in which $\kappa_{Hydraulic} \gg \kappa_{Thermal}$ (i.e., in which the thermal-affected zone is negligible to the size of pressure effected zone), the solution can be further simplified to:

$$\bar{P} = \mathrm{erfc}(\sqrt{\kappa_{Thermal}/\kappa_{Hydraulic}}\,\xi) \qquad 164$$

3.7. Analytical Solution for Two-Phase Flow (Steam/Water)

In this section, it is assumed either that the heated pore water in the caprock will flash to steam, or that steam may diffuse into the bottom part of the caprock. The first case is more likely for low-permeability caprock formations, and the second is more likely for medium- to high-permeability seals above the steam chamber. Figure 3.33 illustrates the configuration of steam interface and steam and water regions for this study. It shows that in this study, it is assumed that the steam interface is a completely horizontal straight line, and that the temperature and pressure at the interface follows the steam saturation curve. Knowing that the boundary condition at the interface is given by:

$$T(z^+_{interface}, t) = T(z^+_{interface}, t) = T_{int} \qquad 165$$

$$P(z^+_{interface}, t) = P(z^+_{interface}, t) = P_{int} \qquad 166$$

Equations 165 and 166 are converted to dimensionless format:

$$\bar{T}(\xi^-_{interface}) = \bar{T}(\xi^+_{interface}) = \bar{T}_{int} \qquad 167$$

$$\bar{P}(\xi^-_{interface}) = \bar{P}(\xi^+_{interface}) = \bar{P}_{int} \qquad 168$$

where $\xi_{interface}$ is defined based on Equation 155:

$$\xi_{interface} = \frac{z_{interface}}{\sqrt{4\kappa^w_{Thermal}\,t}} \qquad 169$$

Similarly to one-phase flow, "dimensionless thermal energy conservation" equations are easily created for either side of the steam interface. Delaney (1982) applied a similar approach and presented the following "dimensionless thermal energy conservation" equations for steam and water zones for rapid intrusion of magma into a water-saturated medium (The same equations are adopted for this study, neglecting the convection controller number (N_{conv}) in Delaney's (1982) energy conservation equations).:

$$\frac{\partial^2 \bar{T}}{\partial \xi^2} + 2\xi\frac{\partial \bar{T}}{\partial \xi} = 0 \qquad ;\text{for } \xi > \xi_{interface} \qquad 170$$

$$\frac{\partial^2 \bar{T}}{\partial \xi^2} + \frac{2}{\Omega_{Thermal}} \xi \frac{\partial \bar{T}}{\partial \xi} = 0 \qquad ; \text{for } \xi < \xi_{interface} \tag{171}$$

where $\Omega_{Thermal}$ is the ratio between thermal diffusivities of the media saturated with steam and water, given by:

$$\Omega_{Thermal} = \frac{\kappa^{st}_{Thermal}}{\kappa^{w}_{Thermal}} \approx \frac{K^{st}_{sf}}{K^{w}_{sf}} = \Omega_K \approx 1.0 \tag{172}$$

where Ω_K is the ratio of thermal conductivity coefficients of the medium saturated with steam to that of water, which is assumed to be equal to 1.0 in this study. Figure 3.34compares the thermal pressurization for different thermal conductivity coefficients ratios (Ω_K). In steam zones, lower thermal conductivity coefficients decrease thermal pressurization. The identical solution to Equation 160 is presented for $\Omega_K = 1$ (Delaney, 1982):

$$\bar{T} = \bar{T}(\xi_{interface}) \frac{erfc(\xi)}{erfc(\xi_{interface})} = \bar{T}_{int} \frac{erfc(\xi)}{erfc(\xi_{interface})} \qquad ; \text{for } \xi > \xi_{interface} \tag{173}$$

$$\bar{T} = 1 - \left[1 - \bar{T}(\xi_{interface})\right] \frac{erfc(\xi)}{erfc(\xi_{interface})} = 1 - \left[1 - \bar{T}_{int}\right] \frac{erfc(\xi)}{erfc(\xi_{interface})} \qquad ; \text{for } \xi < \xi_{interface} \tag{174}$$

Similarly, "dimensionless fluid-mass conservation" equations are given by:

$$\frac{\partial^2 \bar{P}}{\partial \xi^2} + 2 \frac{\kappa^{w}_{Thermal}}{\kappa^{w}_{Hydraulic}} \xi \frac{\partial \bar{P}}{\partial \xi} = 2 \sqrt{\frac{\kappa^{w}_{Thermal}}{\kappa^{w}_{Hydraulic}}} \xi \frac{\partial \bar{T}}{\partial \xi} + \frac{\partial \bar{P}}{\partial \xi} \frac{\partial \bar{T}}{\partial \xi} \gamma_w (T_{st} - T_0) \qquad ; \text{for } \xi > \xi_{interface} \tag{175}$$

$$\frac{\partial^2 \bar{P}}{\partial \xi^2} + 2 \frac{\kappa^{st}_{Thermal}}{\kappa^{st}_{Hydraulic}} \xi \frac{\partial \bar{P}}{\partial \xi} = 2 \sqrt{\frac{\kappa^{st}_{Thermal}}{\kappa^{st}_{Hydraulic}}} \xi \frac{\partial \bar{T}}{\partial \xi} \left[\frac{\gamma_{st}}{\gamma_w} \sqrt{\frac{\Omega_\Lambda}{\Omega_\mu}} \right] + \frac{\partial \bar{P}}{\partial \xi} \frac{\partial \bar{T}}{\partial \xi} \gamma_{st} (T_{st} - T_0) \qquad ; \text{for } \xi < \xi_{interface} \tag{176}$$

Assuming that Ω_K is equal to 1.0, the thermal diffusivities are related as:

$$\kappa^{st}_{Thermal} = \kappa^{w}_{Thermal} = \kappa_{Thermal} \tag{177}$$

Using Equation 177, Equations 175 and 176 are simplified as:

$$\frac{\partial^2 \bar{P}}{\partial \xi^2} + 2\Delta_w \xi \frac{\partial \bar{P}}{\partial \xi} = 2\sqrt{\Delta_w} \xi \frac{\partial \bar{T}}{\partial \xi} + \frac{\partial \bar{P}}{\partial \xi} \frac{\partial \bar{T}}{\partial \xi} \gamma_w (T_{st} - T_0) \qquad ; \text{for } \xi > \xi_{interface} \tag{178}$$

$$\frac{\partial^2 \bar{P}}{\partial \xi^2} + 2\Delta_{st} \xi \frac{\partial \bar{P}}{\partial \xi} = 2\sqrt{\Delta_{st}} \xi \frac{\partial \bar{T}}{\partial \xi} \left[\frac{\gamma_{st}}{\gamma_w} \sqrt{\frac{\Omega_\Lambda}{\Omega_\mu}} \right] + \frac{\partial \bar{P}}{\partial \xi} \frac{\partial \bar{T}}{\partial \xi} \gamma_{st} (T_{st} - T_0) \qquad ; \text{for } \xi < \xi_{interface} \tag{179}$$

where, Ω_Λ is the ratio of the thermal pressurization factor of the medium saturated with steam, to that saturated with water; and Ω_μ is the ratio of the dynamic viscosity of the steam to that of the water, which is given by the following (the ranges are given for practical SAGD steam injection temperatures and formation compressibilities greater than 10^{-8}):

$$\Omega_\Lambda = \frac{\Lambda_{st}}{\Lambda_w} \approx 0.1 - 1 \tag{180}$$

$$\Omega^{vap}_\Lambda = \frac{\Lambda^{vap}_{st}}{\Lambda_w} \approx 5 - 15 \tag{181}$$

$$\Omega_\mu = \frac{\mu_{st}}{\mu_w} \approx 0.07 - 0.2 \tag{182}$$

and

$$\Delta_w = \frac{\kappa_{Thermal}}{\kappa^{w}_{Hydraulic}} \quad 183$$

$$\Delta_{st} = \frac{\kappa_{Thermal}}{\kappa^{st}_{Hydraulic}} \quad 184$$

Figure 3.35 compares parameters for steam/water solution (i.e., Ω_Λ, Ω_Λ^{vap}, and Ω_μ). The solution for pressure distribution can be evaluated using an approach similar to that used in one-phase flow. In this study, the modified format of the solution presented by Delaney (1982) is suggested as:

$$\bar{P} = \left[\bar{P}_{int} + \frac{(T_{int}-T_0)}{(T_{st}-T_0)}\frac{\sqrt{\Delta_w}}{1-\Delta_w}\right]\frac{\operatorname{erfc}\left(\sqrt{\Delta_w}\xi\right)}{\operatorname{erfc}\left(\sqrt{\Delta_w}\xi_{interface}\right)} - \frac{(T_{int}-T_0)}{(T_{st}-T_0)}\frac{\sqrt{\Delta_w}}{1-\Delta_w}\frac{\operatorname{erfc}(\xi)}{\operatorname{erfc}(\xi_{interface})} \quad ; \text{for } \xi > \xi_{interface} \quad 185$$

$$\bar{P} = \bar{P}_{int} + \sqrt{\Delta_{st}}\left[\frac{\gamma_{st}(T_{st}-T_{int})}{\gamma_w(T_{st}-T_0)}\sqrt{\frac{\Omega_\Lambda}{\Omega_\mu}}\right]\times\left\{\frac{2}{\sqrt{\pi}}\frac{\xi_{interface}-\xi}{\operatorname{erf}(\xi_{interface})} - \left[1-\frac{\operatorname{erf}(\xi)}{\operatorname{erf}(\xi_{interface})}\right]\right\} \quad ; \text{for } \xi < \xi_{interface} \quad 186$$

Three parameters such as, $\xi_{interface}$, T_{int}, and P_{int} are unknown in Equations 185 and 186. Figure 3.36 illustrates saturation pressure calculated using the temperature profile. The intersection between the saturation pressure curve and the pressure profile should match the assumed steam interface ($\xi_{interface}$). The proper suggested steam interface ($\xi_{interface}$) can be calculated by changing the assumed steam interface until two points are matching (see Figure 3.36). This can be achieved using *Microsoft Office Excel's Solver* add-in.

The moving boundary problems normally are solved including the latent heat at interface, to calculate the growth of the interface. But in this problem the thermal pressurization would not effected with the location of the interface, and the pressure solution cannot be solved analytically considering interface growth as a function of latent heat. Therefore in this study the simple method has been used.

3.8. Results and Discussion

Table 3.4 and Table 3.5 list the fluid and caprock properties, respectively, used to analyse the theory presented in this study. Figure 2.19 presents the pressure (see Figure 2.19a) and temperature (see Figure 2.19b) progression over time. For longer durations, steam interface propagates more into the caprock. The pressure variation within the steam zone is minor, as the steam has much lower viscosity than water. It must be noted that for smaller formation permeabilities (see Figure 3.38a) and compressibilities (see Figure 3.39), the pressure profile in the steam zone may experience "*thermo-hydro-mechanical pressurization*" and as illustrated in Figure 2.19 not remains constant. In this study, while the steam interface matches the saturation line, no other point in the pressure profile does (see Figure 3.33). This can be a disadvantage for matching the pressure at the bottom of the caprock. The caprock bottom pressure is independent of the steam chamber pressure, and is only evaluated based on physics associated with the thermal pressurization related to caprock properties such as caprock compressibility and permeability. The assumption made in Equation 157c invokes a permeability seal at the bottom of the caprock which is far from reality and should be revised for future studies. Thus, in most SAGD projects, steam is delivered to the injection well under saturation conditions; the steam

chamber is under saturation conditions. This may cause the major challenge of matching two points of the pressure profile with the saturation line.

As presented in Figure 3.38 and Figure 3.39, the major parameters controlling the "*thermo-hydro-mechanical pressurization*" in caprock are its compressibility and permeability. Caprocks with lower permeabilities and stiffer structure are prone to high pressures associated with thermal pressurization.

In complex formations such as Athabasca, different formations can act as a hydraulic seal (see Appendix C). Figure 3.25 shows a wide range in the particle size distribution curves for all test soil samples, which may cause permeability heterogeneity in these formations. In general, in the McMurray oil sand reservoir and the IHS formation, the hydraulic diffusivity ($\kappa_{Hydraulic}$) is much greater than the thermal diffusivity ($\kappa_{Thermal}$) (i.e., $\kappa_{Hydraulic} \gg \kappa_{Thermal}$). This means that the hydraulic field is much wider than the thermal field. In this case, pore fluids can flow from the thermal field and modify the fluid thermal expansion without thermal pressurization. Equations 185 and 186 can be used for the McMurray oil sand reservoir and the IHS formation, substituting Ω_{Λ} from Figure 3.35. However, for the Clearwater formation, hydraulic diffusivity ($\kappa_{Hydraulic}$) is much less than thermal diffusivity ($\kappa_{Thermal}$) (i.e., $\kappa_{Thermal} \gg \kappa_{Hydraulic}$). This means that there is a potential for extreme thermal pressurization. In most of the Clearwater formation area, there is no appreciable fluid flow from the heated region, and it can be assumed that it is in an undrained condition. Equations 185 and 186 can also be used for the Clearwater formation, substituting Ω_{Λ}^{vap} from Figure 3.35. This implies higher thermal pressurization in the steam zone due to vaporization in a closed system, and no steam migration to the heated region. This is important because the Clearwater formation overlays the entire Athabasca oil sand reservoir (McMurray formation), and is considered a regional caprock by the AER. The higher pressures in the steam zone, which happen at the bottom of the caprock, may result in the caprock sliding over the oil sand reservoir following the potential casing failures.

Current state of practice to address the caprock integrity issue during the SAGD operation includes mini-frac tests and *thermal* reservoir/*g*eomechanical simulations. The end results of these studies will give the operators a maximum steam injection operating pressure (MOP). Neither mini-frac tests, nor geomechanical simulations are considering thermal-pressurization in their calculated MOP values. For example if a SAGD operation is running at 2.65 MPa, and suggested MOP using geomechanical study is 3.0 MPa, the caprock have a margin of 0.35 MPa to be failed. But as it is presented in Figure 3.38a differential pressure of 0.35 MPa is plausible for low-perm caprock (0.001 mD permeability). This may cause caprock failure with a margin of 0.35 MPa (i.e., 12% of the MOP). This is more severe for low-compressibility formations (i.e., stiffer caprocks). The final statement concluded that the permeability and compressibility of the porous medium are the most important component of caprock in thermal-pressurization, and in SAGD operations it should be experimentally or numerically calculated. The procedure proposed in this study can be used with great care to address the caprock integrity issue during the SAGD operation.

3.9. Conclusions

This study addresses these issues as cases of "thermal pressurization" (commonly known as "thermo-hydro-mechanical pressurization") in caprocks in SAGD operations. Simply put, thermal pressurization is overpressure of pore fluids due to thermal expansion, which either quickly dissipates (in high-permeability shales) or accumulates (in low-permeability shales). It happens when the volume of pore fluids exceeds pore space due to thermal expansion. In this case, pore space stiffness acted against the expansion of the pore fluid, minimizing its increase in volume. The subsequent increase in pore pressure results in a reduction of effective stress.

This study examines the relative roles of caprock formation properties such as compressibility of the porous medium (β_{sf}) and permeability (k). Caprocks with lower permeabilities and stiffer structure are prone to high pressures associated with thermal pressurization. Compressibility of the porous medium (β_{sf}) is the most important component of caprock in thermal pressurization, and in SAGD applications it should be experimentally calculated with great care.

This study also explores the effect of the phase transition from water to steam. In addressing this effect, differentiation is made between water vaporization in contained and uncontained volume. When water flashes to steam, it undergoes a large increase in volume. Porous medium pressurizes much larger in contained volume. This study treats the thermal pressurization factors of steam differently than those of water, suggesting Ω_Λ and Ω_Λ^{vap}. These are compared in Figure 3.35. Substituting Ω_Λ or Ω_Λ^{vap} in Equations 185 and 186 should match formation properties. For example, Ω_Λ should be used for the McMurray oil sand reservoir and the IHS formation, while Ω_Λ^{vap} should be used for the Clearwater formation. To address the caprock integrity issue during the SAGD operation thermal-pressurization should be experimentally or numerically calculated. The procedure proposed in this study can be used to calculate thermal-pressurization with great care to reduce MOP for either low-permeable or stiff caprocks.

For simplicity, suggested framework to use the analytical solution given in this study is summarized as follows:

1. Use Figure 3.35 to evaluate Ω_Λ or Ω_Λ^{vap} for suggested caprock using the project steam injection temperature and caprock measured compressibility; for Athabasca SAGD projects use Ω_Λ for IHS formation and Ω_Λ^{vap} for Clearwater and Wabiskaw formations;
2. Use Figure 3.35 to evaluate Ω_μ for the project steam injection temperature;
3. Calculate the ratio of thermal diffusivity to hydraulic diffusivity of water-saturated and steam-saturated zones (Δ_w and Δ_{st}) using Equations 183 and 184;
4. Assume the steam interface distance from the bottom of the caprock ($\xi_{interface}$);
5. Calculate the temperature profile in the caprock;
6. Calculate the saturation pressure curve using the temperature profile in step 5.
7. Calculate the pressure profile in the caprock, substituting Ω_Λ or Ω_Λ^{vap} and Ω_μ into Equations 185 and 186.
8. Intersection between the saturation pressure curve and the pressure profile should match the assumed steam interface ($\xi_{interface}$); if it is not matched go to step 4 and change the interface distance ($\xi_{interface}$);
9. Finally, include the pressure rise from Equations 185 and 186 and decrease MOP value calculated either with mini-frac test, or using geomechanical simulation.

SI Metric Conversion Factors		
°API	141.5/(131.5 + °API)	= g/cm^3
cp × 1.0*		E−03 = Pa·s
°F	(°F−32)/1.8	= °C
°F	(°F+459.67)/1.8	= °K
ft × 3.048*		E−01 = m
ft/sec × 3.048*		E−01 = m/sec
ft/sec^2 × 3.048*		E−01 = m/sec^2
in. × 2.54*		E+00 = cm
mD × 9.869 233		E-10 = m^2
psi × 6.894 757		E+00 = kPa
psi^{-1} × 1.450 377		E−01 = kPa^{-1}
psi × 1000*		= ksi

*Conversion factor is exact.

3.10. References

AEUB Decision 99-22, 1999. Imperial Oil Resources Limited Cold Lake Production Project Mahkeses Development.

Anochie-Boateng, J.K., 2007. Advanced Testing and Characterization of Transportation Soils and Bituminous Sands, Ph.D. thesis, University of Illinois.

Biot, M.A., 1941. General Theory of Three-Dimensional Consolidation, Columbia University, New York, New York, Vol. **12.**

Biot, M.A., Willis, D.G., 1957. The Elastic Coefficients of the Theory of Consolidation, *Journal of Applied Mechanics*, Vol. **24**, pp. 594-601.

Bird, R.B., Stewart, W.E., Lightfoot, E.N., 1960. Transport Phenomena, John Wiley & Sons, New York, 780 pp.

Butler, R., 1998, SAGD comes of age!, *Journal of Canadian Petroleum Technology*, Vol. **37**, No. **7**, pp. 9-12.

Butler, R.M., 1997. Thermal Recovery of Oil and Bitumen; Englewood Cliffs, N.J., Prentice Hall 1991, available in paperback from GravDrain Inc., Calgary, AB.

Chen, G., Chenevert, M.E., Sharma, M.M., Yu, M. 2003. A Study of Wellbore Stability in Shales Including Poroelastic, Chemical, and Thermal Effects, *Journal of Petroleum Science & Technology*, Vol. **38**, No. **3-4**, pp. 167-176.

Collins, P.M., 2005. Geomechanical Effects on the SAGD Process, SPE Reservoir Evaluation & Engineering, *2005 SPE International Thermal Operations and Heavy Oil Symposium*, Calgary, Alberta, Canada, 1-3 November, 2005.

Collins, P.M., 2007. Geomechanical Effects on the SAGD Process, SPE Reservoir Evaluation & Engineering, Vol. **10**, No. **4**, pp. 367-375, SPE 97905-PA.

Collins, P.M., Walters, D.A., Perkins, T., Kuhach, J.D. and Veith, E. 2013. Effective Caprock Determination for SAGD Projects, *Journal of Canadian Petroleum Technology*, **52**(2), pp. 112-119.

Delaney, P.T., 1982. Rapid Intrusion of Magma into Wet Rock: Groundwater Flow Due To Pore Pressure Increases, *Journal of Geophysical Research*, Vol. **87**, pp. 7739-7756.

Detournay E., Cheng, A. H. D., 1993. Fundamentals of Poroelasticity, Chapter 5 in Comprehensive Rock Engineering: Principles, Practice and Projects, Vol. II, Analysis and Design Method, ed. C. Fairhurst, Pergamon Press, pp. 113-171.

Dusseault, M.B., Bruno, M.S., Barrera, J., 2001. Casing Shear: Causes, Cases, Cures, *SPE Drilling & Completion*, Vol. **16**, No. **2**, pp. 98-107, SPE 72060-PA.

Energy Resources Conservation Board (ERCB), 2010. Total E&P Canada Ltd. Surface Steam Release of May 18, 2006 Joslyn Creek SAGD Thermal Operation, ERCB Staff Review and Analysis.

Fjær, E., Holt, R.M., Horsrud, P., Raaen, A.M., Risnes, R., 2008. Petroleum Related Rock Mechanics, 2nd Edition, Elsevier, ISBN: 9780444502605.

Garnier, A., Saint-Marc, J., Bois and A.P., Kermanac'h, Y., 2008. A singular methodology to design cement sheath integrity exposed to steam stimulation, SPE/PS/CHOA *International Thermal Operations and Heavy Oil Symposium*, doi:10.2118/117709-MS.

Ghannadi, S., Irani, M., and Chalaturnyk, R., 2013. Evaluation of Induced Thermal Pressurization in Clearwater Shale Caprock in Electromagnetic Steam-Assisted Gravity Drainage (EM-SAGD) Projects, SPEJ, SPE 152217-PA, in press.

Government of Alberta, 2008. Alberta's Oil Sands: Resourceful. Responsible, ISBN 978-07785.

Government of Alberta, 2011. Alberta Oil Sands Industry (AOSID) - Quarterly Update Summer 2011, Reporting on the period: March 5, 2011 to June 3, 2011, www.albertacanada.com

Government of Alberta, 2012. www.energy.gov.ab.ca/OilSands/1715.asp

Grant, M.A., Sorey, M.L., 1979. The Compressibilities and Hydraulic Diffusivity of a Water-Steam Flow, Water Resources Research, Vol. **15**, No. **3**, pp. 684-686.

Harvest Energy, 2009. Harvest Energy BlackGold Expansion Project– Application for Approval of the BlackGold Expansion Project, Volume 1, Section 2.2.5- Caprock Characteristics, Energy Resources Conservation Board, Calgary, Alberta (December 2009), http://www.harvestenergy.ca/upload/media_element/240/01/volume_1_section_2.pdf.

Havens, J., 2011. Mechanical Properties of The Bakken Formation, Master Thesis, Colorado School of Mines, Golden, CO.

Irani, M. and Ghannadi, S. 2013. Understanding the Heat-Transfer Mechanism in the Steam-Assisted Gravity-Drainage (SAGD) Process and Comparing the Conduction and Convection Flux in Bitumen Reservoirs, *SPE J.*, Vol. **18**, No. **1**, pp. 134-145. SPE-163079-PA. http://dx.doi.org/10.2118/163079-PA.

Ito, Y. Hirata, T., Ichikawa, M., 2001. The Growth of the Steam Chamber During the Early Period of the UTF Phase B and Hangingstone Phase I Projects, *Journal of Canadian Petroleum Technology*, **40**(9), pp. 29-36.

Kell, G.S., 1975. Density, Thermal Expansivity, and Compressibility of Liquid Water from 0°C to 150°C: Correlations and Tables for Atmospheric Pressure and Saturation Reviewed and Expressed on 1968 Temperature Scale, *Journal of Chemical & Engineering Data*, Vol. 20, No. 1, *pp. 97-105.*

Klimentos, T., Harouaka, A., Mtawaa, B., Saner, S., 1998. Experimental Determination of the Biot Elastic Constant: Applications in Formation Evaluation (Sonic Porosity, Rock

Strength, Earth Stresses, and Sanding Predictions), *SPE Reservoir Evaluation & Engineering*, Vol. **1**, No. **1**, pp. 57-63.

Krief, M., Garta, J., Stellingwerff, J., and Ventre, J., 1990, A Petrophysical Interpretation Using the Velocities of P and S Waves (full-waveform sonic), *The Log Analyst*, V. **31**, pp. 355-369.

Lachenbruch, A.H., 1980. Frictional Heating, Fluid Pressure, and the Resistance to Fault Motion, *Journal of Geophysical Research*, Vol. **85**, pp. 6097-6112.

Larsen, E.S., Jr., Berman, H., 1934. The Microscopic Determination of the Nonopaque Minerals, U.S. Geology Survey, Bulletin, Vol. **848**, 2nd Ed., pp. 30-32.

Laurent, J., Bouteca, M. J., Sarda, J. P., Bary, D., 1993. Pore-Pressure Influence in the Poroelastic Behavior of Rocks: Experimental Studies and Results, SPE Formation Evaluation, **8**(2), 117-122.

Lee, M.W., 2003. Elastic Properties of Overpressured and Unconsolidated Sediments, U.S. Geological Survey Bulletin 2214, http://geology.cr.usgs.gov/pub/bulletins/b2214.

Lee, M.W., 2002, Biot-Gassmann Theory for Velocities of Gas-Hydrate-Bearing Sediments: Geophysics, V. **67**, pp. 1711-1719.

Mase, C. W., Smith, L., 1987. Effects of Frictional Heating on the Thermal, Hydrologic, and Mechanical Response of a Fault, *Journal of Geophysical Research*, 92(B7), pp. 6249-6272.

Mase, C.W., Smith, L., 1985. Pore-Fluid Pressures and Frictional Heating on a Fault Surface, *Pure and Applied Geophysics*, Vol. **122**, pp. 583-607.

Matthäi, S.K., Roberts, S.G., 1996. The Influence of Fault Permeability on Single-Phase Fluid Flow Near Fault–Sand Intersections: Results from Steady-State High-Resolution Models of Pressure-Driven Fluid Flow, *American Association of Petroleum Geologists Bulletin*, Vol. **80**, No. **11**, pp. 1763-1779.

Neuzil, C.E., 1994. How Permeable are Clays and Shales?, *Water Resources Research*, Vol. **30**, No. **2**, pp. 145-150.

Oldakowski, K., 1994. Stress Induced Permeability Changes of Athabasca Oil Sands, MSc. Thesis, University of Alberta, 227 p.

Raymer, L.L., Hunt, E.R., and Gardner, J.S., 1980, An Improved Sonic Transit Time to Porosity Transform, Paper preseted at the *21st Annual Society of Professional Well Log Analysts Logging Symposium Transactions*.

Sarker, R., Batzle, M., 2008. Effective Stress Coefficient in Shales and its Applicability to Eaton's Equation, *The Leading Edge*, **27**(6). pp. 798-804. doi:10.1190/1.2944165.

Settari, A., 1992. Physics and Modeling of Thermal Flow and Soil Mechanics in Unconsolidated Porous Media, *SPE Production Engineering*, Vol. **7**, No. **1**, pp. 47-55, SPE 18420-PA.

Shafer, J. L., Boitnott, G. N., Ewy, R. T., 2008. Effective Stress Laws for Petrophysical Rock Properties, Presented at the 49th Annual Logging Symposium, Edinburgh, Scotland, 25-28 May.

Skempton, A.W., 1960. Terzaghi's concept of effective stress, in *From Theory to Practice in Soil Mechanics*, edited by L. Bjerrum, A. Casagrande, R. B. Beck, and A. W. Skempton, pp. 42-53, John Wiley, New York.

Smith, R.J., Alinsangan, N.S., Talebi, S., 2002. Microseismic Response of Well Casing Failures at a Thermal Heavy Oil Operation, *SPE/ISRM Rock Mechanics Conference*, Irving, Texas, 20-23 October, SPE78203.

Southern Pacific Resource, 2011. Southern Pacific MacKay Thermal Project – Phase 2 Application and Environmental Impact Assessment, Part B, Section B3.6- Caprock Integrity, Energy Resources Conservation Board, Calgary, Alberta (10 November 2011), http://www.shpacific.com/SAGD2-2012/November2011/Volume1/02PartB-Project%20Description.pdf.

Talebi, S., Nechtschein, S., Boone, T.J., 1998. Seismicity and Casing Failures Due to Steam Stimulation in Oil Sands, *Pure Applied Geophysics*, Vol. **153**, pp. 219-233.

Terzaghi, K., 1923. DieBerechnung der Durchlaeassigkeitszif-fer des Tones aus dem Verlauf der hydrodynamischen Spannungsercheinungen, Akad. Wiss. Wien Math Naturwissl Kl. Abt. 2A, 132,. 105.

Total E&P Canada Ltd., 2007. Summary of Investigations into the Joslyn May 18th 2006 Steam Release, December.

Uwiera-Gartner, M.M.E., Carlson, M.R., Palmgren, C.T.S., 2011a. Evaluation of the Clearwater Formation Caprock for a Proposed, Low-Pressure, Steam-Assisted Gravity Drainage Pilot Project, *SPE Annual Technical Conference and Exhibition*, Denver, Colorado, USA, 30 October-2 November, 2011, SPE 147302, doi:10.2118/147302-MS.

Uwiera-Gartner, M.M.E., Carlson, M.R., Walters, D., Palmgren, C.T.S., 2011b. Geomechanical Simulation of Caprock Performance for a Proposed, Low Pressure, Steam-Assisted Gravity Drainage Pilot Project, *Canadian Unconventional Resources Conference*, Calgary, Alberta, Canada, 15-17 November, 2011, SPE 148886, doi:10.2118/148886-MS.

Vermeer, P.A., de Borst, R., 1984. Non-Associated Plasticity for Soils, Concrete and Rock, **29** (3): 1-64.

Verruijt, A., 1984. The Theory of consolidation, *Fundamentals of Transport Phenomena in Porous Media*, edited by J. Bear and M. Y. Corapcioglu, pp. 349-368, Martinus Nijhoff, Norwell, Mass.

Walls, J., Nur, A., 1979. Pore Pressure and Confining Pressure Dependence of Permeability in Sandstone, presented at the *7th Formation Evaluation Symposium*, Well Logging Society, Calgary, Alberta, Canada, 5-7 May.

Wong, G., 2007. Geomechanical Characterization of Clearwater Formation Shales. Unpublished MSc. Thesis, University of Alberta, 186 p.

Wong, R.C.K., Chau, K.T., 2004. Casing Impairment Induced by Shear Slip along a Weak Layer in Shale due to Fluid (Steam) Injection, *Canadian International Petroleum Conference*, Calgary, Alberta, Canada, 8-10 June.

Wong, R.C.K., Samieh, A.M., 2000. Geomechanical Response of the Shale in the Colorado Group Near a Cased Wellbore Due to Heating, *Journal of Canadian Petroleum Technology*, Vol. **39**, No. **8**, pp. 30-33.

Xie, J. and Zahacy, T.A., 2011. Understanding cement mechanical behavior in SAGD wells, World Heavy Oil Congress, Edmonton, Alberta, March 14-17, Paper WHOC11-557.

Yuan, Y., Xu, B., Palmgren C., 2013. Design of Caprock Integrity in Thermal Stimulation of Shallow Oil-Sands Reservoirs, *Journal of Canadian Petroleum Technology*, Vol. **52**, No. **4**, pp. 266-278.

Yuan, Y., Xu, B., Palmgren C., 2011a. Design of Caprock Integrity in Thermal Stimulation of Shallow Oil-Sands Reservoirs, *Canadian Unconventional Resources Conference*, Calgary, Alberta, Canada, 15-17 November, 2011, SPE 149371.

Yuan, Y., Xu, B., Yang, B., 2011b. Geomechanics for the Thermal Stimulation of Heavy Oil Reservoirs-Canadian Experience, *SPE Heavy Oil Conference and Exhibition*, Kuwait City, Kuwait, 12-14 December, SPE 150293, doi:10.2118/150293-MS.

Zoback, M.D., Byerlee, J.D., 1975. Permeability and Effective Stress, *AAPG Bulletin*, Vol. **59**, No. **1**, pp. 154-158.

Tables

Table 3.3. Parameters used for Clearwater caprock (or shale) formation in Figure 2.18.

Parameter	Value
Caprock Thermal Expansion Properties:	
Shale porous medium thermal expansion, (γ_{sf}),1/ºC	0.1×10^{-4} [A]
Shale solid thermal expansion, (γ_s),1/ºC	$(0.2\text{-}0.3) \times 10^{-4}$ [A,B]
Pore Fluid Thermal Expansion Properties:	
Water thermal expansion (γ_w),1/ºC	
at 25ºC	3.49×10^{-4}
at 100ºC	7.73×10^{-4}
at 200ºC	12.28×10^{-4}
at 300ºC	15.29×10^{-4}

[A] Given in Mase and Smith (1987).

[B] Given in Wong and Samieh (2000).

Table 3.4. Input parameters for evaluation of water and steam properties in Figure 1.2 and Figure 3.31.

Water and Steam Properties:	**Range of Equation Application**	**Reference**
SAGD steam injection temperature	150 °C–270 °C	Garnier et al., 2008; Xie and Zahacy, 2011
Saturation pressure		
$\mathrm{Log}_{10} P_{Sat}\ (\mathrm{Pa}) = 10^6 \left\{ 9.8809 - \left(2.42223 + \frac{326.57}{T + 273.15} \right)^2 \right\}$	100 °C < T < 275 °C	Moss, 1903 (from Butler (1997), page 521)
$P_{Sat}\ (\mathrm{Pa}) = \frac{1}{1000} T^4$	275 °C < T < 373.95 °C	Simplified equation from curve fit
Water density		
$\rho_w (\mathrm{kg/m^3}) = 1001.7 - 0.1616 \times T - 0.00262 \times T^2$	10 °C < T < 290 °C	Butler (1997), page 487
Specific volume of saturated steam		
$\rho_{st} (\mathrm{kg/m^3}) = \frac{1}{v_{st}}$		
$v_{st} (\mathrm{m^3/kg}) = \{ 363.9 (P/6894.8)^{-0.9588} \} / 16.0185$	50 Pa < P < 500 Pa	1st Equation (Farouq Ali, 1974); 2nd Equation (Ejiogu and Fiori, 1987); 3rd Equation (Ejiogu and Fiori, 1987); (from Butler (1997), page 487)
$v_{st} (\mathrm{m^3/kg}) = \{ [490.386 / (P/6894.8)] - 0.04703 \} / 16.0185$	500 Pa < P < 1500 Pa	
$v_{st} (\mathrm{m^3/kg}) = \{ [551.74 / (P/6894.8)] - 0.0887 \} / 16.0185$	1500 Pa < P < 2500 Pa	
Coefficient of isothermal compressibility of water		
$\beta_w (1/\mathrm{Pa}) = 0.001 \left\{ \begin{matrix} 50.83 \times 10^{-8} - 3.68 \times 10^{-9} T + \\ 7.26 \times 10^{-11} T^2 - 6.60 \times 10^{-13} T^3 + \\ 2.88 \times 10^{-15} T^4 \end{matrix} \right\}$	Kell (1975)	
Coefficient of isothermal compressibility of steam		
$\beta_{st} (1/\mathrm{Pa}) = \frac{1}{\rho_{st}} \left(\frac{\partial \rho_{st}}{\partial P} \right)_T$		
Coefficient of isobaric volumetric thermal expansion of water		
$\gamma_w (1/^\circ\mathrm{C}) = -\frac{1}{\rho_w} \left(\frac{\partial \rho_w}{\partial T} \right)_P$		
Coefficient of isobaric volumetric thermal expansion of steam		
$\gamma_{st} (1/^\circ\mathrm{C}) = -\frac{1}{\rho_{st}} \left(\frac{\partial \rho_{st}}{\partial T} \right)_P$		
Enthalpy of water at saturation condition		
$H_w (\mathrm{J/kg}) = (-14.54 + 4.5196 T_{Sat} - 0.002771 T_{Sat}^2 + 0.00000922 T_{Sat}^3) \times 1000$	100 °C < T < 275 °C	Butler (1997), page 522-523
$H_w (\mathrm{J/kg}) = (-3899.18 + 45.085 T_{Sat} - 0.14418 T_{Sat}^2 + 0.0001739 T_{Sat}^3) \times 1000$	275 °C < T < 357 °C	
Enthalpy of steam at saturation condition		
$H_{st} (\mathrm{J/kg}) = (2523.43 + 1.3556 T_{Sat} + 0.003561 T_{Sat}^2 - 0.00001824 T_{Sat}^3) \times 1000$	100 °C < T < 275 °C	Butler (1997), page 522-523
$H_{st} (\mathrm{J/kg}) = (9457.68 - 70.942 T_{Sat} + 0.25514 T_{Sat}^2 - 0.00031058 T_{Sat}^3) \times 1000$	275 °C < T < 357 °C	
Latent heat of vaporization		
$L_v (\mathrm{J/kg}) = H_{st} - H_w$		
Water heat capacity at saturation condition		

$C_w(J/kg^oC) = (4.182 - 1.5\times10^{-4} T_{Sat} + 3.44\times10^{-7} T_{Sat}^{\ 2} + 4.26\times10^{-8} T_{Sat}^{\ 3})\times1000$	10 °C < T < 240 °C	Butler (1997), page 501
$C_w(J/kg^oC) = (11.55 - 0.064518 T_{Sat} + 1.5087\times10^{-4} T_{Sat}^{\ 2})\times1000$	240 °C < T < 300 °C	
Water dynamic viscosity at saturation condition		
$\mu_w(Pa.sec) = \frac{0.001}{0.5462 + 0.021192\times T_{Sat} + 0.00008934\times T_{Sat}^{\ 2}}$	10 °C < T < 100 °C	Butler (1991), page 512 (Data from Schmidt and Grigull, 1981)
$\mu_w(Pa.sec) = \frac{0.001}{0.040079\times T_{Sat} - 0.4997}$	100 °C < T < 300 °C	
Steam dynamic viscosity at saturation temperature		
$\mu_{st}(Pa.sec) = 0.001(0.00879 + 0.0000354\times T_{Sat})$	90 °C < T < 300 °C	Butler (1991), page 513 (Data from Schmidt and Grigull, 1981)

Table 3.5. Parameters used for Clearwater caprock (or shale) formation in Figure 1.2 and Figure 3.31.

Parameter	Value Range	Assumed Value in Figure 2.19
Caprock Hydraulic Properties:		
β_{sf}, 1/Pa	10^{-8} to 10^{-6} [a]	10^{-8} to 10^{-6}
ϕ, no unit	0.10 to 0.35[b]	0.25
μ_w, Pa·s	0.001002 (at 20 ºC)	0.001
k, m^2	10^{-19} to 10^{-17} [b]	10^{-19} to 10^{-17}
Caprock Thermal Properties:		
Caprock Initial Temperature, ºC	8 to 15ºC	15ºC
K_{sf}, W/m•ºC	1.30 to 1.95 [c]	1.50
$\kappa_{Thermal}$, m^2/sec	4.0×10^{-7} to 9.0×10^{-7} [c]	9.0×10^{-7} (for both water-saturated and steam-saturated)
ρ_s, kg/m^3	2500–2800 [d]	2500
C_s, kg/m^3	Varies [e]	

[a] Given in Mase and Smith (1985).

[b] Given in Matthäi and Roberts (1996).

[c] Evaluated based on Fjær et al. (2008).

[d] The range is taken from the unit weight of important shale rock constituents such as Kaolinite, Illite and Montmorillonite, measured by Larsen and Berman (1934); minerals such as Muscovite and Chlorite showing higher densities, such as 2900 and 3000, respectively, which are not common minerals in shale formations and commonly not consisting the major portion of the shale rocks.

[e] The Clearwater solids heat capacity is calculated based on the following equation given by Butler (1991) (page 500) suggested for Athabasca fines, which is roughly equal to the heat capacity of Na-Montmorillonite: $C_s(J/kg^oC) = (0.784 + 0.001367\times T - 9.26\times10^{-7}\times T^2)\times1000$

Figures

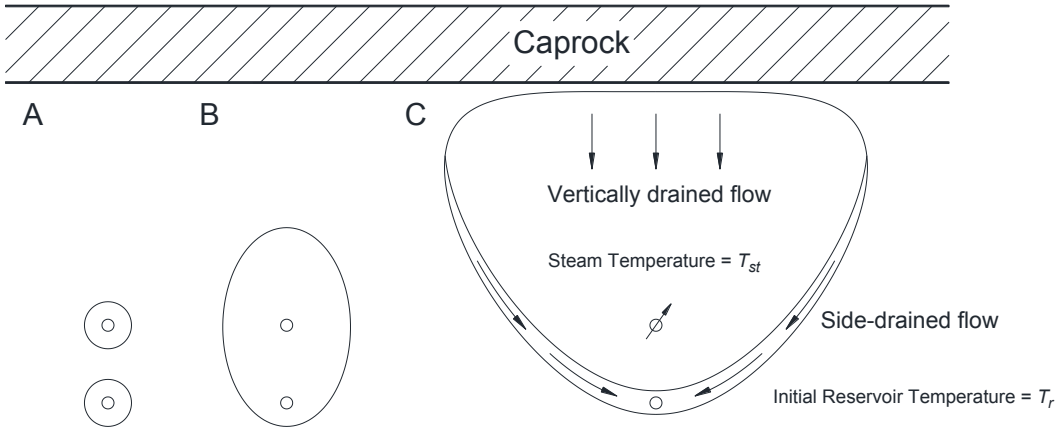

Figure 3.24. Cross section of SAGD process; Section A presents circulation phase, Section B presents early phase, and Section C presents steam injection phase (Modified from Irani and Ghannadi (2013)).

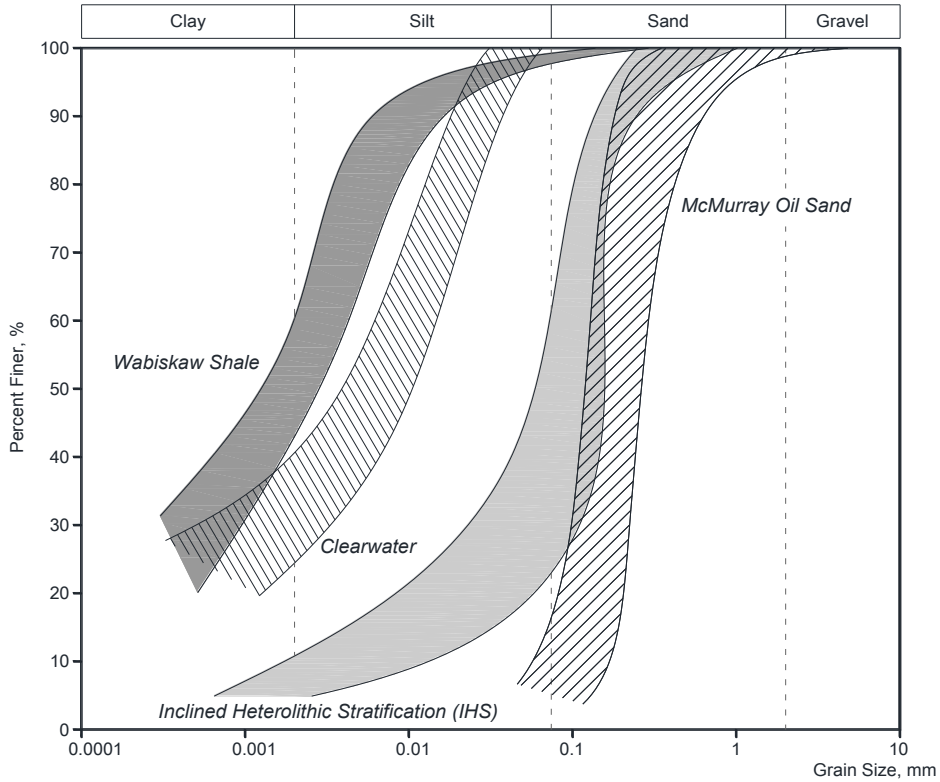

Figure 3.25. Comparison of particle size distribution (PSD) of different formations in Athabasca; Figure created using public literature (Oldakowski, 1994; Anochie-Boateng, 2007; Wong, 2007) and lab data.

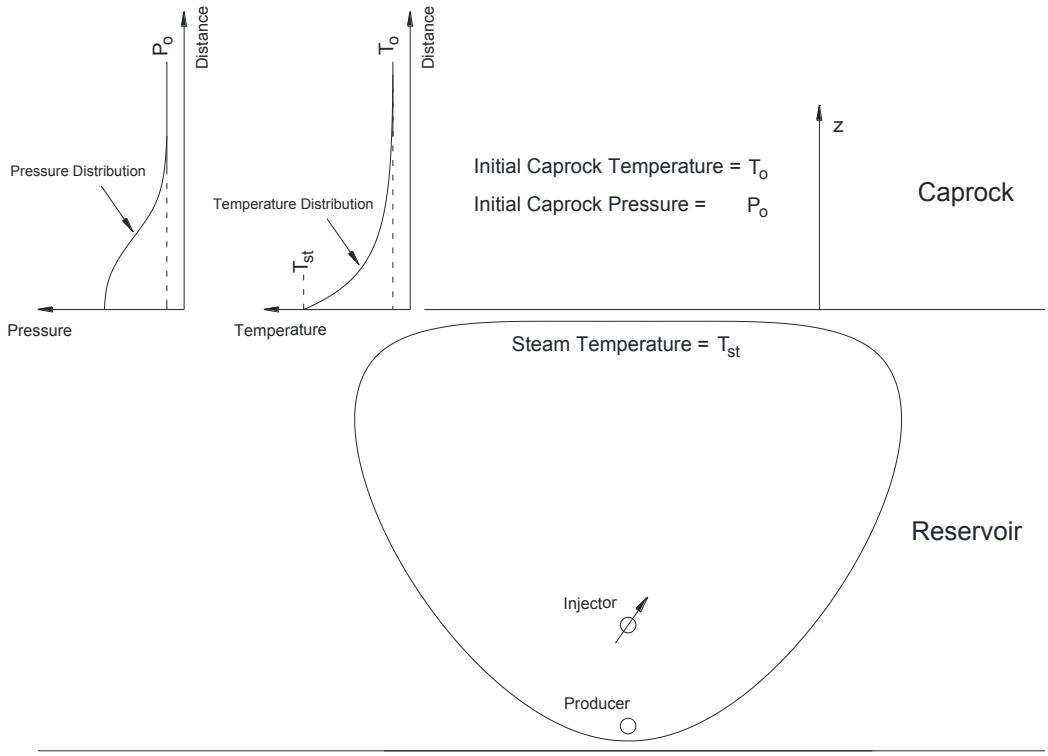

Figure 3.26. Illustration of simplified caprock thermal model used in this study, and related dimensions

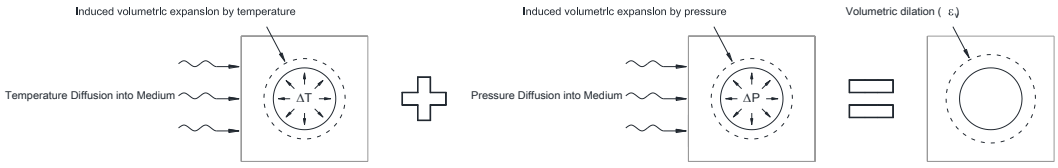

Figure 3.27. Illustration of porous volumetric deformation from temperature and pore-pressure change.

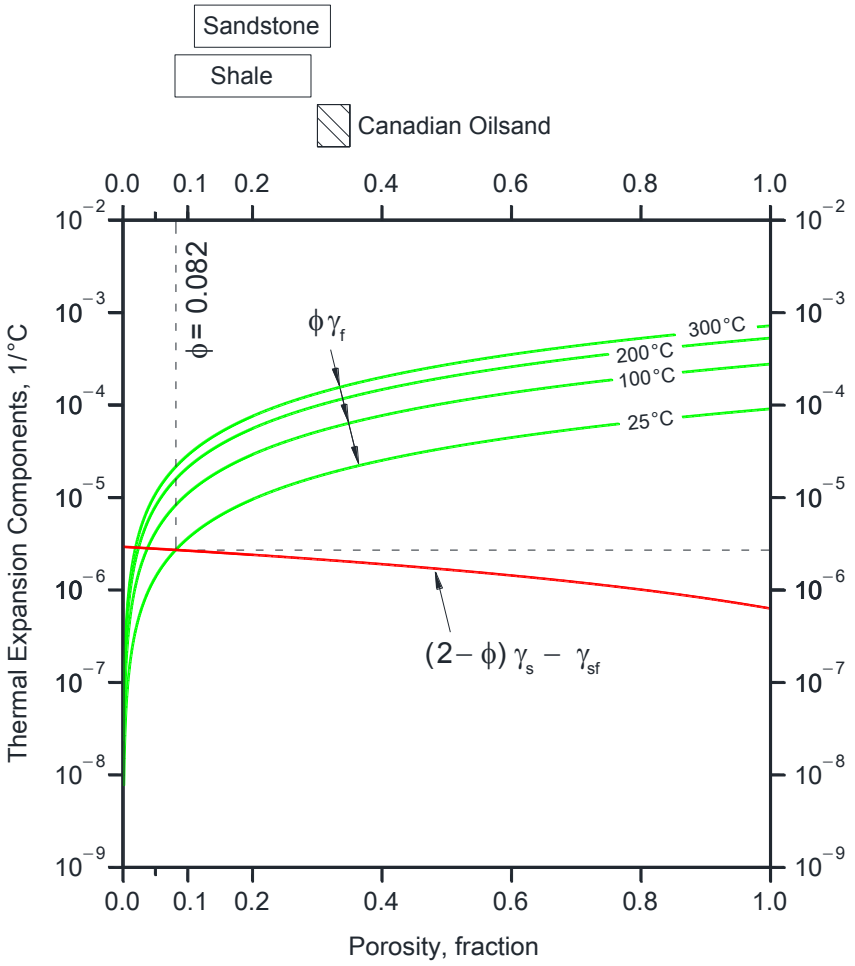

Figure 3.28. Comparison of fluid and solid thermal expansion components for Clearwater shale formation. See Table 2.2 for properties of fluid and caprock.

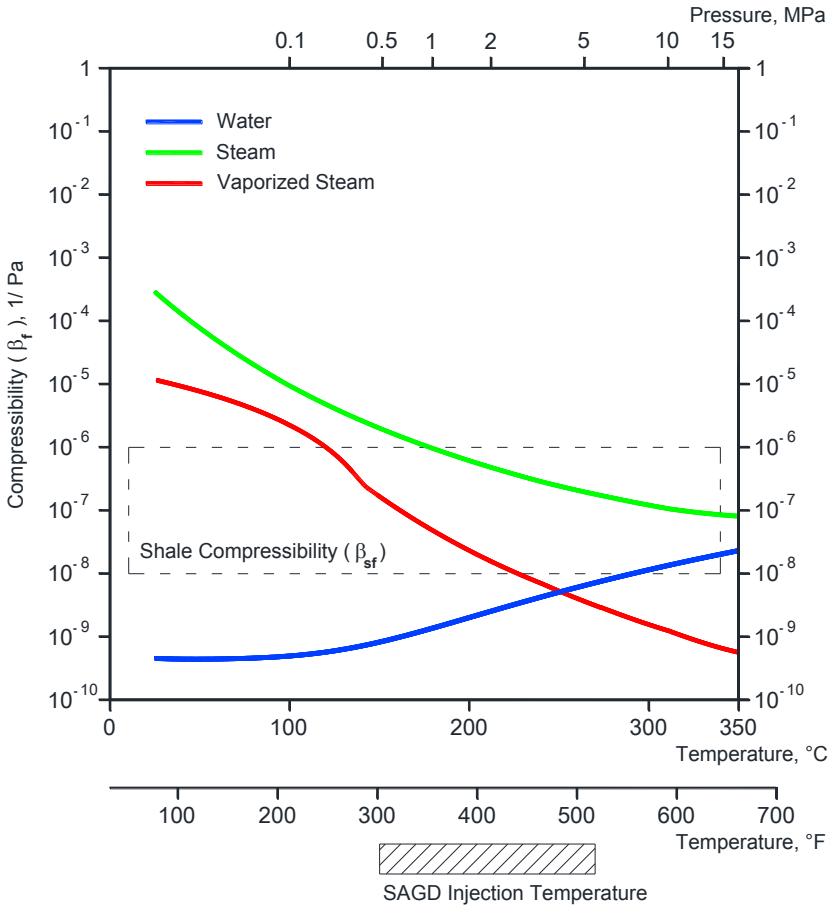

Figure 3.29. Comparison of fluid and shale formation porous medium compressibilities. See Table 3.4 and Table 3.5 for properties of fluid and caprock, respectively.

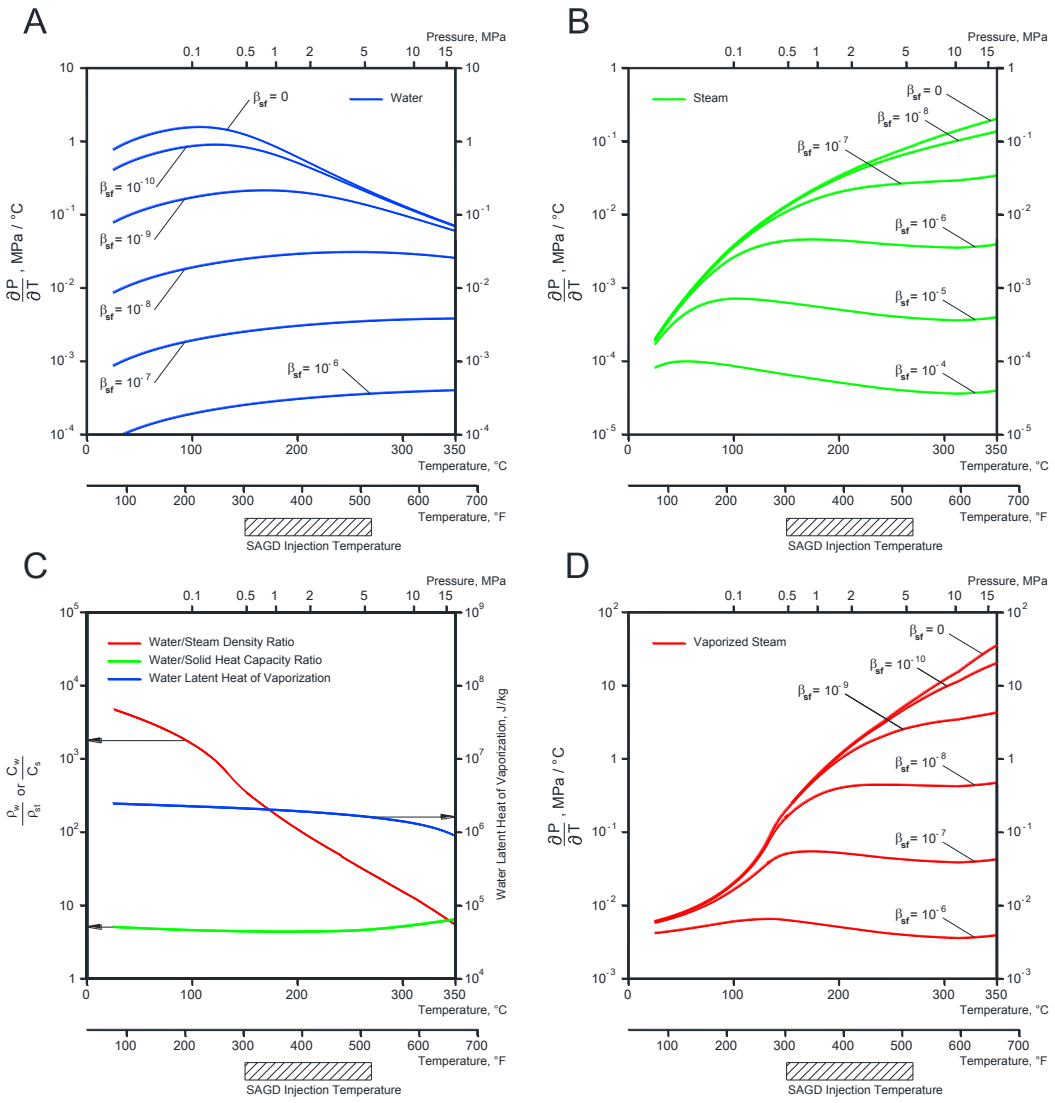

Figure 3.30. Variation of the incremental thermal pressurization of pure water (Section A); variation of the incremental thermal pressurization of steam in drained condition (Section B); variation of the important parameter for incremental thermal pressurization of vaporized steam in undrained condition (i.e., water-to-steam density ratio, water-to-solid heat capacity ratio, and latent heat of vaporization (Section C); and variation of the incremental thermal pressurization of vaporized steam in undrained condition (Section D) versus injection temperature and pressure. See Table 3.4 and Table 3.5 for properties of fluid and caprock, respectively.

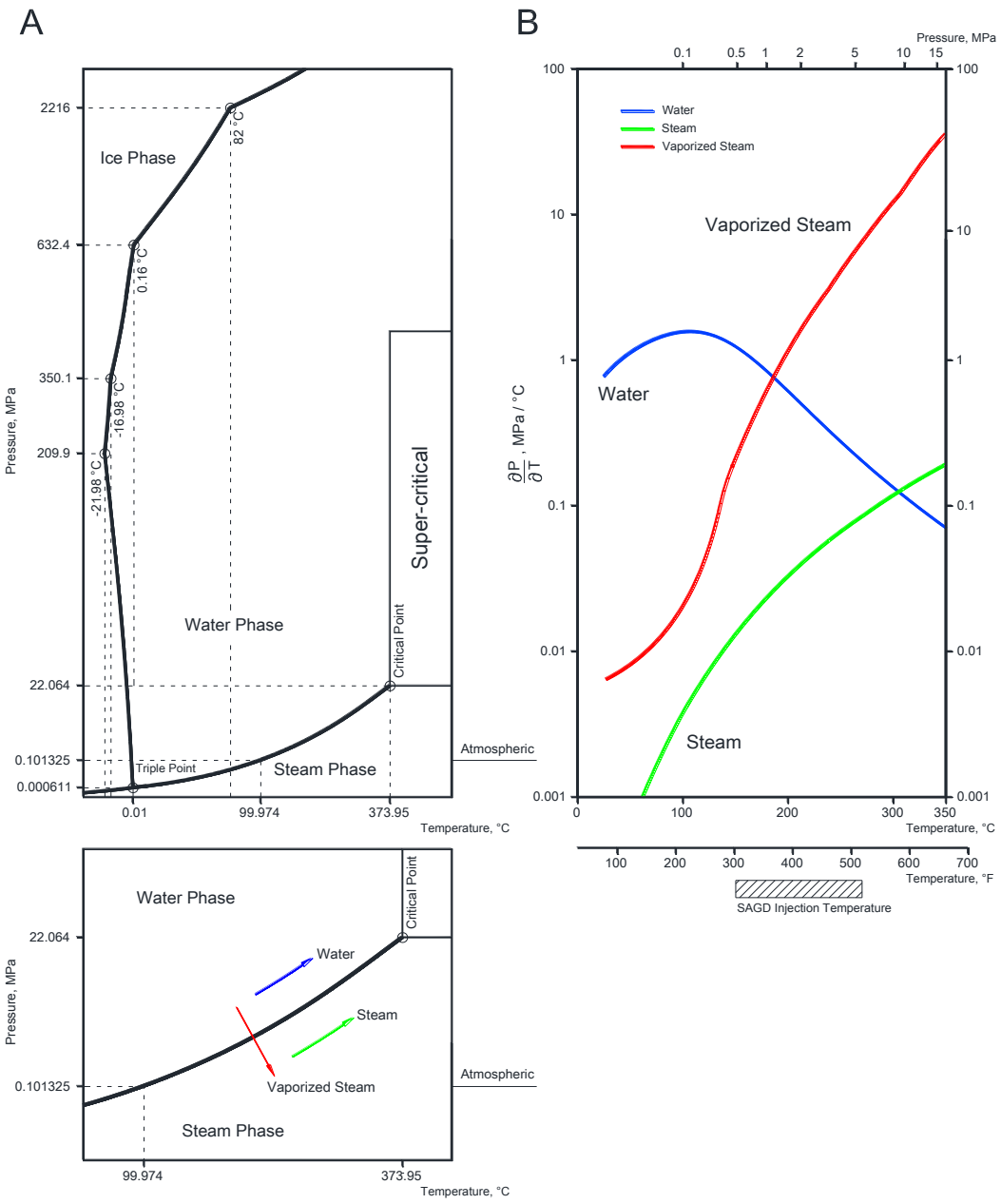

Figure 3.31. Illustration of phase boundaries for ice, water, and steam (modified from Sato et al., 1991) (Section A); and comparison of the incremental thermal pressurization of pure water, steam, and vaporized steam from pore water versus injection temperature and pressure (Section B); relevant phase regarding each curve is shown in magnified section in section A. See Table 3.4 and Table 3.5 for properties of fluid and caprock, respectively.

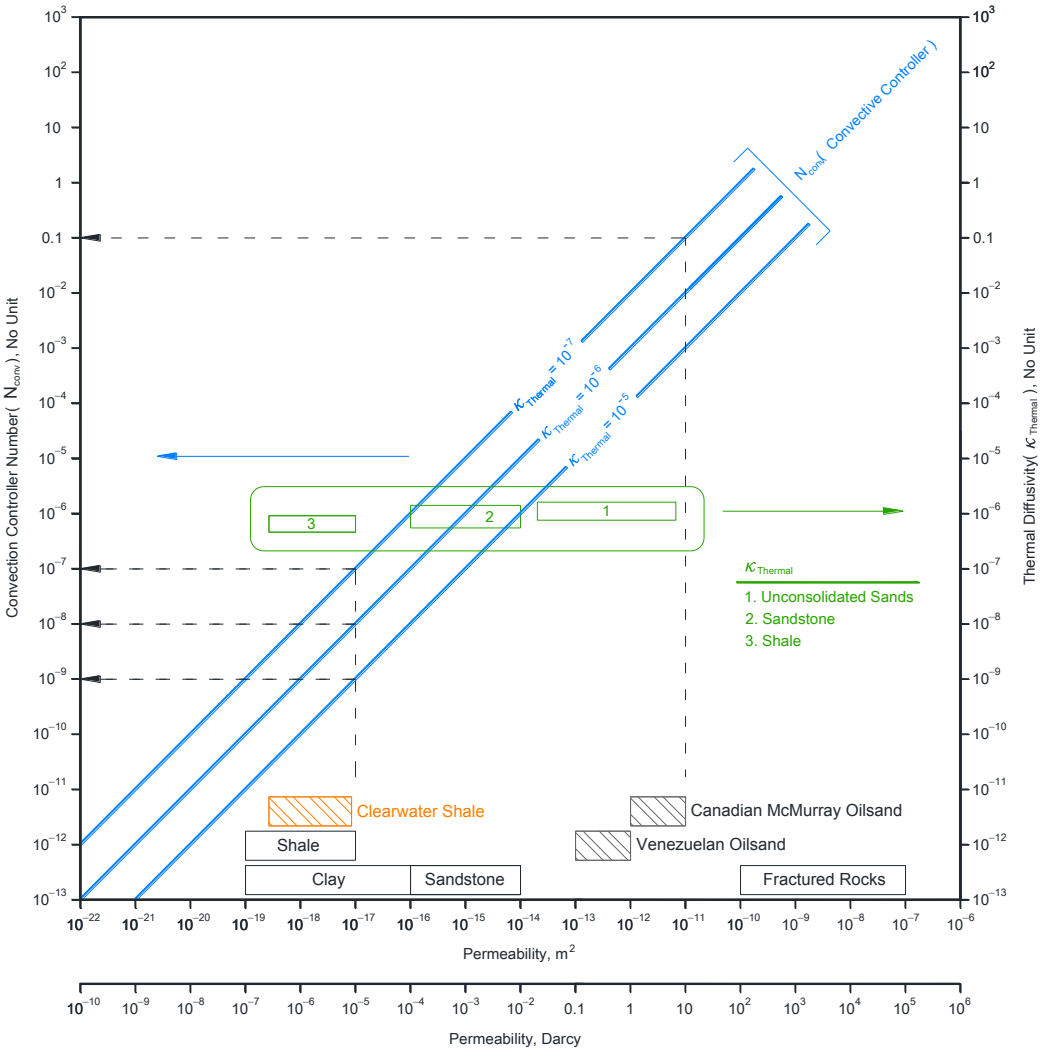

Figure 3.32. Variation of convection controller number (N_{conv}) versus formation permeability (k) for different thermal diffusivities ($\kappa_{Thermal}$) (Ref: Ghannadi et al., 2013)

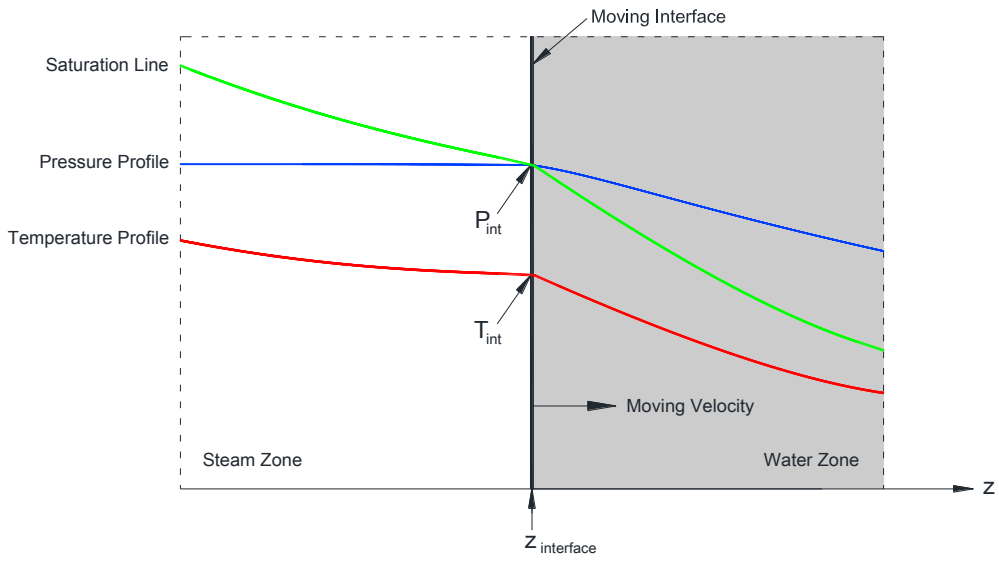

Figure 3.33. Configuration of steam interface and steam and water zones.

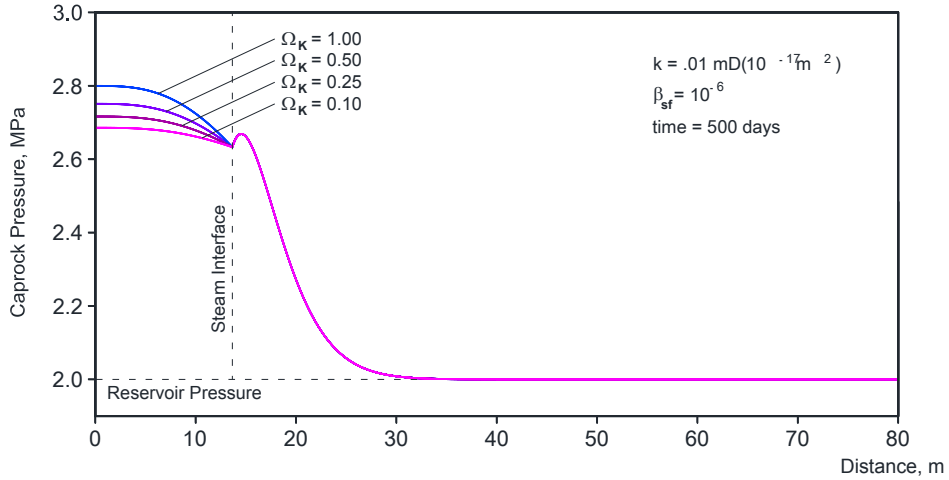

Figure 3.34. Comparison of thermal pressurization for different thermal conductivity coefficients ratios (Ω_K).

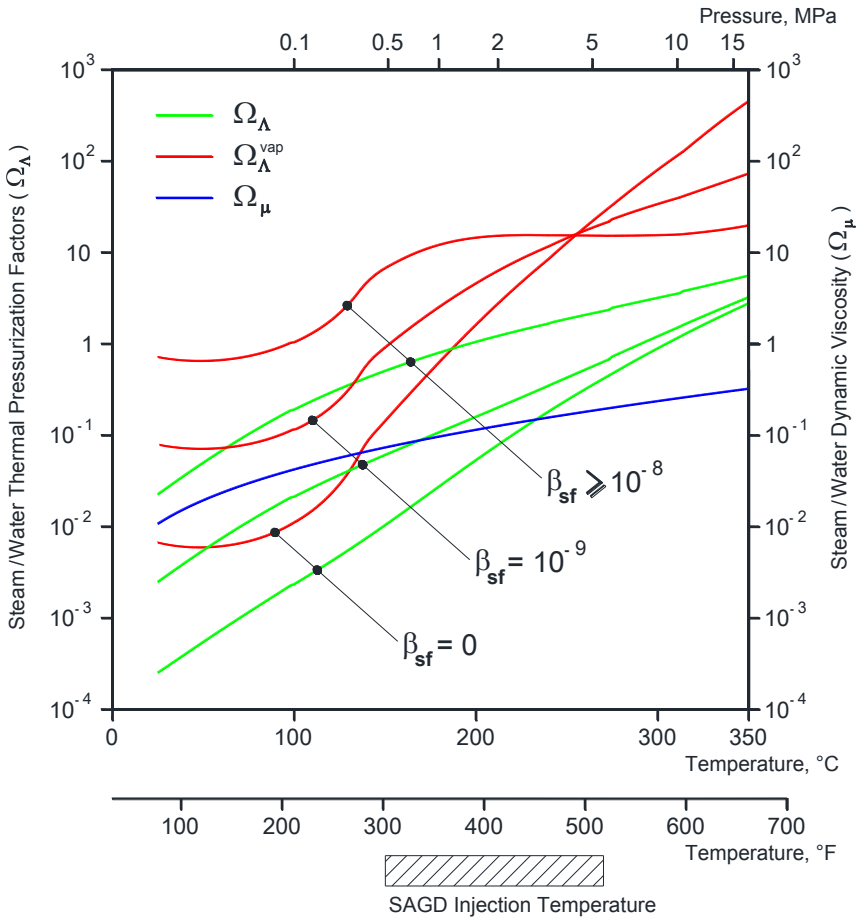

Figure 3.35. Comparison of ratios of different properties of water and steam used in two-phase (steam/water) solution. See Table 3.4 for water and steam properties.

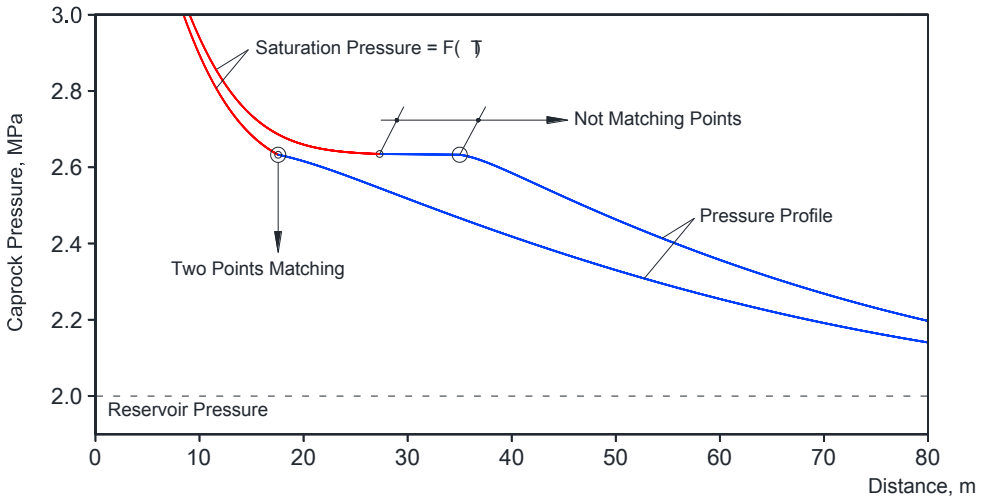

Figure 3.36. Suggested approach for calculation of steam interface location.

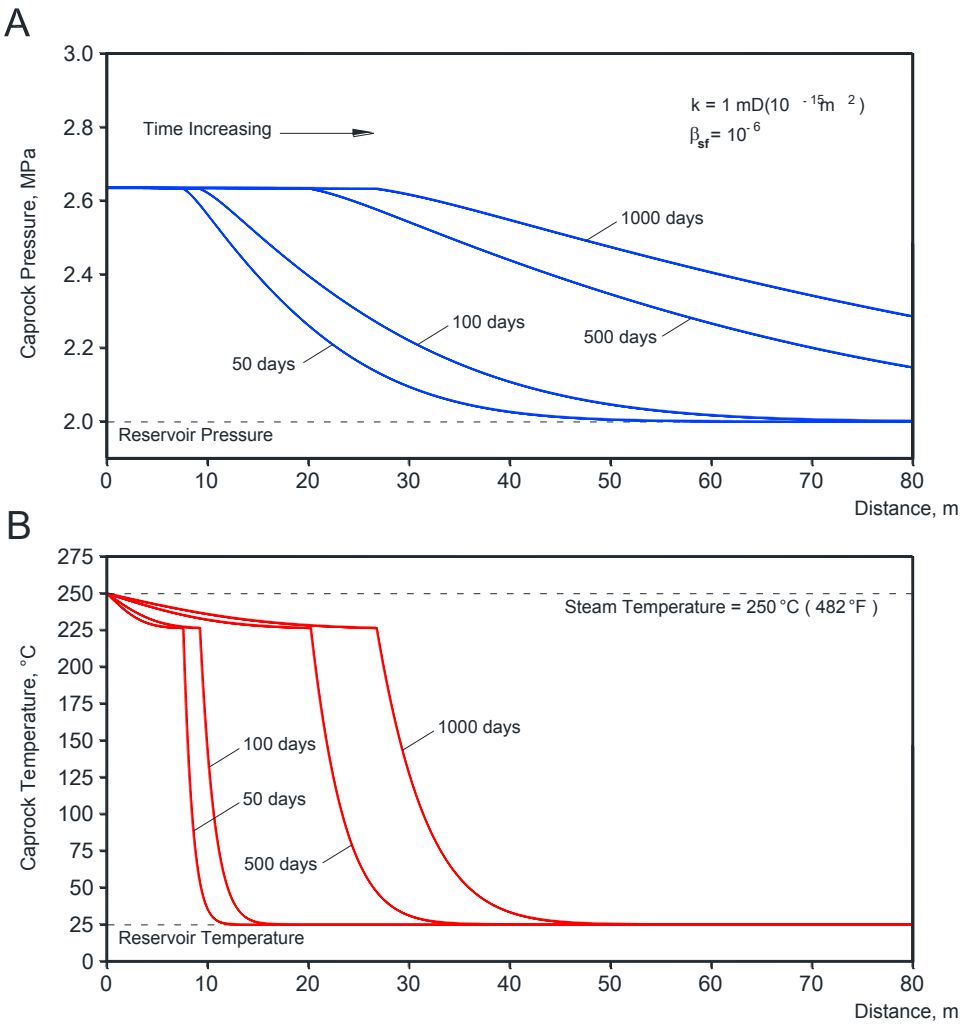

Figure 3.37. Caprock pressure (Section A) and temperature (Section B) progression in time.

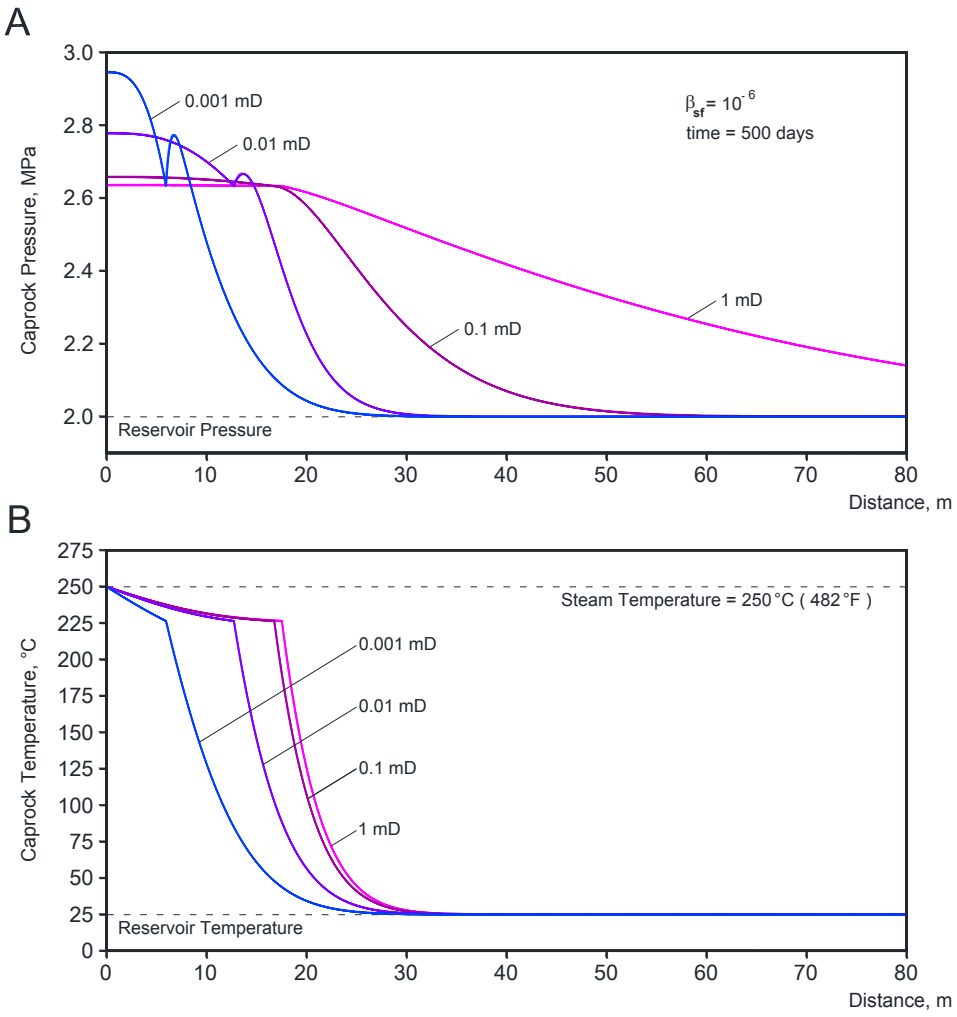

Figure 3.38. Pressure profile (Section A) and temperature profile (Section B) for different caprock permeabilities.

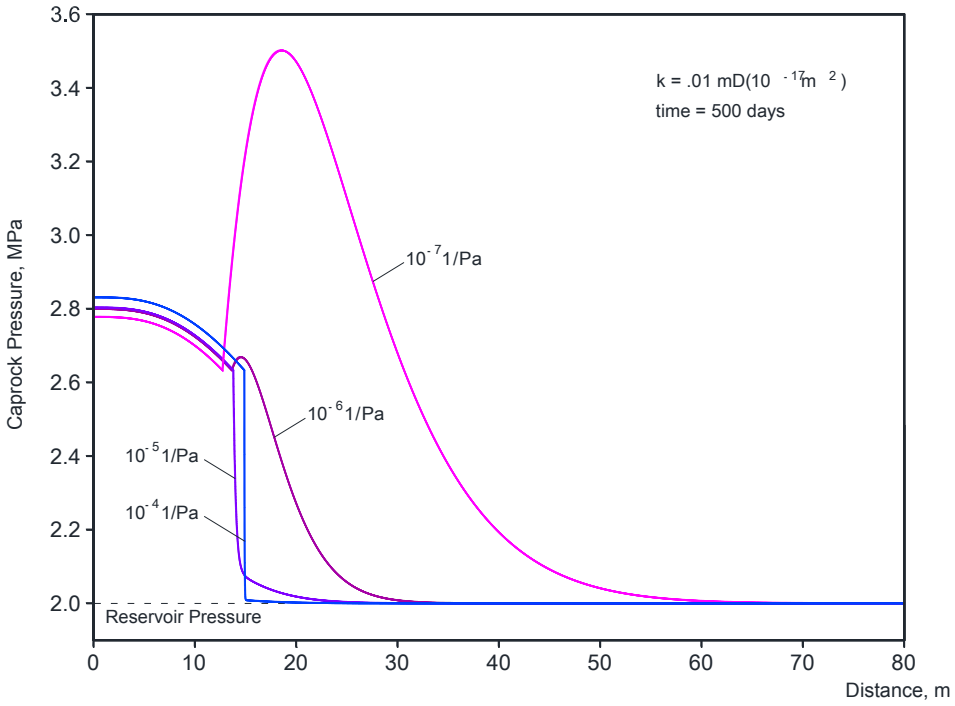

Figure 3.39. Pressure profile for different caprock compressibilities (or stiffnesses).

This page is intentionally left blank.

4. Thermal Pressurization in EM-SAGD Projects[5]

4.1. Introduction

Of Canada's 179 billion barrels of oil reserves, Alberta's oil sand contains 170.4 billion barrels of oil reserves (Government of Alberta, 2011, 2012), and with the recent increase in demand, tremendous efforts are being made to develop bitumen reservoirs in the coming decades. Steam-assisted gravity drainage (SAGD) is one successful thermal recovery technique applied to the oil sands of Alberta, Canada. Approximately 80% of the oil sands are recoverable through in-situ production (i.e., they lie at a depth of 75m to 750m with an average seam thickness of less than 20m), with only 20% recoverable by mining (i.e., they lie at a depth of 75m or less with an average seam thickness of 32m) (Government of Alberta, 2008; Vermeulen and Chute, 1983).

In SAGD, steam injected into a horizontal injection well is forced outward, losing its latent heat when it comes into contact with the cold bitumen at the edge of a depletion chamber. As a consequence, the viscosity of bitumen falls several orders of magnitude, and bitumen flows under gravity toward a horizontal production well located several metres below and parallel to the injection well (i.e., 5 metres, but drilling tolerances often leave variations between 3 and 7 metres). As the oil flows away and is produced, the steam chamber expands both upwards and sideways. A cross section of the SAGD process is displayed in Figure 1.1. Section A shows the circulation stage, Section B presents the early phase in which the chamber is not well developed, and Section C presents the mature steam chamber in the injection phase. Butler's steam-assisted gravity drainage (SAGD) method (Butler, 1998) has been a standard technique in Athabasca deposits bitumen recovery for the past 30 years. The technique has been commercialized and is considered both technically and economically successful. However, there are limitations with any technique, and those of SAGD include the requirement of high vertical permeability, and issues around caprock integrity for shallow formations and thin caprocks. In some locations, bitumen resources are located within 100m of the ground surface and have average caprock thicknesses of about 50m. The mining process is not economical for these reservoirs. As the thin caprock unit overlying the bitumen reservoir cannot withstand high steam pressure, steam injectability is dramatically reduced, impeding steam chamber progression. In such situations, electromagnetic steam-assisted gravity drainage (EM-SAGD) is an alternative. Siemens AG (Koolman et al., 2008) is working with industrial partners to test the technique, running an EM loop along the SAGD well pairs to electromagnetically heat and soften the bitumen. EM-SAGD can be useful for projects located in the very deep McMurray formation (where wellbore heat loss is significant and the quality of the steam reaching the formation is very low), in thin pay-zones (where heat loss to adjacent, non-oil-bearing formations may be significant), and in situations where steam injection may be environmentally unacceptable (such as through permafrost) or uneconomical (as on space-limited offshore platforms). It can also be useful in low-permeability reservoirs (where injected fluid may have difficulty penetrating deep into the reservoir) and in heterogeneous reservoirs (where high permeability streaks or fractures may cause early injected fluid breakthrough and reduce sweep) (Sahni et al., 2000).

4.2. Electromagnetic steam-assisted gravity drainage (EM-SAGD) technology

The major challenge for Alberta's oil industry today is to improve bitumen recovery and to reduce the steam-oil ratio in difficult geological media such as deep, heterogeneous sands and carbonates, and those with high shale content. There are also limitations on steam pressures due to low fracture gradients or low thief zone pressures, which limits steam temperatures and raises bitumen viscosities. Recovery can be improved through thermal, solvent injection, electrical and

[5] A version of this *chapter* has been published. Ghannadi, S., Irani, M. and Chalaturnyk, R., in SPEJ Journal, 19 (3): 443-462. SPE-156876-PA. (2014).

electromagnetic methods. Electromagnetic heating for in-situ production of bitumen reservoirs can be divided into three different groups: low-frequency heating (also called electrical heating[6], medium-frequency heating (i.e., inductive heating), and high-frequency heating (i.e., radio frequency and microwave heating) (Bogdanov et al., 2011 and Wacker et al., 2011). Electrical heating using low-frequency alternating current (either 50 or 60[7] Hertz, the urban and commercial power frequency) for the recovery of bitumen has been studied since the early 1970s (Chute et al., 1978; Vermeulen et al., 1979; Vermeulen and Chute, 1983, Hiebert et al., 1986; Vermeulen et al., 1988; McGee and Vermeulen, 2000; Vermeulen and McGee, 2000; McGee and Vermeulen, 2007). The technology has evolved as an additional technology to SAGD (McGee and Vermeulen, 2007). Down-hole resistive (or ohmic) heaters have also been proposed for heating near the well in heavy oil reservoirs to reduce the skin effect by near well viscosity reduction(Chute and Vermeulen, 1988; McGee et al., 1999), though this is not very efficient for bitumen reservoirs, and its depth of influence is very limited. Radio frequency (RF) electromagnetic stimulation has been proposed for heavy oil recovery heating in several studies (Abernethy, 1976; Islam et al., 1991; Sahni et al., 2000; Sayakhov et al., 2002; Carrizales et al. 2008; Davletbaev et al., 2011; Kovaleva et al., 2011). A number of field tests of bottom hole heating by radio frequency electromagnetic (RF-EM) radiation were carried out in Russia, the USA, and Canada (e.g., Kasevich et al., 1994; Spencer, 1987, 1989). These studies proved the efficiency of the radio frequency electromagnetic (RF-EM) process in heavy oil reservoirs. RF-EM has a short-range effect and this is the reason it is mostly referred as “RF-EM stimulation”. Although its application in bitumen deposits is questioned, few studies such as Davletbaev et al. (2010) proved its efficiency in bitumen deposits with low water cut values (i.e., water cut <30%). Davletbaev et al. (2010) suggest using RF-EM stimulation in heavy oil production wells on early field development stage, and convert RF-EM stimulation to electric heating in production wells when the water front from the injection wells reaches the production zones.

There are two main differences between electromagnetic inductive heating and radio frequency (RF) and microwave (MW) electromagnetic heating. Firstly, the frequency applied in inductive heating is three orders of magnitude smaller than that applied in the radio frequency heating and six orders of magnitude smaller than that applied in the microwave heating. In electromagnetic inductive heating a medium-frequency electric field in the range of 1 kHz to 200 kHz is applied (Wacker et al., 2011) although there are a few cases in which the electromagnetic coil is resonated and excited at frequencies as low as 60 Hz (Vermeulen and Chute, 1983). However, RF heating applies frequencies over the ranges 0.3 MHz to 300 MHz and MW heating applies frequencies greater than 300 MHz (Koolman et al., 2008), well above the inductive heating frequencies. Secondly, the physics of heating is quite different. In inductive heating (used in EM-SAGD), a large solenoidal coil, called the inductor, is placed horizontally within the payzone (representing the electrode in resistive heating). This inductor produces an alternative magnetic field in the reservoir. Eddy currents are generated in the reservoir by the electric field surrounding the inductive cable loop, and the eddy currents are directed opposite to compensate for the source magnetic field from the inductor (Koolman, et al., 2008). However, in radio frequency (RF) and microwave heating, since water molecules have both positive and negative poles (i.e., hydrogen has a positive pole and oxygen a negative pole), they tend to behave like microscopic magnets. As the positive half cycle of the microwave penetrates into the medium, it attracts the negative pole of the molecules. The microwave field attempts to align water molecules with this positive field of energy. Then, when the microwave alternates to the negative half cycle, the negative poles are repelled and the positive poles are attracted, causing a “flipping” motion. This agitation and flipping causes heat inside the medium, called “dipole friction of molecules” (Davletbaev et al., 2011), and the heating process is called “dielectric loss”.

[6] There are two main types of electrical heating: ohmic and resistive heating.

[7] Lower frequencies such as 0.1 Hz have also been applied to the electrodes in some cases (Vermeulen and Chute, 1983)

Electromagnetic steam-assisted gravity drainage (EM-SAGD) is an alternative method of steam injection that uses inductive heating and steam injection simultaneously (Sahni et al., 2000; Gunal and Islam, 2000). In EM-SAGD, a medium-frequency electric field is produced by a subsurface coil fed from a converter located on the surface. Eddy currents are generated in the reservoir by the electric field surrounding the inductive cable loop. The greater the conductivity in the reservoir, the greater the effect of inductive heating (Koolman, et al., 2008). As no contact is needed to generate the currents, neither brine injection (such as electrical resistive heating), nor well stimulation is necessary (Wacker et al., 2011). Also, due to deep electromagnetic penetration, no tight drilling pattern (such as that required for electrical resistive heating) is necessary.

As it was mentioned a medium range frequency is generally used for electromagnetic induction heating (Wacker et al., 2011), with low frequencies used in some specific cases (Vermeulen and Chute, 1983). The trade-off between medium-frequency electromagnetic induction heating and low-frequency electrical resistive heating is embedded in different dominant physics and oil sand properties. Since the electrical conductivity of oil sand formations increases as the square of the water content (i.e., $\sigma \approx 5 \times 10^{-4} w^2$ at room temperature, where w is the water content in weight percent), Athabascan oil sand, typically having a moisture content of 1 to 6 % (Vermeulen and Chute, 1983) permits currents to flow at 60 Hz[8] from one electrode to another in electrical resistive heating, even if they are several hundred metres apart. The penetration depth variation for resistive heating is presented in Section D of Figure 1.2. High-frequency electromagnetic waves are completely absorbed by such a formation within a very short distance (i.e., 1 to 5 metres for 10 MHz or 10 to 50 centimetres for 1 GHz, as illustrated in Section D of Figure 1.2 for oil sand reservoirs), and will not effectively heat the reservoir. In reservoirs with low water saturations (S_w), while electrical conductivity falls rapidly and resistive heating is nearly impossible to conduct, an electromagnetic wave can propagate over much larger distances and can be effectively conducted (Vermeulen and Chute, 1983).

EM-SAGD can be useful for projects located very deep in the McMurray formation (where wellbore heat loss is significant and the quality of steam reaching the formation is very low), in thin pay-zones (where heat losses to adjacent, non-oil-bearing formations may be significant), and where injecting steam may be environmentally unacceptable (such as through permafrost) or uneconomical (as on space-limited offshore platforms). It can also be useful in low-permeability reservoirs (where injected fluid may have difficulty penetrating deep into the reservoir) and in heterogeneous reservoirs (where high-permeability streaks or fractures may cause early injected fluid breakthrough and reduce sweep) (Sahni et al., 2000). The inductive method has been found to be the most technically and economically feasible for sites with overburdens of more than 30m (Koolman et al., 2008). However, in EM-SAGD projects, the caprock overlying the oil sand reservoirs is electromagnetically heated. Since permeability is low in shale formations, the potential exists for water to boil causing pore pressures to dramatically increase as a result of the phase change in the water (i.e., from water to steam). This could lead to shear failure of the formation, and the creation of micro cracks and inadvertent hydraulic fractures, which result in caprock integrity failure.

4.3. Caprock integrity in SAGD and EM-SAGD projects

Although SAGD has become a popular alternative to classical in-situ bitumen recovery methods such as fracture-assisted cyclic steam stimulation (FCSS) and cyclic steam stimulation (CSS), challenges remain in its implementation. These include maintaining caprock integrity in SAGD operations, where potential steam releases to surface may result; formation shearing, which may result in injection or production casing failure and well abandonment; and reservoir

[8] 60 Hz is the common frequency of resistive heating in North America, since it is the continent's base frequency for alternating current

deformations causing surface deformations such as heaving (Collins, 2005, 2007; Dusseault and Collins, 2008a, 2008b).

Caprock integrity assessments have become key in the design and operation of SAGD projects, and a critical element in the selection of a maximum steam injection operating pressure. Caprock integrity is concerned with hydraulic integrity and mechanical integrity. Hydraulic integrity refers to the existence of a hydraulic barrier for reservoir fluids preventing hydrocarbons from migrating upwards through the caprock to shallow groundwater aquifers or the ground surface. Mechanical integrity refers to caprock formation failure, which can endanger future infill drilling or cause surface heave (i.e., that is a reflect of considerable deformations in the caprock) (Yuan et al., 2011a). Caprock integrity is the subject of many studies following the catastrophic failure of the caprock seal at the Joslyn Creek SAGD project on May 18, 2006 (Total E&P Canada Ltd., 2007; Uwiera-Gartner et al., 2011a, 2011b; Yuan et al., 2011a, 2011b). As a result of this failure, Alberta's Energy Resources Conservation Board (ERCB) modified the existing application guidelines and directives (e.g., Directive 051) to include an assessment of caprock integrity. Caprock assessments conducted to date have incorporated varying levels of detail and complexity in each of the major elements of the study, but no studies have focussed on induced thermal-pressurization and more specifically that caused by electromagnetic heating in EM-SAGD projects.

While there are many aspects of caprock integrity, shear slip failure between caprock and reservoir is not discussed in ERCB directives, though it has been the topic of a few studies (e.g., Talebi et al., 1998; Dusseault et al., 2001; Smith et al., 2002; Wong and Chau, 2004) mostly focused on CSS projects. Talebi et al. (1998) reported a well-casing failure due to caprock slip at the level of the Colorado Shale formation in a CSS project at the Cold Lake deposit. Some 250 wells have failed at the Cold Lake heavy-oil field near the base of the Colorado Shale, and at the top of the producing reservoir (Dusseault et al., 2001). Dusseault et al. (2001) attributed these shear failures to localized shear displacements on weak bedding planes because of cyclic reservoir heave and compaction, in turn due to pressure and thermally-induced expansion and contraction of the oil sands. Wong and Chau (2004) also mentioned a possibility of local slips of up to 12 cm along a large discontinuity of low shear resistance (such as a clay seam or fracture) in steam projects. Smith et al. (2002) evaluated the slips causing casing failures for a high percentage of failed wells (> 88%) in the Clearwater bitumen zone top in the Cold Lake field.

Although many researchers are attributing the slip failure to lateral shear in the production zone, which results in horizontal displacements (AEUB Decision 99-22), the induced pore pressure effect should not be neglected. Elevated pore pressures may weaken the caprock formation locally and cause localized plastic deformation or rapid fracture initiation. The pore pressure effect is more pronounced in the case of EM-SAGD, since heat generated from eddy currents in electromagnetic heating is independent of shale thermal conductivity and may warm up the highly resistive formation locally. Also, in low water saturated formations, water can be driven off by heating above the steam point (Vermeulen and Chute, 1983), with the resulting phase change causing the pore pressure to increase dramatically, potentially well above fracture pressures.

Assessing both hydraulic and mechanical risks to caprock integrity and the risk of shear slip failure present a significant challenge to oil and gas industry engineers dealing with both standard SAGD and EM-SAGD projects. This study addresses these issues as one of "thermal pressurization"; or commonly known as "thermo-hydro-mechanical pressurization"; in caprock. Simply thermal pressurization is overpressure of the pore fluids due to thermal expansion, which either quickly dissipates (in high-permeability shales) or accumulates (in low-permeability shales). It happens when the thermal expansion of pore fluids exceeds that of the pore space. In this case, the pore space stiffness tried to act against the expansion of the pore fluid volume, and compressed the fluid by increasing pore pressure to minimize its increase in volume. The subsequent increase in pore pressure results in a reduction of effective stress. At low confining pressures, the shear strength of rock drops significantly due to effective stress reduction (Handing and Hager, 1957), which may lead to inadvertent hydraulic fracturing within the

reservoir (Khan et al., 2010, 2011). In severe scenarios, an effective stress reduction to zero may result in liquefaction or a complete loss of shear strength. In general, thermal pressurization partially reduces caprock shear strength and makes it more prone to fail against shear stresses developed by the SAGD operation. The thermal pressurization may also induce tensile failure, but in this study we focus on failures (i.e., shear failure), which result from reductions in effective stress due to elevated pore pressures.

Model and Mathematical Description

Thermal pressurization is a function of many parameters. The ratio of thermal diffusivity to hydraulic diffusivity ranges from 0.1 (in high-permeability shale) to 100 (in low-permeability shale) (Bois and Mainguy, 2011), causing the variation of induced thermal pressure for the same thermal loading. It also depends on drainage conditions governed by reservoir and overburden permeability. This can impact the pressure build-up in shales (Bois and Mainguy, 2011) by reducing fluid dissipation. In the present analysis, thermal pressurization is evaluated parametrically in closed-form solution, providing an efficient method to evaluate and design against catastrophic failures caused by thermal pressurization.

In this section, the different physics of thermal pressurization in EM-SAGD applications are presented via the simplified geometry of a high-resistivity caprock in Figure 1.4 and the accompanying physics.

4.4. Electromagnetic Heating Governing Equations

Electromagnetic induction heating, or simply "induction heating", is a method of electrical heating using moderate frequency alternating current and conductive materials such as metals. This technology dates back to 1831 (Zinn and Semiatin, 1988), when Michael Faraday wound two coils of wire onto an iron ring and noted that an alternating current passed through one of them induced a voltage in the other. Its practical application in electromagnetic ovens and in melting high-quality steels and nonferrous alloys (e.g., aluminium and copper alloys) was realized in the late 1900s (Zinn and Semiatin, 1988). Currently, this method is being contemplated for use in the in situ recovery of bitumen either individually or in conjunction with conventional SAGD operations.

The mathematical analysis of inductive heating can be quite complex, even for the simplest geometries. Several studies have investigated heat transfer in heavy oil reservoirs stimulated with RF-EM radiation or microwave electromagnetic, and present closed-form solutions for heat transfer for this problem (Abernethy, 1976; Sahni et al., 2000; Ovalles et al. 2002; Davletbaev et al. 2008, 2009, 2011). However, there are many studies focused on RF-EM and microwave heating, to date, there are few research presenting the heat transfer equations for inductive heating in oil reservoirs.

From a physical viewpoint, inductive heating is based on the Joule effect of the eddy currents' induced alternating electromagnetic induction. The conducting path for the eddy currents is through the continuous connate water surrounding the nonconductive sand particles. Electrical energy in the eddy currents is converted into heat along these pathways because of the electrical resistivity of the connate water, which containing a large number of ions resulting from dissolved salts. The heat is transferred to the oil and the sand particles by conduction. The temperature increases over time in the reservoir volume because of this heat generation. Energy transferred from a source to a magnetic material through electromagnetic induction is described as (Barranger, 1965):

$$W = \int_{t_1}^{t_2} \int_{V} \left\{ \nabla \cdot \left[\vec{E}(t) \times \vec{H}(t) \right] \right\} dV dt \qquad 187$$

where $\vec{E}(t)$ is the electric field (or potential field) measured in Newtons per Coulomb (N/C) or Volts per metre (V/m), and $\vec{H}(t)$ is magnetic field intensity (or magnetic field strength) measured in Amperes per metre (A/m). The divergence of $\vec{E}(t)\times\vec{H}(t)$ (the Poynting vector), is extended as (Barranger, 1965):

$$\nabla\cdot\left[\vec{E}(t)\times\vec{H}(t)\right]=\vec{H}(t)\cdot\left[\nabla\times\vec{E}(t)\right]-\vec{E}(t)\cdot\left[\nabla\times\vec{H}(t)\right] \qquad 188$$

If the volume distribution of a magnetic field is completely surrounded by a closed Gaussian surface (S) (i.e., the closed volume), "Divergence Theorem" (also called "Gauss's Theorem") can be applied and volume integral on the left-hand side of Equation 188 can be changed to surface integral (Spiegel et al., 2009):

$$W=\int_{t_1}^{t_2}\int_{V}\left\{\nabla\cdot\left[\vec{E}(t)\times\vec{H}(t)\right]\right\}dVdt=\int_{t_1}^{t_2}\int_{S}\left\{\vec{E}(t)\times\vec{H}(t)\right\}d\vec{S}dt \qquad 189$$

Any change in the magnetic environment of a coil of wire will cause voltage to be induced in the coil, and reciprocally, any change in the potential field of the coil will produce a magnetic field. This phenomenon is presented in Faraday's law (pages 243 and 366 of *Popović and Popović,* 2000):

$$\nabla\times\vec{E}(t)=-\frac{\partial\vec{B}(t)}{\partial t} \qquad 190$$

where $\vec{B}(t)$ is magnetic flux density (or magnetic induction) measured in Teslas (T) in SI units. The magnetic field intensity around an electrical current is proportional to the electrical current that serves as its source. This phenomenon is presented in Ampere's law (page 214 of *Popović and Popović,* 2000):

$$\nabla\times\vec{H}(t)=\vec{J}(t) \qquad 191$$

where $\vec{J}(t)$ is conduction current density (or current per unit area) measured in Amperes per square metre (A/m^2) in SI units. Maxwell proposed that Ampere's law could be made correctly for all applications if it was modified to include this new term. The new form of Ampere's law is consistent with the continuity equation and with the differential form of Gauss's law:

$$\nabla\times\vec{H}(t)=\underbrace{\vec{J}(t)}_{\text{ConductionCurrent}}+\underbrace{\partial\vec{D}(t)/\partial t}_{\text{Displacement Current}} \qquad 192$$

where $\vec{D}(t)$ is electrical flux density. Maxwell defined a new term, "displacement current", in contrast with the term (J), known as "conduction current". He stated that Ampere's law is correct when the sum of the conduction and displacement current is included (Zahn, M., 1979; Voltmer, 2007). Overall, the mechanism for the power flow can be described by substituting Equations 190 and 192 in Equation 188:

$$\vec{H}(t)\cdot\left[\nabla\times\vec{E}(t)\right]-\vec{E}(t)\cdot\left[\nabla\times\vec{H}(t)\right]=-\vec{H}(t)\cdot\frac{\partial\vec{B}(t)}{\partial t}-\vec{E}(t)\cdot\vec{J}(t)-\vec{E}(t)\cdot\frac{\partial\vec{D}(t)}{\partial t} \qquad 193$$

Knowing the two following linear relations (Popović and Popović, 2000[9]):

$$\vec{D}(t) = \varepsilon_0 \varepsilon_r \vec{E}(t) \quad 194$$

$$\vec{B}(t) = \mu_0 \mu_r \vec{H}(t) \quad 195$$

where ε_0 is a constant called permittivity of free space or vacuum (i.e., 8.8542×10^{-12} F/m (or Farads per metre)); ε_r is relative permittivity (or dielectric constant) (no unit); μ_0 is a constant showing the permeability (or magnetic permeability) of free space or vacuum (i.e., $4\pi \times 10^{-7} \approx 1.2566 \times 10^{-6}$ H/m (or Wb/A•m)); and μ_r is relative magnetic permeability (no unit). With derivatives, the two terms on the right-hand side of Equation 193 can be simplified as (Zahn, M., 1979; Rudnev et al., 2003):

$$\vec{E}(t) \cdot \frac{\partial \vec{D}(t)}{\partial t} = \vec{E}(t) \cdot \frac{\varepsilon_0 \varepsilon_r \partial \vec{E}(t)}{\partial t} = \frac{\varepsilon_0 \varepsilon_r}{2} \frac{\partial \left[\vec{E}(t) \cdot \vec{E}(t) \right]}{\partial t} = \frac{\varepsilon_0 \varepsilon_r}{2} \frac{\partial \left| \vec{E}(t) \right|^2}{\partial t} = \frac{\partial W_{\text{Displacement Current}}}{\partial t} \quad 196$$

and

$$\vec{H}(t) \cdot \frac{\partial \vec{B}(t)}{\partial t} = \vec{H}(t) \cdot \frac{\mu_0 \mu_r \partial \vec{H}(t)}{\partial t} = \frac{\mu_0 \mu_r}{2} \frac{\partial \left[\vec{H}(t) \cdot \vec{H}(t) \right]}{\partial t} = \frac{\mu_0 \mu_r}{2} \frac{\partial \left| \vec{H}(t) \right|^2}{\partial t} = \frac{\partial W_{\text{Hysteresis}}}{\partial t} \quad 197$$

A common approximation to the electric field (or potential) relation with current density assumes that the current is simply proportional to the electric field, expressed by Ohm's law (Barranger, 1965):

$$\vec{E}(t) = \frac{\vec{J}(t)}{\sigma} = \rho \vec{J}(t) \quad 198$$

where ρ is electrical resistivity, and σ is electrical conductivity. Conductivity (σ) is the inverse of resistivity (ρ), and is measured in Siemens per metre (S/m) in SI units. Substituting Equations 196, 197, and 198 in Equation 193 yields:

$$W = \int_V \left\{ \frac{\partial W_{\text{Hysteresis}}}{\partial t} + \underbrace{\int_{t_1}^{t_2} \frac{J^2(t)}{\sigma} dt}_{\text{Eddy Current}} + \frac{\partial W_{\text{Displacement Current}}}{\partial t} \right\} dV = W_{\text{Hysteresis}} + W_{\text{Eddy Current}} + W_{\text{Displacement Current}} \quad 199$$

where $W_{\text{Hysteresis}}$, $W_{\text{Eddy Current}}$, and $W_{\text{Displacement Current}}$ are hysteresis loss, eddy current loss and displacement current loss, respectively.

"Hysteresis loss" is caused by the alternating magnetic field flux, which causes the dipoles of the material to oscillate as the magnetic poles change their polar orientation in every cycle (see Figure 4.43A). A minor amount of heat is produced by the friction of each oscillation (McMaster, 1976; Haimbaugh, 2001). The magnetization curves below the Curie temperature for ferromagnetic materials such as steel can appear as two different cases of friction loss. Hysteresis loss is proportional to the area enclosed by the hysteresis loop (see Figure 4.43B). Narrow loops greatly reduce this loss:

[9] Page 91 and 213 of Introductory Electromagnetics, 1st Edition.

$$W_{Hysteresis} = \int_V \left\{ \underbrace{\int_{B_1}^{B_2} (H dB)}_{Hysteresis} \right\} dV \quad 200$$

In non-magnetic materials such as oil sand and Clearwater Shale, no reversal of dipoles can appear. As a result, the friction loss is zero (McMaster, 1976; Haimbaugh, 2001), and the hysteresis term is neglected.

Each of the other two terms, $W_{Eddy\ Current}$ and $W_{Displacement\ Current}$, can be a dominating factor for different frequencies. Alternating current (AC) flowing through the coil generates an alternating magnetic field that cuts through the reservoir, and the so-called eddy currents dissipate energy and cause heat in a phenomenon called "eddy current loss". This loss only propagated in a conductive medium. However, there is another loss which is called "displacement loss," which propagates in both conducting and non-conducting mediums. Both losses need alternating current (AC), and if direct current (DC) is passed through a solenoid coil, the resulting field will not produce any heat inside the reservoir. Displacement loss is caused by displacement current, and eddy current loss is caused by conductive current. The new form of Ampere's law presented in Equation 192 is rewritten as:

$$\nabla \times \vec{H} = \vec{J}_c + \vec{J}_d \quad 201$$

where $\vec{J}_c$ is conductive current and $\vec{J}_d$ is displacement current:

$$\vec{J}_d = \frac{\partial \vec{D}}{\partial t} \quad 202$$

Displacement current allows electromagnetic waves to propagate in non-conducting mediums, while conduction current only propagates in conducting mediums. If a conducting medium is characterized by conductivity of σ and permittivity of $\varepsilon_0\varepsilon_r$, then the conduction current density is given by Ohm's law:

$$\vec{J}_c = \sigma \vec{E} \quad 203$$

and the displacement current density is given by:

$$\vec{J}_d = \varepsilon_0\varepsilon_r \frac{\partial \vec{E}}{\partial t} \quad 204$$

Assume that the electric field is a sinusoidal function of time, which is the valid assumption for AC:

$$E = E_0 \cos\omega t \quad 205$$

Substituting Equation 205 in Equations 203 and 204 allows the calculation of conduction current and displacement current, respectively, as follows:

$$J_c = \sigma E_0 \cos\omega t \quad 206$$

$$J_d = -\omega\varepsilon_0\varepsilon_r E_0 \sin\omega t \quad 207$$

Then the maximum conduction current and displacement current are calculated, respectively, as:

$$\left|J_c\right|_{max} = \sigma E_0 \quad 208$$

$$\left|J_d\right|_{max} = \omega \varepsilon_0 \varepsilon_r E_0 \quad 209$$

And finally, the conduction to displacement current ratio is calculated as:

$$\frac{\left|J_c\right|_{max}}{\left|J_d\right|_{max}} = \frac{\sigma}{\omega \varepsilon_0 \varepsilon_r} \quad 210$$

The ratio of conduction current to displacement current for oil sand reservoirs with different water content is presented in Section C in Figure 1.2,. As shown, this ratio for frequencies lower than 100 kHz (i.e., in the range of inductive heating such as EM-SAGD) is in the range of 100 to 1000. This shows the dominance of conductive current over displacement current, and that of eddy current loss over displacement loss. In contradiction to inductive heating, in high frequencies such as RF and microwave heating, displacement current or electrical polarization effect is the main heating component, and conduction current or eddy current loss should be neglected (Figure 1.2, Section C). Overall, eddy current loss is considered the basic component of an induction heating (or EM-SAGD) application. And for induction heating both hysteresis loss and displacement current loss are neglected.

The "eddy current loss" is also referred as the "skin effect" because the eddy currents are concentrated on the outside of a conductor. It should be noted that these induced eddy currents in reservoirs run opposite to the source current of the inductor. Eddy currents induced in the reservoir diminish towards the further points. Their density inside a reservoir at a distance r from the inductor is roughly calculated by the following equation (Popović and Popović, 2000[10]):

$$J_r = J_0 \exp\left(-\frac{(r - r_{coil})}{\delta}\right) \quad 211$$

where J_r is the current density at distance r from the inductor (A/m^2), J_0 is the current density at the inductor surface (A/m^2), r is the distance from the inductor to the core (m), r_{coil} is the mean radius of the coil turns (m), and δ is the penetration depth (m). The "penetration depth" or "skin depth" (δ) is the depth at which the field strength decreases to e^{-1} (i.e., exp(-1) = 0.37) of its value at the surface. That is the thickness of the layer in which 87% (i.e., 1- [exp(-1)]^2 = 0.87) of the power is developed. The penetration depth (δ) is defined as (Popović and Popović, 2000[5]; Wacker et al., 2011):

$$\delta = \sqrt{\frac{2\rho}{\omega \mu_0 \mu_r}} = \sqrt{\frac{2}{\omega \mu_0 \mu_r \sigma}} \quad 212$$

where ω is the angular frequency of the current (i.e., $2\pi \times$ frequency). In frequency format, this is changed to:

$$\delta = \sqrt{\frac{\rho}{\pi \mu_0 \mu_r f_s}} = \sqrt{\frac{1}{\pi \mu_0 \mu_r f_s \sigma}} \quad 213$$

[10] Page 385 of Introductory Electromagnetics, 1st Edition.

where ρ is the electrical resistivity of the reservoir formation (Ωm); σ is the conductivity (A/m^2); and f_s is the switching frequency (Hz) or cycle per second. The penetration depth is described in metres as:

$$\delta = 503\sqrt{\frac{\rho}{\mu_r f_s}} = 503\sqrt{\frac{1}{\mu_r f_s \sigma}} \qquad 214$$

As seen, the penetration depth of the electromagnetic field depends upon the frequency applied, the current in the coil loop, and the conductivity of the formation surrounding the inductor. The variation of the penetration depth is illustrated in Section D of Figure 1.2 for different applied frequencies and oil sand reservoir conductivity variation. Typical oil sand may have a specific resistivity of 100 to 1000 Ωm (or electrical conductivity of 0.01 to 0.001 S/m) (Wacker et al., 2011). Since the conductivity in the reservoir is due to ions dissolved in formation water, in specific cases it can differ severely from the ranges above. Conductivity is a function of temperature, moisture content, and stress. Vermeulen and Chute (1983) suggested that electrical conductivity variation will follow the following equation for frequencies ranging from 100 Hz to 1 GHz:

$$\sigma = \sigma_{24^\circ C}\left[1 + 2.24\times 10^{-2}(T - 24^\circ C)\right] \qquad 215$$

where T is the temperature in degrees Celsius. In other research, Vermeulen and Chute (1983) expressed electrical conductivity at room temperature and a given moisture content as:

$$\sigma \cong 5\times 10^{-4} w^2 \qquad 216$$

where w is the moisture content in weight percent. Figure 2.7 shows small variations in the penetration depth of the electromagnetic field due to changes in both temperature (see Section A) and water content (see Section B). There are many studies evaluating the effect of stress on conductivity (e.g., Brace and Orange, 1968). In laboratory experiments, Brace and Orange (1966, 1968) observed that when water-saturated crystalline rocks were stressed to fracture, electrical conductivity increased by as much as an order of magnitude. While they did not suggest an empirical equation, it is expected that in EM-SAGD applications, penetration depth will be reduced over time as more fracturing appears in reservoir formations due to increases in temperature and pressure.

The following is a more general expression for penetration depth, which is more exact in the case of poor conductors (non-metals) at high frequencies (page 130 of *Jordan and Balmain, 1968*):

$$\delta = \frac{1}{\omega}\left\{\left(\frac{\mu_0\mu_r\varepsilon_0\varepsilon_r}{2}\right)\left[\sqrt{1+\left(\frac{\sigma}{\omega\varepsilon_0\varepsilon_r}\right)^2} - 1\right]\right\}^{-1/2} \qquad 217$$

This formula can be rearranged as follows to reveal departures from the common penetration depth formula (Equation 212):

$$\delta = \sqrt{\frac{2\rho}{\omega\mu_0\mu_r}}\sqrt{\sqrt{1+(\omega\rho\varepsilon_0\varepsilon_r)^2} + \omega\rho\varepsilon_0\varepsilon_r} \ll 1/\rho\varepsilon_0\varepsilon_r \quad \text{or} \quad 1 \ll \sigma/\omega\varepsilon_0\varepsilon_r \text{ (see Figure 3, Section C)} \qquad 218$$

At frequencies much below $1/\rho\varepsilon_0\varepsilon_r$, the quantity inside the radical is close to unity and Equation 212 is valid. For example, Equation 212 is valid in copper for frequencies lower than 10^{19} Hz[11], but it should be lower than 10^8 Hz[12] in oil sand reservoirs. Since EM-SAGD deals with frequencies in the range of 10^3 to 10^5 Hz, Equation 212 is easily used. However, in very poor conductors such as oil sand and Clearwater shale and at very high frequencies as experienced in RF-EM applications, the factor on the right increases and the following formula can be used:

$$\delta \approx 2\rho\sqrt{\frac{\varepsilon_0\varepsilon_r}{\mu_0\mu_r}} \qquad \omega >> 1/\rho\varepsilon_0\varepsilon_r \quad \text{or} \quad 1 >> \sigma/\omega\varepsilon_0\varepsilon_r \,(\text{see Figure4.36c}) \tag{219}$$

At very high frequencies (i.e., RF-EM application), penetration depth is independent of applied frequency. The simplest method to evaluate formation resistivity is to use an induction log, which is one of the common logs in reservoir evaluation. The calculated penetration depth based on Equation 214 is presented in Figure 1.2 for a medium-frequency electric field range and common oil reservoirs range. The Athabascan oil sand reservoir shown in Figure 1.2 allows penetration in the range of 10 to 100 metres - the greater the frequency, the lesser the skin depth. EM-SAGD is plausible for larger skin depths, as this is correlated with improved induced current and inductive heating.

To calculate eddy current loss, Faraday's line integral is applied around the path of the inductor (see Figure B-1, Section A):

$$\oint \vec{E}(t)\cdot dl = -\frac{d\Phi(t)}{dt} \tag{220}$$

where $\Phi(t)$ is the total flux within the inductor (circle O in Figure B-1, Section A). Multiplying both sides by conductivity (σ) and using Ohm's law (Equation 198) yields:

$$\oint \vec{J}_0(t)\cdot dl = -\sigma\frac{d\Phi(t)}{dt} \tag{221}$$

The length around the inductor is $2\pi r_{coil}$. The current density around the inductor is in complex form:

$$J_0 = \frac{j\omega\sigma\Phi}{2\pi r_{coil}} \tag{222}$$

The absolute value is:

$$|J_0| = \frac{\omega\sigma|\Phi|}{2\pi r_{coil}} \tag{223}$$

Total EM power radiated across the radius r is calculated by integrating Equation 199 and substituting Equation 223:

[11] Assuming $\omega < 0.1/\rho\varepsilon_0\varepsilon_r$ and copper electrical resistivity and relative permittivity are 1.72×10^{-8} S/m, 2.51, respectively.

[12] Assuming $\omega < 0.1/\rho\varepsilon_0\varepsilon_r$ and oil sands electrical resistivity and relative permittivity are 1000 S/m, 3, respectively.

$$P_{EM} = \int_V \left(\frac{1}{T} \int_0^T W_{Eddy\,Current}\, dt \right) dV = \int_V \left(\frac{1}{T} \int_0^T \frac{J_r^{\,2} \sin^2(\omega t)}{\sigma}\, dt \right) dV$$
$$= \int_V \left(\frac{1}{T} \times \frac{J_r^{\,2}}{\sigma} \int_0^T \frac{1-\cos(2\omega t)}{2}\, dt \right) dV = \int_V \left(\frac{1}{T} \times \frac{J_r^{\,2}}{\sigma} \times \frac{T}{2} \right) dV = \int_V \left(\frac{J_r^{\,2}}{2\sigma} \right) dV \quad (224)$$

where T is the switching period. If a direct current is passed through a thin solenoid coil, the resulting magnetic flux is identified using Ampere's law (see Appendix A):

$$|\Phi| = \mu_0\, \mu_r^{core}\, \wp_{coil} \left[\pi (r_{coil})^2 \right] \frac{N}{l_{coil}} \times \cot(\eta) = \mu_0\, \mu_r^{core}\, \wp_{coil} \left[\pi (r_{coil})^2 \right] \bar{n} \times \cot(\eta) \quad (225)$$

where N is the number of coil turns, μ_r^{core} is the magnetic permeability of the coil's core, which can be as large as 6000 for ferromagnetic cores such as steel, l_{coil} is the coil length, $\wp_{coil}$ is the current flowing in the coil wires, or simply the coil current, r_{coil} is the mean radius of the coil turns, η is the pitch angle of the coil, and $\bar{n}$ is the number of coil turns per unit length. Then:

$$|J_0| = \frac{\omega\sigma}{2} \mu_0\, \mu_r^{core}\, \wp_{coil}\, r_{coil} \times \frac{N}{l_{coil}} \times \cot(\eta) \quad (226)$$

Finally, the eddy current loss is evaluated, combining Equations 211 and 224:

$$P_{EM} = \int_V \left(\frac{J_0^{\,2}}{2\sigma} \exp\left[-\frac{2}{\delta}(r - r_{coil}) \right] \right) dV$$
$$= \frac{\sigma}{8} \left\{ \omega\, \mu_0\, \mu_r^{core}\, \wp_{coil}\, r_{coil} \times \frac{N}{\ell_{coil}} \times \cot(\eta) \right\}^2 \int_V \left(\exp\left[-\frac{2}{\delta}(r - r_{coil}) \right] \right) dV \quad (227)$$
$$= \bar{P} \int_V \left(\exp\left[-\frac{2}{\delta}(r - r_{coil}) \right] \right) dV$$

where

$$\bar{P} = \frac{\sigma}{8} \left[\omega \mu_0\, \mu_r^{core}\, \wp_{coil}\, r_{coil} \times \frac{N}{l_{coil}} \times \cot(\eta) \right]^2 \quad (228)$$

4.5. Fluid and Solid Mass Conservation Equations (or Hydraulic Transport Governing Equations)

Assuming that the caprock medium is fully saturated with water, and that the solid and fluid phases are separate and distinct, the equation for fluid mass is written as (Mase and Smith, 1985):

$$\underbrace{-\left\{ \frac{\partial q_z}{\partial z} \right\}}_{\text{Fluid transport}} \underbrace{-\left\{ \beta_f \left(\frac{\partial P}{\partial z} \right) - \gamma_f \left(\frac{\partial T}{\partial z} \right) \right\} q_z}_{\text{Contraction or thermal expansion of fluids}} + \underbrace{\left\{ \left(\phi \gamma_f + (1-\phi) \gamma_s \right) \frac{\partial T}{\partial t} \right\}}_{\text{Difference in thermal expansivities of the fluid and solid}} =$$
$$\underbrace{\left\{ \frac{\partial \varepsilon_v}{\partial t} \right\}}_{\text{Dilatation}} + \underbrace{\left\{ \phi \beta_f \frac{\partial P}{\partial t} + (1-\phi) \beta_s \frac{\partial \bar{\sigma}}{\partial t} \right\}}_{\text{Difference in compressibility between the fluid and solid}} \quad (229)$$

where q_z is the Darcy flux; ϕ and ε_v are the porosity and volumetric dilation, respectively, of the porous medium; β_f is the compressibility of the fluid; γ_f is the thermal expansion coefficient (i.e., the 3-dimensional thermal expansion coefficient) of the fluid (in this study, water); β_s is the compressibility of the solid phase; γ_s is the thermal expansion coefficient (i.e., the 3-dimensional thermal expansion coefficient) of the solid phase; and $\overline{\sigma}$ is the average effective normal stress. In the general case of a gas, liquid, or solid, the compressibility β is given by:

$$\beta = -\frac{1}{V}\left(\frac{\partial V}{\partial P}\right)_T \qquad 230$$

where V is the volume of the medium, and the subscript T indicates that the temperature is held constant during the expansion. Also, in the general case of a gas, liquid, or solid, the volumetric coefficient of thermal expansion γ is given by:

$$\gamma = \frac{1}{V}\left(\frac{\partial V}{\partial T}\right)_P \qquad 231$$

The subscript P denotes an isobaric process, and the pressure is held constant during the expansion. Also, the Darcy flux q_z can be calculated as:

$$q_z = -\frac{k}{\mu_f}\left(\frac{\partial P}{\partial z} - \rho_f g\right) \qquad 232$$

where k is the absolute permeability, μ_f is the dynamic viscosity of fluid (in this study, water), ρ_f is the density of fluid (in this study, water), and g is the magnitude of the gravitational acceleration. By assuming that the fluid flow due to gravitational forces is negligible, Equation 71 can be shortened to:

$$q_z = -\frac{k}{\mu_f}\left(\frac{\partial P}{\partial z}\right) \qquad 233$$

The pore pressure helps to counteract the mechanical stress carried through grain-to-grain contact. The efficiency of the pore pressure effect is measured by the poro-elastic factor (α_{Biot}) or Biot-Willis coefficient (usually called the Biot coefficient). The relationship between effective and total stress is given as:

$$\sigma'_{ij} = \sigma_{ij} - \alpha_{Biot} P \delta_{ij} \qquad 234$$

where σ'_{ij} is the effective stress and σ_{ij} is the total stress. The Biot coefficient (α_{Biot}) is calculated for a saturated non-fractured porous medium using the following relationship (Biot, 1941; Biot and Willis, 1957; Skempton, 1960; Nur and Byerlee, 1971; Verruijt, 1984):

$$\alpha_{Biot} = 1 - \frac{K_b}{K_s} \qquad 235$$

where K_s is the bulk modulus of the solid grains, and K_b is the bulk modulus of the porous medium (or matrix bulk modulus). The same expression obtained by Tuncay and Corapcioglu (1995) for a saturated fractured porous medium:

$$\alpha_{Biot} = 1 - \frac{K_{fr}}{K_s} \quad 236$$

where K_{fr} is the bulk modulus of the fractured porous medium (Fjær et al. (2008)[13]). These three bulk moduli (i.e., K_s, K_b and K_{fr}) can be determined experimentally by conducting standard soil mechanics tests. For this study, it has been assumed the caprock has no extensive fracture systems and so Equation 235 is assumed to be valid.

For media with appreciable porosity, matrix stiffness is much smaller than grain stiffness (i.e., $K_b << K_s$), the Biot coefficient (α_{Biot}) is roughly equal to 1, and the fluid volume expelled is equal to the volumetric dilation (Mase and Smith, 1987). Using Equation 235 the caprock equilibrium equations can be presented as:

$$\frac{\partial}{\partial z}\sigma'_{zz} + \frac{\partial}{\partial z}\alpha_{Biot}P = \frac{\partial}{\partial z}\sigma_{zz} = 0 \quad \text{(suggesting constant total stress)} \quad 237a$$

$$\frac{\partial}{\partial z}\tau_{zy} = 0 \quad 237b$$

If there is no constraint above the caprock (i.e., no stiffness in the overburden), the total stress increase in the z direction due to thermal expansion is zero, and in the case of overburden with low stiffness, the total stress change due to thermal expansion is negligible, and can be neglected. The total stress in the z direction is roughly equal to the integration of the overburden density in low-depth reservoirs such as those in the Athabasca oil sands. Assuming constant total stress in the z direction and negligible variation of total stress in the x and y directions, the average change in value of effective normal stress acting on the solid grains ($\overline{\sigma}$) varies with pore pressure:

$$\overline{\sigma} = -\alpha_{Biot} P \quad 238$$

There is a flaw in this assumption, since the total stress is usually not constant when there is a change in pore pressure. This effect is mostly referred to “stress redistribution”. But the stress redistribution is mostly small and can be ignored for an uniform change in pore pressure. For a linear-elastic porous medium, the volumetric strain is presented by Mase (1985, 1987) as:

$$\frac{\partial \varepsilon_v}{\partial t} = \frac{\partial}{\partial t}\left[\frac{(1-2\nu)\alpha_{Biot}}{2G(1-\nu)}(P - P_0) + \gamma_{sf}(T - T_0)\right] \quad 239$$

where solid matrix strains are positive in extension, P_0 and T_0 are the initial caprock pressure and temperature, G is the formation shear modulus and ν is Poisson’s ratio. The pore volume dilation associated with increases in fluid pressure result in a mechanism to accommodate the thermal expansion of pore water. As this study concerns conditions in which the caprock does not fail, it considers only the elastic extension within the caprock caused by the thermal and fluid pressure loads, and dilation due to plastic deformations is neglected.

Because the quantity in front of the pressure term in Equation 239 has the unit of compressibility, it is identified as the compressibility of the solid-fluid or the porous medium (β_{sf}). This parameter shows the volumetric dilation that takes place for each unit change in effective stress:

[13] Page 33 of Petroleum Related Rock Mechanics, 2nd Edition.

$$\beta_{sf} = \frac{(1-2\nu)\alpha_{Biot}}{2G(1-\nu)} \qquad 240$$

where β_{sf} is compressibility of the porous medium due to a pore pressure change *while holding the applied stress constant.* For condition which the Biot coefficient (α_{Biot}) is equal to 1, similar condition to Clearwater formation, β_{sf} is equal to the compressibility of the porous medium at drained condition which can be obtained by measuring the volumetric strain due to changes in applied stress *while holding pore pressure constant*. The compressibility of the porous medium at drained condition is much lower than compressibility values at undrained condition. Using the compressibility of the porous medium (β_{sf}), the corresponding volumetric strain is:

$$\frac{\partial \varepsilon_v}{\partial t} = \frac{\partial}{\partial t}\left[\beta_{sf}(P-P_0)+\gamma_{sf}(T-T_0)\right] \qquad 241$$

Substituting the Darcy flux from Equation 72, the volumetric strain rate from Equation 241, and the average value of effective normal stress from Equation 238, Equation 93 yields the final form of the equation governing the pressure increase:

$$\frac{\partial}{\partial z}\left(\frac{k}{\mu_f}\frac{\partial(P-P_0)}{\partial z}\right)+\frac{k}{\mu_f}\left[\beta_w\left(\frac{\partial(P-P_0)}{\partial z}\right)^2-\gamma_w\left(\frac{\partial(T-T_0)}{\partial z}\right)\left(\frac{\partial(P-P_0)}{\partial z}\right)\right]+\left[\phi\gamma_f+(1-\phi)\gamma_s-\gamma_{sf}\right]\frac{\partial(T-T_0)}{\partial t}= \qquad 242$$
$$\left[\phi\beta_f-(1-\phi)\beta_s+\beta_{sf}\right]\frac{\partial(P-P_0)}{\partial t}$$

Equation 94 can be simplified by defining two important parameters for this study. The first is the coefficient of thermal pressurization (Λ), which characterizes the increase in fluid pressure per unit change in temperature for undrained conditions:

$$\Lambda = \frac{\phi\gamma_f+(1-\phi)\gamma_s-\gamma_{sf}}{\phi\beta_f-(1-\phi)\beta_s+\beta_{sf}} \qquad 243$$

Since the thermal expansion (i.e., $\gamma_f=\gamma_w\approx 2.07\times10^{-4}/^oC$) of the water is an order of magnitude larger than that in the solids (i.e., $\gamma_s\approx 2\times10^{-5}/^oC$ [14]), and the compressibility of the porous medium (β_{sf}) in clay formations (i.e., in the range of 10^{-8} to 10^{-6} 1/Pa^3) is two to four orders of magnitude larger than that of the pore fluid (i.e., water compressibility is 4.2×10^{-10} 1/Pa^3), thermal pressurization (Λ) in Equation 97 can be approximated by:

$$\Lambda \cong \frac{\phi\gamma_w}{\beta_{sf}} \qquad \beta_{sf} >> \beta_w=\beta_f;\ \gamma_{sf}<\gamma_s<<\gamma_w=\gamma_f \qquad 244$$

For cases where porous medium compressibility (β_{sf}) is much less than water compressibility, the thermal pressurization (Λ) in Equation 97 can be approximated by:

$$\Lambda \cong \frac{\gamma_w}{\beta_w} \qquad \beta_{sf} << \beta_w=\beta_f;\ \gamma_{sf}<\gamma_s<<\gamma_w=\gamma_f \qquad 245$$

[14] Mase and Smith, 1987.

The second parameter, hydraulic diffusivity ($\kappa_{Hydraulic}$), characterizes the rate at which the disturbance in fluid pressure propagates from the thermal source:

$$\kappa_{Hydraulic} = \frac{k}{\mu_f\left(\phi\beta_f - (1-\phi)\beta_s + \beta_{sf}\right)} \quad 246$$

For a compressible medium such as shale formations, the hydraulic diffusivity ($\kappa_{Hydraulic}$) can be approximated by:

$$\kappa_{Hydraulic} \cong \frac{k}{\mu_w \beta_{sf}} \qquad \beta_{sf} >> \beta_w = \beta_f \quad 247$$

In the same manner, for a stiff porous medium such as consolidated sandstone reservoirs, the hydraulic diffusivity ($\kappa_{Hydraulic}$) can be approximated by:

$$\kappa_{Hydraulic} \cong \frac{k}{\phi\mu_w \beta_w} \qquad \beta_{sf} << \beta_w = \beta_f \quad 248$$

Then the pressure and temperature variations are defined as:

$$\bar{P} = P - P_0 \quad 249$$

$$\bar{T} = T - T_0 \quad 250$$

The final modified form of Equation 94 is presented as follows, substituting Equations 249 and 250:

$$\kappa_{Hydraulic}\left(\frac{\partial^2 \bar{P}}{\partial z^2}\right) + \kappa_{Hydraulic}\left[\beta_f\left(\frac{\partial \bar{P}}{\partial z}\right)^2 - \gamma_f\left(\frac{\partial \bar{T}}{\partial z}\right)\left(\frac{\partial \bar{P}}{\partial z}\right)\right] + \Lambda\frac{\partial \bar{T}}{\partial t} = \frac{\partial \bar{P}}{\partial t} \quad 251$$

It must be noted that in SAGD operations, steam injection raises reservoir pressure and temperature, which alters reservoir stresses sufficiently to cause shear failure within and beyond the growing steam chamber (Collins, 2005, 2007). This stress variation inside the reservoir induced by the steam chamber is neglected.

4.6. Energy Conservation Equation (or Thermal Transport Governing Equation)

The energy conservation equation describing the transient temperature distribution in a saturated porous medium is given by[15]:

$$\underbrace{\left\{\frac{\partial}{\partial z}\left(K_{sf}\frac{\partial T}{\partial z}\right)\right\}}_{\text{Conduction heat transport}} - \underbrace{\left\{\rho_f c_f q_z\left(\frac{\partial T}{\partial z}\right)\right\}}_{\text{Convective heat transport}} + \underbrace{\left\{\phi\gamma_f\left[\frac{\partial P}{\partial t} + \frac{q_z}{\phi}\left(\frac{\partial P}{\partial z}\right)\right]T\right\}}_{\text{Reversible work done on the fluid}} + \overbrace{\dot{Q}_{EM}}^{\text{EM-heating}} = \underbrace{\left\{(\rho c)_{sf}\frac{\partial T}{\partial t}\right\}}_{\text{Internal heat storage}} \quad 252$$

where T is the temperature, K_{sf} is the thermal conductivity of the solid-fluid composite, $(\rho c)_{sf}$ is the heat capacity of the solid-fluid composite, $\rho_f c_f$ is the heat capacity of the fluid inside the pores, γ_f is the volumetric coefficient of thermal expansion of the pore fluid, ϕ is the porosity, q_z is the Darcy flux, and $\dot{Q}_{EM}$ is the EM-heating flux. Substituting the Darcy flux from Equation 72, Equation 252 yields the final form of the equation governing the temperature increase:

[15] Equation 252 is modified format of the equation presented by Mase and Smith (1987) which is customized for EM-SAGD projects case specific.

$$\frac{\partial}{\partial z}\left(K_{sf}\frac{\partial \bar{T}}{\partial z}\right)+\left(\rho_f c_f\frac{k}{\mu_f}\right)\left(\frac{\partial \bar{T}}{\partial z}\right)\left(\frac{\partial \bar{P}}{\partial z}\right)+\phi\gamma_f\left[\frac{\partial \bar{P}}{\partial t}-\frac{k}{\phi\mu_f}\left(\frac{\partial \bar{P}}{\partial z}\right)^2\right](\bar{T}+T_0)+\dot{Q}_{EM}=(\rho c)_{sf}\frac{\partial \bar{T}}{\partial t} \quad 253$$

which yields:

$$\frac{K_{sf}}{(\rho c)_{sf}}\left(\frac{\partial^2 \bar{T}}{\partial z^2}\right)+\left(\frac{(\rho c)_f}{(\rho c)_{sf}}\frac{k}{\mu_f}\right)\left(\frac{\partial \bar{T}}{\partial z}\right)\left(\frac{\partial \bar{P}}{\partial z}\right)+\frac{\phi\gamma_f}{(\rho c)_{sf}}\left[\frac{\partial \bar{P}}{\partial t}-\frac{k}{\phi\mu_f}\left(\frac{\partial \bar{P}}{\partial z}\right)^2\right](\bar{T}+T_0)+\frac{\dot{Q}_{EM}}{(\rho c)_{sf}}=\frac{\partial \bar{T}}{\partial t} \quad 254$$

The thermal diffusivity of the formation ($\kappa_{Thermal}$) is given by:

$$\kappa_{Themal}=\frac{K_{sf}}{(\rho c)_{sf}} \quad 255$$

The Peclet number (N_{pe}) is the ratio of the rate of heat convection due to flow (or convection gradient) to the rate of heat conduction (or conduction gradient):

$$N_{Pe}=\frac{(\rho c)_f}{(\rho c)_{sf}}\frac{k}{\mu_f\,\kappa_{Thermal}} \quad 256$$

Following these definitions, the final format is presented as:

$$\kappa_{Thermal}\left(\frac{\partial^2 \bar{T}}{\partial z^2}\right)+N_{Pe}\,\kappa_{Thermal}\left(\frac{\partial \bar{T}}{\partial z}\right)\left(\frac{\partial \bar{P}}{\partial z}\right)+\frac{\phi\gamma_f}{(\rho c)_{sf}}\left[\frac{\partial \bar{P}}{\partial t}-\frac{k}{\phi\mu_f}\left(\frac{\partial \bar{P}}{\partial z}\right)^2\right](\bar{T}+T_0)+\frac{\dot{Q}_{EM}}{(\rho c)_{sf}}=\frac{\partial \bar{T}}{\partial t} \quad 257$$

In shale formations, letting $(\rho c)_f/(\rho c)_{sf}\approx 1$, $\mu_f=\mu_w=10^{-3}\,Pa\bullet sec$, and $\kappa_{Thermal}$ varies from 10^{-7} to 10^{-5}, Figure 2.18 illustrates how the Peclet number (N_{pe}) varies with permeability. It also shows that for shale formations, when permeability varies from 10^{-19} to 10^{-16} m^2 (Neuzil, 1994), the Peclet number (N_{pe}) varies from 10^{-9} to 10^{-7}.These values show negligible Peclet numbers (N_{pe}<<1) for shale formations. The same figure shows Peclet number as high as 10^{-1} for Venezuelan oil sands, which cannot be neglected. Therefore, in shale caprock formations such as the Clearwater formation, heat transfer is accomplished with little convection in comparison with conduction, and convection can be neglected in caprock. Reversible work done on the fluid is negligible due to the very small amount of water thermal expansion compared to shale thermal conductivity (i.e., $(\gamma_f=\gamma_w\approx 2.07\times 10^{-4}/^{\circ}C)<<(K_{sf}\approx 1.30-1.95\ W/m\bullet^{\circ}C)$ [16]). Then, the simplified format of the thermal transport governing Equation 149 is presented as:

$$\kappa_{Thermal}\left(\frac{\partial^2 \bar{T}}{\partial z^2}\right)+\frac{\dot{Q}_{EM}}{(\rho c)_{sf}}=\frac{\partial \bar{T}}{\partial t} \quad 258$$

[16] The porosity has a minor reducing effect which is not very important. Since shale porosity is not a very small value in most cases. Shale porosity varies from 0.10 to 0.35, although most are less than 0.15 (but clay's porosity varies from 0.30 to 0.60 nearly twice as shale).

4.7. Solution Technique

Since the inductor is far from the caprock, it is assumed that Equation 227 can be converted to a 1-dimensional format, and r converted to z. The rate of heat generation resulting from EM is obtained by differentiating Equation 227 with respect to z (see Figure 1.4):

$$\dot{Q}_{EM} = \left(\frac{dQ}{dt}\right)_{EM} = -\frac{\partial P_{EM}(z)}{\partial z} = \frac{2}{\delta}\bar{P}\exp\left[-\frac{2}{\delta}(z + z_{caprock} - r_{coil})\right] \quad 259$$

The partial differential equation governing the thermal transport converts to:

$$\kappa_{Thermal}\frac{\partial^2 \bar{T}}{\partial z^2} + \frac{2}{\delta(\rho c)_{sf}}\bar{P}\exp\left[-\frac{2}{\delta}(z + z_{caprock} - r_{coil})\right] = \frac{\partial \bar{T}}{\partial t} \quad 260$$

It must be noted that in this analysis, eddy current heat loss dominates, the inductor coil stands alone, there is no other electrically-conductive structure in proximity, and the inductor is an infinitely long single-layer solenoid producing a homogeneous magnetic field.

The initial condition is assumed to be uniform constant temperature:

$$T(z,0) = T_0 \quad 261$$

and the boundary conditions are:

$$T(0,t) = T_{steam} \quad 262$$

$$\frac{\partial T(\infty,t)}{\partial z} = 0 \quad 263$$

where T_{steam} is the steam temperature injected for SAGD applications. The physical meaning of Equation 262 is that the temperature at the bottom of the caprock is equal to steam chamber temperature in whole process of warming. Which means the steam chamber is well matured and caprock bottom temperature is just governed by steam chamber heat transfer. The physical meaning of Equation 263 is that the variation of temperature in infinity is equal to zero, which means temperature in infinity or far distance from bottom of the caprock is constant. The solution for this problem is given by Sahin (1992), who presents the temperature distribution as:

$$T = T_0 + (T_{steam} - T_0)\left\{\begin{array}{l}\operatorname{erfc}\left(\frac{\xi}{2\sqrt{\lambda}}\right) + \\ \frac{A}{T_{steam} - T_0}\left[\operatorname{erfc}\left(\frac{\xi}{2\sqrt{\lambda}}\right) - \exp(-\xi) - 0.5\exp(\lambda+\xi)\operatorname{erfc}\left(\sqrt{\lambda} + \frac{\xi}{2\sqrt{\lambda}}\right) + 0.5\exp(\lambda-\xi)\operatorname{erfc}\left(\sqrt{\lambda} - \frac{\xi}{2\sqrt{\lambda}}\right)\right]\end{array}\right\} \quad 264$$

Where

$$\xi = \frac{2}{\delta}z = 0.004 z\sqrt{\mu_r f_s \sigma} \quad 265$$

$$\lambda = \frac{4}{\delta^2}\kappa_{Thermal}\, t = 1.6\times10^{-5}\times\kappa_{Thermal}\, t(\mu_r f_s \sigma) \quad 266$$

$$A = \frac{\delta \bar{P} \exp\left(\frac{2}{\delta}\left[r_{coil} - z_{caprock}\right]\right)}{2K_{sf}} \quad 267$$

In SPE 156876 for the solution presented for temperature variation within the caprock (in Eq. 264) the initial condition is suggested to be equal to reservoir temperature:

$$T(z,0) = T_0 \quad 268$$

and the boundary conditions are:

$$T(0,t) = T_{steam} \quad 269$$

$$\frac{\partial T(\infty,t)}{\partial z} = 0 \quad 270$$

where T_{steam} is the steam temperature injected for SAGD applications.

The physical meaning of Eq. 270 is that the variation of temperature in infinity is equal to zero, which means temperature in infinity or far distance from bottom of the caprock is constant. The concern on Eq. 270 raised by few readers is that being constant at infinity will not provide temperature equal to T_0, and the solution will yield constant temperature which is not equal to T_0. The base for this question is mostly derived by considering Figure 4.48 for EM-heating in the rage of 100 kHz frequency

There is embedded assumption in Eq. 269, and that is yielding temperature towards initial caprock temperature from Eq. 268; which is T_0. Combining Eqs. 268 and . 270, mathematically means:

$$T(\infty,t) = T_0 \quad 271$$

If we extend the axis it is well presented that even for 100 kHz the temperature will yield to reservoir temperature (see Figure 4.50a). Variation of infinite boundary depth (at which temperature reaches 10 + 0.001 °C) vs. source frequency are presented for 100 and 100 days (see Figure 4.50b). as it is shown the infinite boundary depth reaches its peak at lower frequencies and then as frequency is increasing the heating zone is shrinking.

One the effective methods to see if the hydraulic and thermal physics should be coupled or studied separately is to evaluate the zone of influence of hydraulic and thermal physics. Few studies (e.g., Lachenbruch, 1980; Delaney, 1982) have compared the widths of the hydraulic and thermal zones by defining a characteristic length for each field. The hydraulic diffusion length is defined as:

$$L_{Hydraulic} = \sqrt{4\kappa_{Hydraulic} t} \quad 272$$

and reflects the distance a fluid pressure perturbation propagates from its thermal source in time "t" (Lachenbruch, 1980; Delaney, 1982; Mase and Smith, 1987). The thermal conduction length is defined as:

$$L_{Thermal} = \sqrt{4\kappa_{Thermal} t} \qquad 273$$

and reflects the distance a temperature perturbation propagates by thermal conduction from its heat source in time "t" (Lachenbruch, 1980; Delaney, 1982; Mase and Smith, 1987). These distances are present when the heat source is applied on boundaries, but this methodology can still be used to understand the concept, when the heat source is in the medium (such as EM-SAGD and EM heating operations).

The hydraulic field is much wider than the thermal field (i.e., $L_{Hydraulic} >> L_{Thermal}$) if the hydraulic diffusivity is much greater than the thermal diffusivity (i.e., $\kappa_{Hydraulic} >> \kappa_{Thermal}$). In this case, pore fluids can flow from the thermal field and modify the fluid thermal expansion without thermal pressurization. If the hydraulic diffusivity ($\kappa_{Hydraulic}$) is much less than the thermal diffusivity ($\kappa_{Thermal}$) (i.e., $\kappa_{Thermal} >> \kappa_{Hydraulic}$), there is extreme thermal pressurization, no appreciable fluid flow from the heated region, and, it is assumed, undrained conditions (see Figure 1.4). In undrained loading the pore pressure cannot be released due to closed boundary condition. Therefore the fluid pressure increases is linearly with temperature:

$$\overline{P} \cong \Lambda \overline{T} \qquad 274$$

Figure 4.47 illustrates the variation of the ratio of hydraulic diffusivity ($\kappa_{Hydraulic}$) to thermal diffusivity ($\kappa_{Thermal}$) versus formation permeability (k) for different compressibilities of the porous medium (β_{sf}). As shown in Figure 4.47, the undrained condition is a valid assumption for shale formations acting as caprock, since the hydraulic diffusivity ($\kappa_{Hydraulic}$) is much smaller than the thermal diffusivity ($\kappa_{Thermal}$). Under this assumption, the fluid pressure or induced thermal pressure rise is given as:

$$P \cong P_0 + \Lambda\left(T_{steam} - T_0\right)\left\{\begin{array}{l} \operatorname{erfc}\left(\frac{\xi}{2\sqrt{\lambda}}\right) + \\ \frac{A}{T_{steam} - T_0}\left[\operatorname{erfc}\left(\frac{\xi}{2\sqrt{\lambda}}\right) - \exp(-\xi) - 0.5\exp(\lambda+\xi)\operatorname{erfc}\left(\sqrt{\lambda} + \frac{\xi}{2\sqrt{\lambda}}\right) + 0.5\exp(\lambda 5\xi)\operatorname{erfc}\left(\sqrt{\lambda} - \frac{\xi}{2\sqrt{\lambda}}\right)\right] \end{array}\right\} \qquad 27$$

This pressure rise will weaken the caprock and can trigger slippage between caprock and reservoir in EM-SAGD projects. Figure 2.19 presents the temperature variation in caprock for different applied frequencies versus distance from the caprock boundary. The temperature variation is very much identical for 1 kHz and 10 kHz, as it only varies for durations longer than 300 days. The temperature variation along the caprock is comparable for 1 kHz and 10 KHz, in longer durations such as 300 and 1000 days (see Figure 2.19, Section D for comparison of 1 kHz and 10 KHz temperature variation for 300 and 1000 days). The small difference between 1 kHz and 10 KHz is due to negligible EM heat generation compared with the heat flux coming from the SAGD chamber in frequencies lower than 10 kHz In higher frequencies, the power will raise with power 2 of the frequency (see Equation 228) then the EM heat generation is dominating the heat flux coming from the steam chamber and is the controlling factor in caprock temperature variation (see Figure 2.19, Section G).

Figure 2.19 illustrates the induced thermal pressure for different compressibilities of the porous medium (β_{sf}). This shows that even in high frequencies, the induced thermal pressure is

negligible for porous mediums with high compressibility (β_{sf}) (i.e., 10^{-6} /Pa) or softer caprocks. However, the induced thermal pressure in mediums with low compressibility is comparable even for low frequencies, and can be problematic for shallow reservoirs. Hydrostatic pressure is roughly equal to 1 MPa for every 100 metres. For example if the formation has the hydrostatic pressure and assuming formation stress gradient equal to 20 kPa/m then induced pressure of 1 MPa can liquefy the caprock at a depth of 100 metres. For example in results presented in Figure 2.19, if injection temperature is 250ºC which relates to a steam pressure of 3.98 MPa, ignoring the thermal pressurization the caprock deoth of 500 metres will have a margin of 1 MPa to be liquefied. But as it is presented in Figure 2.19 a differential pressure of 1 MPa is plausible for low-compressibility formations (i.e., stiffer caprocks), even for low frequencies (see Figure 2.19). This may cause caprock liquefaction even with a margin of 1 MPa. The final statement concluded that the compressibility of the porous medium (β_{sf}) is the most important component of caprock in thermal pressurization, and in EM-SAGD applications it should be experimentally calculated with great care.

4.8. Discussion

As it is shown in Figure 4.48 even for low frequencies the induced pressure can be as high as 1 MPa for formations with low compressibility values. This effect is more conspicuous for higher frequencies (e.g., 100 kHz). As it is shown in Section I in Figure 4.48, the thermal induced pressure is roughly equal to 1.5 MPa for 100 days and it is equal to 5.3 MPa for 1000 days for porous mediums with low compressibility (β_{sf})(i.e., stiffer caprocks). Considering the SAGD temperature variation between 150 to 270ºC (302 to 518ºF) (Garnier et al., 2008; Xie and Zahacy, 2011) the injection pressure is ranging between 0.48 to 5.50 MPa. The thermal induced pressure increase of 5.3 MPa cannot be neglected for caprocks with any practical depth in SAGD operation.

One of the limitations of this study is constant temperature boundary assumption at the bottom of the caprock. As it shown in Figure 4.48 this assumption is valid for frequency range between 1 to 10 kHz. But the EM heating rate for frequency of 100 kHz is faster than conductive heat transfer from constant temperature at the bottom of the caprock. The larger heating rate from inductive heating result in the caprock bottom boundary to be colder than the upper parts of the caprock, which cannot be true in reality. However, the results of this study can be used with small error for frequency ranges between 1 to 10 kHz.

The variation of temperature along a vertical axis within the caprock as a function of different temperatures at the base of the caprock is illustrated in Figure 4.49 the effect of varied temperature is studied. Although in this study the solution for varied temperature boundary condition is not presented, the effect of reservoir or bottom of caprock warming up can be studied by changing the temperature at the bottom of caprock as a constant boundary condition. Results in Figure 4.49 shows that the variation of temperature along the caprock is experiencing its maximum at bottom of the caprock for higher bottom temperatures. This is a reasonable temperature variation which should happen for higher frequencies such as 100 kHz.

4.9. Conclusions

This study examines the relative roles of frequencies in EM-SAGD applications. The temperature enhancement of electromagnetic heating takes place with high frequencies (or high coil current). The induced thermal pressure in low-compressibility mediums is comparable even for low frequencies, and can be problematic for shallow reservoirs. Compressibility of the porous

medium (β_{sf}) is the most important component of caprock in thermal pressurization, and in EM-SAGD applications it should be experimentally calculated with great care.

4.10. References

Abernethy, E.R., 1976. Production Increase of Heavy Oils by Electromagnetic Heating, *Journal of Canadian Petroleum Technology*, Vol. **15**, No. **3**, pp. 91-97.

AEUB Decision 99-22, 1999. Imperial Oil Resources Limited Cold Lake Production Project Mahkeses Development.

Barranger, J., 1965. Hysteresis and Eddy-Current Losses of a Transformer Lamination Viewed as an Application of the Poynting Theorem, NASA Technical Note.

Biot, M.A., 1941. General Theory of Three-Dimensional Consolidation, Columbia University, New York, New York, Vol. **12.**

Biot, M.A., Willis, D.G., 1957. The Elastic Coefficients of the Theory of Consolidation, *Journal of Applied Mechanics*, Vol. **24**, pp. 594-601.

Bogdanov, I.I., Torres, J.A., Akhlaghi, H.A., Kamp, A.M., 2011. The Influence of Salt Concentration in Injected Water on Low-Frequency Electrical-Heating-Assisted Bitumen Recovery, *SPE Journal*, Vol. **16**, No. **3**, pp. 548-558.

Bois, A-P, Mainguy, M., 2011. Importance of Thermal Consolidation of Shale During SAGD Process, *SPE Heavy Oil Conference and Exhibition*, Kuwait City, Kuwait, 12-14 December, SPE 150420.

Brace, W.F., Orange, A.S., 1968. Electrical Resistivity Changes in Saturated Rocks during Fracture and Frictional Sliding, *Journal of Geophysical Research*, Vol. **73**, No. **4**, pp. 1433-1445.

Brace, W.F., Orange, A.S., 1966. Electrical Resistivity Changes in Saturated Rock under Stress, *Science*, Vol. **153**, No. **3743**, pp. 1525-1526.Carrizales, M.A., Lake, L.W., Johns, R.T., 2008. Production Improvement of Heavy-Oil Recovery by using Electromagnetic Heating, *2008 SPE Annual Technical Conference and Exhibition*, Denver, Colorado, USA, 21-24 September.

Butler, R., 1998, SAGD comes of age!, *Journal of Canadian Petroleum Technology*, Vol. **37**, No. **7**, pp. 9-12.

Carrizales, M.A., Lake, L.W., Johns, R.T., 2008. Production Improvement of Heavy Oil Recovery by Using Electromagnetic Heating, *SPE Annual Technical Conference and Exhibition*, Denver, Colorado, USA, 21-24 September, SPE 115723-MS.

Chute, F.S., Vermeulen, F.E., 1988. Present and Potential Applications of Electromagnetic Heating in the In-Situ Recovery of Oil, *OSTRA Journal of Research*, Vol. **4**, pp. 19-33.

Chute, F.S., Vermeulen, F.E., Cervenan, M.R., 1978. Physical Modelling of the Electrical Heating of the Oil Sand Deposits, Technical Report, AOSTRA Agreement #31, Applied Electromagnetics Group, University of Alberta.

Collins, P.M., 2005. Geomechanical Effects on the SAGD Process, SPE Reservoir Evaluation & Engineering, *2005 SPE International Thermal Operations and Heavy Oil Symposium*, Calgary, Alberta, Canada, 1-3 November, 2005.

Collins, P.M., 2007. Geomechanical Effects on the SAGD Process, SPE Reservoir Evaluation & Engineering, Vol. **10**, No. **4**, pp. 367-375, SPE 97905-PA.

Davletbaev, A.Y., Kovaleva, L.A., Babadagli, T., 2011. Mathematical Modeling and Field Application of Heavy Oil Recovery by Radio-Frequency Electromagnetic Stimulation, *Journal of Petroleum Science and Engineering*, Vol. 78, No. 3-4, pp. 646-653.

Davletbaev, A.Y., Kovaleva, L.A., Babadagli, T., 2010. Heavy Oil and Bitumen Recovery Using Radiofrequency Electromagnetic Irradiation and Electrical Heating: Theoretical Analysis and Field Scale Observations, *Canadian Unconventional Resources and International Petroleum Conference*, Calgary, Alberta, Canada, 19-21 October, SPE 136611-MS.

Davletbaev, A.Y., Kovaleva, L.A., Nasyrov, N.M., 2009. An Investigation of the Processes of Heat And Mass Transfer in a Multilayer Medium under Conditions of Injection of a Miscible Agent with Simultaneous Electromagnetic Stimulation, *High Temperature*, Vol. **47**, No. **4**, pp. 574-579.

Davletbaev, A.Y., Kovaleva, L.A., Nasyrov, N.M., 2008. Numerical Simulation of Injection of a Solvent into a Production Well under Electromagnetic Action, *Fluid Dynamics*, Vol. **43**, No. **4**, pp. 583-589.

Delaney, P.T., 1982. Rapid Intrusion of Magma into Wet Rock: Groundwater Flow Due To Pore Pressure Increases, *Journal of Geophysical Research*, Vol. **87**, pp. 7739-7756.

Dusseault, M.B., Bruno, M.S., Barrera, J., 2001. Casing Shear: Causes, Cases, Cures, *SPE Drilling & Completion*, Vol. **16**, No. **2**, pp. 98-107, SPE 72060-PA.

Dusseault, M.B., Collins, P.M., 2008a. Geomechanics Effects in Thermal Processes for Heavy Oil Exploitation, CSEG RECORDER June 2008

Dusseault, M.B., Collins, P.M., 2008b. Geomechanics Effects in Thermal Processes for Heavy Oil Exploitation, *Canadian Society of Exploration Geophysicists (CSEG) Recorder*, Vol. **33**, pp. 20-23.

Energy Resources Conservation Board (ERCB), 2010. Total E&P Canada Ltd. Surface Steam Release of May 18, 2006 Joslyn Creek SAGD Thermal Operation, ERCB Staff Review and Analysis.

Fjær, E., Holt, R.M., Horsrud, P., Raaen, A.M., Risnes, R., 2008. Petroleum Related Rock Mechanics, 2nd Edition, Elsevier, ISBN: 9780444502605.

Garnier, A., Saint-Marc, J., Bois and A.P., Kermanac'h, Y., 2008. A singular methodology to design cement sheath integrity exposed to steam stimulation, SPE/PS/CHOA *International Thermal Operations and Heavy Oil Symposium*, doi:10.2118/117709-MS.

Government of Alberta, 2012. www.energy.gov.ab.ca/OilSands/1715.asp

Government of Alberta, 2011. Alberta Oil Sands Industry (AOSID) - Quarterly Update Summer 2011, Reporting on the period: March 5, 2011 to June 3, 2011, www.albertacanada.com

Government of Alberta, 2008. Alberta's Oil Sands: Resourceful. Responsible, ISBN 978-07785.

Gunal, G.O., Islam, M.R., 2000, Alteration of Asphaltic Crude Rheology with Electromagnetic and Ultrasonic Irradiation, *Petroleum Science and Engineering*, Vol. **26**, No. **1**, pp. 263-272.

Haimbaugh, R.E., 2001. Practical Induction Heat Treating, ASM International, Materials Park, ISBN:0871707438.

Halliday, D., Resnick, R., 1966. Physics, Wiley, New York.

Handin, J., Hager, R.V. Jr., 1957. Experimental Deformation of Sedimentary Rocks under Confining Pressure: Tests at Room Temperature on Dry Samples, *Bulletin of the American Association of Petroleum Geologists*, Vol. **41**, No. **1**, pp. 1-50.

Hiebert A.D., Vermeulen, F.E., Chute, F.S., Capjack, C.E., 1986. Numerical Simulation Results for the Electrical Heating of Athabasca Oil-Sand Formations, SPE Reservoir Engineering, Vol. **1**, No. **1**, pp. 76-84.

Irani, M., and Ghannadi, S., 2012. Understanding the Heat Transfer Mechanism in the Steam-Assisted Gravity Drainage (SAGD) Process and Comparing the Conduction and Convection Flux in Bitumen Reservoirs, SPEJ, SPE-163079-PA.

Islam, M.R., Wadadar, S.S., Banzal, A., 1991. Enhanced Oil Recovery of Ugnu Tar Sands of Alaska Using Electromagnetic Heating with Horizontal Wells, Paper SPE 22177, *International Arctic Technology Conference,* Anchorage, Alaska, US, 29-31 May.

Jordan, E.C., Balmain, K.G., 1968. Electromagnetic Waves and Radiating Systems, 2nd Edition, Prentice Hall, ISBN 978-0132499958.

Kasevich, R.S., Price, S.L., Faust, D.L., Fontaine, M.F., 1994. Pilot testing of a radio frequency heating system for enhanced oil recovery from diatomaceous earth, *69th Annual Technical Conference and Exhibition*, New Orleans, USA, 25-28 September.

Khan, S., Han, H., Ansari, S., Khosravi, N., 2010. An Integrated Geomechanics Workflow for Caprock-Integrity Analysis of a Potential Carbon Storage Site, *International Conference on CO_2 Capture, Storage, and Utilization*, New Orleans, Louisiana, USA, 10-12 November, SPE 139477.

Khan, S., Han, H., Ansari, S., Khosravi, N., 2011. Geomechanical Modeling to Assess Caprock Integrity in Oil Sands, *CSPG CSEG CWLS Convention*.

Koolman, M., Huber, N., Diehl, D., Wacker, B., 2008. Electromagnetic Heating Method to Improve Steam Assisted Gravity Drainage, *International Thermal Operations and Heavy Oil Symposium*, 20-23 October 2008, Calgary, Alberta, Canada, SPE117481-MS, doi:10.2118/117481-MS.

Kovaleva, L., Davletbaev, A., Babadagli, T., Stepanova, Z., 2011. Effects of Electrical and Radio-Frequency Electromagnetic Heating on the Mass Transfer Process During Miscible Injection for Heavy-Oil Recovery, *Energy and Fuels*, Vol. **25**, No. **2**, pp. 482-486.

Lachenbruch, A.H., 1980. Frictional Heating, Fluid Pressure, and the Resistance to Fault Motion, *Journal of Geophysical Research*, Vol. **85**, pp. 6097-6112.

Mase, C. W., Smith, L., 1987. Effects of Frictional Heating on the Thermal, Hydrologic, and Mechanical Response of a Fault, *Journal of Geophysical Research*, 92(B7), pp. 6249-6272.

Mase, C.W., Smith, L., 1985. Pore-Fluid Pressures and Frictional Heating on a Fault Surface, *Pure and Applied Geophysics*, Vol. **122**, pp. 583-607.

Matthäi, S.K., Roberts, S.G., 1996. The Influence of Fault Permeability on Single-Phase Fluid Flow Near Fault–Sand Intersections: Results from Steady-State High-Resolution Models of Pressure-Driven Fluid Flow, *American Association of Petroleum Geologists Bulletin*, Vol. **80**, No. **11**, pp. 1763-1779.

McGee, B.C.W., Vermeulen, F.E., 2007. The Mechanisms of Electrical Heating for the Recovery of Bitumen From Oil Sands, *Journal of Canadian Petroleum Technology*, Vol. **46**, No. **1**, pp. 28-34.

McGee, B.C.W., Vermeulen, F.E., 2000. In-Situ Electromagnetic Heating for Hydrocarbon Recovery and Environmental Remediation; *Journal of Canadian Petroleum Technology*, Distinguished Authors Series, Vol. **39**, No. **8**, pp. 24-28.

McGee, B.C.W., Vermeulen, F.E., and Yu, L., 1999. Field Test of Electrical Heating with Horizontal and Vertical Wells, *Journal of Canadian Petroleum Technology*, Vol . **38**, No. **3**, pp. 46-53.

McGee, B.C.W., Vermeulen, F. E., Yu, L., 1999. Field test of electrical heating with horizontal and vertical wells, CHOA Handbook, 2nd Edition, ISBN 0969521316, pp. 565-572.

McMaster, R.C., 1976. Metals Handbook, 8th Edition, Vol. **11**, ASM International, Metals Park.

Neuzil, C.E., 1994. How Permeable are Clays and Shales?, *Water Resources Research*, Vol. **30**, No. **2**, pp. 145-150.

Nur, A., Byerlee, J.D., 1971. An Exact Effective Stress Law for Elastic Deformation of Rock with Fluids, *Journal of Geophysical Research*, Vol. **76**, pp. 6414-6419.

Ovalles, C., Fonseca, A., Lara, A., Alvarado, V., Urrecheaga, K., Ranson, A., Mendoza, H., 2002. Opportunities of Downhole Dielectric Heating in Venezuela: Three Case Studies Involving Medium, Heavy and Extra-Heavy Crude Oil Reservoirs, *International Thermal Operations and Heavy Oil Symposium and International Horizontal Well Technology Conference*, Calgary, Alberta, Canada, 4-7 November, SPE 78980.

Popović , Z., Popović, B., 2000. Introductory Electromagnetics, 1st Edition, Prentice Hall, Inc.

Rudnev, V., Loveless, D., Cook, R., Black, M., 2003. Handbook of Induction Heating, Marcel Dekker, 796 pages, ISBN: 0824708482.

Sahin, A.Z., 1992. Transient Heat Conduction in Semi-Infinite Solid with Spatially Decaying Exponential Heat Generation, *International Communications in Heat and Mass Transfer*, Vol. **19**, No. **3**, pp. 349-358.

Sahni, A., Kumar, M., Knapp, R.B., 2000. Electromagnetic Heating Methods for Heavy Oil Reservoirs, *SPE/AAPG Western Regional Meeting*, Long Beach, California, 19-23 June, SPE 62550.

Sayakhov, F.L., Kovaleva, L.A., Nasyrov, N.M., 2002. Heat and Mass Transfer in the Well-Stratum System under the Electromagnetic Action on Massive Oil Deposits, *Journal of Engineering Physics and Thermophysics*, Vol. **75**, No. **1**,.pp. 126-133.

Skempton, A.W., 1960. Terzaghi's concept of effective stress, in *From Theory to Practice in Soil Mechanics*, edited by L. Bjerrum, A. Casagrande, R. B. Beck, and A. W. Skempton, pp. 42-53, John Wiley, New York.

Smith, R.J., Alinsangan, N.S., Talebi, S., 2002. Microseismic Response of Well Casing Failures at a Thermal Heavy Oil Operation, *SPE/ISRM Rock Mechanics Conference*, Irving, Texas, 20-23 October, SPE78203.

Spencer, H.L. 1987. Electromagnetic Oil Recovery Ltd. Calgary.

Spencer, H.L., 1989. Electric Heat Breaks Paraffins, Boosts Production, *Enhanced Recovery Week*, 30.10, pp. 1-2.

Spiegel, M.R., Lipcshutz, S., Spellman, D., 2009. Vector Analysis, 2nd Edition, Schaum's Outlines, McGraw Hill (USA), ISBN 978-0-07-161545-7.

Talebi, S., Nechtschein, S., Boone, T.J., 1998. Seismicity and Casing Failures Due to Steam Stimulation in Oil Sands, *Pure Applied Geophysics*, Vol. **153**, pp. 219-233.

Total E&P Canada Ltd., 2007. Summary of Investigations into the Joslyn May 18th 2006 Steam Release, December.

Tuncay, K, Corapcioglu, M.Y., 1995. Effective stress principle for saturated fractured porous media, *Water Resources Research*, Vol. **31**, No. **12**, pp. 3103-3106.

Uwiera-Gartner, M.M.E., Carlson, M.R., Palmgren, C.T.S., 2011a. Evaluation of the Clearwater Formation Caprock for a Proposed, Low-Pressure, Steam-Assisted Gravity Drainage Pilot Project, *SPE Annual Technical Conference and Exhibition*, Denver, Colorado, USA, 30 October-2 November, 2011, SPE 147302, doi:10.2118/147302-MS.

Uwiera-Gartner, M.M.E., Carlson, M.R., Walters, D., Palmgren, C.T.S., 2011b. Geomechanical Simulation of Caprock Performance for a Proposed, Low Pressure, Steam-Assisted Gravity Drainage Pilot Project, *Canadian Unconventional Resources Conference*, Calgary, Alberta, Canada, 15-17 November, 2011, SPE 148886, doi:10.2118/148886-MS.

Vermeulen F.E., Chute, F. S., 1983. Electromagnetic Techniques in the In-Situ Recovery of Heavy Oils, *Journal of Microwave Power*, Vol. **18**, No. **1**, pp. 15-29.

Vermeulen, F., McGee, B., 2000. In-Situ Electromagnetic Heating for Hydrocarbon Recovery and Environmental Remediation, Vol. **39**, No. **8**, pp. 25-29.

Vermeulen, F.E., Chute, F.S., Cervenan, M.R., 1979. Physical Modelling of the Electromagnetic Heating of Oil Sand and Other Earth-Type and Biological Materials, *Canadian Electrical Engineering Journal*, Vol. **4**, pp. 19-28.

Vermeulen, F.E., Chute, F.S., Mcpherson, R.G., 1988. Physical Modelling of Electrothermal Processes in Oil Sand, *Alberta Oil Sands Technology and Research Journal of Research*, Vol. **4**, pp. 299-305.

Verruijt, A., 1984. The Theory of consolidation, *Fundamentals of Transport Phenomena in Porous Media*, edited by J. Bear and M. Y. Corapcioglu, pp. 349-368, Martinus Nijhoff, Norwell, Mass.

Voltmer, D.R., 2007. Fundamentals of Electromagnetics 2: Quasistatics and Waves, Morgan and Claypool, 196 pages, ebook, ISBN: 1598291734.

Wacker, B., Karmeileopardus, D., Trautmann, B., Helget, A., Torlak, M., 2011. Electromagnetic Heating for In-Situ Production of Heavy Oil and Bitumen Reservoirs, *Canadian Unconventional Resources Conference*, Calgary, Alberta, Canada, 15-17 November, CSUG/SPE 148932.

Wong, R.C.K., Chau, K.T., 2004. Casing Impairment Induced by Shear Slip along a Weak Layer in Shale due to Fluid (Steam) Injection, *Canadian International Petroleum Conference*, Calgary, Alberta, Canada, 8-10 June.

Xie, J. and Zahacy, T.A., 2011. Understanding cement mechanical behavior in SAGD wells, World Heavy Oil Congress, Edmonton, Alberta, March 14-17, Paper WHOC11-557.

Yuan, Y., Xu, B., Palmgren C., 2011a. Design of Caprock Integrity in Thermal Stimulation of Shallow Oil-Sands Reservoirs, *Canadian Unconventional Resources Conference*, Calgary, Alberta, Canada, 15-17 November, 2011, SPE 149371.

Yuan, Y., Xu, B., Yang, B., 2011b. Geomechanics for the Thermal Stimulation of Heavy Oil Reservoirs-Canadian Experience, *SPE Heavy Oil Conference and Exhibition*, Kuwait City, Kuwait, 12-14 December, SPE 150293, doi:10.2118/150293-MS.

Zahn, M., 1979. Electromagnetic Field Theory: A Problem Solving Approach, Wiley, 298 pages, ISBN: 0471021989.

Zinn, S., Semiatin, S.L., 1988. Elements of Induction Heating: Design, Control, and Applications, Electric Power Research Institute, Carnes Publication Services Inc.

Tables

Table 4.6. Parameters used for Clearwater caprock (or shale) formation in Figure 2.19.

Parameter	Value Range	Assumed Value in Figure 2.19
Caprock Hydraulic Properties:		
β_{sf} , 1/Pa	10^{-8} to 10^{-6} [A]	10^{-8} to 10^{-6}
ϕ, no unit	0.10 to 0.35 [B]	0.25
γ_w , 1/ ºC	2.07×10^{-4} [A]	2.07×10^{-4}
μ_w, Pa·s	0.001002 (at 20 ºC)	0.001
k, m^2	10^{-19} to 10^{-17} [B]	10^{-19} to 10^{-17}
Caprock Thermal Properties:		
Caprock Initial Temperature, ºC	25	25
Steam Chamber Temperature, ºC	250	250
K_{sf}, W/m•ºC	1.30 to 1.95 [C]	1.50
$\kappa_{Thermal}$, m^2/sec	4.0×10^{-7} to 9.0×10^{-7} [C]	5.0×10^{-7}
Caprock Magnetic Properties:		
μ_r, no unit	1	1
Coil Properties:		
Coil Radius, m		0.10
Coil Length, m		500
Number of Turns, no unit		200
Pitch Angle, degrees		15
Caprock Vertical Distance from Coil Center, m		5
Coil Current, A	48 to 84 [D]	10
Core Magnetic Relative Permeability, no unit	1000 to 6000	1000

[A] Given in Mase and Smith (1985).

[B] Given in Matthäi and Roberts (1996).

[C] Evaluated based on Fjær et al. (2008).

[D] Evaluated based on Vermeulen and Chute (1983).

Figures

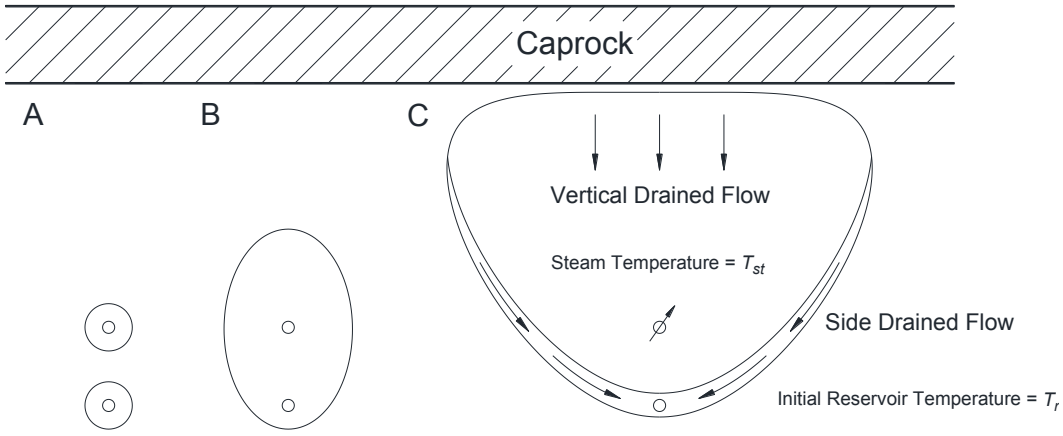

Figure 4.40. Cross section of SAGD process; Section A presents circulation phase, Section B presents early phase, and Section C presents steam injection phase (Modified from Irani and Ghannadi, 2013).

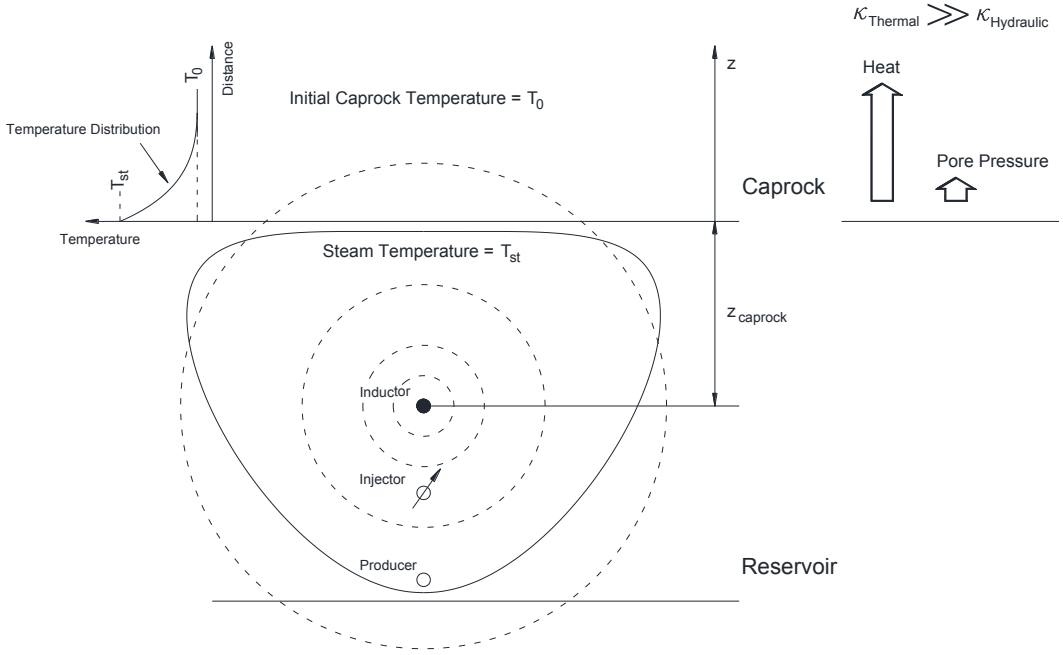

Figure 4.41. Illustration of simplified caprock thermal model used in this study, and related dimensions

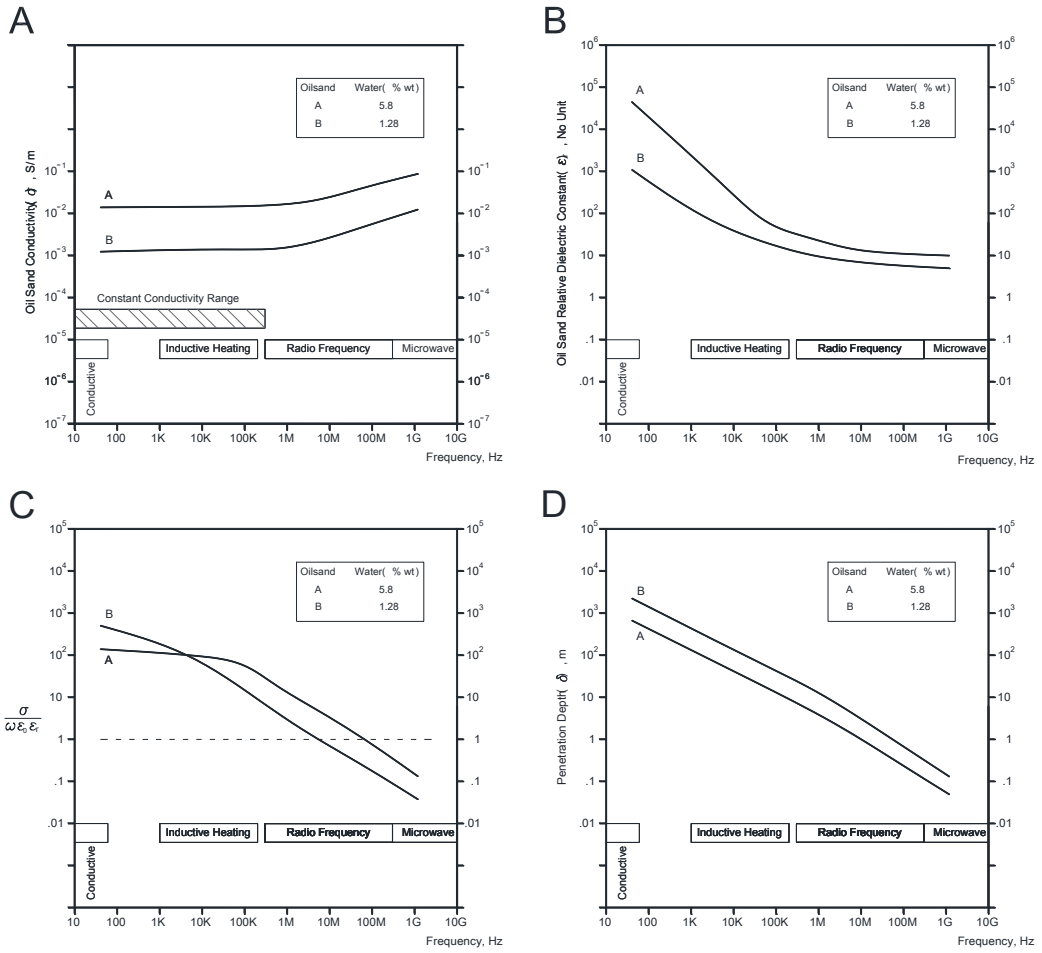

Figure 4.42. Average oil sand conductivity (Section A), relative dielectric constant (Section B), loss tangent (Section C) and penetration depth (Section D) a function of frequency

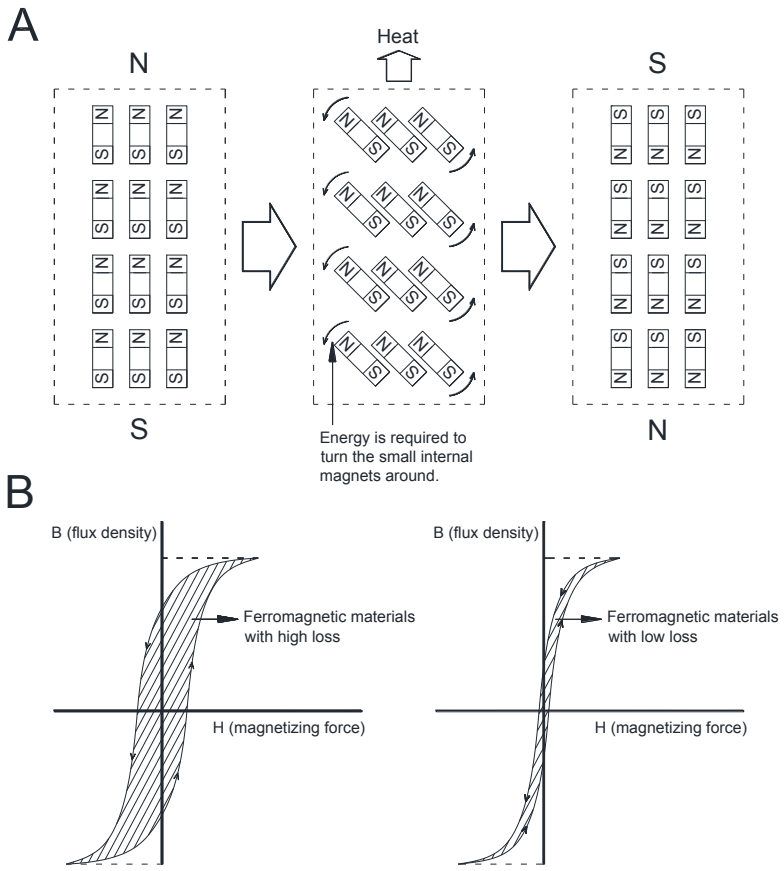

Figure 4.43. Illustration of hysteresis loss and effect on magnetic flux field strength (Section A); magnetization curves for ferromagnetic material with high loss and reservoir material with low loss (Section B) (modified from McMaster (1976) and Haimbaugh (2001))

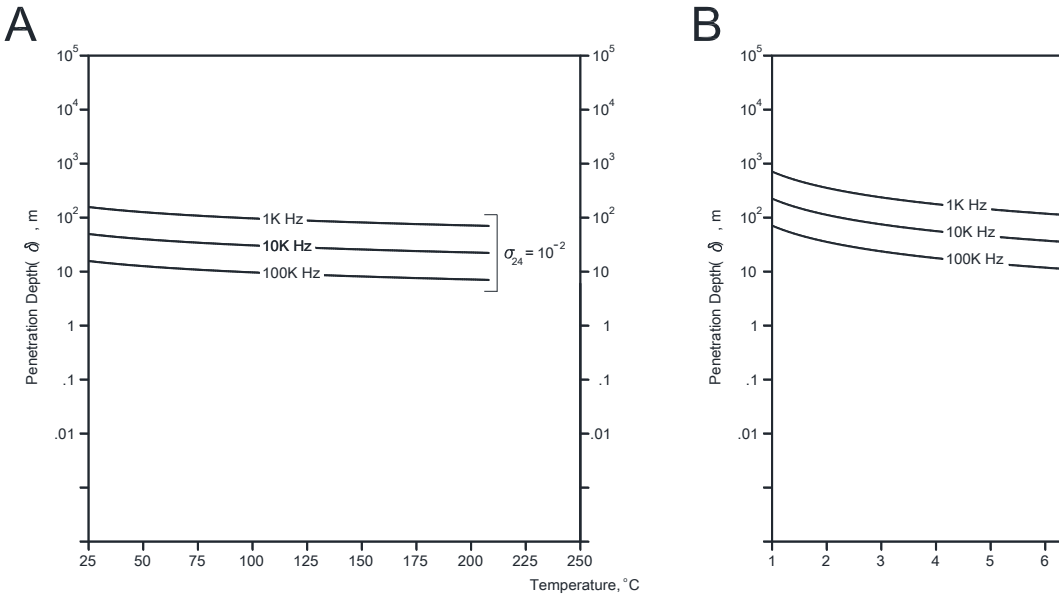

Figure 4.44. Variation of oil sand penetration depth a function of temperature (Section A), and a function of water content (Section B)

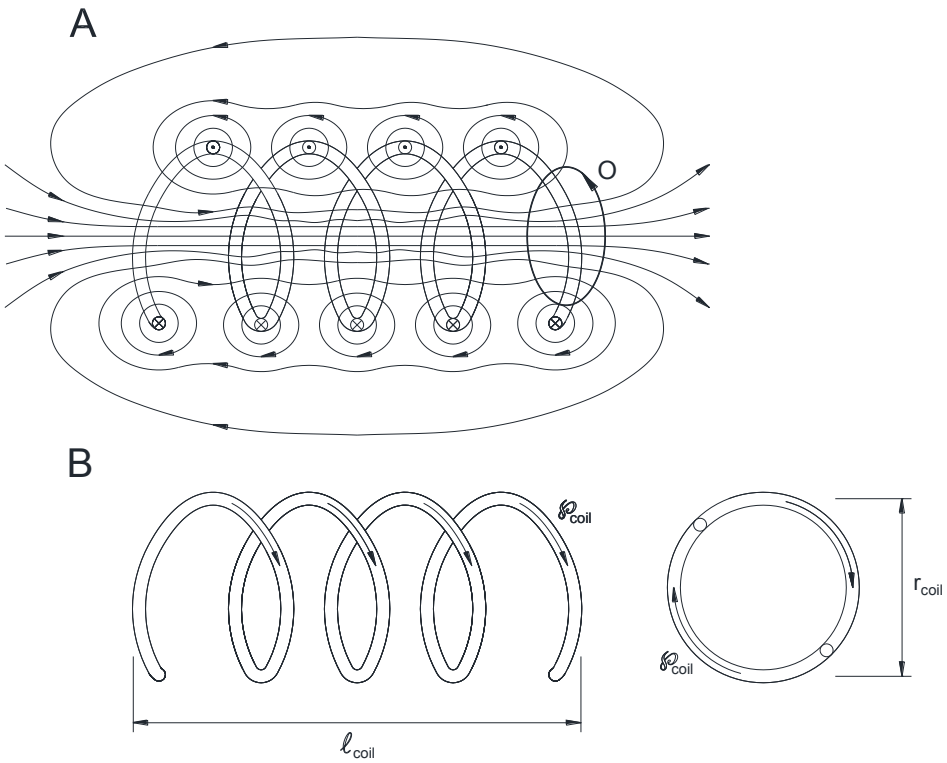

Figure 4.45. Illustration of field of magnetic induction associated with solenoid coil carrying electric current (Section A) (modified from Halliday and Resnick (1966)); and the solenoid coil dimensions (Section B)

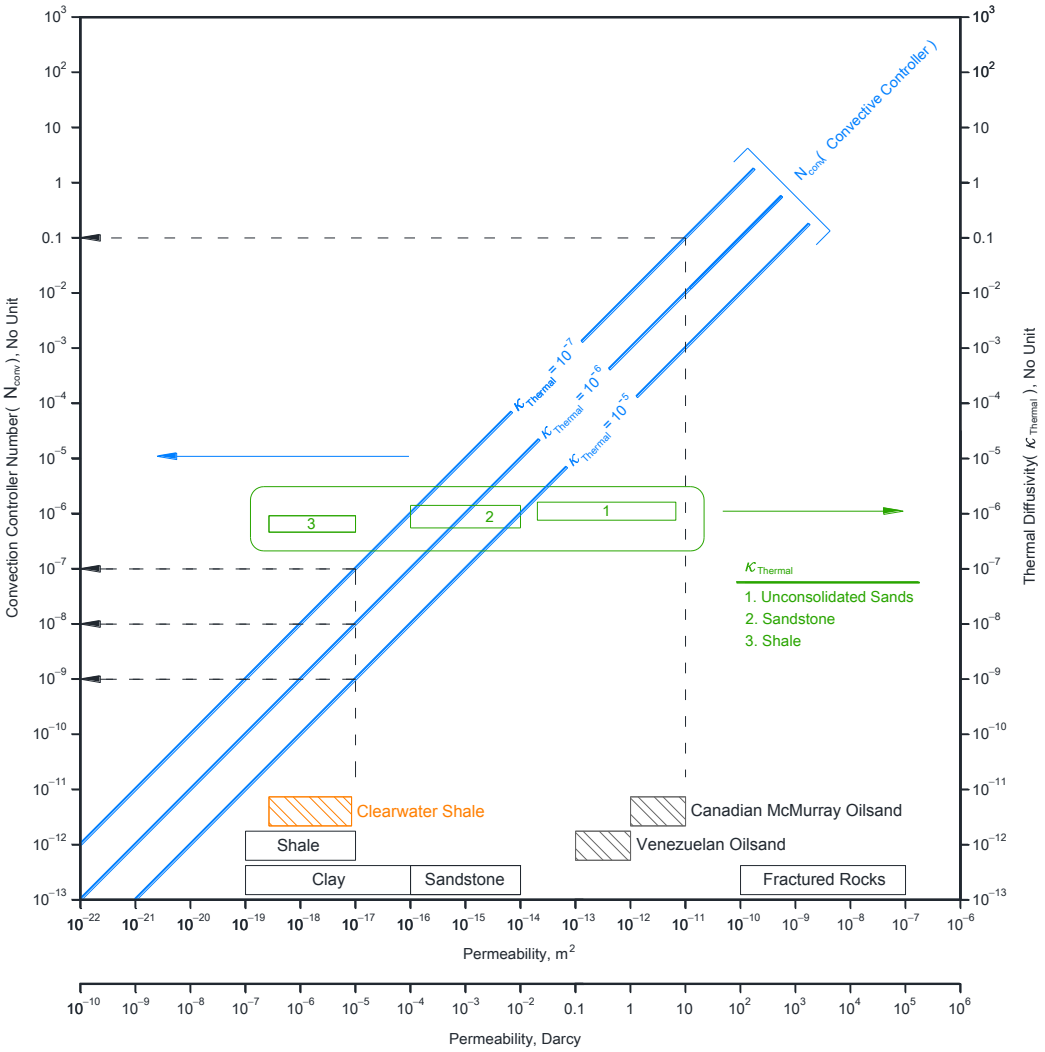

Figure 4.46. Variation of convection controller number (N_{conv}) versus formation permeability (k) for different thermal diffusivities ($\kappa_{Thermal}$)

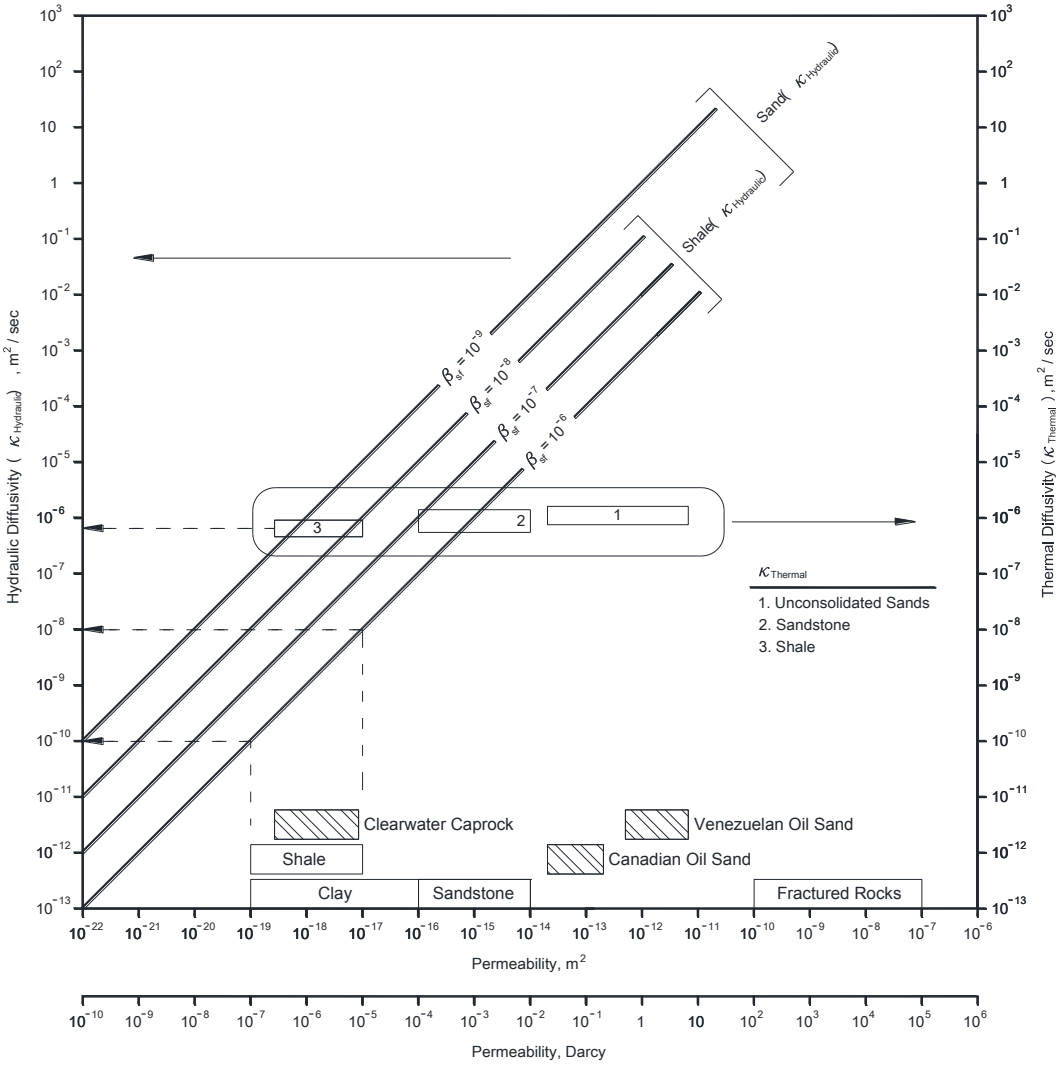

Figure 4.47. Variation of hydraulic diffusivity ($\kappa_{Hydraulic}$) and thermal diffusivity ($\kappa_{Thermal}$) versus formation permeability (k) for different compressibility of porous medium (β_{sf}), and their comparison for shale formations.

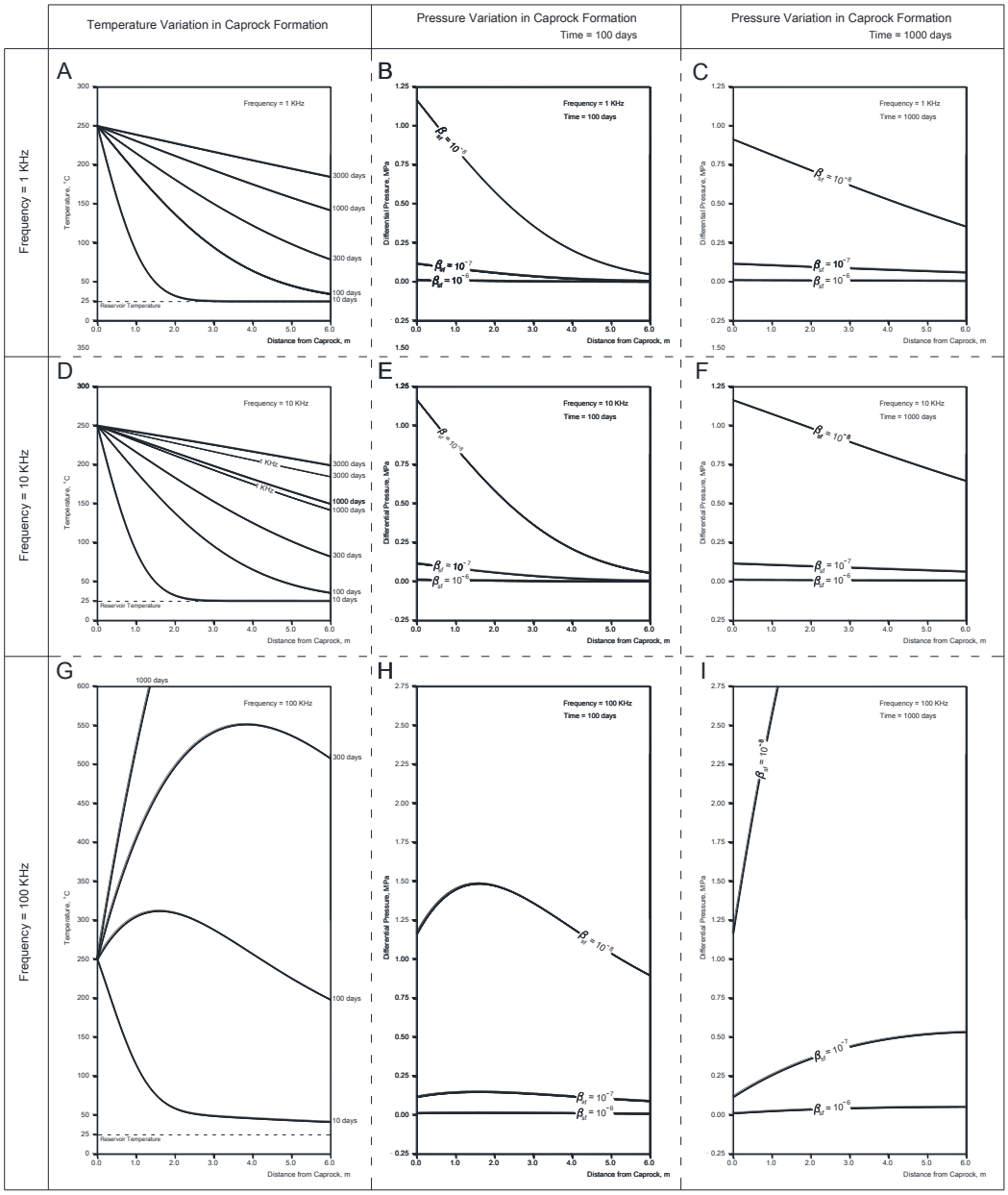

Figure 4.48. Variation of temperature in caprock for different applied frequencies (Section A, D, and G) and induced thermal pressure for different compressibility of porous medium (β_{sf}) (Sections B and C for 1 kHz; Sections E and F for 10 kHz; Sections H and I for 100 kHz). See Table 2.2 for caprock and coil properties.

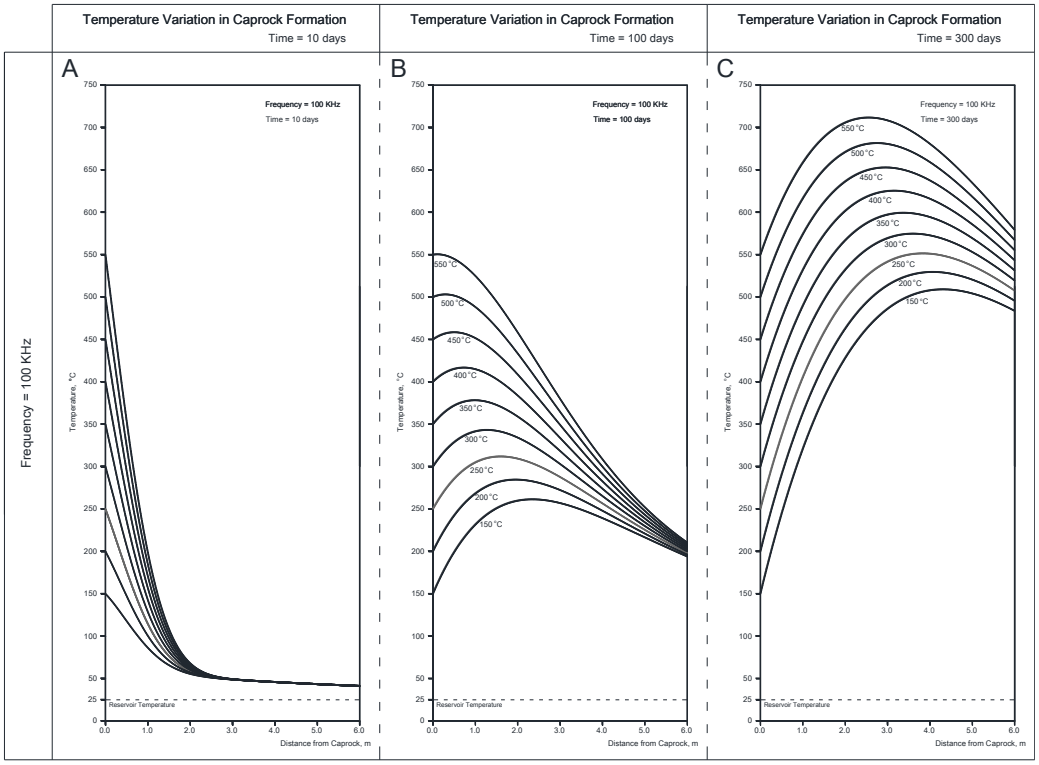

Figure 4.49. Variation of temperature in caprock for different bottom caprock boundary conditions; in the first 10 days (Section A), in the first 100 days (Section B) and in the first 300 days (Section C). The temperature variation is evaluated for 100 kHz.

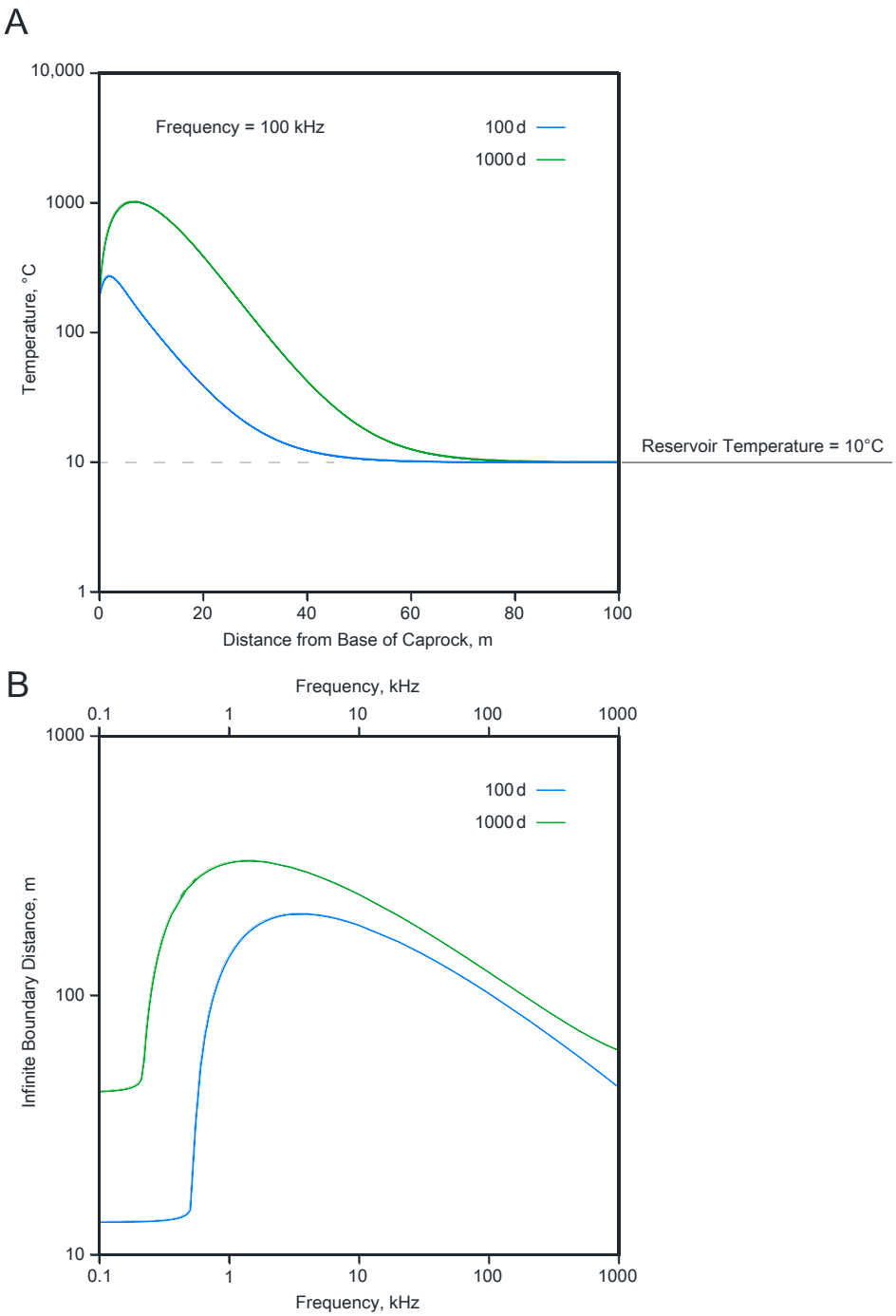

Figure 4.50. Temperature variation along the caprock width at 100 and 100 days (Section A); and variation of infinite boundary depth (at which temperature reaches 10 + 0.001 °C) vs. source frequency for 100 and 100 days (Section B).

This page is intentionally left blank.

5. Conclusions and Recommendations

5.1. Thesis Conclusions

The overall objective of this thesis is to evaluate the thermal pressurization in both SAGD and EM-SAGD process and also evaluate different method start-up phase. Specific objectives include:

- The analytical equation is presented for in Induction and RF-heating.
- In this thesis, we developed analytical equation for transient temperature profile within caprock of EM-SAGD.
- Developed the physics of thermo-hydro-mechanical pressurization in both one and two-phase flow.
- In this thesis, we developed pressurization in SAGD process for one and two-phase flow.
- In this thesis, we developed pressurization in EM-SAGD process for one-phase flow.
-
- The followings are highlights of this study:
-
- This study examines the relative roles of frequencies in EM-SAGD applications. The temperature enhancement of electromagnetic heating takes place with high frequencies (or high coil current).
- In EM-SAGD operation, the induced thermal pressure in low-compressibility mediums is comparable even for low frequencies, and can be problematic for shallow reservoirs.
- For thermal pressurization evaluation in EM-SAGD operations, the compressibility of the porous medium (β_{sf}) is the most important component of caprock in thermal pressurization, and it should be experimentally calculated with great care.
- In this study a framework is suggested to use the analytical solution given in this chapter 3 that is summarized as follows:
-

I. Use Figure 3.35 to evaluate Ω_{Λ} or Ω_{Λ}^{vap} for suggested caprock using the project steam injection temperature and caprock measured compressibility; for Athabasca SAGD projects use Ω_{Λ} for IHS formation and Ω_{Λ}^{vap} for Clearwater and Wabiskaw formations;

II. Use Figure 3.35 to evaluate Ω_{μ} for the project steam injection temperature;

III. Calculate the ratio of thermal diffusivity to hydraulic diffusivity of water-saturated and steam-saturated zones (Δ_w and Δ_{st}) using Equations 183 and 184;

IV. Assume the steam interface distance from the bottom of the caprock ($\xi_{interface}$);

V. Calculate the temperature profile in the caprock;

VI. Calculate the saturation pressure curve using the temperature profile in step 5.

VII. Calculate the pressure profile in the caprock, substituting Ω_{Λ} or Ω_{Λ}^{vap} and Ω_{μ} into Equations 185 and 186.

VIII. Intersection between the saturation pressure curve and the pressure profile should match the assumed steam interface ($\xi_{interface}$); if it is not matched go to step 4 and change the interface distance ($\xi_{interface}$);

IX. Finally, include the pressure rise from Equations 185 and 186 and decrease MOP value calculated either with mini-frac test, or using geomechanical simulation.

5.2. Directions for Future Work

We pointed out some potential directions for generalizing and improving upon the results presented in this thesis in the summaries of the individual chapters. Some other relevant issues are discussed below with the hope that solving these problems will move us closer towards finding a general solution for the pressurization in EM-heating projects.

- It is likely that the optimal solution to the start-up is not unique. And combination of different techniques such as solvent combination with RF-heating will be explored.
- Compared the analytical theories for RF-heating with ESEIEH™ field results.
- To this end, it is useful to modify the one-phase assumption for pressurization in inductive heating and present the analytical equation for two-phase flow system.
- Developing the numerical simulation to compare the results with analytical equation presented for pressurization due to EM-heating.
- Explored heterogeneity in EM-heating and also pressurization due to different EM-heating techniques.

This page is intentionally left blank.

Appendix A: Magnetic Flux (Φ) Passing Through Coil

A current-carrying wire produces a magnetic field in the area around it. A closed-loop wire such as a coil is sought in this study. Magnetic flux is a measure of the size of a magnetic field proportional to the net number of field lines passing through a loop of area (A) if the loop is tilted at an angle (η) from the field (B). The magnetic flux through the loop (i.e., coil shown in Figure A1) is identified using a dot-product:

$$\Phi = \vec{B} \cdot \vec{A} \qquad \text{A-1}$$

or

$$|\Phi| = |B| \times |A| \cos(\eta) \qquad \text{A-2}$$

where η is an angle between $\vec{A}$ and $\vec{B}$ which is the angle at which the loop has been tilted or simply a pitch angle of the coil.

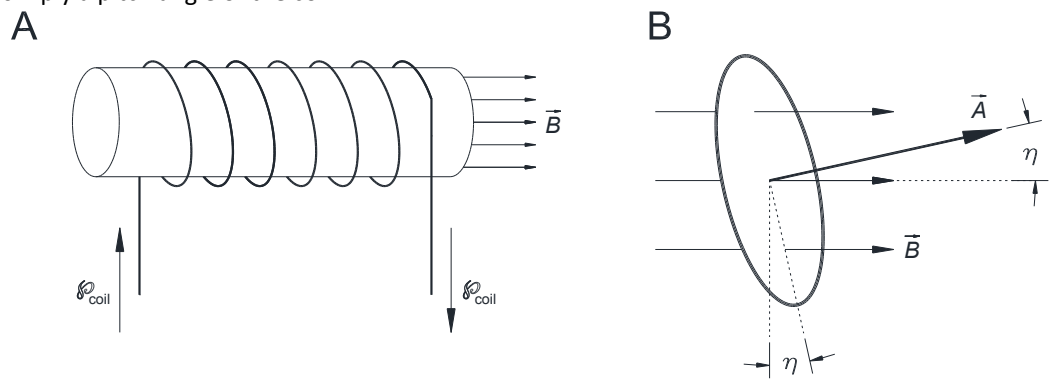

Figure A1. Finite wired-up coil (Section A) and magnetic flux passing through one loop, in which there is an angle η between loop and magnetic field (Section B).

The magnetic flux density (B) depends on the material of the core:

$$B = \mu_0 \mu_r^{core} H \qquad \text{A-3}$$

where μ_r^{core} is the magnetic relative permeability of the coil's core (no unit), which ranges between 2000 and 6000 for steel. The greater the relative permeability, the greater the flux. μ_0 is a constant showing the permeability (or magnetic permeability) of free space or vacuum (i.e., $4\pi \times 10^{-7} \approx 1.2566 \times 10^{-6}$ H/m (or Wb/A•m)); H is the effort a current applies to produce a magnetic field, called magnetic field intensity (H), which is calculated for a coil as:

$$H = \wp_{coil} \frac{N}{l_{coil}} = \wp_{coil} \bar{n} \qquad \text{A-4}$$

where $\wp_{coil}$ is the current flowing in the wires of the coil, or simply the coil current (A), N is the number of coil turns, l_{coil} is the mean length of the coil (m), and $\bar{n}$ is the number of coil turns per unit length. Substituting Equation A-4 in A-3, the magnetic flux density value (B) is:

$$B = \mu_0 \mu_r^{core} \wp_{coil} \frac{N}{l_{coil}} = \mu_0 \mu_r^{core} \wp_{coil} \bar{n} \qquad \text{A-5}$$

The cross-sectional area in Equation A-2 is an ellipse, with a and b equal to r and r/sin(η), respectively. The cross-sectional area is calculated as:

$$A = \pi a b = \pi r \times \frac{r}{\sin(\eta)} = \frac{\pi (r_{coil})^2}{\sin(\eta)} \qquad \text{A-6}$$

Substituting Equations A-5 and A-6 in A-2, the magnetic flux (Φ) value is:

$$|\Phi| = \mu_0 \mu_r^{core} \wp_{coil} \left[\pi (r_{coil})^2\right] \frac{N}{\ell_{coil}} \times \cot(\eta) = \mu_0 \mu_r^{core} \wp_{coil} \left[\pi (r_{coil})^2\right] \bar{n} \times \cot(\eta) \qquad \text{A-7}$$

Appendix B: Heat Generation for Inductive Heating

This appendix discusses and calculates heat generation for inductive heating processes. It is a modification of the work in 156876-PA (Ghannadi et al. 2013). The mathematical analysis of inductive heating can be quite complex, even for the simplest geometries. Electrical energy in eddy currents is converted into heat along these pathways because of electrical resistivity of connate water, which contains a large number of ions resulting from dissolved salts.

Inductive heating and RF heating have different heat generation mechanisms. Inductive heating is based on the Joule effect of eddy currents, and eddy current loss is based on displacement current (Figure 1.2c). Alternating current (AC) flowing through the coil generates an alternating magnetic field that cuts through the reservoir, and the so-called eddy currents dissipate energy and cause heat in a phenomenon called "eddy current loss". This loss is only propagated in a conductive medium. However, there is another, called "displacement loss," which propagates in both conducting and non-conducting mediums. Both losses need alternating current (AC), and if direct current (DC) is passed through a solenoid coil, the resulting field will not produce any heat inside the reservoir. Displacement loss is caused by displacement current, and eddy current loss by conductive current. Ampere's law is the main equation for calculating heat loss:

$$\nabla \times \vec{H} = \vec{J}_c + \vec{J}_d \qquad \text{B-1}$$

where $\vec{J}_c$ is conductive current and $\vec{J}_d$ is displacement current:

$$\vec{J}_d = \frac{\partial \vec{D}}{\partial t} \qquad \text{B-2}$$

Displacement current allows electromagnetic waves to propagate in non-conducting mediums, while conduction current only propagates in conducting mediums. If a conducting medium is characterized by conductivity of σ and permittivity of $\varepsilon_0\varepsilon_r$, then conduction current density is given by Ohm's law:

$$\vec{J}_c = \sigma \vec{E} \qquad \text{B-3}$$

and displacement current density is given by:

$$\vec{J}_d = \varepsilon_0\varepsilon_r \frac{\partial \vec{E}}{\partial t} \qquad \text{B-4}$$

Assuming that the electric field is a sinusoidal function of time (a valid assumption for AC):

$$E = E_0 \cos\omega t \qquad \text{B-5}$$

Substituting Equation B-5 in Equations B-3 and B-4 allows the calculation of conduction current and displacement current, respectively, as follows:

$$J_c = \sigma E_0 \cos\omega t \qquad \text{B-6}$$

$$J_d = -\omega\varepsilon_0\varepsilon_r E_0 \sin\omega t \qquad \text{B-7}$$

Then the maximum conduction current and displacement current are calculated, respectively, as:

$$\left|J_c\right|_{max} = \sigma E_0 \qquad \text{B-8}$$

$$\left|J_d\right|_{max} = \omega\varepsilon_0\varepsilon_r E_0 \qquad \text{B-9}$$

Finally, the ratio of conduction current to displacement current is calculated as:

$$\frac{\left|J_c\right|_{max}}{\left|J_d\right|_{max}} = \frac{\sigma}{\omega\varepsilon_0\varepsilon_r} \qquad \text{B-10}$$

"Eddy current loss" is also referred to as the "skin effect" because the eddy currents are concentrated on the outside of a conductor. It should be noted that these induced eddy currents in reservoirs run opposite to the source current of the inductor. Eddy currents induced in the reservoir diminish towards the further points. Their density inside a reservoir at distance r from the inductor is roughly calculated by the equation:

$$J_r = J_0 \exp\left(-\frac{(r - r_{coil})}{\delta_{Inductive}}\right) \quad \text{B-11}$$

where J_r is the current density at distance r from the inductor, J_0 is the current density at the inductor surface, r is the distance from the inductor to the core, r_{coil} is the mean radius of the coil turns, and δ is the penetration depth. The penetration depth ($\delta_{Inductive}$) is given by:

$$\delta_{Inductive} = \sqrt{\frac{2\rho}{\omega \mu_0 \mu_r}} = \sqrt{\frac{2}{\omega \mu_0 \mu_r \sigma}} \quad \text{B-12}$$

where ω is the angular frequency of the current (i.e., $2\pi \times$ frequency). In frequency format, this is changed to:

$$\delta_{Inductive} = \sqrt{\frac{\rho}{\pi \mu_0 \mu_r f_s}} = \sqrt{\frac{1}{\pi \mu_0 \mu_r f_s \sigma}} \quad \text{B-13}$$

where ρ is the electrical resistivity of the reservoir formation; σ is the conductivity; and f_s is the switching frequency. The penetration depth is described in metres as:

$$\delta_{Inductive} = 503\sqrt{\frac{\rho}{\mu_r f_s}} = 503\sqrt{\frac{1}{\mu_r f_s \sigma}} \quad \text{B-14}$$

To calculate eddy current loss, Faraday's line integral is applied around the path of the inductor (see Figure B-1, Section A):

$$\oint \vec{E}(t) \cdot dl = -\frac{d\Phi(t)}{dt} \quad \text{B-15}$$

where $\Phi(t)$ is the total flux within the inductor (circle O in Figure B-1, Section A). Multiplying both sides by conductivity (σ) and using Ohm's law yields:

$$\oint \vec{J}_0(t) \cdot dl = -\sigma \frac{d\Phi(t)}{dt} \quad \text{B-16}$$

The length around the inductor is $2\pi r_{coil}$. The current density around the inductor is in complex form:

$$J_0 = \frac{j\omega\sigma\Phi}{2\pi r_{coil}} \quad \text{B-17}$$

The absolute value is:

$$|J_0| = \frac{\omega\sigma|\Phi|}{2\pi r_{coil}} \quad \text{B-18}$$

Knowing eddy current loss as:

$$W_{EddyCurrent} = \frac{J^2(t)}{\sigma} \quad \text{B-19}$$

Total EM power radiated across radius r is calculated by integrating Equation B-19:

$$P_{Inductive} = \int_V \left(\frac{1}{T}\int_0^T W_{EddyCurrent}\, dt\right) dV = \int_V \left(\frac{1}{T}\int_0^T \frac{J_r^2 \sin^2(\omega t)}{\sigma}\, dt\right) dV = \int_V \left(\frac{1}{T} \times \frac{J_r^2}{\sigma}\int_0^T \frac{1-\cos(2\omega t)}{2}\, dt\right) dV = \int_V \left(\frac{1}{T} \times \frac{J_r^2}{\sigma} \times \frac{T}{2}\right) dV = \int_V \left(\frac{J_r^2}{2\sigma}\right) dV \quad \text{B-20}$$

where T is the switching period. If a direct current is passed through a thin solenoid coil, the resulting magnetic flux is identified using Ampere's law (see Appendix A):

$$|\Phi| = \mu_0 \mu_r^{core} \wp_{coil}\left[\pi (r_{coil})^2\right] \frac{N}{\ell_{coil}} \times \cot(\eta) = \mu_0 \mu_r^{core} \wp_{coil}\left[\pi (r_{coil})^2\right] \bar{n} \times \cot(\eta) \quad \text{B-21}$$

where N is the number of coil turns, μ_r^{core} is the magnetic permeability of the coil's core, which can be as large as 6000 for ferromagnetic cores such as steel, l_{coil} is the coil length, $\wp_{coil}$ is the

current flowing in the coil wires, or simply the coil current, r_{coil} is the mean radius of the coil turns, η is the pitch angle of the coil, and $\overline{n}$ is the number of coil turns per unit length. Then:

$$\left|J_0\right| = \frac{\omega\sigma}{2}\mu_0\,\mu_r^{core}\,\wp_{coil}\,r_{coil}\times\frac{N}{l_{coil}}\times\cot(\eta) \qquad \text{B-22}$$

Finally, the eddy current loss is evaluated, combining Equations B-11, B-20, and B-22:

$$P_{Inductive} = \int_V\left(\frac{J_0^{\,2}}{2\sigma}\exp\left[-\frac{2}{\delta}(r-r_{coil})\right]\right)dV = \frac{\sigma}{8}\left\{\omega\,\mu_0\,\mu_r^{core}\,\wp_{coil}\,r_{coil}\times\frac{N}{\ell_{coil}}\times\cot(\eta)\right\}^2\int_V\left(\exp\left[-\frac{2}{\delta}(r-r_{coil})\right]\right)dV$$

$$= \overline{P}_{Inductive}\int_V\left(\exp\left[-\frac{2}{\delta}(r-r_{coil})\right]\right)dV \qquad \text{B-23}$$

where

$$\overline{P}_{Inductive} = \frac{\sigma}{8}\left[\omega\mu_0\,\mu_r^{core}\,\wp_{coil}\,r_{coil}\times\frac{N}{\ell_{coil}}\times\cot(\eta)\right]^2 \qquad \text{B-24}$$

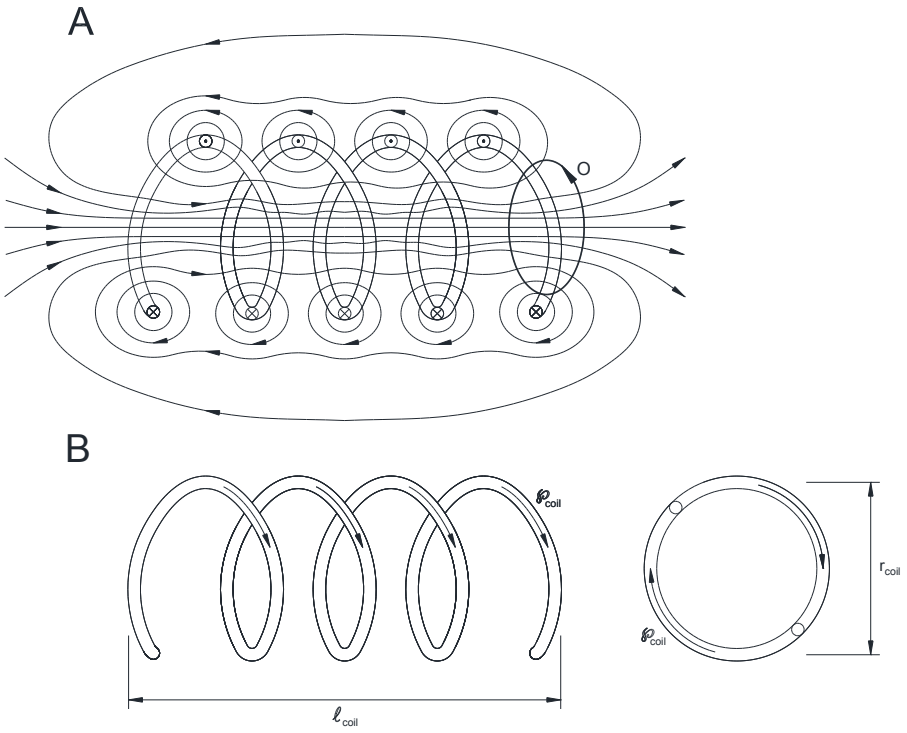

Figure B-1. Illustration of field of magnetic induction associated with solenoid coil carrying electric current (Section A) and of coil dimensions (Section B) (Courtesy of Ghannadi et al., 2013).

Appendix C- Sealability Effectiveness of Wabiskaw and IHS Formations

The purpose of this appendix is to discuss sealability effectiveness of Wabiskaw shaly unit (Wabsikaw D) and IHS formations. Although Clearwater formation considered as a regional caprock by the AER, the definition of the caprock and including other formations as a caprock is an ongoing question for SAGD industry.

Some previous studies show that steam rise during SAGD operation is constrained at the bottom of Upper McMurray shale and Wabiskaw shaly unit (Wabiskaw D). Chalaturnyk (1996) studied the observation wells and showed that Upper McMurray shale unit is halting steam vertical rise. Harvest Energy (2009) interpreted that the Wabiskaw D interval is laterally continuous marine shales (8 to 10 m thick) forms an effective caprock for BlackGold SAGD operations for both the McMurray formation and the Wabiskaw member bitumen reservoirs. Southern Pacific Resource (2011) proposed that the Wabiskaw shale and the Clearwater shale comprise the caprocks for Southern Pacific's MacKay Project. But due to Clearwater shale larger thickness and its uniformity, Southern Pacific interprets the Clearwater shale to be the primary caprock. Collins et al. (2013) proposed that Upper McMurray tidal-flat and Wabiskaw D mudstone can be considered as effective caprock for all SAGD projects and specifically for Ivanhoe's Tamarack project.

Although Upper McMurray shale and Wabiskaw shaly unit (Wabiskaw D) are acting as buffer zone to vertical steam rise and vertical pressure transmission, their capability as a competent caprock for SAGD projects need a more detail study. Their effectiveness is doubted as a result of small thickness (roughly 5 meters). Also as a result of shoreface environment in Wabiskaw D and channel deposition environment in Upper McMurray shale these members are generally coarser than Clearwater member and irregularly interbedded with *thin silty layers*. Total's Joslyn Creek SAGD blowout event can be an example of ineffectiveness of Upper McMurray shale which failed at the start-up phase of this project (Total E&P Canada Ltd., 2007; Uwiera-Gartner et al., 2011a, 2011b).

Ito et al. (2001) explore the growth of the steam chamber in UTF Phase B using numerical simulation. He discover that the steam chamber can penetrate into the IHS unit, but steam penetration is limited to two metres of the vertical distance from the bottom of the IHS unit. Although IHS deposits in the fluvial environment and are relatively discontinuous as a result. The erosional channels, estuarine tidal bar settings are the main results of discontinuity. It must be noted estuarine tidal bar mud beds are highly discontinuous compared to the lateral accretion of marine mud beds such as Clearwater shaly units in Athabasca deposits.

Appendix D- Theory of Linear Poroelasticity in Caprock Formations in SAGD Projects

In saturated formations, the pore space is filled with fluid. The pore pressure helps to counteract the mechanical stress carried through grain-to-grain contact. Pore pressure partly counters the load applied to the medium. As shown in Figure B1, the total stress in simplified manner is equal to the sum of the effective stress and the pore pressure. Pore pressure tends to push the grains apart and decrease the effective stress and frictional resistance in the formation. The poro-elastic factor (α_{Biot}) or Biot-Willis coefficient (usually called the Biot's coefficient) measures the efficiency of the pore pressure effect. The relationship between effective and total stress is given as:

$$\sigma'_{ij} = \sigma_{ij} - \alpha_{Biot} P \delta_{ij} \qquad \text{D1}$$

where σ'_{ij} is the effective stress and σ_{ij} is the total stress.

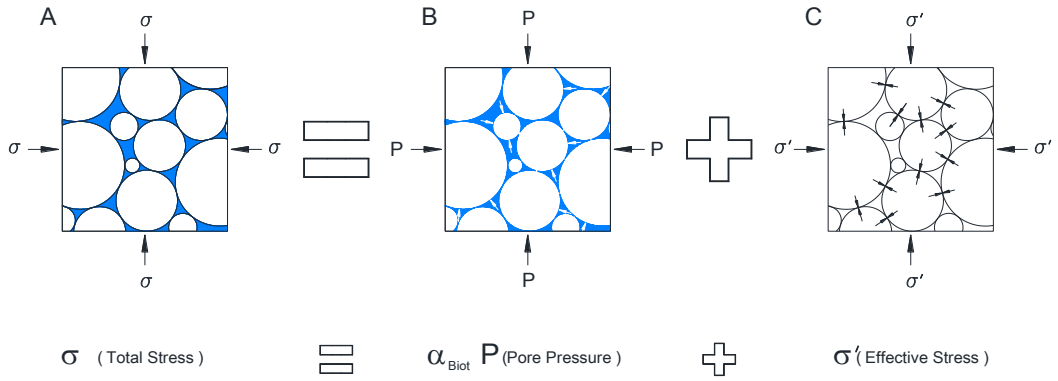

Figure D1. Illustration of "total stress" (Section A), "pore pressure" (Section B) and "effective stress" (Section C).

Biot's coefficient is the topic of many *seismic* and geophysical researches such as: Zoback and Byerlee (1975), Walls and Nur (1979), Raymer et al. (1980), Krief et al. (1990), Laurent et al. (1993), Klimentos et al. (1998), Lee (2002, 2003), Shafer et al. (2008), Sarker and Batzle (2008) and Havens (2011). The value of the Biot's coefficient (α_{Biot}) ranges between 0 and 1. However, studies such as Zoback and Byerlee (1975) and Walls and Nur (1979) experimentally calculate a Biot's coefficient (α_{Biot}) larger than unity. Authors of the present study believe that these values are associated with experimental errors and cannot be valid. The variation of the Biot's coefficient as a function of porosity is presented in Figure B2 for different formations. As shown for unconsolidated formations Biot's coefficient yields unity for porosities greater than 0.3, that means for both Athabascan oil sand reservoirs and Clearwater Shale Biot's coefficient is roughly equal to unity.

Biot coefficient is also a function of the confining stress (Klimentos et al. 1998), and it reduces as overburden stress increases. Based on Klimentos et al. (1998) for sandstone reservoirs with confining stress less than 6.9 MPa (1000 psi) which is equivalent to depths less than 350 meters such as the one in Athabasca oil sand reservoirs the Biot's coefficient is larger than 0.9. This can be a reason that Sarker and Batzle (2008) suggested Biot's coefficient of one for shallow reservoirs. Although some studies such as Chen et al. (2003) and Havens (2011) suggested values as low as 0.8 and 0.4, respectively, for shale formations. But these values measured for deep enviornments and cannot be a correct analogue for Clearwater Shale.

The following relationship is the basic equation that employed to calculate the Biot's coefficient (α_{Biot}) for a saturated non-fractured porous medium (Biot, 1941; Biot and Willis, 1957; Skempton, 1960; Nur and Byerlee, 1971; Verruijt, 1984):

$$\alpha_{Biot} = 1 - \frac{K_b}{K_s} \qquad \text{D2}$$

where K_s is the bulk modulus of the solid grains, and K_b is the bulk modulus of the porous medium (or matrix bulk modulus). The bulk moduli of the solid grains and the porous medium (i.e., K_s and K_b) can be determined experimentally by conducting standard soil mechanics tests. As this study assumes that the caprock has no extensive fracture systems, Equation B2 is assumed to be valid. Generally, for media with stiff matrix (i.e., $K_b \approx K_s$) the Biot's coefficient yielding small values close to zero (for example, Detournay and Cheng (1993) reported Biot's coefficient of Westerly granite equal to 0.01). And for media with appreciable porosity, matrix stiffness is much smaller than grain stiffness (i.e., $K_b << K_s$), the Biot's coefficient (α_{Biot}) is roughly equal to 1 [similar to Terzaghi's effective-stress principle (Terzaghi,1923)], and as a result the fluid volume expelled is equal to the volumetric dilation (Mase and Smith, 1987).

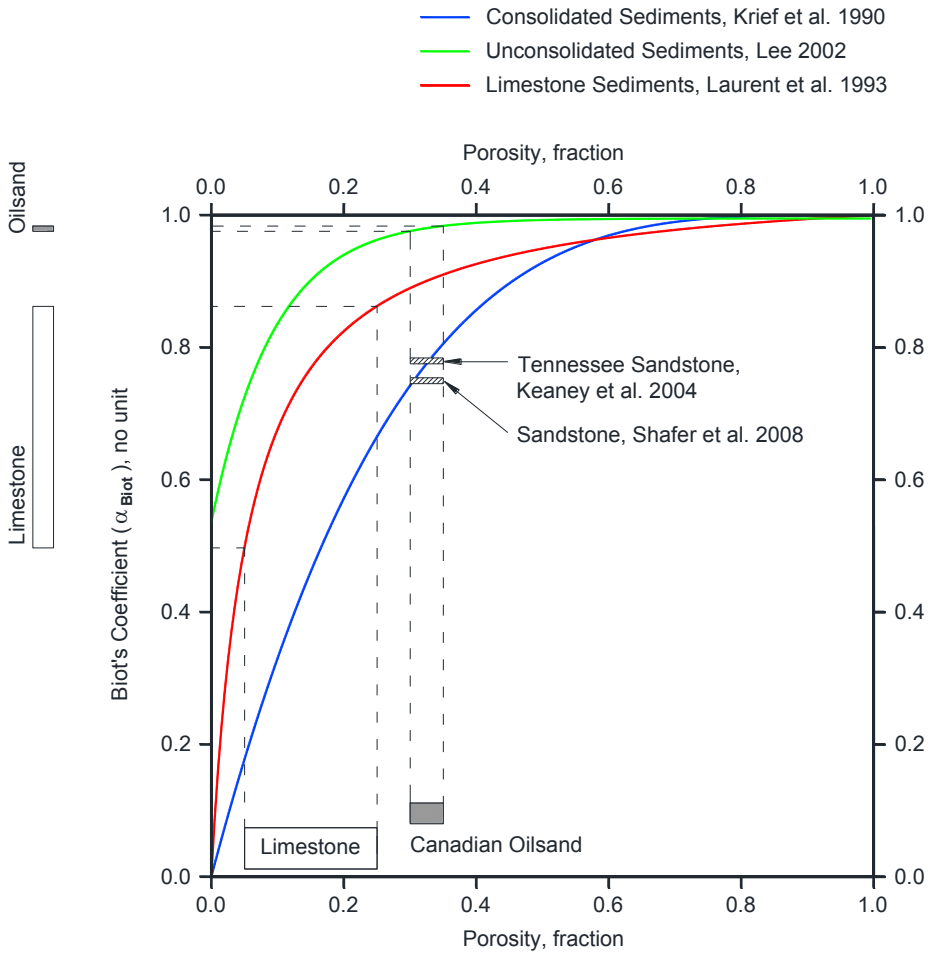

Figure D2. Variations of Biot's coefficient as a function porosity for different formations.

Figure D1 presents the relationship between total stress and effective stress for a Biot's coefficient equal to 1. Using Equation A1, the caprock equilibrium equations can be presented as:

$$\frac{\partial \sigma'_{zz}}{\partial t} + \frac{\partial (\alpha_{Biot} P)}{\partial t} = \frac{\partial \sigma_{zz}}{\partial t} \qquad \text{D3}$$

The effective stress can be calculated when making three possible assumptions. Firstly, assume that total stresses remains constant, which is valid if there is no constraint above the caprock (i.e., no stiffness in the overburden), or if the total stress increase in the z-direction due to thermal expansion is zero (i.e., thermal expansion coefficient of the caprock is equal to zero). Assuming constant total stress in the z-direction and negligible variation of total stress in the x-

and y-directions, the average change in value of effective normal stress acting on the solid grains ($\overline{\sigma}$) depends only on the pore pressure variation:

$$\frac{\partial \overline{\sigma}}{\partial t} = -\alpha_{Biot} \frac{\partial P}{\partial t} \quad \text{D4}$$

Secondly, assuming that the caprock does not experience shear deformation and is confined in all directions [i.e., strains in all directions are similar and compressive (uniform compression or Π -loading)], the resulting thermo-elastic effective stress is given by:

$$\frac{\partial \overline{\sigma}}{\partial t} = -\gamma_{sf} K \frac{\partial T}{\partial t} = -\gamma_{sf} \frac{E}{3(1-2\nu)} \frac{\partial T}{\partial t} \quad \text{D5}$$

where K is the bulk modulus of the caprock obtained by measuring the volumetric strain due to changes in applied stress *while holding pore pressure constant*. In other words, K can be called the drained bulk modulus.

Thirdly, assuming that caprock movements are only allowed in the z-direction, and that all other strains are zero, the resulting thermo-elastic effective stress is given by:

$$\frac{\partial \overline{\sigma}}{\partial t} = -\gamma_{sf} M \frac{\partial T}{\partial t} = -\gamma_{sf} \frac{E(1-\nu)}{(1+\nu)(1-2\nu)} \frac{\partial T}{\partial t} \quad \text{D6}$$

where M is the drained longitudinal modulus of the caprock.

For Clearwater shale and Colorado shale (i.e., regional caprocks for Athabasca and Cold Lake deposits), Equation D4 is the most suitable assumption. Uniform deformation assumption (Equation D5) cannot be valid since:

1. Both Clearwater and Colorado shales are shallow, and overburden weight is not large enough to confine caprock and create uniform deformation condition;
2. The overburden stiffness is small and cannot give enough support to the caprock, failing to satisfy the caprock confinement;
3. Heaving is the major challenge in SAGD application, supporting the idea of vertical movement, and;
4. Previous studies showed shear stress or deviatoric stress in the caprock during the SAGD operation. Yuan et al. (2011a, 2013) showed an increase in deviatoric stress is larger in deeper reservoirs.

While assuming caprock movement is limited to vertical movement (Equation D6) is not far from reality, there is an associated lateral movement in heaving distortion. This supports that there is a small lateral confinement in Clearwater shale and Colorado shale, and may cause a flaw in Equation D6.

A flaw is present in constant total stress assumption (Equation D4), since the total stress is usually not constant when there is a change in pore pressure. Known as “stress redistribution”, this is mostly small and can be ignored for uniform changes in pore pressure. As well as “stress redistribution”, the “jacking effect” caused by heaving reduces vertical total stress. *Error* using this assumption to calculate thermal-pressurization is much *less* to describe shallow reservoirs (such as Clearwater shale in Athabasca deposit), and it is larger to describe deep reservoirs (such as Colorado shale in Cold Lake deposit).

Appendix E- Volumetric Dilation as a Function of Temperature and Pore Pressure

The purpose of this appendix is to derive changes in volumetric strain (or volumetric dilation) as a function of temperature and pore pressure. The assumptions in Appendix E are valid for an isothermal system. Let us consider a system of porous medium of volume V_{Total}, including a pore space of volume V_{Pore}. Assuming a fully saturated medium, the volume of fluid containing the pore space is equal to the pore volume (i.e., $V_{Fluid} = V_{Pore}$). Then, the total combined volume of the solid and fluid is given by:

$$V_{Total} = V_{Solid} + V_{Pore} = V_{Solid} + V_{Fluid} \rightarrow V_{Pore} = V_{Total} - V_{Solid} \quad \text{E1}$$

Using porosity (ϕ) defined as:

$$\phi = \frac{V_{Pore}}{V_{Total}} \quad \text{E2}$$

Using Equation E2, the following identities are calculated as:

$$V_{Pore} = \phi V_{Total} \quad \text{E3-a}$$

$$V_{Solid} = (1-\phi) V_{Total} \quad \text{E3-b}$$

Using Equation E1, the first-time derivative for change in pore volume is given by:

$$\frac{\partial V_{Pore}}{\partial t} = \frac{\partial}{\partial t}\left[V_{Total} - V_{Solid}\right] = \frac{\partial V_{Total}}{\partial t} - \frac{\partial V_{Solid}}{\partial t} \quad \text{E4}$$

Then, using Equation C3-a, the right side of Equation E4 is given by:

$$\frac{\partial V_{Pore}}{\partial t} = \frac{\partial}{\partial t}\left[\phi V_{Total}\right] = V_{Total}\frac{\partial \phi}{\partial t} + \phi\frac{\partial V_{Total}}{\partial t} \quad \text{E5}$$

which, when substituted into Equation E4, becomes:

$$V_{Total}\frac{\partial \phi}{\partial t} + \phi\frac{\partial V_{Total}}{\partial t} = \frac{\partial V_{Total}}{\partial t} - \frac{\partial V_{Solid}}{\partial t} \quad \text{E6}$$

Equation E6 can be rearranged to give:

$$\frac{\partial \phi}{\partial t} = \frac{1}{V_{Total}}\left[\frac{\partial V_{Total}}{\partial t} - \phi\frac{\partial V_{Total}}{\partial t} - \frac{\partial V_{Solid}}{\partial t}\right] = \frac{1-\phi}{V_{Total}}\frac{\partial V_{Total}}{\partial t} - \frac{1}{V_{Total}}\frac{\partial V_{Solid}}{\partial t} \quad \text{E7}$$

Substituting V_{Total} from Equation E3-b into Equation E7, the time derivative for porosity can be evaluated as:

$$\frac{\partial \phi}{\partial t} = \frac{1-\phi}{V_{Total}}\frac{\partial V_{Total}}{\partial t} - \frac{1-\phi}{V_{Solid}}\frac{\partial V_{Solid}}{\partial t} \quad \text{E8}$$

The time derivatives for total volume and solid grains volume can be calculated using a derivative of effective stress ($\overline{\sigma}$) and the temperature:

$$\frac{\partial V_{Total}}{\partial t} = \left(\frac{\partial V_{Total}}{\partial \overline{\sigma}}\right)_T \frac{\partial \overline{\sigma}}{\partial t} + \left(\frac{\partial V_{Total}}{\partial T}\right)_{\overline{\sigma}} \frac{\partial T}{\partial t} \quad \text{E9-a}$$

$$\frac{\partial V_{Solid}}{\partial t} = \left(\frac{\partial V_{Solid}}{\partial \overline{\sigma}}\right)_T \frac{\partial \overline{\sigma}}{\partial t} + \left(\frac{\partial V_{Solid}}{\partial T}\right)_{\overline{\sigma}} \frac{\partial T}{\partial t} \quad \text{E9-b}$$

Substituting Equations E9-a and E9-b into Equation C8 yields:

$$\frac{\partial \phi}{\partial t} = (1-\phi)\left[\left(\frac{1}{V_{Total}}\frac{\partial V_{Total}}{\partial \overline{\sigma}} - \frac{1}{V_{Solid}}\frac{\partial V_{Solid}}{\partial \overline{\sigma}}\right)_T \frac{\partial \overline{\sigma}}{\partial t} + \left(\frac{1}{V_{Total}}\frac{\partial V_{Total}}{\partial T} - \frac{1}{V_{Solid}}\frac{\partial V_{Solid}}{\partial T}\right)_{\overline{\sigma}} \frac{\partial T}{\partial t}\right] \quad \text{E10}$$

The compressibility ($\overline{\beta}_{sf}$) and volumetric thermal expansion coefficient (γ_{sf}) of the porous medium are given by:

$$\overline{\beta}_{sf} = -\frac{1}{V_{Total}}\left(\frac{\partial V_{Total}}{\partial \overline{\sigma}}\right)_T \quad \text{E11-a}$$

$$\overline{\beta}_s = -\frac{1}{V_{Solid}}\left(\frac{\partial V_{Solid}}{\partial \overline{\sigma}}\right)_T \qquad \text{E11-b}$$

$$\gamma_{sf} = \frac{1}{V_{Total}}\left(\frac{\partial V_{Total}}{\partial T}\right)_{\overline{\sigma}} \qquad \text{E11-c}$$

$$\gamma_s = \frac{1}{V_{Solid}}\left(\frac{\partial V_{Solid}}{\partial T}\right)_{\overline{\sigma}} \qquad \text{E11-d}$$

Equation E10 can be simplified using Equations E11-a to E11-d. Assuming that the solid grains are incompressible (i.e., $\overline{\beta}_s \approx 0$):

$$\frac{\partial \phi}{\partial t} = (1-\phi)\left[(\overline{\beta}_s - \overline{\beta}_{sf})\frac{\partial \overline{\sigma}}{\partial t} + (\gamma_{sf} - \gamma_s)\frac{\partial T}{\partial t}\right] \approx (1-\phi)\left[-\overline{\beta}_{sf}\frac{\partial \overline{\sigma}}{\partial t} + (\gamma_{sf} - \gamma_s)\frac{\partial T}{\partial t}\right] \qquad \text{E12}$$

where $\overline{\beta}_{sf}$ and γ_{sf} are the linear elastic compressibility and volumetric thermal expansion coefficient of the porous medium. In laboratory work, two different linear volumetric thermal expansion coefficients are defined: *undrained* (γ_{sf}^{u}) and *drained* (γ_{sf}^{dr}). Since the undrained thermal expansion coefficient includes the increase in volume owing to an increase in pore pressure, it is larger than the drained thermal expansion coefficient (Settari, 1992). Since in this study, the porous volumetric deformation from pore-pressure change is presented separately, the drained thermal expansion coefficient should be considered ($\gamma_{sf} = \gamma_{sf}^{dr}$). Using the drained and undrained linear volumetric thermal expansion coefficient, the porous volumetric deformation can be presented as:

$$\Delta V_{Pore} = \gamma_{sf}^{dr} V_{Pore}\,\Delta T + \beta_{sf} V_{Pore}\Delta P = \gamma_{sf}^{u} V_{Pore}\,\Delta T \qquad \text{E13}$$

The volumetric strain can be evaluated as a function of porosity (Vermeer and De Borst, 1984):

$$\frac{\partial \varepsilon_v}{\partial t} = \frac{1}{(1-\phi)}\frac{\partial \phi}{\partial t} \qquad \text{E14}$$

Substituting Equation E12 in Equation E14, the volumetric strain (or volumetric dilation) is given by:

$$\frac{\partial \varepsilon_v}{\partial t} = \left[-\overline{\beta}_{sf}\frac{\partial \overline{\sigma}}{\partial t} + (\gamma_{sf} - \gamma_s)\frac{\partial T}{\partial t}\right] \qquad \text{E15}$$

Then, assuming that the total stresses in caprock remain constant (discussed in detail in Appendix D), the average change in value of effective normal stress acting on the solid grains ($\overline{\sigma}$) depends only on the pore pressure variation (from Equation D4):

$$\frac{\partial \overline{\sigma}}{\partial t} = -\alpha_{Biot}\frac{\partial P}{\partial t} \qquad \text{E16}$$

The rationale behind the constant total stresses in caprock as well as the proof for Equation E16 is discussed in Appendix D. In this case, the volumetric strain can be simplified as:

$$\frac{\partial \varepsilon_v}{\partial t} = \left[\overline{\beta}_{sf}\,\alpha_{Biot}\frac{\partial P}{\partial t} + (\gamma_{sf} - \gamma_s)\frac{\partial T}{\partial t}\right] \qquad \text{E17}$$

The solid-fluid compressibility can be calculated using a linear-elastic porous medium. If it is assumed that the caprock does not deform and is confined in all directions, the linear elastic compressibility can be evaluated using the bulk modulus:

$$\overline{\beta}_{sf} = \frac{1}{K} \qquad \text{E18}$$

where K is the bulk modulus of the caprock, given by:

$$K = \frac{2G(1+\nu)}{3(1-2\nu)} = \frac{E}{3(1-2\nu)} \qquad \text{E19}$$

where E is Young's modulus; G is the shear modulus, and ν is Poisson's ratio. Assuming that caprock movements are only allowed in the z-direction, and all the other strains are zero, the linear elastic compressibility can be evaluated using the longitudinal modulus:

$$\overline{\beta}_{sf} = \frac{1}{M} \quad \text{E20}$$

where M is the longitudinal modulus of the caprock, given by:

$$M = \frac{2G(1-\nu)}{1-2\nu} = \frac{E(1-\nu)}{(1+\nu)(1-2\nu)} \quad \text{E21}$$

The solid-fluid compressibility term can be given using the linear elastic compressibility and the Biot's coefficient as:

$$\beta_{sf} = -\overline{\beta}_{sf}\,\alpha_{Biot} == \frac{1}{V_{Pore}}\left(\frac{\partial V_{Pore}}{\partial P}\right)_T \quad \text{E22}$$

Equation E17 can be simplified, substituting the solid-fluid compressibility term for the linear elastic compressibility:

$$\frac{\partial \varepsilon_v}{\partial t} = \left[\beta_{sf}\frac{\partial P}{\partial t} + (\gamma_{sf} - \gamma_s)\frac{\partial T}{\partial t}\right] \quad \text{E23}$$

Knowing that the vertical strain is allowed in caprock formations, the compressibility of the solid-fluid or porous medium (β_{sf}) is given by:

$$\beta_{sf} = \frac{(1-2\nu)\alpha_{Biot}}{2G(1-\nu)} = \frac{(1+\nu)(1-2\nu)\alpha_{Biot}}{E(1-\nu)} \quad \text{E24}$$

This page is intentionally left blank.